Straight and Twisted Hollow-Core Waveguides for Integrated Photonic Applications

Johannes Bürger

München 2024

Straight and Twisted Hollow-Core Waveguides for Integrated Photonic Applications

Johannes Bürger

Dissertation
der Fakultät für Physik
der Ludwig-Maximilians-Universität
München

vorgelegt von
Johannes Bürger
aus Bremen

München, den 21.12.2023

Erstgutachter: Prof. Dr. Stefan A. Maier
Zweitgutachter: Prof. Dr. Alexander Szameit
Tag der mündlichen Prüfung: 20.02.2024

“Tout ce qu’un homme est capable d’imaginer,
d’autres hommes seront capables de le réaliser.”

— Jules Verne, Correspondence to his father, 1867 —

List of Publications

Related to this thesis

(8) Nov 2023 — J. Bürger, A. C. Valero, T. Weiss, S. A. Maier, and M. A. Schmidt | *Impact of coordinate frames on mode formation in twisted waveguides* | submitted, preprint on arXiv (2311.15770)

(7) Jan 2023 — J. Kim, J. Bürger, B. Jang, M. Zeisberger, J. Gargiulo, L. S. Menezes, S. A. Maier, and M. A. Schmidt | *3D-nanoprinted on-chip antiresonant waveguide with hollow core and microgaps for integrated optofluidic spectroscopy* | Optics Express (Vol. 31, 2833)

(6) Oct 2022 — J. Kim, R. Förster, T. Wieduwilt, B. Jang, J. Bürger, J. Gargiulo, L. S. Menezes, C. Rossner, A. Fery, S. A. Maier, and M. A. Schmidt | *Locally structured on-chip optofluidic hollow-core light cages for single nanoparticle tracking* | ACS Sensors (Vol. 7, 2951)

(5) Oct 2022 — J. Kim, B. Jang, T. Wieduwilt, S. C. Warren-Smith, J. Bürger, S. A. Maier, and M. A. Schmidt | *On-chip fluorescence detection using photonic bandgap guiding optofluidic hollow-core light cage* | APL Photonics (Vol. 7, 106103)

(4) Sep 2022 — J. Bürger, V. Schalles, J. Kim, B. Jang, M. Zeisberger, J. Gargiulo, L. S. Menezes, M. A. Schmidt, and S. A. Maier | *3D-nanoprinted anti-resonant hollow-core microgap waveguide - an on-chip platform for integrated photonic devices and sensors* | ACS Photonics (Vol. 9, 3012)

Featured on the **supplementary cover** of ACS Photonics.

(3) Jun 2021 — B. Jang, J. Gargiulo, J. Kim, J. Bürger, S. Both, H. Lehmann, T. Wieduwilt, T. Weiss, S. A. Maier, and M. A. Schmidt | *Fiber-integrated hollow-core light cage for gas spectroscopy* | APL Photonics (Vol. 6, 061301)

(2) Mar 2021 J. Bürger, J. Kim, B. Jang, J. Gargiulo, M. A. Schmidt, and S. A. Maier | *Ultrahigh-aspect-ratio light cages: fabrication limits and tolerances of free-standing 3D nanoprinted waveguides* | Optical Materials Express (Vol. 11, 1046)

Highlighted as Spotlight on Optics by Optica Publishing Group.

(1) Dec 2020 J. Kim, B. Jang, J. Gargiulo, J. Bürger, J. Zhao, S. Upendar, T. Weiss, S. A. Maier, and M. A. Schmidt | *The optofluidic light cage on-chip integrated spectroscopy using an antiresonance hollow core waveguide* | Analytical Chemistry (Vol. 93, 752)

Further works

(S5) Jul 2023 S. Lee, C. Fan, A. Movsesyan, J. Bürger, F. J. Wendisch, L. S. Menezes, S. A. Maier, H. Ren, T. Liedl, L. V. Besteiro, A. O. Govorov, and E. Cortés | *Unraveling the chirality transfer from circularly polarized light to single plasmonic nanoparticles* | submitted

(S4) Oct 2023 L. Kühner, F. J. Wendisch, A. A. Antonov, J. Bürger, L. Hüttenhofer, L. S. Menezes, S. A. Maier, M. V. Gorkunov, Y. Kivshar, and A. Tittl | *Unlocking the out-of-plane dimension for photonic bound states in the continuum to achieve maximum optical chirality* | Light Science & Applications (Vol. 12, 250)

(S3) Mar 2022 M. Ossiander, K. Golyari, K. Scharl, L. Lehnert, F. Siegrist, J. Bürger, D. Zimin, J. A. Gessner, M. Weidman, I. Floss, V. Smejkal, S. Donsa, C. Lemell, F. Libisch, N. Karpowicz, J. Burgdörfer, F. Krausz, and M. Schultze | *The speed limit of optoelectronics* | Nature Communications (Vol. 13, 1620)

(S2) Nov 2020 S. Pathak, R. Obaid, S. Bhattacharyya, J. Bürger, X. Li, J. Tross, T. Severt, B. Davis, R. C. Bilodeau, C. A. Trallero-Herrero, A. Rudenko, N. Berrah, and D. Rolles | *Differentiating and quantifying gas-phase conformational isomers using coulomb explosion imaging* | The Journal of Physical Chemistry Letters (Vol. 11, 10205)

(S1) Sep 2020 H. Ren, X. Fang, J. Jang, J. Bürger, J. Rho, and S. A. Maier | *Complex-amplitude metasurface-based orbital angular momentum holography in momentum space* | Nature Nanotechnology (Vol. 15, 948)

Contents

List of Figures

List of Tables

Zusammenfassung

Hohlkernfasern leiten Licht direkt innerhalb von Flüssigkeiten oder Gasen und eignen sich daher ideal für Anwendungen, die eine starke Licht-Materie Wechselwirkung erfordern. Insbesondere verdrillte Varianten dieser Fasern sind aktuell von Interesse, da sie die Nutzung von Licht mit zirkularer Polarisation oder Bahndrehimpuls (OAM) ermöglichen. Einer breiten Verwendung stehen allerdings fehlende Methoden zur Chipintegration und lange Analyt-Austauschzeiten entgegen, da der hohle Kern nur von den Endflächen aus zugänglich ist.

Hier lösen wir diese Probleme mithilfe eines 3D-Nanodruckverfahrens, basierend auf Zwei-Photonen-Polymerisation, welches erlaubt Hohlkernwellenleiter direkt auf Siliziumchips herzustellen. Zwei Geometrien werden durch Transmissionsmessungen, Simulationen und analytischer Theorie untersucht: "Light Cages" und "Microgap" Wellenleiter. Durch einen seitlich offenen Kern können die Diffusionszeiten deutlich reduziert werden, was am Beispiel von Absorptions- und Fluoreszenzspektroskopie verdeutlicht wird. Im Vergleich zu Kapillaren sind die Austauschzeiten für Flüssigkeiten um das Fünffache reduziert, während sich die Füllzeiten für Gase kaum von denen in Küvetten unterscheiden.

Im Vergleich der beiden Wellenleiter zeigt sich, dass Microgap Wellenleiter geringere Transmissionsverluste (0,4 - 0,7 dB/mm im sichtbaren Bereich), größere Transmissionsfenster ($\Delta\lambda = 200$ nm) und kürzere Herstellungszeiten (10 min/mm) bieten. Statistische Analysen verdeutlichen die hohe Reproduzierbarkeit des Herstellungsverfahrens, mit Abweichungen von 2 nm innerhalb eines Chips und 15 nm zwischen verschiedenen Chargen.

Darüber hinaus demonstrieren wir den ersten chipintegrierten verdrillten Hohlkernwellenleiter. Die hergestellten verdrillten Light Cages weisen eine Ganghöhe von 90 µm auf, weniger als die Hälfte von vergleichbaren Glasfasern. Optische Messungen zeigen, dass die Verdrillung chirale Resonanzen erzeugt, in denen Licht einer bestimmten Händigkeit mit einer verlustbehafteten Kernmode höherer Ordnung gekoppelt wird, was zu einem starken zirkularen Dichroismus von 0,8 dB/mm führt. Unterstützend wird eine theoretische Analyse der verdrillungsinduzierten Phänomene in axial und außeraxial verdrillten Wellenleitern präsentiert, einschließlich des Auftretens superchiraler Felder, Spin- und OAM-abhängiger räumlicher Modeneigenschaften, des Ursprungs von zirkularer und OAM-Doppelbrechung und einer Erläuterung der häufigsten Koordinatentransformationen für deren Simulation.

Diese Ergebnisse ebnen den Weg, um die jahrelange Forschung an (verdrillten) Hohlkernfasern in chipintegrierte Anwendungen umzusetzen, wie kompakte Echtzeit-Sensoren für Umweltüberwachung, Point-of-Care Diagnostik, chemische Analysen, Lab-on-a-Chip Geräte und chirale Spektroskopie sowie im Bereich nichtlinearer Optik und Quantenoptik.

Abstract

Hollow-core fibers guide light directly inside liquids or gases making them ideal for applications requiring strong light-matter interaction. Recently, twisted versions of these fibers have attracted additional interest, unlocking applications involving circular polarization or orbital angular momentum (OAM). However, their widespread use in practical devices is hindered by the lack of methods for chip integration, and impracticably long analyte exchange times, given that the hollow core can only be accessed from its end faces.

In this thesis, we overcome these limitations by using two-photon-polymerization-based 3D nanoprinting to implement hollow-core waveguides directly on silicon chips. Two geometries are investigated via transmission measurements, simulations, and analytical theory: the previously reported light cage, and the newly introduced microgap waveguide. Their unique design allows side-wise access to the core leading to drastically decreased diffusion times, showcased on the example of absorption and fluorescence spectroscopy. Remarkably, the exchange times for liquid analytes were reduced five-fold compared to equivalent capillaries, while filling times for gases were nearly indistinguishable from those of cuvettes.

Comparing the two waveguides, microgap waveguides were found to offer better performance metrics, such as lower propagation loss (0.4 - 0.7 dB/mm in the visible, 1.3 dB/mm at $\lambda = 1400$ nm), larger spectral transmission windows ($\Delta\lambda = 200$ nm), and shorter fabrication times (10 min/mm). A statistical evaluation indicates high repeatability of the fabrication method with variations in the realized dimensions as low as 2 nm in a single fabrication run and 15 nm for different batches.

Furthermore, this thesis marks the first demonstration of an on-chip twisted hollow-core waveguide. The realized twisted light cages feature a record helical pitch distance of 90 µm, less than half that of comparable glass fibers. Optical measurements reveal twist-induced chiral resonances selectively coupling light of one handedness to a lossy higher-order core mode, resulting in strong circular dichroism of 0.8 dB/mm. The results are supported by extensive theoretical analysis of twist-induced phenomena in both on- and off-axis twisted waveguides, including the emergence of superchiral fields, spin- and OAM-dependent spatial mode properties, the origin of circular and OAM birefringence, and a discussion of the most common coordinate transformations used in their simulation.

The presented results open the door for translating years of (twisted) hollow-core fiber research to on-chip devices, enabling compact optical sensors for real-time applications like environmental monitoring, point-of-care testing, chemical analysis, lab-on-a-chip devices, and chiral spectroscopy, as well as applications in nonlinear and quantum optics.

Chapter 1

Introduction

Beginning with the first successful demonstration of a laser in 1960 [1], the field of photonics has shaped both our everyday world and scientific research beyond recognition. The high level of control over the electromagnetic field reached by advances in modern laser technology nowadays gives experimental access to timescales of attoseconds (10^{-18} s) [2], lengthscales of a thousandth of the diameter of a proton (10^{-18} m) [3], and allows trapping and manipulation of single atoms [4]. Maybe unsurprisingly, many Nobel Prizes in physics have been awarded for these advances and related applications, with the most recent examples being the detection of gravitational waves in 2017 [5], the pioneering of quantum information science using entangled photon pairs in 2022 [6], and the generation of ultrashort laser pulses in 2018 [7] and 2023 [8].

On the technological side, applications of photonics were similarly disruptive, for example, extreme ultraviolet lithography used by high-end chipmakers today allows to create **integrated circuits** with feature sizes down to 8 nm [9], while photolithography in general enables virtually all electronic devices that we rely on.

Transitioning to the topic of this thesis, a further application of photonic technology are **optical fibers**, the photonic analog of an electronic wire, transporting light from one location to another. Similar to lasers, research into optical fibers took off in the 1960s with the development of so-called **step-index fibers** [10]. These consist of at least two elements, a core made of a material with a high refractive index, and a cladding of a lower refractive index (Fig. 1.1(a)). When light is coupled into the core, it impinges onto the core-cladding interface under a shallow angle and is reflected back due to total internal reflection (similar to a diver not being able to look out of the water if the viewing angle is too shallow because the refractive index of water is higher than that of air). Such fibers are created by heating a glass preform to temperatures of about 2000°C (above the glass transition temperature) [11], after which the softened material is drawn into a micrometer-sized strand using large (∼10 m high) fiber drawing towers. Such fibers can readily be fabricated on kilometer lengthscales and transmit light over a distance of about 100 km before amplification is required. Such a low signal attenuation and the fact that light can be used to transmit information independently at multiple wavelengths make fibers far superior to electronic cables for telecommunication purposes. Today, fiber

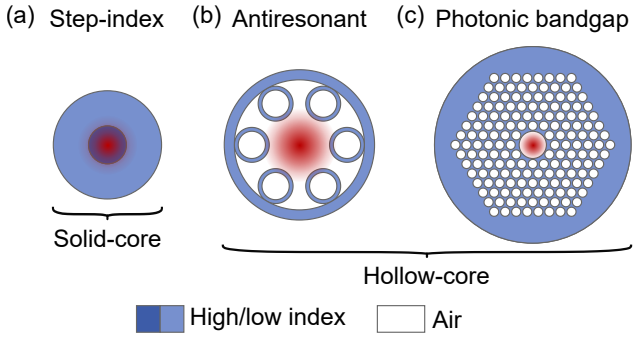

Figure 1.1: Common fiber geometries. (a) In a step-index waveguide, light is confined in a material of higher refractive index by total internal reflection. (b,c) In hollow-core waveguides, light propagates in air or other low-index media. Confinement can be provided by the antiresonance effect shown in (b) for a revolver hollow-core fiber. A periodic cladding provides confinement via a photonic bandgap with an example being the photonic crystal fiber in (c). Waveguide mode is sketched in red.

optical communication forms the backbone of the internet with undersea cables connecting different continents. Due to the large social impact of this innovation, Charles Kao, who initially identified suitable materials for these fibers [12], was awarded the Nobel Prize in 2009 [13].

While the propagation loss of step-index fibers has reached extremely low values, it is always fundamentally limited by Rayleigh scattering on residual material impurities or absorption of the material. Therefore, the idea seemed appealing to create fibers where light is guided in air or vacuum, where the losses are not limited by the material. However, for such **hollow-core waveguides** another light guidance mechanism needed to be identified as the index of air is lower than that of common materials preventing guidance via total internal reflection. To understand the alternative approaches, it is important to be familiar with the concept of waveguide modes, which are a set of solutions to the underlying Maxwell's equations (explained in more detail in Section 2.1). Generally, modes are localized either to the core, cladding, or the space surrounding the waveguide. Confining light to the core therefore requires that light cannot couple from the core mode to any of the cladding or free-space modes. One approach to achieve this involves creating a cladding with a periodic microstructure (Fig. 1.1(c)). Similar to electrons in crystalline solids, this periodicity creates a gap in the band structure for certain frequency ranges [14]. Within this **photonic bandgap** no modes are available in the cladding, thus preventing light from leaving the core volume. It turns out, however, that even simpler geometries can be used, which just consist of a single ring of cladding elements (Fig. 1.1(b)). Here, light is confined in the low-index medium by the **antiresonance effect** [15]. In essence, a difference in the momenta of photons of the core mode and those of the cladding mode inhibit coupling as, otherwise, momentum conservation would be violated. Designing such antiresonant waveguides typically relies on numerical or analytical calculations of the involved modes, which is introduced in Section 3.1. Generally, the distinction between photonic bandgap guidance and antiresonance guidance lacks a clear boundary (for an in-depth comparison of the guidance mechanisms and an overview of possible fiber geometries see [16] and Fig. 1.7 therein). Meticulous engineering of the cladding elements and refining of the fiber-drawing

process led to substantial advances ever since the first demonstration of a microstructured hollow-core fiber in 1999 [17]. Today, the lowest loss achieved with a hollow-core fiber is 0.17 dB/km [18], which matches that of the best solid-core fibers (0.14 dB/km) [19]. Further improvements in the accuracy of the fabrication process might therefore result in hollow-core fibers replacing the current solid-core fibers for telecommunication purposes in the coming years [20].

Apart from the potentially lower propagation loss, hollow-core waveguides have a further advantage over solid-core waveguides: as light is guided inside the hollow core, one can fill the core with gases or liquids, which can then interact with the confined light over long distances. This **strong light-matter interaction** can be used for a number of purposes [21]. Most relevant is currently the use in nonlinear optics, where light-gas interaction at high intensities is employed for supercontinuum generation and compression of ultrashort laser pulses[1]. In this thesis, we study the application of hollow-core waveguides in **optical sensing techniques**, which can similarly benefit from the increased interaction length. Here, some of the most relevant techniques used in chemical analysis and biomedical applications are infrared (IR) absorption spectroscopy, Raman spectroscopy, and fluorescence spectroscopy. All three techniques characterize a sample based on the energy of molecular vibrations (and rotations) as shown in Fig. 1.2.

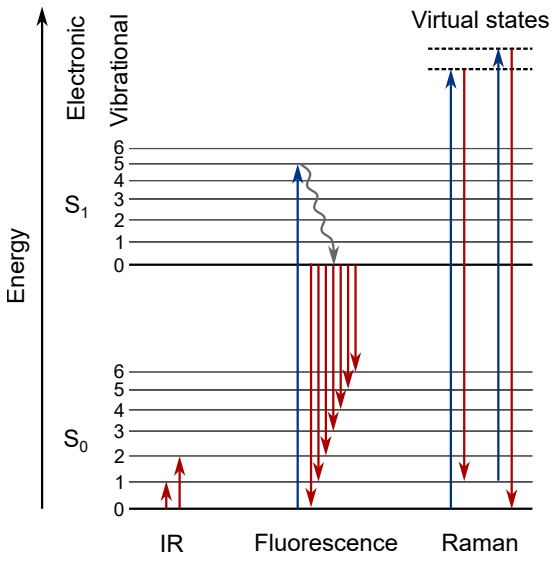

Figure 1.2: Jablonski diagram illustrating key processes for spectroscopic sensing applications. Red arrows denote the measured energy, either via absorption (IR spectroscopy), emission (fluorescence spectroscopy), or scattering (Raman spectroscopy). Fluorescence involves nonradiative transitions (curved gray arrow) to the lowest vibrational level of the excited electronic state, mediated by collision with other molecules. Raman scattering can be included in this diagram via virtual excited states. A decay from these states can either reduce or increase the energy of the scattered photon by that of the vibrational excitation (Stokes or Anti-Stokes scattering, respectively).

In **IR spectroscopy**, the energy of a photon is absorbed and excites the molecule to a higher vibrational state, leaving a characteristic absorption line in the spectrum of the transmitted light. Raman spectroscopy, on the other hand, relies on inelastic scattering of light on a molecule, reducing or increasing the energy of the photon by the energy of the vibration. Both techniques are complementary, as IR absorption probes transitions where the dipole moment of the molecule changes, while Raman scattering probes transitions

[1] As a side note, spectral broadening in gas-filled hollow-core fibers is often the first step in the aforementioned generation of attosecond pulses.

with a change in polarizability[2]. Lastly, **fluorescence spectroscopy** drives an electronic transition of the molecule using light of a short wavelength (typically in the ultraviolet) and measures the characteristic spectrum of the re-emitted light, which covers a range of longer wavelengths due to the loss of energy to the different molecular vibrations, as shown in Fig. 1.2. The resulting characteristic spectral features then allow to quantify which functional groups or specific molecules are present in the sample. All of these three techniques have previously been used in the context of hollow-core fibers [22], demonstrating fiber-integrated IR absorption [23, 24] and fluorescence spectroscopy [25, 26], as well as fiber-enhanced Raman spectroscopy [27, 28, 29]. The measured detection limits can be comparable to those of established techniques used in analytical chemistry labs, for example, a concentration of 0.02 nM of fluorescein dye has been detected in a hollow-core fiber [26] compared to 0.025 nM of a similar dye in liquid chromatography-mass spectrometry (LC-MS) [30]. However, it is worth noting that lower detection limits down to molecular monolayers or even single molecule detection can be achieved by using surface-enhanced infrared or Raman spectroscopy with nanostructured substrates (SEIRA [31]/SERS [32, 33]) - a limit that has not been reached in fibers. Moreover, it is important to point out that many widely used analytical techniques use labeled antibodies, such as ELISA (Enzyme-linked immunosorbent assay), LIA (luminescent immunoassay), and FIA (fluorescent immunoassay), which allow highly specific and sensitive detection down to concentrations of 1-100 pM. While specific detection of biomolecules has been demonstrated in hollow-core fibers via fluorophore-labeled antibodies, the detection limits are still orders of magnitude larger than in the established laboratory techniques [34].

Nonetheless, optical sensors based on hollow-core fibers can be used in a variety of **applications**, as such ultralow detection limits are rarely required, particularly in low-cost devices and portable applications. Foreseeable use cases are sensing of climate-relevant gases in environmental monitoring [35], breath analysis [36], industrial process monitoring [37], detection of explosives [38], point-of-care drug monitoring, and food safety [28, 39]. Apart from these analytical techniques, hollow-core waveguides are also of interest in quantum optical applications where light needs to interact with atomic or ionic vapors [40].

The main advantage of using hollow-core fibers in these systems is the higher level of integration, as bulky free-space optics can be replaced by fibers, simplifying alignment and making the devices more robust against mechanical damage. The next logical step in this development is the full **integration of optical sensing techniques** onto a single chip for mass fabrication. In this context, considerable progress has been made in recent years with integrated light sources [41, 42, 43] and on-chip spectrometers [44, 45, 46] being demonstrated. At the same time, less attention has been directed to the integration of the waveguide element in between them, while glass fibers are not compatible with the typically used planar photolithography techniques. However, since the waveguide defines the interaction region between light and analyte, it has a major influence on the properties of

[2]Since water is a polar molecule, it has many IR-active vibrational transitions, resulting in a substantial background signal in certain spectral regions in IR spectroscopy. Raman spectroscopy, on the other hand, does not capture these transitions, making it particularly useful for the analysis of aqueous solutions.

the resulting device, like response times, detection limits, or decoherence times of quantum states, thus requiring further research.

So far, most **integrated waveguides** still rely on solid cores, where - as in step-index fibers - light is guided mostly inside the core and only a small fraction of the field - the evanescent waves - can be exploited for analyte interactions [47, 48, 49], as shown in Fig. 1.3(a).

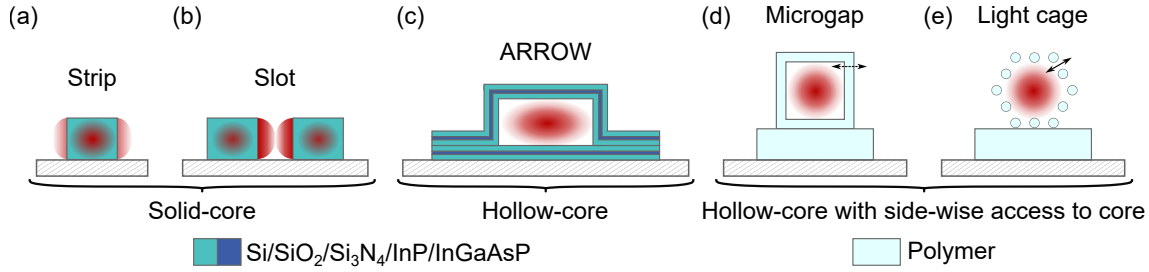

Figure 1.3: Chip-integrated waveguides. (a,b) In strip and slot waveguides a considerable fraction of the optical power (shown in red) is present inside the solid core. (c) Antiresonant reflecting optical waveguides (ARROWs) feature a hollow core that can only be accessed from the end faces. (d,e) Microgap waveguides and light cages allow side-wise access to the core via the introduction of gaps along the waveguide axis or the open spaces between polymer strands (indicated by black arrows).

To some degree, this issue can be overcome. For instance, single- [50, 51] and multi-slotted waveguides [52] have been developed, where two or more subwavelength-sized solid cores in close proximity provide a larger evanescent field region, thereby increasing the volume of light-matter interaction (Fig. 1.3(b)). However, a non-negligible fraction of the field remains inside the waveguides material, which is an inherent problem to solid core guidance.

The ideal solution would be the integration of hollow-core waveguides on a chip, where the guided mode overlaps nearly completely with the medium. However, the only common approach in this context is represented by antiresonant reflecting optical waveguides (ARROWs), which confine light by a sophisticated multilayer cladding [53, 54, 55], and thus require a lengthy multi-step fabrication process (Fig. 1.3(c)). Furthermore, they come at the cost of poor accessibility of the core volume due to the tube-like geometry - a major problem that applies identically to all hollow-core fibers. In practice, passive introduction of analytes into the micrometer-sized core via diffusion from its end faces is impracticably slow, requiring devices to actively pump the analyte through the waveguide which cannot be integrated straightforwardly [56]. Such **filling times** are particularly long for low-pressure atomic vapors used in quantum optical experiments and can be on the order of months for a waveguide length of a few centimeters [57, 58, 59], while passive exchange times for liquids are on the order of hours [25].

To mitigate this issue, several techniques have been developed to increase the side-wise accessibility, i.e., "openness" of hollow-core waveguides by introducing lateral holes

into their cladding - including femtosecond laser drilling [60, 61, 62], application of heat and pressure [63], and etching [64, 65]. Although such perforated hollow-core waveguides feature orders of magnitude lower analyte exchange times, the inserted holes increase the propagation loss, require an additional lengthy post-processing step, and can lead to variations between different waveguide batches.

In light of these shortcomings, our collaboration pioneered the use of a novel fabrication approach for realizing on-chip hollow-core waveguides featuring a large structural openness while maintaining low propagation loss: **3D nanoprinting** using two-photon absorption based direct laser writing of polymeric photoresists (in the following abbreviated as 3D nanoprinting). As a result, so-called **light cages** were realized two years prior to the beginning of this thesis [66]. Light cages consist of a hexagonal array of polymer strands and offer unhindered side-wise access to the core volume - a unique feature that cannot be realized in fiber drawing or two-dimensional fabrication approaches (Fig. 1.4(a)). Furthermore, 3D nanoprinting is a simple two-step process, that does not rely on cleanroom conditions, high temperatures, or harsh chemicals, thus overall reducing the fabrication complexity compared to ARROWs.

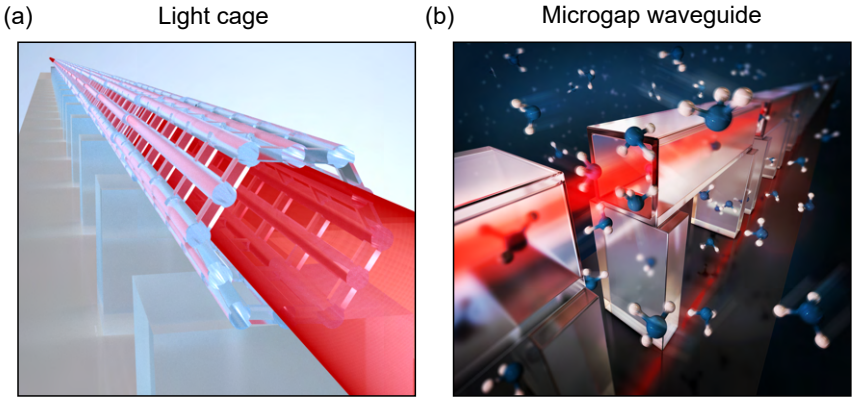

Figure 1.4: Illustration of 3D-nanoprinted hollow-core waveguides investigated in this thesis. (a) The light cage allows analytes to enter the light-guiding core via the open space between strands while the light remains confined via the antiresonance effect. (b) Microgap waveguides enable entry of analytes in the core region by micrometer-sized gaps along the waveguide (shown here for ammonia molecules). Artwork in (b) was created by Vera Hiendl, e-conversion (DFG cluster of excellence) and is part of [67].

As a parenthesis: the origin of this **fabrication method** ultimately dates back to 1931 when Nobel laureate Maria Göppert-Mayer theoretically outlined the process of two-photon absorption in atoms in her PhD thesis [68]. She showed that atoms can absorb two photons of lower energy to transition to their excited state instead of a single high-energy photon. As the probability for this process scales proportionally to the square of the intensity, two-photon absorption is in general only possible in the focus of a high-intensity pulsed laser beam. Yet, this property is of advantage in photopolymer-based microfabrication because it allows a laser beam to be scanned in three dimensions through a photoresist,

solidifying it precisely at the center of the focused beam and nowhere else. This idea was first demonstrated in 1997 by Shoji Maruo et al. [69] and matured quickly into a reliable commercially available technology, now enabling fabrication of complex three-dimensional structures with the smallest feature sizes being on the order of 100 nm (more details in Section 3.2). Consequently, 3D nanoprinting found applications across a variety of fields, including 2D metasurfaces [70], 3D metamaterials [71, 72], photonic crystals [73], microlens systems [74], free-form optics [75], photonic wire bonding [76], biocompatible cell-culture scaffolds [77], tissue engineering [78], and microneedles for drug delivery [79], all with the ability of using multiple materials [80].

Building on the previous works on light cages, we present here a second type of 3D-nanoprinted hollow-core waveguide with a simplified design, making it more accessible for reproduction by other researchers, reducing the fabrication time and propagation losses, and allowing for a straightforward analytical description of its optical properties. The design of these **microgap waveguides** features two elements which alternate on the micrometer scale as shown in Fig. 1.4(b): (1) a square-shaped hollow waveguide segment responsible for confining light via the antiresonance effect and (2) an open gap region allowing fast side-wise access to the core.

Starting with a description of the relevant theoretical aspects for this thesis in **Chapter** 2, and the used experimental and numerical methods in **Chapter** 3, the latest results on light cages and microgap waveguides are presented in **Chapter** 4. Specifically, we demonstrate the experimental realization of microgap waveguides up to lengths of 5 cm, report their optical properties based on transmission measurements, and compare the results to two analytical models. Coming back to the aforementioned optical sensing applications, proof-of-principle experiments on absorption spectroscopy of gases and liquids in this on-chip waveguide are conducted, revealing- most importantly - a drastic decrease in the analyte exchange time compared to capillaries of the same length.

Regarding light cages, several **earlier studies** were already conducted before the beginning of this thesis. First of all, it was shown that increasing the number of polymer strands in so-called dual ring light cages can reduce the propagation losses, as it is expected for antiresonant waveguides [81]. Furthermore, it had been shown that light cages can be coated with aluminum oxide nanofilms (Al_2O_3) via atomic layer deposition allowing to fine-tune the wavelengths of the resonances after the initial fabrication, and potentially making the waveguide more resistant against polymer-degrading chemicals [82]. While a full integration of light cages with light sources and spectrometers on a single chip has not yet been attempted, a higher level of integration was demonstrated in Ref. [83], where light cages were interfaced with fibers. This was achieved by fixing a delivery and a collection fiber to the ends of a V-shaped groove on a silicon chip (which aligns the fibers correctly), and subsequently fabricating the light cage in the groove in between these fibers. All waveguides presented in this thesis can principally be interfaced with fibers in this way, which allows the waveguide chip to be plugged into external light sources and spectral analyzers. In terms of sensing applications, absorption spectroscopy of gases [83] and liquids [84] had been demonstrated, as well as electromagnetically induced transparency in light cages filled with atomic vapors, relevant for integrated quantum optics [57].

Still missing in all of these works, is a quantitative study of the fabrication limits imposed by the chosen 3D nanoprinting approach. Based on this motivation, we present a detailed experimental study of various light cage properties in **Chapter** 4.2. Specifically, we reveal the current limit of maximally feasible device length, unlock the fabrication accuracy of the nanoprinting from optical measurements, and discuss the mechanical stability of the light cage geometry. Furthermore, we demonstrate that light cages can be used for on-chip fluorescence spectroscopy, one of the important optical sensing applications that had not yet been investigated. To increase the amount of captured fluorescence, dual ring light cages were used, with the results corroborating the earlier findings of a strongly reduced filling time. Overall, the findings presented in Chapter 4 clearly indicate the potential of 3D-nanoprinted hollow-core waveguides in the context of chip-integrated optical sensing devices, offering short response times, customizable optical properties by changing the geometrical parameters, and long light-matter interaction lengths.

The second part of this thesis explores an additional opportunity held by the application of 3D nanoprinting, namely the ability to fabricate **twisted waveguides** - an idea that has remained largely unexplored so far. Twisted waveguides belong to the class of chiral optical materials, which has attracted considerable attention in recent years, both on the fundamental [85, 86] as well as the applied side [87, 88, 89]. A key driving force behind these developments is the quest to find new ways to synthesize, sort, and detect chiral biomolecules, as their left- and right-handed versions can have dramatically different physiological effects on living organisms [90]. With optical techniques, chiral molecules can be distinguished based on their interaction with left- or right-handed circularly polarized light (LCP or RCP, respectively). These interactions manifest in **circular dichroism** (a difference in absorption between LCP and RCP light) and **circular birefringence** (a rotation of the direction of linearly polarized light during propagation).

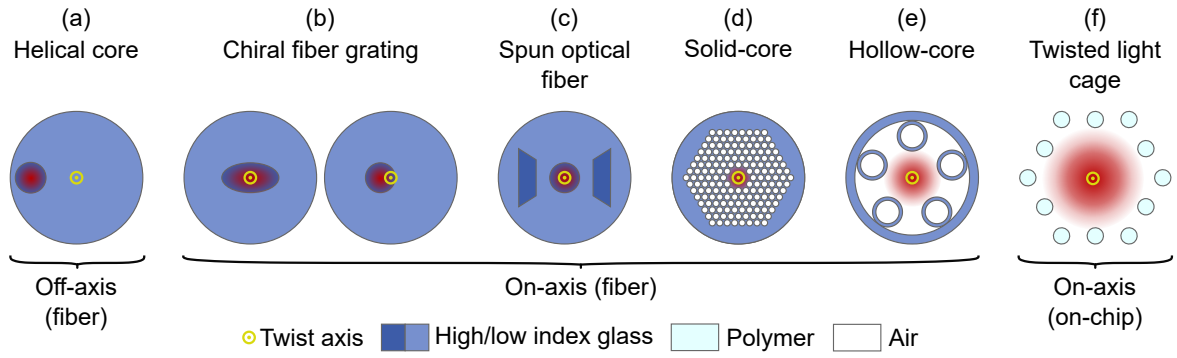

Figure 1.5: On- and off-axis twisted waveguide geometries. The waveguides are twisted along the axial direction (into the plane of the paper) with the location of the twist axis shown in yellow. Twisted waveguides are typically realized from fibers (a-e), while this thesis investigates 3D-nanoprinted twisted waveguides, allowing on-chip integration (f). Note that chiral fiber gratings either feature an elliptical core or a slightly eccentric circular core (b). Spun optical fibers are often realized from bow-tie fibers (c).

In the context of waveguides, these chiroptical effects are not present if the waveguide is straight[3] but can be realized in a twisted geometry. Among other applications, this enables the polarization state of circularly polarized light to be maintained under external perturbations (vibrations, mechanical stress, etc.), which is of utmost importance in the above-mentioned sensing of the weak optical response of chiral molecules.

Twisted waveguides generally fall into two categories, based on whether the light-guiding core lies on the twist axis or off-axis as shown for some common examples in Fig. 1.5. The vast majority of these waveguides are twisted fibers (i.e., made out of glass) produced by spinning the preform during the drawing process or in a thermal post-processing step. An example of a simple twisted fiber geometry are chiral fiber gratings, which are created by twisting fibers with an elliptical or slightly eccentric core (often a small fabrication-induced asymmetry is sufficient). In such fibers, very high twist rates (up to 1 turn per 24 µm [91]) can be realized resulting in strong circular dichroism (up to 3 dB/mm [92]). However, in more complex geometries, such as the commercially available spun optical fibers (created from fibers with strong linear birefringence) or photonic crystal fibers, such high **twist rates** could not yet be achieved (see Fig. 1.6 and detailed overview in Table C.1). The same issue is inherent to the complex geometry of twisted hollow-core fibers which - to our knowledge - were first demonstrated in 2017/2018 by Edavalath and Roth et al. [120, 119].

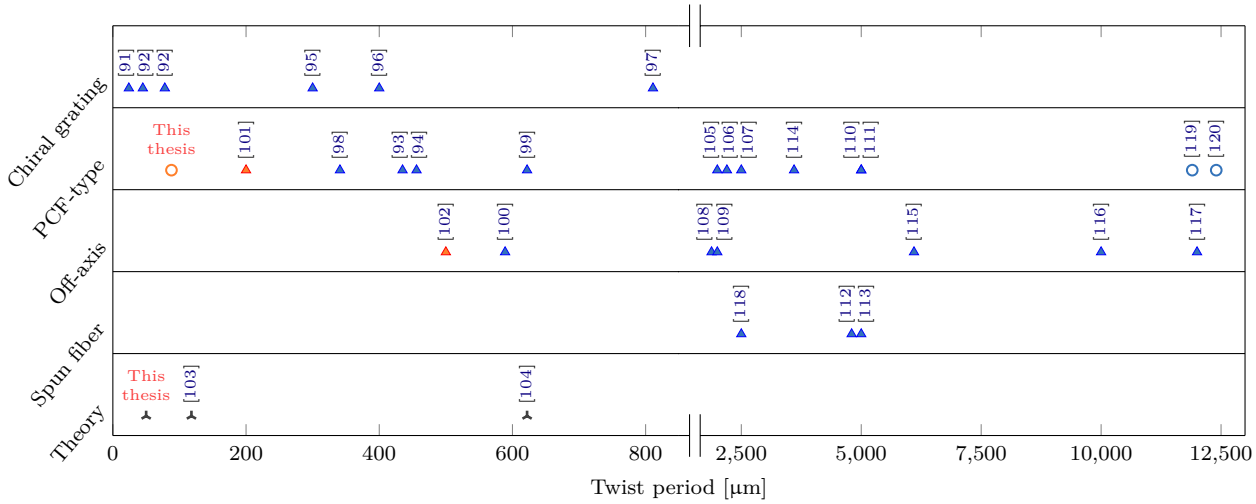

Figure 1.6: Achieved twist rates for the waveguide geometries shown in Fig. 1.5. Solid-core waveguides are shown as filled triangles, hollow-core waveguides as rings, and theoretical investigations as stars. Blue denotes glass-based waveguides, while 3D-nanoprinted waveguides are shown in orange. Works from this thesis are the twisted light cage ("PCF-type"), and a theoretical investigation on off-axis twisted waveguides ("Theory"). All works are listed in more detail in Table C.1.

[3]Straight waveguides do not possess circular birefringence or circular dichroism provided that the material itself is not chiral.

Still, as motivated earlier, hollow-core waveguides are generally more desirable from an applications perspective, especially for sensing devices.

In this thesis, we demonstrate that this limitation in twist rate can be overcome by the use of 3D nanoprinting, which allows to directly fabricate twisted structures without any further processing steps. Although two previous works already applied this novel approach demonstrating an off-axis twisted waveguide [102] and an on-axis twisted photonic crystal fiber [101], the authors did not fully investigate the optical properties of the resulting waveguides neither by experiment, nor by simulation or analytical modeling. Here, we cover all of these aspects in a detailed study on **twisted light cages** - the first twisted hollow-core waveguide realized on a chip (Fig. 1.7(b)).

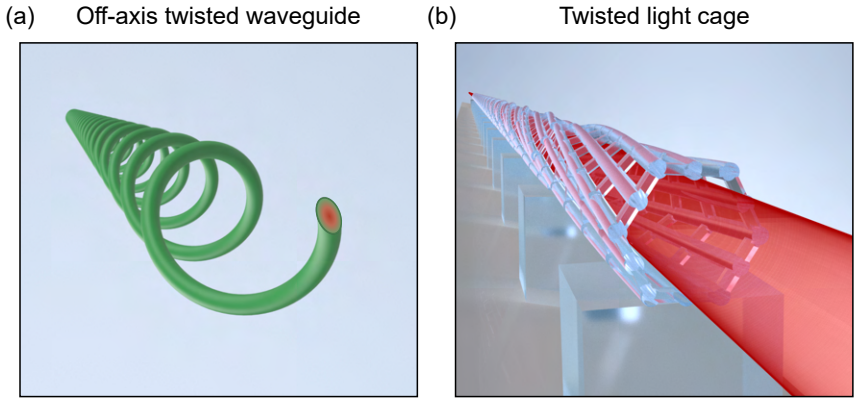

Figure 1.7: Illustration of twisted waveguides investigated in this thesis. (a) Off-axis twisted waveguides guide light along a helical path. Their optical properties were studied by simulations and analytical theory. (b) Twisted light cages are on-axis twisted waveguides, which were realized by 3D nanoprinting.

As an introduction to twisted light cages, we first study a single **off-axis twisted polymer strand** in **Chapter** 5 to gain an understanding of the effect of twisting on the cladding modes of light cages. In this theoretical study, we provide a guide to the simulation of twisted waveguides, which relies on the use of suitable coordinate frames such that the waveguide becomes invariant along one of the new coordinates. In this context, we point out that helical waveguides defined in the three most commonly used coordinate frames (Frenet-Serret, helicoidal, and Overfelt frame) generally differ in their geometry and optical properties[4] - an important but so far overlooked fact, that applies to all works on twisted waveguides. Furthermore, we report the emergence of superchiral fields on the surface of the waveguides, which have attracted interest due to their ability to enhance the weak chiroptical response of chiral molecules [85, 121]. Lastly, we analyzed more theoretical aspects of these waveguides manifesting in the form of spin- and orbital angular momentum-dependent splittings in the spatial properties of the modes - which

[4]In principle, all three coordinate frames are equivalent but twisted waveguides are often defined as having a **circular** cross section in the plane spanned by two of the coordinates. The three geometries resulting from this definition are physically different.

are potentially related to the photonic spin Hall and orbital Hall effects (introduced in Section 2.4).

Experimental and simulation results on twisted light cages are presented in **Chapter** 6. Specifically, we investigate the formation of twist-induced resonances between different core modes of the light cage and measure the resulting circular dichroism at several twist rates. Furthermore, the presence of circular birefringence is discussed based on the simulation results and compared to an analytical model [99, 104].

The presented results open an avenue for translating the vast amount of research on twisted waveguides to on-chip devices. Possible applications include circular polarization filtering [119], twist and tension sensing [93], and the broadband generation of orbital angular momentum [122, 123, 124]. The full potential of twisted hollow-core waveguides could be used in applications requiring the interaction of liquids or gases with a stable circular polarization state, such as for circularly polarized supercontinuum generation [125], Raman lasers with tunable polarization states [126], or in chiral spectroscopy.

Chapter 2

Theoretical Background

Understanding the mode formation in 3D-nanoprinted waveguides requires knowledge of the underlying equations and terminology of waveguide physics, which is introduced here. For the studies on twisted waveguides, further basics on optical chirality, including spin and orbital angular momentum are required. Furthermore, three suitable coordinate frames for the simulation of twisted waveguides are introduced. Lastly, the spin-orbit interaction of light traveling on curved trajectories is covered, which is of relevance to off-axis twisted waveguides.

2.1 Theory of Waveguides

2.1.1 Maxwell's Equations and Wave Equations

All optical theory and simulations in this thesis are governed by Maxwell's equations in matter, containing - in the most general form - the free charge density ρ_{free} and current density $\mathbf{J}_{\text{free}}$ [127]:

$$\begin{array}{ll} \boldsymbol{\nabla}\cdot\mathbf{D}=\rho_{\text{free}}, & \boldsymbol{\nabla}\cdot\mathbf{B}=0, \\ \underbrace{\boldsymbol{\nabla}\times\mathbf{H}=\mathbf{J}_{\text{free}}+\dfrac{\partial\mathbf{D}}{\partial t},}_{\text{inhomogeneous equations}} & \underbrace{\boldsymbol{\nabla}\times\mathbf{E}=-\dfrac{\partial\mathbf{B}}{\partial t}.}_{\text{homogeneous equations}} \end{array} \tag{2.1}$$

"Free" means that these quantities are not attributable to the charges or currents confined within the material on a microscopic level. When a material interacts with electromagnetic radiation, a polarization density $\mathbf{P}$ or magnetization density $\mathbf{M}$ can be induced in this material (or be present without a field, e.g., in permanent magnets). $\mathbf{P}$ and $\mathbf{M}$ contain an average of the microscopic interactions and are used to separate the total charge density ρ and total current density $\mathbf{J}$ into their free and bound parts [128]:

$$\begin{array}{ll} \rho_{\text{bound}}=-\boldsymbol{\nabla}\cdot\mathbf{P}, & \mathbf{J}_{\text{bound}}=\boldsymbol{\nabla}\times\mathbf{M}+\dfrac{\partial\mathbf{P}}{\partial t}, \\ \rho=\rho_{\text{free}}+\rho_{\text{bound}}, & \mathbf{J}=\mathbf{J}_{\text{free}}+\mathbf{J}_{\text{bound}}. \end{array} \tag{2.2}$$

Electric flux density $\mathbf{D}$ and magnetic field strength $\mathbf{H}$ were introduced above as auxiliary fields and are related to the electric field strength $\mathbf{E}$ and the magnetic flux density $\mathbf{B}$ by:

$$\mathbf{D} = \epsilon_0 \mathbf{E} + \mathbf{P}, \qquad \mathbf{H} = \frac{1}{\mu_0}\mathbf{B} - \mathbf{M}, \tag{2.3}$$

where ϵ_0 is the vacuum permittivity and μ_0 is the vacuum permeability. If the material response (polarization, current, or magnetization) is linear in $\mathbf{E}$ or $\mathbf{H}$, respectively, the following simplification can be made:

$$\mathbf{D} = \epsilon_0 \underline{\epsilon_r} \mathbf{E}, \qquad \mathbf{J}_{\text{free}} = \mathbf{J}_{\text{ext}} + \underline{\sigma}\mathbf{E}, \qquad \mathbf{B} = \mu_0 \underline{\mu_r} \mathbf{H}, \tag{2.4}$$

where $\underline{\epsilon_r}$ is the relative permittivity, $\underline{\sigma}$ is the electrical conductivity, and $\underline{\mu_r}$ the relative permeability. The separation of the free current into a conduction current $\underline{\sigma}\mathbf{E}$ and an external current $\mathbf{J}_{\text{ext}}$ depends on the specific problem. For anisotropic materials (where the material response is not always parallel to the inducing field) these parameters are second-rank tensors, for isotropic materials they reduce to a scalar.

In general, all fields introduced in this section depend on space and time, and the material properties may be non-local and dependent on all previous times [129]. For problems involving conductive materials, like plasmons in metals, it is beneficial to modify the relative permittivity to include the conductivity as an imaginary part, which results in a different classification of bound and free currents [129]. Low-order nonlinear optical processes can be treated by expanding the polarization density $\mathbf{P}$ as a power series in $\mathbf{E}$ [130].

This thesis deals with linear dielectric materials which are insulating ($\underline{\sigma} = \underline{0}$), not time-dependent, and in some instances anisotropic in $\underline{\epsilon_r}$ and $\underline{\mu_r}$. Free charges or currents do not occur. By applying the curl operator to Maxwell's curl equations (Eq. 2.1) two separate wave equations for $\mathbf{E}$ and $\mathbf{H}$ are obtained. These equations are called **vector wave equations** of linear media:

$$\boxed{\begin{aligned} \boldsymbol{\nabla} \times \left(\underline{\mu_r}^{-1} \boldsymbol{\nabla} \times \mathbf{E}\right) + \frac{1}{c_0^2}\,\underline{\epsilon_r}\,\frac{\partial^2 \mathbf{E}}{\partial t^2} &= 0, \\ \boldsymbol{\nabla} \times \left(\underline{\epsilon_r}^{-1} \boldsymbol{\nabla} \times \mathbf{H}\right) + \frac{1}{c_0^2}\,\underline{\mu_r}\,\frac{\partial^2 \mathbf{H}}{\partial t^2} &= 0, \end{aligned}} \tag{2.5}$$

where $c_0 = \frac{1}{\sqrt{\epsilon_0 \mu_0}}$ is the speed of light in vacuum.

2.1.2 Waveguides

Waveguides are optical elements that guide light along a certain path by confining it to a cross section that is usually on the order of a few micrometers for visible light. Ideal waveguides are translationally invariant along one coordinate z of the underlying coordinate system, infinitely long, and feature a constant cross section in the plane spanned by the

remaining two coordinates x and y. These assumptions are well justified for optical fibers, which can be several kilometers in length and are manufactured with very high precision. With these simplifications, the eigenmodes of the waveguide can be expressed in a separable form [131]:

$$\boxed{\begin{aligned}\mathbf{E}(x,y,z,t) &= \mathbf{e}(x,y)\mathrm{e}^{\mathrm{i}\beta z}\mathrm{e}^{-\mathrm{i}\omega t},\\ \mathbf{H}(x,y,z,t) &= \mathbf{h}(x,y)\mathrm{e}^{\mathrm{i}\beta z}\mathrm{e}^{-\mathrm{i}\omega t},\end{aligned}} \tag{2.6}$$

where β denotes the **propagation constant**, and a harmonic time dependence with frequency ω has been assumed. If the coordinate system (x, y, z) is a Cartesian system, and the materials of the waveguide are isotropic and nonmagnetic ($\underline{\mu_r} = 1$), the vector wave equations (Eq. 2.5) can be simplified yielding:

$$\boxed{\begin{aligned}\left(\nabla^2 + \frac{n^2}{c_0^2}\omega^2\right)\mathbf{E} &= -\boldsymbol{\nabla}\left(\mathbf{E}\cdot\boldsymbol{\nabla}\ln\left(n^2\right)\right),\\ \left(\nabla^2 + \frac{n^2}{c_0^2}\omega^2\right)\mathbf{H} &= -\left(\boldsymbol{\nabla}\ln\left(n^2\right)\right)\times\left(\boldsymbol{\nabla}\times\mathbf{H}\right),\end{aligned}} \tag{2.7}$$

where $n(x,y) = \sqrt{\epsilon_r}$ is the refractive index and derivatives $\frac{\partial}{\partial z}$ of the fields can be replaced by $\mathrm{i}\beta$. The right-hand side of Eq. 2.7 contains the term $\boldsymbol{\nabla}\ln\left(n^2\right)$, which couples the different Cartesian field components. Methods to solve this equation for a variety of geometries are well described in Ref. [131].

The simplest waveguide geometry is a **step-index fiber**. It consists of a core made of a high refractive index material surrounded by a cladding of a lower refractive index. Light is guided in the core by total internal reflection at the core-cladding boundary. In this case $\boldsymbol{\nabla}\ln\left(n^2\right)$ vanishes everywhere except for the boundary between the two regions. Inside of these regions, Eq. 2.7 reduces to the **scalar wave equation** (Eq. 2.8) for all Cartesian field components f of $\mathbf{e}$ and $\mathbf{h}$. As an approximation, the scalar wave equation can furthermore describe a waveguide with arbitrary index profile if the index difference between the highest index n_{co} and the lowest index n_{cl} of the cross section is small. Such structures are referred to as **weakly guiding fibers**.

$$\boxed{\left(\frac{1}{k_0^2}\left(\frac{\partial^2}{\partial x^2}+\frac{\partial^2}{\partial y^2}\right)+n^2(x,y)\right)f(x,y) = n_{\mathrm{eff}}^2\, f(x,y) \quad \text{for } \Delta \ll 1} \tag{2.8}$$

The relation $c_0 = \omega/k_0$ was used and two important quantities of waveguides were introduced:

$$\boxed{\begin{aligned} n_{\mathrm{eff}} &= \frac{\beta}{k_0}\ \textbf{(effective mode index)},\\ \Delta &= \frac{n_{\mathrm{co}}^2 - n_{\mathrm{cl}}^2}{2n_{\mathrm{co}}^2}\ \textbf{(refractive index contrast)}.\end{aligned}} \tag{2.9}$$

The z dependence of the modes can then be stated as $e^{i\beta z} = e^{ik_0 n_{\text{eff}} z}$ showing that a mode propagates in waveguides like in a material with refractive index n_{eff}. The real part of n_{eff} describes the phase evolution of the mode and its imaginary part the losses. A mode with $n_{\text{cl}} < n_{\text{eff}} \leq n_{\text{co}}$ is a **bound mode**, which decays evanescently in the cladding, while a mode with $0 \leq n_{\text{eff}} < n_{\text{cl}}$ is a **radiation mode** which oscillates in the cladding and therefore carries energy away from the core [131]. These two types completely describe the properties of the waveguide but often it is convenient to introduce a third type of mode, so-called **leaky modes**. Leaky modes are still localized to the core region but continuously dissipate energy as they propagate due to a weak oscillating field outside of the core. Their effective index therefore features a nonzero imaginary part. Mathematically, leaky modes can be constructed from the continuum of radiation modes [132], i.e., the real part of the effective index fulfills $0 \leq \text{Re}\{n_{\text{eff}}\} < n_{\text{cl}}$. While leaky modes correspond to the experimentally measured modes in antiresonant fibers, their mathematical treatment can be complicated as their fields diverge at large distances from the core when assuming infinitely long waveguides, thus preventing normalization (see Sec. 24-11 in Ref. [131]).

The occurrence of bound modes in fibers can be understood more intuitively when noting that Eq. 2.8 has the same form as the time-independent Schrödinger equation [133], with "mass" $m = \hbar^2 k_0^2/2$, "energy" $E = -n_{\text{eff}}^2$ and "potential" $V = -n^2(x, y)$. Like in quantum mechanical potential wells, fibers with small core sizes and small refractive index contrast support less bound modes than fibers with large refractive index contrast and large core sizes. At least one bound mode exists since a finite two-dimensional potential well always supports at least one bound mode [134]. If the fiber has exactly one such bound mode (or two when considering two possible polarization directions) it is referred to as **single-mode fiber**, otherwise it is a **multimode fiber**.

A simple estimate of the number of modes in a step-index fiber can be obtained by calculating its ***V* number** [131]:

$$\boxed{V = \frac{2\pi}{\lambda} r_c \sqrt{n_{\text{co}}^2 - n_{\text{cl}}^2},} \tag{2.10}$$

where r_c is the radius of the core. A fiber is single-mode for $V < 2.405$ and the number of modes in a multimode fiber can be estimated by $V^2/2$ for large V [131]. When the wavelength increases, the V number decreases meaning that the modes of highest order are not able to propagate anymore in the fiber. This phenom - known as modal **cut-off** - occurs when $n_{\text{eff}} = n_{\text{cl}}$ and is crucial for understanding the light guidance mechanism in light cages, as explained in Section 4.2.2.

The full solution for a step-index fiber is obtained by imposing boundary conditions (derived from Maxwell's equations) at the interface between the solutions of the homogeneous regions. For circular step-index fibers the exact solutions are well known and available in Ref. [135]. Due to the coupling of field components by the $\boldsymbol{\nabla} \ln(n^2)$ term, all modes have at least one longitudinal field component. Specifically, the modes of a circular fiber can be categorized into four groups [131]: $\mathbf{TE_{0,}}_{m}$ or **transverse electric** ($E_z = 0$), $\mathbf{TM_{0,}}_{m}$ or **transverse magnetic** ($H_z = 0$), and two **hybrid modes** where neither the electric nor

the magnetic field is transverse. The hybrid modes are denoted as $\mathbf{HE}_{\nu,m}$ (E_z is dominant) and $\mathbf{EH}_{\nu,m}$ (H_z is dominant). $\nu \geq 1$ and $m \geq 1$ are integers classifying the modes. TE and TM modes are nondegenerate while HE and EH modes are two-fold degenerate: HE^e and EH^e have radial field components which are even functions of the azimuthal angle ϕ while they are odd functions for HE^o and EH^o.

The polarization state of these vector modes can be quite complex. Therefore, it is often beneficial to use an approximation to the exact solutions under the weak guidance approximation ($\Delta \ll 1$). In this case, the modal fields are to good approximation transverse (i.e., $E_z = H_z = 0$) and uniformly polarized [131]. Therefore they are called $\mathbf{LP}_{l,m}$ or **linearly polarized modes**. $l = 0, 1, 2, ...$ denotes the mode order in the azimuthal direction and $m = 1, 2, ...$ the mode order in the radial direction. Field distributions of LP modes can be found in Refs. [136, 135]. As the index contrast Δ or the mode order l increases, the approximation of the eigenmodes as LP modes becomes worse. For $\Delta = 0$, on the other hand, the vector modes coincide with the scalar LP modes with the vector modes being grouped together as shown in Table 2.1.

Table 2.1: Correspondence between scalar LP modes and vector modes in the weak guidance approximation ($\Delta \to 0$). The fundamental modes (with the highest effective index) are $\mathrm{HE}^e_{1,1}$ and $\mathrm{HE}^o_{1,1}$ corresponding to the two-fold degenerate $\mathrm{LP}_{0,1}$ mode.

Order l	Scalar mode	Vector modes
0	$\mathrm{LP}_{0,m}$	$\mathrm{HE}^e_{1,m}$, $\mathrm{HE}^o_{1,m}$
1	$\mathrm{LP}_{1,m}$	$\mathrm{HE}^e_{2,m}$, $\mathrm{HE}^o_{2,m}$, $\mathrm{TE}_{0,m}$, $\mathrm{TM}_{0,m}$
≥ 2	$\mathrm{LP}_{l,m}$	$\mathrm{HE}^e_{l+1,m}$, $\mathrm{HE}^o_{l+1,m}$, $\mathrm{EH}^e_{l-1,m}$, $\mathrm{EH}^o_{l-1,m}$

Therefore, LP modes are two-fold degenerate for $l = 0$ and four-fold degenerate for $l \geq 1$. The degeneracy arises because the direction of the transverse polarization of LP modes is arbitrary, yielding two linearly independent solutions with the same effective index. For $l \geq 1$ the fields of LP modes contain a phase term $\mathrm{e}^{\pm \mathrm{i} l \phi}$ which results in another two-fold degeneracy due to the arbitrary choice of the sign.

The **intensity distribution of a mode**, which can be measured with a CCD camera, is equal to the time-averaged longitudinal component of its Poynting vector $\langle \mathbf{S} \rangle_z$. The Poynting vector can be obtained from the calculated fields as [137]:

$$\boxed{\langle \mathbf{S} \rangle = \frac{1}{2} \mathrm{Re}\{\mathbf{E} \times \mathbf{H}^*\}.} \tag{2.11}$$

2.1.3 Coupled Mode Theory

During the course of the thesis, several situations arise where two waveguide modes couple and form a supermode. This phenomenon can be understood based on coupled mode

theory (**CMT**), which will be introduced here based on Chapter 4 of Ref. [135].

CMT is a perturbative approach based on the assumption that the solution to Maxwell's equations in the coupled system $\mathbf{E}(x,y,z)$, $\mathbf{H}(x,y,z)$ can be described as a superposition of two (or a finite number) of modes in the uncoupled system (labeled with subscripts 1,2)[1]:

$$\mathbf{E}(x,y,z) = A(z)\mathbf{e}_1(x,y)\mathrm{e}^{\mathrm{i}\beta_1 z} + B(z)\mathbf{e}_2(x,y)\mathrm{e}^{\mathrm{i}\beta_2 z}, \tag{2.12}$$

$$\mathbf{H}(x,y,z) = A(z)\mathbf{h}_1(x,y)\mathrm{e}^{\mathrm{i}\beta_1 z} + B(z)\mathbf{h}_2(x,y)\mathrm{e}^{\mathrm{i}\beta_2 z}, \tag{2.13}$$

where β_1 and β_2 are the propagation constants of the modes in the uncoupled system. The coefficients A and B depend on z because the modes of the uncoupled system are generally not eigenmodes of the coupled system.

Using the fact that modes 1 and 2 fulfill Maxwell's equations in the uncoupled system, the coefficients of the supermodes in the coupled system are given by the following **coupled mode equations** [135]:

$$\frac{\mathrm{d}A}{\mathrm{d}z} + c_{12}\frac{\mathrm{d}B}{\mathrm{d}z}\mathrm{e}^{+\mathrm{i}2\delta z} - \mathrm{i}\kappa_{11}A - \mathrm{i}\kappa_{12}B\mathrm{e}^{+\mathrm{i}2\delta z} = 0, \tag{2.14a}$$

$$\frac{\mathrm{d}B}{\mathrm{d}z} + c_{21}\frac{\mathrm{d}A}{\mathrm{d}z}\mathrm{e}^{-\mathrm{i}2\delta z} - \mathrm{i}\kappa_{22}B - \mathrm{i}\kappa_{21}A\mathrm{e}^{-\mathrm{i}2\delta z} = 0, \tag{2.14b}$$

where $\delta = (\beta_2 - \beta_1)/2$. Assuming that the power carried by the modes is normalized as $\iint dxdy\ \mathrm{Re}\left\{\mathbf{e}_p \times \mathbf{h}_p^*\right\}_z = 1$, the coupling coefficient κ_{pq}, self-coupling coefficient κ_{pp}, and mode-overlap coefficient c_{pq} are given by:

$$\kappa_{pq} = \omega\epsilon_0 \iint dxdy\,(n^2 - n_q^2)\,\mathbf{e}_p^* \cdot \mathbf{e}_q \qquad \forall (p,q) \in \{1,2\}^2, \tag{2.15}$$

$$c_{pq} = \iint dxdy\,(\mathbf{e}_p^* \times \mathbf{h}_q + \mathbf{e}_q \times \mathbf{h}_p^*)_z \quad \forall (p,q) \in \{(1,2),(2,1)\}, \tag{2.16}$$

where $n(x,y,z)$ is the refractive index distribution in the coupled system and $n_p(x,y,z)$ corresponds to the uncoupled system. How this division is done in practice is outlined in Fig. 2.1 for two common examples. If the two modes are located in different waveguides, which are brought in close proximity to each other, n_p would correspond to a single waveguide, and the coupled system is described by $n = n_1 + n_2$. For light cages, one can dissect the waveguide into core and cladding as shown in Section 4.2.2. On the other hand, if the modes are located within the same waveguide ($n_1 = n_2$), the modes can only couple[2] if there is an index modulation such that $n^2 - n_p^2 \neq 0$. This situation arises in twisted light cages, where the index modulation is the difference in the index profile between the untwisted and the twisted waveguide as discussed in Chapter 6.

[1] The time dependence $\mathrm{e}^{-\mathrm{i}\omega t}$ is omitted here.

[2] Modes of the same waveguide are not necessarily orthogonal if the system is lossy [138].

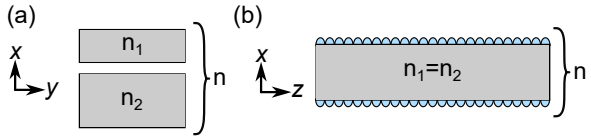

Figure 2.1: Examples of waveguides to which coupled mode theory can be applied. (a) In a directional coupler, the modes of the individual waveguides with refractive index profiles n_1 and n_2 are coupled due to the spatial proximity of the waveguides. (b) In a Bragg waveguide two core modes of the same waveguide are coupled by a grating. In this case, the uncoupled system is given by the waveguide without the grating as $n_1 = n_2$ (gray). The grating represents the index modulation $n - n_1$ (light blue) required for coupling.

In many cases, the coupling coefficients c_{pq} and κ_{pp} are small compared to κ_{pq} and can be neglected [135]. To find the supermodes of the coupled system for this simplified case, it is beneficial to include the phase evolution term of Eq. 2.12 in the coefficients: $\tilde{A} = A\mathrm{e}^{\mathrm{i}\beta_1 z}, \tilde{B} = B\mathrm{e}^{\mathrm{i}\beta_2 z}$. With this adaptation, the coupled mode equations for $c_{pq} = \kappa_{pp} = 0$ read:

$$\frac{\mathrm{d}}{\mathrm{d}z}\begin{pmatrix}\tilde{A}\\ \tilde{B}\end{pmatrix} = \mathrm{i}\underbrace{\begin{pmatrix}\beta_1 & \kappa_{12}\\ \kappa_{21} & \beta_2\end{pmatrix}}_{\underline{\mathbf{M}}}\begin{pmatrix}\tilde{A}\\ \tilde{B}\end{pmatrix}. \tag{2.17}$$

The eigenmodes of the coupled system can now be obtained as the eigenvectors of $\underline{\mathbf{M}}$, while their propagation constants $\beta_\pm$ are given by its eigenvalues:

$$\boxed{\beta_\pm = \frac{\beta_1 + \beta_2}{2} \pm \sqrt{\delta^2 + \kappa^2},} \tag{2.18}$$

where $\kappa = \sqrt{\kappa_{12}\kappa_{21}}$. For lossy modes, such as the leaky modes investigated in this thesis, the effective index difference δ is complex with real part δ_r and imaginary part δ_i. This allows three different regimes to be distinguished [139], which we denote according to the terminology used in light-matter coupling [140] (for a graphical overview see Fig. 2.2):

1. **Weak coupling**: $\kappa \leq |\delta_i|$

   On resonance ($\delta_r = 0$) the square root term in Eq. 2.18 is purely imaginary resulting in a crossing of the real parts of the effective indices and an anti-crossing of the imaginary parts. If the system is excited in mode 1, the fraction of power in mode 2 is always lower than in mode 1. Therefore, this regime is also referred to as incomplete coupling.

2. **Exceptional point**: $\kappa = |\delta_i|$ On resonance, the two eigenvalues coalesce into one because the square root term is zero. A small reduction in the coupling constant leads to a square root-dependent change in the loss of the supermodes. Due to this large response, exceptional points are interesting for sensing applications [142].

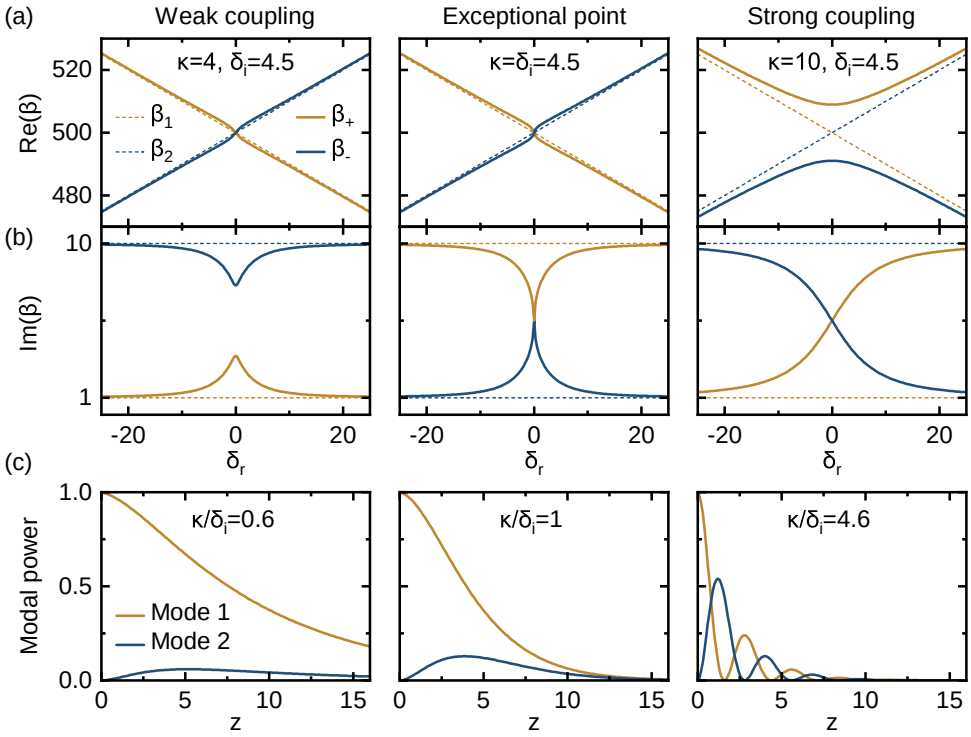

Figure 2.2: Different regimes in coupled mode theory based on Eq. 2.18. Regimes are indicated on the top of each column. Real part (a) and imaginary part (b) of the propagation constants of the modes in the uncoupled system (dashed lines) and of the supermodes in the coupled system (solid lines). (c) Resonant coupling occurs when the real parts of the effective indices match ($\delta_r = 0$). Assuming that the coupled system is excited in state 1 of the uncoupled system at $z = 0$, power is exchanged between modes 1 and 2 during propagation. In (a,b) $\mathrm{Im}\{\beta_1\} = 1$, $\mathrm{Im}\{\beta_2\} = 10$. In (c) $\mathrm{Im}\{\beta_1\} = 0.01$, $\mathrm{Im}\{\beta_2\} = 0.5$. Idea for (a,b) is taken from [141].

3. **Strong coupling**: $\kappa > |\delta_i|$

   On resonance, the square root term is purely real. Consequently, there is a crossing in the imaginary parts of the effective indices and an anti-crossing in the real parts. If the system is excited in mode 1, the power oscillates between modes 1 and 2. At certain locations in the waveguide, all power is present in mode 2. Therefore, this regime is also called complete coupling. Coupling between (lossless) bound modes always falls in this category because $\delta_i = 0$ in this case.

In summary, lossy waveguide modes couple and form resonances if the real part of their propagation constants match and if the modal overlap integral in Eq. 2.15 is nonzero. Strong coupling additionally requires the losses of the mode to be similar, or the coupling constant to be large.

2.2 Chirality

The photons of the fundamental modes of twisted waveguides typically carry spin angular momentum, while higher-order modes additionally carry orbital angular momentum. These quantities are defined and discussed here along with the optical chirality density, which is one way to characterize the chirality of the modal fields.

2.2.1 Spin Angular Momentum (Circular Polarization)

When photons carrying spin angular momentum (**SAM**) are absorbed by a small particle, it starts to rotate around its center with the direction depending on the sign of the SAM [143]. SAM is closely related to circular polarization in a beam of light. Unfortunately, two opposing conventions exist to define circular polarization. Here, we follow the convention typically used in optics which defines the sense of rotation of the field vector as seen from the point of view of the receiver (looking into the beam) [144]. **Right circular polarization (RCP)** is then defined as a clockwise rotation of the polarization vector in time and **left circular polarization (LCP)** as an anticlockwise rotation. According to this convention, a photon that is part of a circularly polarized beam carries a SAM of $s\hbar$ with $s = +1$ for LCP and $s = -1$ for RCP [145]. For a mathematical definition, we define the temporal and spatial evolution of a transverse plane wave as:

$$\boxed{\mathbf{E} = E_0 \,\mathrm{Re}\Big\{|\Psi\rangle \, \mathrm{e}^{\mathrm{i}(kz-\omega t)}\Big\},} \tag{2.19}$$

where $|\Psi\rangle$ lies in the plane transverse to the propagation direction, and E_0 is the field amplitude. Consistent with the optics convention, LCP and RCP plane waves can then be stated as:

$$\boxed{|s\rangle = \frac{1}{\sqrt{2}} \begin{pmatrix} 1 \\ si \\ 0 \end{pmatrix} \qquad \begin{array}{l} s = +1 \text{ for LCP} \rightarrow \text{receiver sees anti-clockwise rotation} \\ s = -1 \text{ for RCP} \rightarrow \text{receiver sees clockwise rotation} \end{array}} \tag{2.20}$$

When drawing the polarization vector in the xy plane such that the propagation direction (z) points out of the plane towards the reader's eye, it rotates clockwise in time for RCP light and anticlockwise for LCP light.

In particle and quantum physics [144], engineering [146], and radio astronomy [147], on the other hand, the sense of rotation is typically defined from the point of view of the source. This definition would interchange the names of LCP and RCP.

In general, a beam of light may be only partially polarized, the part that is polarized may not be circular or may point out of the transverse plane. In this general case, the polarization vector moves along an elliptical path which can be characterized by the four Stokes parameters S_0, S_1, S_2, S_3. For transverse waves, these can be easily retrieved from measurements [148, 149]. While S_0 is the total intensity I of the beam, S_1, S_2, and S_3 can

be measured by recording the intensity after a linear polarizer under 4 angles separated by 45°, and a circular polarizer set to transmit RCP or LCP, respectively.

Taking S_1, S_2, and S_3 as the axes of a Cartesian coordinate system, a certain polarization state lies on a sphere - the Poincaré sphere - with radius Ip where p is the degree of polarization. While S_1 and S_2 describe the tilt of the polarization ellipse, S_3 is related to its ellipticity. A detailed description of all Stokes parameters can be found in Ref. [137].

Here, we mainly focus on the intensity normalized Stokes parameter $\hat{S}_3 = \frac{S_3}{I}$ which is defined as [137]:

$$\boxed{\hat{S}_3 = \frac{I_{\mathrm{RCP}} - I_{\mathrm{LCP}}}{I} \quad \xrightarrow{p=1} \quad \begin{array}{l} \hat{S}_3 = -1 \text{ for LCP} \\ \hat{S}_3 = +1 \text{ for RCP} \end{array},} \tag{2.21}$$

where I_{RCP} and I_{LCP} are the intensities measured after a circular polarizer set to transmit RCP or LCP, respectively. Note that $\hat{S}_3$ and spin have opposite signs in this commonly used definition.

More generally, spin is a vectorial quantity and the spin contribution $\mathbf{s}$ of the electric and magnetic field can be defined as [150, 151]:

$$\boxed{\mathbf{s_E} = \mathrm{Im}\left\{\hat{\mathbf{E}}^* \times \hat{\mathbf{E}}\right\}, \qquad \mathbf{s_H} = \mathrm{Im}\left\{\hat{\mathbf{H}}^* \times \hat{\mathbf{H}}\right\},} \tag{2.22}$$

with the normalized field vectors (i.e., of unit length) $\hat{\mathbf{E}}$ and $\hat{\mathbf{H}}$. Since the spin vector is oriented perpendicular to the polarization ellipse, it contains additional information about the polarization structure of the mode. The degree of circularity of the respective field is then given by:

$$\boxed{\left|\hat{S}_3\right| = |\mathbf{s}|.} \tag{2.23}$$

The direction of the spin vector relative to the propagation direction of the mode is used to set the correct sign for $\hat{S}_3$. If the spin vector contains a component parallel to the propagation direction a negative sign is used for $\hat{S}_3$, if it contains an antiparallel component a positive sign is used.

2.2.2 Orbital Angular Momentum (OAM)

Apart from spin angular momentum, light can also possess orbital angular momentum (**OAM**). Interest in this topic was sparked by Allen et al. in 1992 who showed that a photon of a Laguerre-Gaussian beam carries an OAM of $l\hbar$ [152]. The OAM has its origin in the helical wavefronts of the beam, manifested in the $e^{il\phi}$ phase factor of the field[3]. Later, other beams were found to possess OAM, including Bessel beams, Bessel-Gaussian beams, and Hermite-Gaussian beams [153]. Laguerre-Gaussian beams are most common in free-space optics since they can be generated from a Gaussian beam using a Q-plate [154] or spatial light modulator to imprint the helical phase profile. OAM manifests itself in the rotation of a small absorbing particle around the phase singularity of the beam. This

[3]This definition of the sign of the OAM is valid for the phase propagation factor defined in Eq. 2.19 [145].

can result in the particle rotating around its center (if the particle is placed on-axis) [155], or orbiting the beam axis (if the particle is located off-axis) [156]. A detailed description of theory, generation, measurement, and applications of OAM beams can be found in Ref. [157].

In the context of step-index **fibers**, modes carrying an OAM of l can be expressed as a superposition of its even and odd vector modes. The following equations hold for the transverse field components $|\mathrm{XX}_{\nu,m}\rangle$ of the vector modes [158]:

$$G_{lm}(r)\,\mathrm{e}^{\mathrm{i}l\phi} \quad |+\rangle = \left|\mathrm{HE}^{e}_{l+1,m}\right\rangle + \mathrm{i}\,\left|\mathrm{HE}^{o}_{l+1,m}\right\rangle, \tag{2.24}$$

$$G_{lm}(r)\,\mathrm{e}^{\mathrm{i}l\phi} \quad |-\rangle = \left|\mathrm{EH}^{e}_{l-1,m}\right\rangle + \mathrm{i}\,\left|\mathrm{EH}^{o}_{l-1,m}\right\rangle, \tag{2.25}$$

$$G_{lm}(r)\,\mathrm{e}^{-\mathrm{i}l\phi}\ |+\rangle = \left|\mathrm{EH}^{e}_{l-1,m}\right\rangle - \mathrm{i}\,\left|\mathrm{EH}^{o}_{l-1,m}\right\rangle, \tag{2.26}$$

$$G_{lm}(r)\,\mathrm{e}^{-\mathrm{i}l\phi}\ |-\rangle = \left|\mathrm{HE}^{e}_{l+1,m}\right\rangle - \mathrm{i}\,\left|\mathrm{HE}^{o}_{l+1,m}\right\rangle, \tag{2.27}$$

where $G_{lm}(r)$ is the radial dependence of the corresponding LP mode, $|+\rangle$ denotes LCP and $|-\rangle$ denotes RCP as defined in Eq. 2.20. The index ν denotes the magnitude of the total angular momentum $|l+s|$. For $l=0$ and $l=1$ only those two equations involving the HE modes are valid because $\nu \geq 1$. For $l=1$, there are two additional relations involving the TE and TM modes:

$$G_{lm}(r)\,\frac{1}{2}\,\left(\mathrm{e}^{\mathrm{i}\phi}\,|-\rangle + \mathrm{e}^{-\mathrm{i}\phi}\,|+\rangle\right) = |\mathrm{TM}_{0,m}\rangle\,, \tag{2.28}$$

$$G_{lm}(r)\,\frac{-\mathrm{i}}{2}\left(\mathrm{e}^{\mathrm{i}\phi}\,|-\rangle - \mathrm{e}^{-\mathrm{i}\phi}\,|+\rangle\right) = |\mathrm{TE}_{0,m}\rangle\,. \tag{2.29}$$

Note that these equations cannot be simplified to obtain pure OAM states because TE and TM modes feature different effective indices.

For more general types of waveguides, in particular hollow-core waveguides, more than one OAM state can contribute to an eigenmode of the waveguide. To dissect these contributions, an orthonormal basis set with OAM-carrying basis states is required. Here, we use **Bessel beams** as such a basis, because it is closely related to the Fourier basis used in Cartesian coordinates [159]. Since the decomposition will be carried out for simulation results defined in a finite area, boundary conditions need to be imposed on the basis states. Here, we set the basis states Ψ_{lp} to zero at a certain radius R_0 from the origin, yielding [159]:

$$\boxed{\Psi_{lp}(\rho,\phi) = \frac{1}{\sqrt{N_{lp}}}\,J_l\left(\frac{\rho}{R_0}u_{l,p}\right)\mathrm{e}^{\mathrm{i}l\phi},} \tag{2.30}$$

where $J_l(x)$ is the l^{th} order Bessel function of the first kind, $u_{l,p}$ is the p^{th} root of $J_l(x)$, and $N_{lp} = \pi R_0^2 J_{l+1}^2(u_{l,p})$ is a normalization constant. A transverse field of uniform polarization can then be expanded as:

$$E(\rho,\phi) = \sum_{l=-\infty}^{\infty}\sum_{p=1}^{\infty} a_{l,p}\Psi_{lp}(\rho,\phi), \tag{2.31}$$

with the complex amplitudes $a_{l,p}$:

$$a_{l,p} = \int_0^{R_0} d\rho \int_0^{2\pi} d\phi \, E(\rho,\phi)\, \Psi^*_{lp}(\rho,\phi)\, \rho. \tag{2.32}$$

2.2.3 Total Angular Momentum (TAM)

A clear distinction between spin and OAM was possible for the beams in the preceding subsections because their fields were transverse [160]. However, such a simple distinction is not possible if the field is non-transverse. The conflict is most obvious when passing a transverse beam with a specific spin through a high numerical aperture lens. The lens does not break the rotational symmetry of the system but in the focus of the lens, one finds that part of the spin is converted to OAM [161]. In this case, only the total angular momentum (**TAM**) j is conserved, with the total angular momentum density[4] $\mathbf{j}$ given by [163]:

$$\mathbf{j} = \frac{1}{c^2}\mathbf{r} \times \langle \mathbf{S} \rangle, \tag{2.33}$$

where $\mathbf{r}$ is the position with respect to the center of the beam and $\langle \mathbf{S} \rangle$ is the time-averaged Poynting vector (cf. Eq. 2.11). The similarity to angular momentum in mechanics can be seen by noting that the linear momentum of light is given by $\mathbf{p} = \frac{1}{c^2}\langle \mathbf{S} \rangle$.

Accompanying the total angular momentum density $\mathbf{j}$, there is also an angular momentum flux density $\underline{\mathbf{M}}$, related by the conservation law:

$$\frac{\partial}{\partial t} j_i + \sum_l \frac{\partial}{\partial x_l} M_{l,i} = 0, \tag{2.34}$$

where $M_{l,i}$ described the flux of the i component of the angular momentum through a surface oriented perpendicular to the l direction. $\underline{\mathbf{M}}$ is defined in Ref. [164]. This conservation law is analogous to the energy conservation law, where the Poynting vector $\mathbf{S}$ plays the role of $\underline{\mathbf{M}}$. Agreeing with this analogy, the measurable TAM in a waveguide is characterized by the component $M_{z,z}$. Interestingly, $M_{z,z}$ can be separated in spin and OAM contributions even if the beam is non-paraxial. Integrated over the whole beam, the spin contribution $\mathcal{M}^s_{z,z}$ and OAM contribution $\mathcal{M}^l_{z,z}$ read [164]:

$$\mathcal{M}^s_{z,z} = \frac{1}{2\omega} \operatorname{Im}\left\{ \iint \mathrm{d}x\mathrm{d}y (E_x H_x^* + E_y H_y^*) \right\}, \tag{2.35a}$$

$$\mathcal{M}^l_{z,z} = \frac{1}{4\omega} \operatorname{Im}\left\{ \iint \mathrm{d}x\mathrm{d}y (-H_x^* \frac{\partial}{\partial\phi} E_y + E_y \frac{\partial}{\partial\phi} H_x^* - E_x \frac{\partial}{\partial\phi} H_y^* + H_y^* \frac{\partial}{\partial\phi} E_x) \right\}. \tag{2.35b}$$

To match this result with the spin s and OAM l used in the paraxial approximation, $\mathcal{M}^s_{z,z}$ needs to be normalized by the total energy flux of the beam[5] $P_z = \iint \mathrm{d}x\mathrm{d}y \, \langle \mathbf{S_z} \rangle$:

$$s = \frac{\mathcal{M}^s_{z,z}\,\omega}{P_z}, \qquad l = \frac{\mathcal{M}^l_{z,z}\,\omega}{P_z}, \qquad j = l + s. \tag{2.36}$$

[4] While not directly obvious from this expression, $\mathbf{j}$ also contains the spin contribution as discussed in Refs. [152, 162].

[5] Note that in Eq. 37 of Ref. [164] the energy flux (denoted as $\mathcal{F}$) is incorrectly defined by a factor $1/\omega$.

2.2.4 Optical Chirality Density

Twisted waveguides possess geometrical chirality, i.e., a helical waveguide cannot be superimposed with its mirror image. Chirality of optical fields, on the other hand, can be characterized by their chirality density C. For nondispersive media C is given by [165]:

$$\boxed{C(\mathbf{r}) = \frac{\omega n^2}{2c^2} \operatorname{Im}\{\mathbf{E} \cdot \mathbf{H}^*\}.} \tag{2.37}$$

Please note that during the calculation of the dot product, the vector $\mathbf{E}$ is not to be complex conjugated as one would typically do for a complex-valued scalar product. The dispersion of the material was neglected here because there is no resonance of the polymer within the investigated wavelength range $\left(-\lambda\frac{\partial n}{\partial \lambda} \ll n\right)$. Formulas for the chirality density inside lossy and/or dispersive media are available in Ref. [165].

C has a direct physical meaning in the sensing of small chiral molecules. Taking into account only the electric and magnetic dipole transitions of the molecule, the absolute difference in absorbance[6] of RCP and LCP light was shown to be proportional to the chirality density: $(A^R - A^L) \sim C$ [85].

To obtain a better understanding of the chirality density, it is calculated here for a circularly polarized plane wave with spin $s = \pm 1$:

$$\mathbf{E} = E_0 \mathrm{e}^{\mathrm{i}(k_0 n z - \omega t)} \frac{1}{\sqrt{2}} \begin{pmatrix} 1 \\ si \\ 0 \end{pmatrix}, \qquad \mathbf{B} = -s\mathrm{i}\frac{n}{c} E_0 \mathrm{e}^{\mathrm{i}(k_0 n z - \omega t)} \frac{1}{\sqrt{2}} \begin{pmatrix} 1 \\ si \\ 0 \end{pmatrix}, \tag{2.38}$$

$$\boxed{C(\mathbf{r}) = s\frac{\epsilon_0 \omega n^3}{2c} E_0^2 \quad \text{(circularly polarized plane wave).}} \tag{2.39}$$

As evident from this result, C has the same sign as the spin s and increases with intensity.

2.2.5 Superchiral Light

In typical sensing experiments, one is not interested in the absolute differences between two signals but its relative change. Applied to chiral sensing, the quantity of interest is usually the difference in absorbance between right- and left-circularly polarized light normalized to the average absorbance. This quantity is called Kuhn's dissymmetry factor or g-factor [166]:

$$\boxed{g = \frac{A^L - A^R}{\frac{1}{2}\left(A^L + A^R\right)}.} \tag{2.40}$$

[6] Absorbance is defined as the negative decadic logarithm of the ratio of transmitted to incident power on a sample: $A = -\log_{10}\left(\frac{I_{\text{transmitted}}}{I_{\text{incident}}}\right)$.

Since molecules are much smaller than the pitch of the circularly polarized wave (i.e., the wavelength), their measured g-factors are very low, with typical values being smaller than 10^{-3} [167].

Approximating the small molecule as a dipole, a relationship between the optical chirality density of the electromagnetic field and the measured response of the chiral molecule was shown theoretically [85] and experimentally [121] to be:

$$\boxed{g = g_{\text{molecule}} \cdot \underbrace{\frac{cC}{2\langle U_e \rangle \omega}}_{g_{\text{field}}},} \tag{2.41}$$

where $\langle U_e \rangle = \frac{1}{2}\langle \mathbf{D} \cdot \mathbf{E} \rangle = \frac{1}{4}|\mathbf{D}||\mathbf{E}|$ is the time-averaged energy density of the electric field. g_{molecule} is the g-factor that would be obtained in a measurement with plane wave CPL and only depends on the properties of the molecule (energy levels and transition moments). The second factor g_{field} describes a possible enhancement of the dissymetry factor relative to plane wave CPL. Note that this formula is only valid for isotropic samples of molecules that are much smaller than the wavelength of light and neglects any nonlinear interactions. For molecules immobilized on surfaces or larger molecules, higher-order multipole transitions need to be taken into account [85].

Interestingly, Eq. 2.41 shows that the measured g-factor of a given molecule can be enhanced by engineering a suitable field with a large value of g_{field}. This can be achieved by reducing the amplitude of the electric field while maintaining a high chirality density (e.g., strong magnetic field, and circular polarization of $\mathbf{E}$ and $\mathbf{H}$). In the following chapters, the quantity g_{field} will be used to characterize the chirality of the fields in the twisted waveguides. For linear media one can simplify g_{field} as:

$$g_{\text{field}} = Z_0 \frac{\text{Im}\{\mathbf{E} \cdot \mathbf{H}^*\}}{|\mathbf{E}|^2}, \tag{2.42}$$

with $Z_0 = \sqrt{\frac{\mu_0}{\epsilon_0}}$ being the vacuum impedance. For a linearly polarized wave g_{field} is equal to 0 and plugging in the values for a circularly polarized plane wave from Eq. 2.38 yields:

$$\boxed{g_{\text{field}} = s\,n \quad \text{(circularly polarized plane wave).}} \tag{2.43}$$

Consequently, any field distribution with $|g_{\text{field}}| > n$ can increase the measured g-factor and is referred to as **superchiral field**.

2.3 Coordinate Systems for Twisted Waveguides

A helical waveguide can best be analyzed in a coordinate system that follows the twist of the structure such that the waveguide becomes invariant along one of the new coordinates. Here, three different choices of a suitable coordinate system are introduced. While helicoidal coordinates are used for all simulations in this thesis, the section starts with a more general discussion of the Frenet-Serret frame. At the end, a coordinate system used by Overfelt [168] is presented.

2.3.1 Frenet-Serret Frame

Any differentiable curve $\mathbf{c}$ that is parametrized by a single parameter t can be described in a "self-defined" local orthonormal coordinate system, the Frenet-Serret frame. This coordinate frame will turn out to be the natural choice for off-axis twisted waveguides.

In three dimensions, the Frenet-Serret frame consists of the tangent vector $\hat{\mathbf{T}}$ at a given point of the curve, the normal vector $\hat{\mathbf{N}}$, and the binormal vector $\hat{\mathbf{B}}$ which are defined as follows [169]:

$$\hat{\mathbf{T}} = \frac{\mathbf{c}'(t)}{\|\mathbf{c}'(t)\|}, \qquad \hat{\mathbf{N}} = \frac{\hat{\mathbf{T}}'(t)}{\left\|\hat{\mathbf{T}}'(t)\right\|}, \qquad \hat{\mathbf{B}} = \hat{\mathbf{T}} \times \hat{\mathbf{N}}. \tag{2.44}$$

Since $\hat{\mathbf{T}}$ is a unit vector, its derivative $\hat{\mathbf{N}}$ can not point along $\hat{\mathbf{T}}$ (its length does not change) and therefore $\hat{\mathbf{T}}$ is orthogonal to $\hat{\mathbf{N}}$. Since $\hat{\mathbf{B}}$ is orthogonal to the other two vectors by definition, $(\hat{\mathbf{T}}, \hat{\mathbf{N}}, \hat{\mathbf{B}})$ defines an orthonormal coordinate system.

Further insights can be gained by looking at the derivatives of the basis vectors which are governed by the Frenet equations [169]:

$$\underbrace{\hat{\mathbf{T}}'(t) = a\bar{\kappa}\hat{\mathbf{N}}}_{(a)}, \qquad \underbrace{\hat{\mathbf{N}}'(t) = a(-\bar{\kappa}\hat{\mathbf{T}} + \tau\hat{\mathbf{B}})}_{(b)}, \qquad \underbrace{\hat{\mathbf{B}}'(t) = -a\tau\hat{\mathbf{N}}}_{(c)}, \tag{2.45}$$

where $a = \|\mathbf{c}'(t)\|$. Since the definition of the Frenet-Serret frame is independent of the parametrization, a can be chosen to be 1 if the curve is parametrized by the arc length. Remarkably, these equations are general, holding for any sufficiently differentiable curve. Eq. 2.45(a) and (c) serve as the definition of two proportionality constants, the curvature[7] $\bar{\kappa}$ and the torsion τ. Curvature $\bar{\kappa}(t)$ describes the deviation of the curve from a straight line, which can locally be described as a circle with radius[8] $1/\bar{\kappa}$ where $\hat{\mathbf{N}}$ points towards its center. Torsion $\tau(t)$ is a measure of twist - in the sense that it describes how fast the binormal vector $\hat{\mathbf{B}}$ rotates around the tangent $\hat{\mathbf{T}}$. For a curve defined on a 2D plane, both $\hat{\mathbf{T}}$ and $\hat{\mathbf{N}}$ lie within this plane meaning that $\hat{\mathbf{B}}$ is perpendicular to this plane and never changes direction. Therefore, a curve having zero torsion at every point is equivalent to the curve lying in a 2D plane.

Helices

A helix is a special type of curve that is defined by a constant curvature $\bar{\kappa}$ and torsion τ at every point of the curve [169]. The main parameters of a helix, which are used throughout the thesis are defined in Table 2.2.

[8] $1/\bar{\kappa}$ is also referred to as the radius of curvature.

Table 2.2: Definition of parameters used to describe a helix. Any curve with constant curvature and torsion is a helix [169]. Based on the definitions in Eq. 2.45(c) τ is positive for a right-handed helix and negative for a left-handed helix. The sign of α depends on the choice of the coordinate system and will be defined in each subsection.

Pitch: P	Twist rate: $1/P$	Curvature: $\bar{\kappa} = \frac{\rho}{\rho^2+\left(\frac{P}{2\pi}\right)^2}$
Radius: ρ	Angular twist rate: $\lvert\alpha\rvert = 2\pi/P$	Torsion: $\lvert\tau\rvert = \frac{2\pi P}{(2\pi\rho)^2+P^2}$

All simulations in this thesis are performed for left-handed helices. A helix is left-handed when it is possible to move the left thumb along the helix axis such that the remaining fingers curl along the helix trajectory. Note that the handedness does not depend on the direction under which you look at the helix. This definition is in line with the definition of circular polarization in Eq. 2.20: the curve traced out by the tip of the polarization vector of an LCP beam in space (at a fixed moment in time) is a left-handed helix.

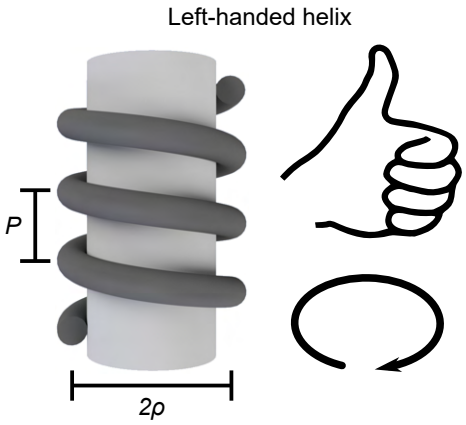

Figure 2.3: Definition of a left-handed helix with pitch P and radius ρ. When moving the thumb of the left hand along the helix axis and rotating the hand in the direction of the curled fingers, the fingertips move along the path of a left-handed helix. Note that the same result is obtained when pointing the thumb downwards. Drawing of hand was adapted from Ref. [170].

The definition of the unit vectors of the Frenet-Serret frame can be well understood on the example of an off-axis twisted waveguide that follows a left-handed helical path $\mathbf{c}(t)$ with $\alpha > 0$:

$$\mathbf{c}(t) = \begin{pmatrix} \rho\cos(\alpha t) \\ -\rho\sin(\alpha t) \\ t \end{pmatrix}. \tag{2.46}$$

For this helical trajectory, the basis vectors can be calculated according to Eq. 2.44 yielding:

$$\hat{\mathbf{T}} = \frac{1}{\sqrt{1+(\alpha\rho)^2}} \begin{pmatrix} -\alpha\rho\sin(\alpha t) \\ -\alpha\rho\cos(\alpha t) \\ 1 \end{pmatrix}, \quad \hat{\mathbf{N}} = \begin{pmatrix} -\cos(\alpha t) \\ \sin(\alpha t) \\ 0 \end{pmatrix}, \quad \hat{\mathbf{B}} = \frac{1}{\sqrt{1+(\alpha\rho)^2}} \begin{pmatrix} -\sin(\alpha t) \\ -\cos(\alpha t) \\ -\alpha\rho \end{pmatrix}. \tag{2.47}$$

These orthonormal unit vectors are shown below in Fig. 2.4. $\hat{\mathbf{T}}$ points in the tangential direction, $\hat{\mathbf{N}}$ lies in the xy plane and points towards the twist axis, and $\hat{\mathbf{B}}$ is orthogonal to

both. Therefore, a helical waveguide can be created by defining a refractive index profile in the NB plane and extending it infinitely along the $\hat{\mathbf{T}}$ coordinate. The simplest helical waveguide consists of a circular cross section in the NB plane and will be referred to as a **Frenet-Serret waveguide** in the following.

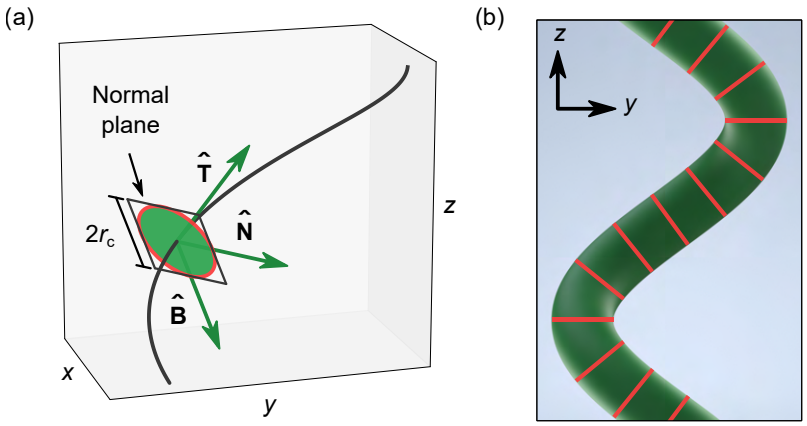

Figure 2.4: Definition of a helical waveguide in the Frenet-Serret frame. The basis vectors of the Frenet-Serret frame for a left-handed helix are shown in (a). $\hat{\mathbf{N}}$ and $\hat{\mathbf{B}}$ lie in the plane which is normal to the tangent vector $\hat{\mathbf{T}}$ of the helical path. When defining a circle in the NB plane (green with red border) and extending it infinitely along the third direction, a Frenet-Serret waveguide is created. An orthographic side-view of the waveguide is depicted in (b). Red stripes show the orientation of the circular cross sections.

2.3.2 Helicoidal Frame

Another local coordinate system to describe structures that are invariant along a helical path is the helicoidal frame. Helicoidal coordinates (ξ_1, ξ_2, ξ_3) are related to Cartesian coordinates (x, y, z) via [106]:

$$\mathbf{r} = \begin{pmatrix} x \\ y \\ z \end{pmatrix} = \begin{pmatrix} \xi_1 \cos(\alpha\xi_3) + \xi_2 \sin(\alpha\xi_3) \\ -\xi_1 \sin(\alpha\xi_3) + \xi_2 \cos(\alpha\xi_3) \\ \xi_3 \end{pmatrix} \quad \Leftrightarrow \quad \begin{pmatrix} \xi_1 \\ \xi_2 \\ \xi_3 \end{pmatrix} = \begin{pmatrix} x\cos(\alpha z) - y\sin(\alpha z) \\ x\sin(\alpha z) + y\cos(\alpha z) \\ z \end{pmatrix}. \tag{2.48}$$

For fixed values ξ_1 and ξ_2, the curve $\mathbf{r}(\xi_3)$ is a left-handed helix for $\alpha > 0$ (see Table 2.2). From this definition, the basis vectors of the helicoidal frame can be derived as:

$$\boldsymbol{\xi_1} = \frac{\partial \mathbf{r}}{\partial \xi_1} = \begin{pmatrix} \cos(\alpha\xi_3) \\ -\sin(\alpha\xi_3) \\ 0 \end{pmatrix}, \qquad \boldsymbol{\xi_2} = \frac{\partial \mathbf{r}}{\partial \xi_2} = \begin{pmatrix} \sin(\alpha\xi_3) \\ \cos(\alpha\xi_3) \\ 0 \end{pmatrix},$$

$$\boldsymbol{\xi_3} = \frac{\partial \mathbf{r}}{\partial \xi_3} = \begin{pmatrix} -\xi_1\alpha\sin(\alpha\xi_3) + \xi_2\alpha\cos(\alpha\xi_3) \\ -\xi_1\alpha\cos(\alpha\xi_3) - \xi_2\alpha\sin(\alpha\xi_3) \\ 1 \end{pmatrix}. \tag{2.49}$$

Note that ξ_3 is not normalized and the system (ξ_1, ξ_2, ξ_3) is not orthogonal. Since ξ_1 and ξ_2 always lie in the xy plane, the helicoidal coordinate system is especially useful if the wavefronts of the fundamental mode are perpendicular to the z axis. This is usually true for on-axis twisted structures.

A helical waveguide can be constructed in this coordinate system by defining a permittivity profile ϵ in the $\xi_1\xi_2$ plane (which is identical to the xy plane) and extending it infinitely along the ξ_3 coordinate:

$$\begin{gathered}\epsilon(\xi_1, \xi_2, \xi_3) = \epsilon(\xi_1, \xi_2, 0) \\ \Longleftrightarrow \\ \epsilon(x, y, z) = \epsilon(x\cos(\alpha z) - y\sin(\alpha z), x\sin(\alpha z) + y\cos(\alpha z), 0).\end{gathered} \tag{2.50}$$

When this profile is defined to be a circle, we refer to the resulting structure as a **helicoidal waveguide**. Note that the helicoidal waveguide differs from the Frenet-Serret waveguide in the way the circles are oriented (cf. Figs. 2.4 and 2.5).

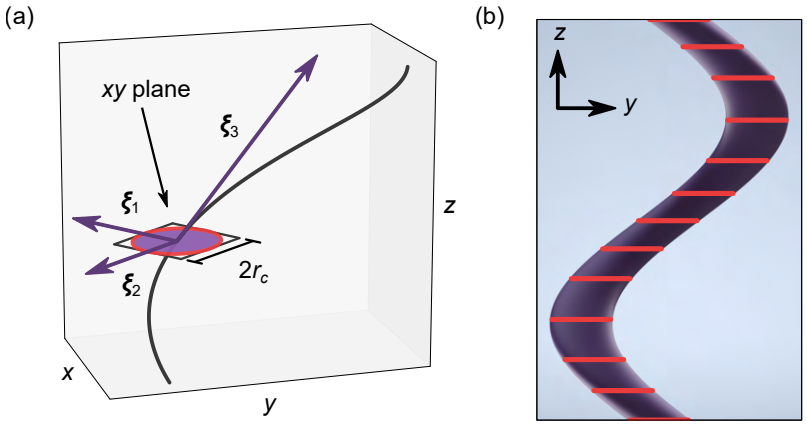

Figure 2.5: Definition of a helical waveguide in the helicoidal frame. The basis vectors of the helicoidal frame for a left-handed helix are shown in (a). Note that only ξ_1 and ξ_2 are normalized, which simplifies calculations. When defining a circle in the xy plane (purple with red border) and extending it infinitely along the ξ_3 direction, a helicoidal waveguide is created. An orthographic side-view of the waveguide is depicted in (b). Red stripes show the orientation of the circular cross sections.

In this thesis, the invariance of twisted waveguides along the ξ_3 coordinate is used to perform the optical simulations in two dimensions reducing computation time compared to a full 3D simulation. This is possible because the vector wave equations (Eq. 2.5) have the same form in any coordinate frame if the material properties ($\underline{\epsilon}$, $\underline{\mu}$) are replaced by **modified material properties** ($\underline{\epsilon}'$, $\underline{\mu}'$) [171]:

$$\underline{\epsilon}' = \underline{\mathbf{T}}^{-1}\underline{\epsilon}\,(\underline{\mathbf{T}}^{-1})^{\top}\det(\underline{\mathbf{T}}), \qquad \underline{\mu}' = \underline{\mathbf{T}}^{-1}\underline{\mu}\,(\underline{\mathbf{T}}^{-1})^{\top}\det(\underline{\mathbf{T}}), \tag{2.51}$$

where $\underline{\mathbf{T}}^{-1}$ is the inverse of the Jacobian $\underline{\mathbf{T}} = (\xi_1, \xi_2, \xi_3)$ of the coordinate transformation (calculated in Appendix B), $^{\top}$ denotes the transposed matrix, and det the determinant.

As the waveguides discussed in this thesis are made from isotropic materials (i.e., material properties are scalars), Eq. 2.51 reduces to [172]:

$$\underline{\epsilon'} = \epsilon \underline{\mathbf{G}}^{-1}, \qquad \underline{\mu'} = \mu \underline{\mathbf{G}}^{-1}, \tag{2.52a}$$

$$\text{with} \quad \underline{\mathbf{G}}^{-1} = \left(\frac{\underline{\mathbf{T}}^{\top} \underline{\mathbf{T}}}{\det(\underline{\mathbf{T}})} \right)^{-1} = \begin{pmatrix} 1+\alpha^2\xi_2^2 & -\alpha^2\xi_1\xi_2 & -\alpha\xi_2 \\ -\alpha^2\xi_1\xi_2 & 1+\alpha^2\xi_1^2 & \alpha\xi_1 \\ -\alpha\xi_2 & \alpha\xi_1 & 1 \end{pmatrix}. \tag{2.52b}$$

Twisting a waveguide therefore effectively results in the material properties becoming anisotropic, with the degree of anisotropy increasing with twist rate and distance from the twist axis. Furthermore, it is important to note that the curl operator in Eq. 2.5 takes on a nontrivial form as the helicoidal coordinate frame is not orthogonal [173].

2.3.3 Overfelt Frame

A third coordinate system in which a helical structure is translationally invariant along one axis is the coordinate frame (ρ, ϕ, ζ) used by Overfelt [168]. Its relation to the Cartesian lab frame is similar to the definition of cylindrical coordinates but includes an additional dependence on the angular twist rate α:

$$\mathbf{r} = \begin{pmatrix} x \\ y \\ z \end{pmatrix} = \begin{pmatrix} \rho\cos(\phi) \\ \rho\sin(\phi) \\ \zeta + \phi/\alpha \end{pmatrix} \qquad \Longleftrightarrow \qquad \begin{pmatrix} \rho \\ \phi \\ \zeta \end{pmatrix} = \begin{pmatrix} \sqrt{x^2+y^2} \\ \tan^{-1}(y/x) \\ z - \tan^{-1}(y/x)/\alpha \end{pmatrix}. \tag{2.53}$$

When fixing a particular value of ρ and ζ, $\mathbf{r}(\phi)$ describes a right-handed helix for $\alpha > 0$. By contrast, the helicoidal coordinate system describes a left-handed helix for $\alpha > 0$. The basis of the Overfelt system $(\mathbf{e}_\rho, \mathbf{e}_\phi, \mathbf{e}_\zeta)$ is nonorthogonal and can be calculated as:

$$\mathbf{e}_\rho = \frac{\partial \mathbf{r}}{\partial \rho} = \begin{pmatrix} \cos(\phi) \\ \sin(\phi) \\ 0 \end{pmatrix}, \qquad \mathbf{e}_\phi = \frac{\partial \mathbf{r}}{\partial \phi} = \frac{1}{\alpha} \begin{pmatrix} -\alpha\rho\sin(\phi) \\ \alpha\rho\cos(\phi) \\ 1 \end{pmatrix}, \qquad \mathbf{e}_\zeta = \frac{\partial \mathbf{r}}{\partial \zeta} = \begin{pmatrix} 0 \\ 0 \\ 1 \end{pmatrix}. \tag{2.54}$$

To construct a helical waveguide, a refractive index profile is defined in the $\rho\zeta$ plane (which is identical to the ρz plane of the cylindrical coordinate system) and extended infinitely along the ϕ coordinate. When this profile is a circle, we refer to the resulting structure as an **Overfelt waveguide**.

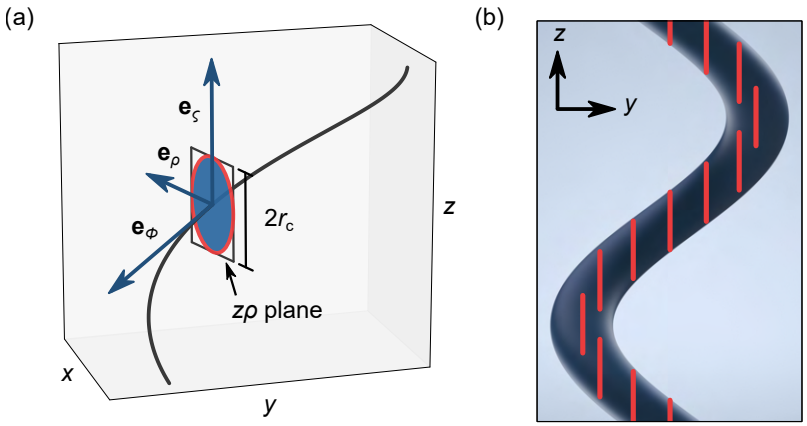

Figure 2.6: Definition of a helical waveguide in the Overfelt frame. The normalized basis vectors of the Overfelt frame for a left-handed helix are shown in (a). When defining a circle in the $z\rho$ plane (blue with red border) and extending it infinitely along the $\mathbf{e}_\phi$ direction, an Overfelt waveguide is created. An orthographic side-view of the waveguide is depicted in (b). Red stripes show the orientation of the circular cross sections.

2.4 Photonic Spin Hall and Orbital Hall Effect

Circularly polarized light traveling along curved trajectories (as in off-axis twisted waveguides) has been observed to split into two beams of opposite spin [174]. This unexpected behavior is an example of the photonic spin Hall effect akin to the electronic spin Hall effect observed in semiconductors [175, 176].

Both effects are based on the **spin-orbit interaction**, which is well known for electrons bound to a nucleus. A similar term that couples the spin and orbital motion of photons can be derived by approximating the complex electromagnetic fields as a single wavepacket, describing only the motion of its center of gravity [177, 161]. Such a **"semi-geometrical approximation"** can be applied when the trajectory of the wavepacket changes on lengthscales much larger than the wavelength. More specifically the parameter $\mu = \lambda_0/(2\pi \min(\bar{\kappa}^{-1}, \tau^{-1}))$ should be small. For a helical path, $\bar{\kappa}^{-1}$ and τ^{-1} are always larger than the radius ρ of the helix. Therefore, $\mu < 9 \times 10^{-3}$ with the parameters used in this thesis ($\rho = 14$ µm, $\lambda_0 = 770$ nm) and the approximation is principally valid.

The motion of the wavepacket can then be described to first order in μ as [178, 174]:

$$\frac{\partial \hat{\mathbf{T}}}{\partial s} = \bar{\kappa}\,\hat{\mathbf{N}}, \qquad \frac{\partial \mathbf{r}}{\partial s} = \hat{\mathbf{T}} \underbrace{-\hat{S}_3 \frac{\lambda_0}{2\pi n}\,\bar{\kappa}\,\hat{\mathbf{B}}}_{\text{Spin-orbit splitting}}, \tag{2.55}$$

where $\mathbf{r}$ describes the position of the wavepacket parametrized by the arc length s of its trajectory and ($\hat{\mathbf{T}}$, $\hat{\mathbf{N}}$, $\hat{\mathbf{B}}$) are the unit vectors of the Frenet-Serret frame for the trajectory that the light would take without spin-orbit coupling. The Frenet-Serret coordinate system

is defined in Section 2.3.1. $\bar{\kappa}$ is the local curvature, $\hat{S}_3$ is the third Stokes parameter and n is the refractive index.

The term on the right side is a consequence of the spin-orbit interaction of photonic wavepackets and results in a spin-dependent splitting of the beam along the B axis. For the helical waveguide with the highest investigated twist rate ($\rho = 14$ µm, P = 50 µm, $\lambda_0 =$ 770 nm, n = 1.54), the magnitude of the spin-orbit splitting term is equal to $\frac{\lambda_0}{2\pi n}\bar{\kappa} = 4.3 \times 10^{-3}$. This value is about three orders of magnitude larger than in a well-known free-space demonstration of the photonic spin Hall effect illustrated in Fig. 2.7. In this demonstration, a beam was constrained to a helical path at the inner surface of a macroscopic glass cylinder ($\rho = 8$ mm, $P = 16$ mm, $\lambda_0 = 633$ nm, $n \approx 1.5$, $\frac{\lambda_0}{2\pi n}\bar{\kappa} = 7.6 \times 10^{-6}$) [174]. In this case, the LCP and RCP beams are found to be displaced along the z axis (i.e., along the twist axis), which follows from integration of the spin-orbit splitting term over one turn of the helix. In other words, the two beams propagate along helices with the same radius but different pitch lengths. Experimentally, a splitting of about 2 µm was observed after a propagation distance of 96 mm.

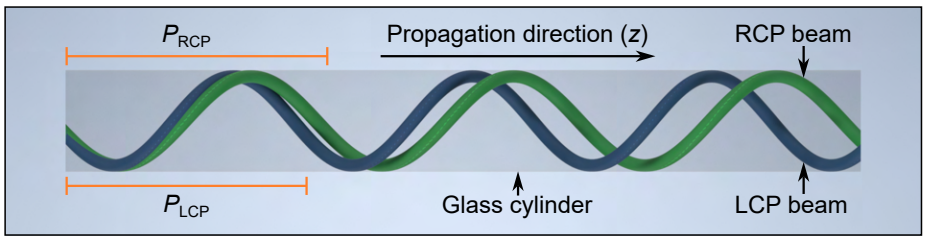

Figure 2.7: Experimental demonstration of the photonic spin Hall effect performed in Ref. [174]. A beam of LCP light (blue) and RCP light (green) is coupled into a cylinder under identical conditions and propagates along a helical path on its inner surface. For a left-handed helix, the RCP beam propagates with a larger helical pitch distance P than the LCP beam leading to a spin-dependent separation. Magnitude of the effect is exaggerated.

Apart from this demonstration, two main scenarios have been identified where the photonic spin Hall effect results in a spin-dependent splitting of a beam, i.e., refraction and reflection at the interface between two homogeneous media [179, 180], and propagation of light in a spatially inhomogeneous medium (referred to as the optical Magnus effect) [177, 181, 178].

Akin to the spin-orbit interaction, there is also an **orbit-orbit interaction** of photons, which couples the intrinsic OAM of a mode (caused by an $e^{il\phi}$ phase dependence) with its orbital motion (extrinsic OAM). The OAM-dependent spatial shifts caused by this interaction are referred to as **photonic orbital Hall effect** [182, 183]. The equations of motion for $\mu \ll 1$ are analogous to those of the spin Hall effect with the spin being replaced by the total angular momentum [183]:

$$\boxed{\frac{\partial \hat{\mathbf{T}}}{\partial s} = \bar{\kappa}\,\hat{\mathbf{N}}, \qquad \frac{\partial \mathbf{r}}{\partial s} = \hat{\mathbf{T}} - (s+l)\,\frac{\lambda_0}{2\pi n}\,\bar{\kappa}\,\hat{\mathbf{B}}.} \tag{2.56}$$

Therefore, the orbit-orbit interaction results in the same spatial splitting [184, 185] as the spin-orbit interaction but with a potentially much larger amplitude since the value of l can become arbitrarily large (within the number of available spatial modes).

Chapter 3

Experimental and Numerical Methods

3.1 Numerical Simulation

While the propagation of electromagnetic waves can be solved analytically for a variety of simple geometries, many real-world devices are more complex and require Maxwell's equations to be solved numerically. In the case of waveguides consisting of linear materials the governing equations are the vector wave equations (Eq. 2.5) combined with the separation ansatz of Eq. 2.6. These equations are also valid for twisted waveguides noting that the material properties become anisotropic and the differential operators need to be expressed in the twisted reference frame. Here, the nonorthogonal helicoidal coordinate system is used where the curl operator takes the form described in Ref. [173]. The discussion in this section is based on Refs. [186, 187].

3.1.1 Basics of Computational Electromagnetism

A common numerical technique to solve partial differential equations - like the vector wave equations - is the **finite element method (FEM)**. FEM solvers expand the field in terms of a finite set of basis functions $\mathbf{\Psi}_j$ which are nonzero only on a discrete patch of a mesh and its surrounding elements (Fig. 3.2):

$$\mathbf{E} = \sum_{i=j}^{N} c_j \mathbf{\Psi}_j. \tag{3.1}$$

The goal of the FEM solver is to determine the scalar expansion coefficients c_i. For two-dimensional problems like waveguides, the mesh is often triangular while three-dimensional problems typically use tetrahedral or prism-shaped elements. An example of a mesh is shown in Fig. 3.1. FEM solvers typically work in the **frequency domain**, i.e., the fields are expressed in terms of their (temporal) Fourier components $\mathbf{E}(x, y, z, \omega)$ such that:

$$\mathbf{E}(x, y, z, t) = \frac{1}{\sqrt{2\pi}} \int_{\mathbb{R}} \mathbf{E}(x, y, z, \omega) \mathrm{e}^{-\mathrm{i}\omega t} d\omega. \tag{3.2}$$

In this case, the vector wave equation for the electric field simplifies to[1]:

$$\boldsymbol{\nabla} \times \left(\underline{\mu_r}^{-1} \boldsymbol{\nabla} \times \mathbf{E} \right) - \frac{\omega^2}{c_0^2} \underline{\epsilon_r}\, \mathbf{E} = 0. \tag{3.3}$$

To discretize this equation, it is multiplied by a basis function $\boldsymbol{\Psi}_i$ from the left-hand side and integrated over the complete simulation domain Ω. Integration by parts[2] and assuming that the field vanishes at the boundary $\partial\Omega$ (**Dirichlet boundary condition**) yields:

$$\int_\Omega (\boldsymbol{\nabla} \times \boldsymbol{\Psi}_i) \cdot \underline{\mu_r}^{-1} \boldsymbol{\nabla} \times \mathbf{E} - \frac{\omega^2}{c_0^2} \boldsymbol{\Psi}_i \cdot \underline{\epsilon_r}\, \mathbf{E}\, dV = 0. \tag{3.4}$$

If this equation is fulfilled for any test function $\boldsymbol{\Psi}_i$, then $\mathbf{E}$ is a solution to the vector wave equation[3]. This statement is called the **weak form of Maxwell's equations**. Now, the expansion for $\mathbf{E}$ from Eq. 3.1 is inserted which results in a set of N linear equations that can be written in the form of a matrix as:

$$\underline{\mathbf{A}}\mathbf{c} = 0, \tag{3.5}$$

with $\mathbf{c} = (c_1, c_2, ...c_N)^{\mathrm{T}}$ containing the coefficients of the electric field and $\underline{\mathbf{A}}$ being an NxN matrix with entries:

$$\underline{\mathbf{A}}_{i,j} = \int_\Omega (\boldsymbol{\nabla} \times \boldsymbol{\Psi}_i) \cdot \underline{\mu_r}^{-1} \boldsymbol{\nabla} \times \boldsymbol{\Psi}_j - \frac{\omega^2}{c_0^2} \boldsymbol{\Psi}_i \cdot \underline{\epsilon_r}\, \boldsymbol{\Psi}_j\, dV. \tag{3.6}$$

Since a basis function is defined to be nonzero only near a specific mesh cell with limited overlap to other basis functions, the matrix $\underline{\mathbf{A}}$ is populated only near the diagonal. Such a sparse matrix can be efficiently inverted with LU solvers to find the solution for the electric field coefficients $\mathbf{c}$ [186]. If only the eigenvalue of a mode is to be determined, it can be found by the condition $\det(\underline{\mathbf{A}}) = 0$[4].

Having found the solution for $\mathbf{E}$, the solution for $\mathbf{H}$ can be directly calculated from Maxwell's curl equation (Eq. 2.1), which reads in frequency space:

$$\mathbf{H}(x, y, z, \omega) = \frac{1}{\mathrm{i}\omega\mu_0} \underline{\mu_r}^{-1} \boldsymbol{\nabla} \times \mathbf{E}(x, y, z, \omega). \tag{3.7}$$

Alternatively, the vector wave equation for $\mathbf{H}$ can be solved and the solution for $\mathbf{E}$ is subsequently calculated from the curl equation for $\mathbf{H}$.

In the derivation of the weak form of Maxwell's equations, the fields were assumed to vanish at the boundary $\partial\Omega$. To implement such a condition in a finite-sized simulation

[1] For better readability $\mathbf{E}(x, y, z, \omega)$ is abbreviated as $\mathbf{E}$.

[2] Integration by parts for curl operators reads: $\int_\Omega \mathbf{A} \cdot (\boldsymbol{\nabla} \times \mathbf{B})\, dV = \int_\Omega (\boldsymbol{\nabla} \times \mathbf{A}) \cdot \mathbf{B}\, dV - \int_{\partial\Omega} (\mathbf{A} \times \mathbf{B}) \cdot \mathbf{dS}$ and is based on the vector identity $\boldsymbol{\nabla} \cdot (\mathbf{A} \times \mathbf{B}) = (\boldsymbol{\nabla} \times \mathbf{A}) \cdot \mathbf{B} - \mathbf{A} \cdot (\boldsymbol{\nabla} \times \mathbf{B})$.

[3] The mathematical details are well explained in Ref. [187].

[4] Otherwise the matrix would not be invertible and no solution for the electric field would exist. Note that the basis functions $\boldsymbol{\Psi}_j$ need to fulfill the separation ansatz of Eq. 2.6.

region, a **perfectly matched layer (PML)** can be used as the outermost part of the simulation region, which was first shown in 1994 by Jean-Pierre Bérenger [188]. Today, PMLs are understood as a coordinate transformation that maps the spatial coordinates to the complex plane and are therefore referred to as stretched-coordinate PMLs [189, 190]. An example of the transformation in 1D is [187]:

$$x(\tau) = x_0 + (\gamma_r + \mathrm{i}\gamma_i)\tau, \tag{3.8}$$

where γ_r and γ_i are positive, and $\tau = 0$ at the location where the PML interfaces to the rest of the simulation region. γ_i results in the decay of oscillating waves since inside the PML $\exp(\mathrm{i}kx) = \exp(\mathrm{i}k(x_0 + \gamma_r\tau))\exp(-k\gamma_i\tau)$. The decay of evanescent waves entering the PML is enhanced by γ_i because $\exp(-kx)$ is mapped to $\exp(-kx_0 - \mathrm{i}k\gamma_i\tau)\exp(-k\gamma_r\tau)$. Such a coordinate transformation effectively changes the material properties as described in another context in Section 2.3.2.

For the exact wave equation, this PML perfectly absorbs every incoming wave. However, the numerical discretization can introduce reflections due to the change in material properties at the interface to the PML. This problem can be alleviated by gradually increasing the parameters γ_r and γ_i and choosing a sufficiently large upper value for τ. Optimizing the PML for a given problem nevertheless remains a challenging task in computational electromagnetism.

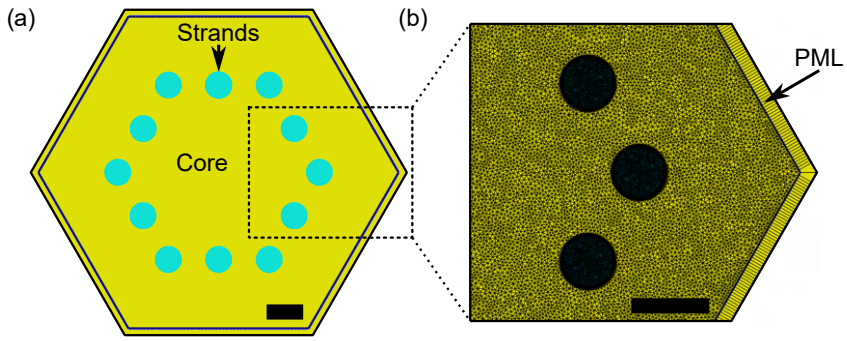

Figure 3.1: Simulation region of a twisted light cage used as input for the FEM solver. (a) Refractive index profile with air core (yellow) and polymer strands (cyan). (b) Triangular mesh with different cell sizes in the core and strand. The simulation region is surrounded by a PML to absorb outgoing waves. Scale bars denote 5 µm.

Apart from the Dirichlet boundary condition, other boundary conditions can be applied to $\partial\Omega$. Among the most common are **periodic boundary conditions** (e.g., for metasurfaces), **perfect electrical conductor (PEC)** or **perfect magnetic conductor (PEC)** boundary conditions which set the tangential component of the respective field to zero to simplify the simulations of symmetric structures.

Other popular numerical tools to solve Maxwell's equations are **rigorous coupled-wave analysis (RCWA)** and the **finite-difference time-domain (FDTD)** technique.

For **RCWA**, the structure is subdivided into uniform layers and within each layer, the fields and the geometry are expressed as a truncated (spatial) Fourier series[5]. Often RCWA is used for periodic structures where the wavefunction is expressed as a Bloch wave. The full solution is determined by imposing Maxwell's boundary conditions at the interfaces between the layers. RCWA is advantageous if the structure can be well divided into several uniform layers since the computation time only depends on the number of layers but not the height of each layer. Since RCWA is performed in Fourier space, large index contrast at edges of the structure cannot be well resolved or require a large number of Fourier modes to be simulated.

The **FDTD** technique discretizes the field solutions into regularly spaced time steps [191]. It uses the fact that the **E** field at the next time step can be calculated from the spatial distribution of the **H** field at the current time step using Maxwell's curl equations (Eq. 2.1). Conversely, the **H** field at the following time step can be updated based on the calculated spatial distribution of the **E** field. As a result, the fields are updated alternately at each time step. In terms of spatial discretization, the field components are often represented on a Yee lattice [192]. On this lattice, the Cartesian field components of **E** and **H** are interlaced such that a given component of **E** is surrounded by the four components of **H** required to calculate the next time step for **E**, and vice versa. The main advantage of FDTD is its ability to analyze the system's response across a wide frequency range in a single simulation run by using a broadband excitation pulse. FDTD is also particularly well-suited for describing nonlinear processes, that depend on the varying field amplitude.

However, both the RCWA and the FTDT method suffer from a common disadvantage: they discretize the fields on a regularly spaced lattice which means that the lattice spacing needs to reflect the smallest feature size throughout the entire structure. The finite element method offers a significant advantage in this regard because it allows the size of the mesh cells to vary across the geometry. Locations where the field undergoes rapid changes like interfaces can be resolved with a finer mesh and areas where the the transverse wavevector of the field is small can be approximated by a larger mesh. This flexibility in mesh cell sizes leads to a substantial reduction in computation time.

A further degree of freedom is presented by the choice of the basis functions, which are often polynomials. While tuning the mesh size is referred to as **h-refinement**, tuning the polynomial degree is referred to as **p-refinement** (Fig. 3.2). In many cases, the solver can automatically perform these refinements, enhancing the accuracy of the simulation with minimal additional computation time.

Since many problems in physics and engineering are based on partial differential equations, FEM solvers are well-developed and widely used. Practical course material on computational electromagnetism including videos of lectures can be found in Ref. [193].

[5]Therefore RCWA is also referred to as Fourier modal method (FMM).

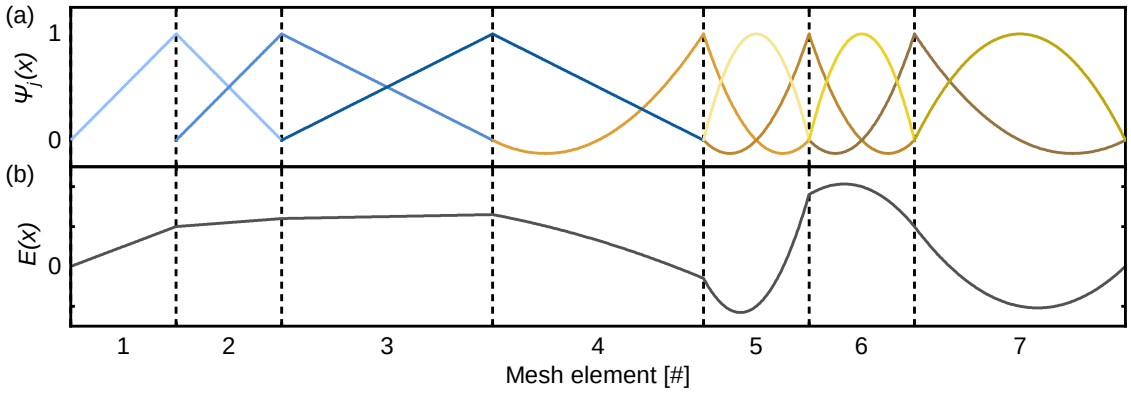

Figure 3.2: Example of adaptive meshing in 1D FEM. (a) Polynomial basis functions $\mathbf{\Psi}_j$ of linear (blue) and quadratic (yellow/orange) degree. (b) A field E represented as superposition of these basis functions. Finer details can be resolved if the mesh elements become smaller (h-refinement) or the polynomial degree is increased (p-refinement).

3.1.2 Setup and Convergence of the FEM Solver

In this thesis two commercial FEM solvers are used, COMSOL Multiphysics (RF module) for untwisted waveguides and JCMsuite (PropagatingMode module) for twisted waveguides since JCMsuite natively supports the helicoidal coordinate system. The workflow is similar for both software packages and will be outlined for **JCMsuite** here.

First, the waveguide is defined by specifying a 2D refractive index profile and surrounding the simulation region with a PML as shown in Fig. 3.1. The dispersion of the **refractive index of the polymerized resist**, from which the waveguide is made, is provided by Nanoscribe GmbH in the form of a single-term Sellmeier equation (shown in Fig. 3.3):

$$n(\lambda) = \sqrt{1 + \frac{A_1 \lambda^2}{\lambda^2 - \lambda_1^2}}, \tag{3.9}$$

with $A_1 = 1.3424689$ and $\lambda_1 = 0.128436$ µm. More detailed formulas including the imaginary part of the refractive index and its changes under different polymerization conditions can be found in Ref. [194]. In our analysis, we neglected the losses of the polymer because (1) only a negligible portion of the field is guided inside the polymer, and (2) scattering losses due to surface roughness of the polymer are likely higher than the intrinsic loss of the material.

Next, a **triangular mesh** is created with the resolution in each domain being determined by the "MaximumSidelength" option. Since JCMsuite currently does not support adaptive meshing for twisted structures, these values need to be determined manually. If the transverse wavevector component $k_{\text{transverse}}$ can be estimated, a good first guess is to limit the cell size to 1/6 of the typical transverse wavelength ($2\pi/k_{\text{transverse}}$) within each domain.

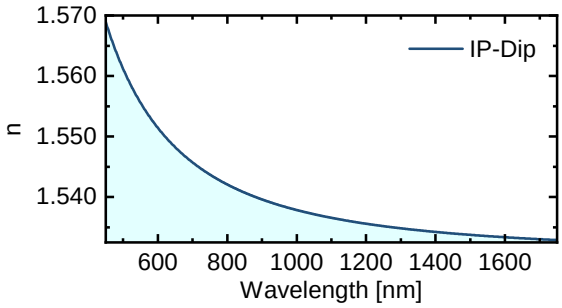

Figure 3.3: Refractive index of the polymerized resist (IP-Dip, Nanoscribe GmbH) calculated using Eq. 3.9.

An important parameter is the **"Precision"** setting of the solver which allows tuning the accuracy of the matrix solver, the PML, and - in case of untwisted structures - any mesh refinements, simultaneously[195]. A higher precision setting should generally be preferred but needs to be reduced if the matrix solver fails to find solutions at this precision level.

The settings of the **PML** are determined automatically by JCMsuite, i.e., the stretching parameters and the thickness are determined such that the numerical errors due to reflected waves from the PML remain below the set precision level. This is done by iteratively increasing the thickness of the PML until the reflectance is small enough. The process can be accelerated by defining a certain "StartThicknessLevel" to avoid the iteration starting with a too low PML thickness.

Lastly, the **convergence** of the computed eigenvalues under changes in the mesh size needs to be checked. The convergence of the real and imaginary part of n_{eff} with decreasing mesh size in the core and strands of a twisted light cage (discussed later in Chapter 6) with a strand diameter of $D = 3.6$ µm is shown in Fig. 3.4. As evident from Fig. 6.13 the fundamental mode of the twisted light cage develops more and more fine features as the twist rate increases which requires the use of finer meshes. A mesh size that yields sufficient convergence for this geometry at all investigated twist rates was $\lambda/6$ in the strands and $\lambda/2$ in the core[6]. For a $\lambda = 770$ nm this results in a mesh consisting of 117,950 triangles.

If the eigenvalues do not converge with decreasing mesh size, the distance between the outermost part of the structure and the PML should be adjusted. If the distance is too small, unwanted interactions with the PML might occur. If the distance is too large, the solver might not be able to find the correct eigenmode.

[6] λ denotes the free-space wavelength.

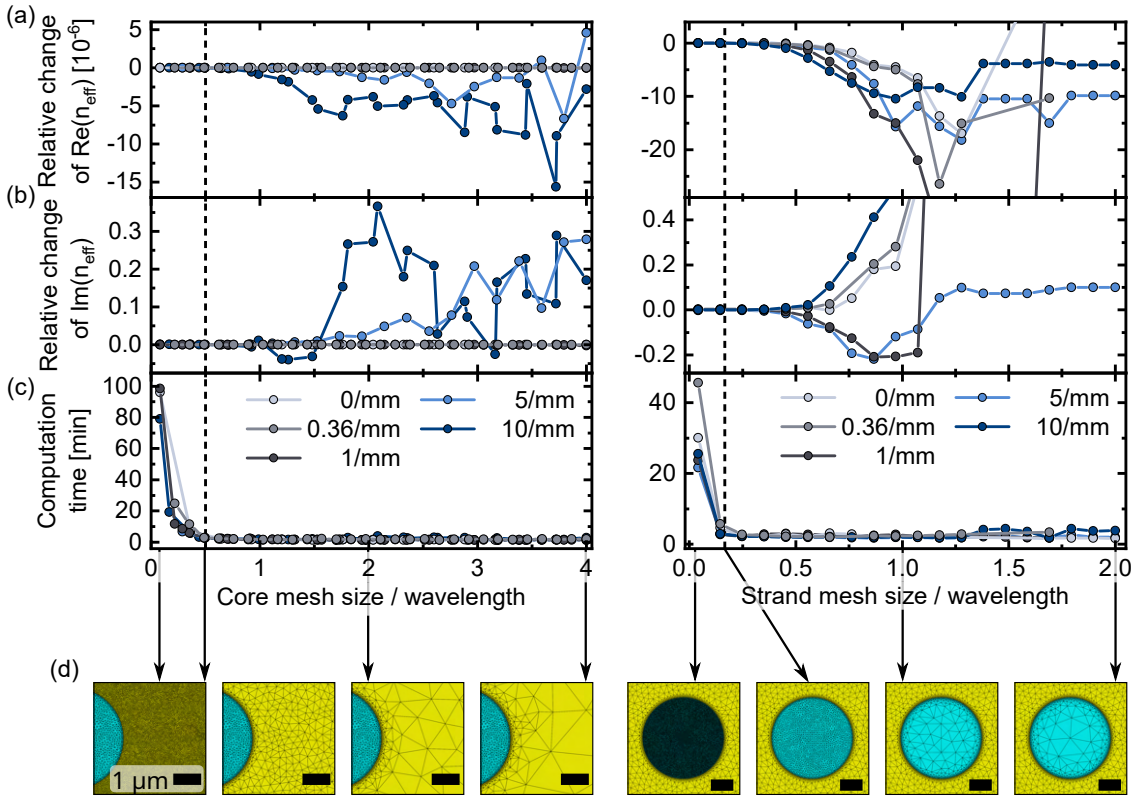

Figure 3.4: Convergence of the FEM simulation of the effective index n_{eff} with decreasing mesh size on the example of a twisted light cage. The cross section of the waveguide is depicted in Fig. 3.1. The convergence was checked for twist rates ranging from 0 to 10 twists per mm as indicated in the legend. The mesh size was varied both in the hollow core (left panels) and in the strands (right panels). Real (a) and imaginary (b) part of n_{eff} have converged to a satisfactory level for all twist rates once the mesh size reaches $\lambda/2$ in the core and $\lambda/6$ in the strands (dashed black lines). For even smaller mesh sizes, the computation time increases strongly (c). Selected meshes for the sizes indicated by the arrows are depicted in (d). The right-circularly polarized fundamental mode of the light cage was simulated at $\lambda = 770$ nm. For the simulations in the left panels, the mesh size in the strands was fixed to $\lambda/6$, while the mesh size in the core was fixed to $\lambda/2$ in the right panels.

3.2 Fabrication via 3D Nanoprinting

The waveguides investigated in this thesis are fabricated by **3D-laser-nanoprinting via two-photon-polymerization** of liquid photoresist, abbreviated throughout as 3D nanoprinting. The technology emerged in 1997 [69] and became widely available through commercialization by Nanoscribe GmbH in 2007.

Today, 3D nanoprinting is a mature technology enabling fabrication of 3D structures with feature sizes down to hundreds of nanometers and total sample footprints reaching

up to several centimeters. Three advantages set it apart from other lithographic techniques such as photolithography or electron-beam lithography: (1) the ability to create 3D structures in a single processing step, (2) short manufacturing times allowing fabrication of large-scale structures, and (3) cost-effective fabrication without the need for high temperatures, harsh chemicals or cleanroom conditions.

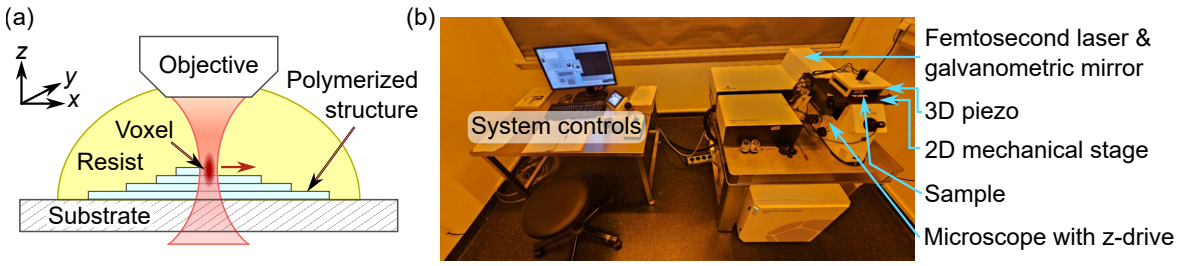

Figure 3.5: 3D nanoprinting setup. (a) Sketch of the dip-in configuration, where the objective is immersed in the photoresist. The beam is scanned in the xy plane by a galvanometric mirror. Structures are fabricated layer by layer within a single processing step (red arrow denotes fabrication direction). (b) Photographic image of the Nanoscribe Photonic Professional GT system used in this thesis indicating the main components. The room is illuminated by yellow light to avoid unwanted polymerization of the resist.

As illustrated in Fig. 3.5(a), 3D nanoprinting works by scanning a focused laser beam through a **photoresist** containing monomers and a small concentration of a photoinitiator, typically around 1% [196]. The photoinitiator molecules absorb light at twice the photon energy and start a polymerization reaction in the focal volume. Achieving the necessary rates for this third-order nonlinear process demands high peak intensities, which typically requires the use of pulsed femtosecond lasers. The polymerized volume resulting from a point exposure is referred to as a **voxel** - the building block of 3D nanoprinting. In analogy to a conventional 3D printer, structures are built up layer by layer by raster scanning of the laser focus through the resist. The spacing between these layers is referred to as **slicing distance** and between the individual lines in one layer as **hatching distance** as depicted in Fig. 3.6. To achieve the highest resolution, a high numerical aperture objective is inserted directly into the resist in what is known as the **dip-in configuration**. This

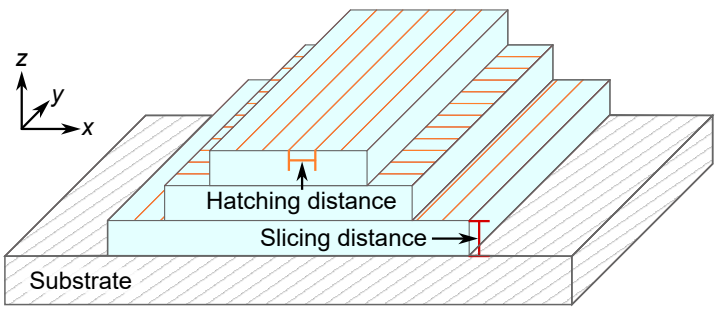

Figure 3.6: Slicing and hatching in 3D nanoprinting. Polymer layers (blue) are separated by the slicing distance. Each layer is created by scanning the focused laser beam along the hatch lines (orange), which are separated by the hatching distance. Direction of hatch lines typically alternates between layers.

configuration is selected to avoid any aberrations of the focus during fabrication. Following laser exposure, the structures are developed by immersion in a solvent which removes any unpolymerized resist. This type of resist is referred to as **negative-tone resist**. In contrast, **positive-tone resists** start from a gel or solid state and any unexposed areas remains after the development, which is advantageous if a structure with holes or voids is to be created [89]. The **refractive index** of 3D-nanoprinted polymers typically falls within the range of 1.5-1.7 in the visible, close to that of common glasses [197]. Furthermore, materials like conductive or biocompatible polymers, metals, high-refractive index glasses, and composite materials can be used with additional processing steps albeit with varying tradeoffs [197].

In this thesis, a commercial **3D nanoprinting system** (Photonic Professional GT, Nanoscribe GmbH, Fig. 3.5(b)) was used and all waveguides were realized on polished Silicon substrates in negative-tone IP-Dip resist (Nanoscribe GmbH). Laser pulses from a femtosecond laser with a center wavelength of 780 nm, repetition rate of 80 MHz, and pulse length of 100 fs are focused through a high numerical aperture objective (Plan-Apochromat 63x/1.40 Oil DIC, Zeiss, NA = 1.4) to induce polymerization of the resist. The waveguides are created laterally (xy) by scanning the focused laser beam using a galvanometric mirror and axially (z) by piezo-driven displacement of the substrate. Due to the occurrence of aberrations and a decrease in intensity towards the edges of the print field, the waveguides are divided into a number of segments with maximal lengths of 180 µm. After completing a segment, the substrate is shifted along the waveguide axis (here: x) by means of a mechanical stage. Artifacts arising from the stitching process were minimized by calibrating the mechanical stage and could further be improved by using stitch-free nanoprinting where mechanical stage and galvanometric mirror move in sync [198]. All the above commands are defined in a .gwl file using the DeScribe software. Typical printing parameters are listed in Table 3.1. Note that the reported value for the acceleration of the galvanometric mirror is only applicable within the framework of machines by Nanoscribe GmbH. Generally, a low mirror acceleration should be used to achieve a high quality of the edges of the printed structures.

Table 3.1: Typical parameters used for the fabrication of waveguides via 3D nanoprinting.

Parameter	Value
Slicing distance	200 nm
Hatching distance	150 nm
Acceleration of galvanometric mirror	1 V/ms^2
Scanning speed	70,000 µm/s
Laser power	37 mW (setting in Describe: 74%)

After laser exposure, the unpolymerized resist was removed by immersion in propylene glycol monomethyl ether acetate (PGMEA, Sigma Aldrich) for 30 min and Methoxynonafluorobutane (Novec 7100 Engineered Fluid, 3M) for 15 min, followed by evaporative

drying in air. Methoxy-nonafluorobutane is used in the last step of the development process because it has a low surface tension which reduces the capillary forces acting on the sample during the drying process.

An important aspect to understand in 3D nanoprinting is the advantage provided by the two-photon absorption process for the achievable **feature sizes and resolution**. For a voxel to form, the photoinitiator needs to absorb light to become activated (typically forming a radical). The probability for this process scales proportional to the intensity for single-photon absorption, while it is proportional to the square of the intensity for two-photon absorption. Assuming a Gaussian beam [130], the focal intensity distribution follows an exponential decay in the radial direction proportional to $\exp(-2(r/w_0)^2)$, and drops off slowly as $1/(1+z/z_r)^2$ in the axial direction, where w_0 is the beam waist in the focal plane, and $z_r = \pi w_0^2 n/\lambda$ is the Rayleigh length. Consequently, the two-photon absorption process results in a better confinement of the voxel, especially along the axial direction v_z as shown in Fig. 3.7. The resulting shape of the voxel is ellipsoidal with an **aspect ratio** v_z/v_{xy} of typically around 3.5 for high-NA objectives [199]. From a practical point of view, voxels with low aspect ratios are desirable in order to achieve the same printing resolution along all dimensions.

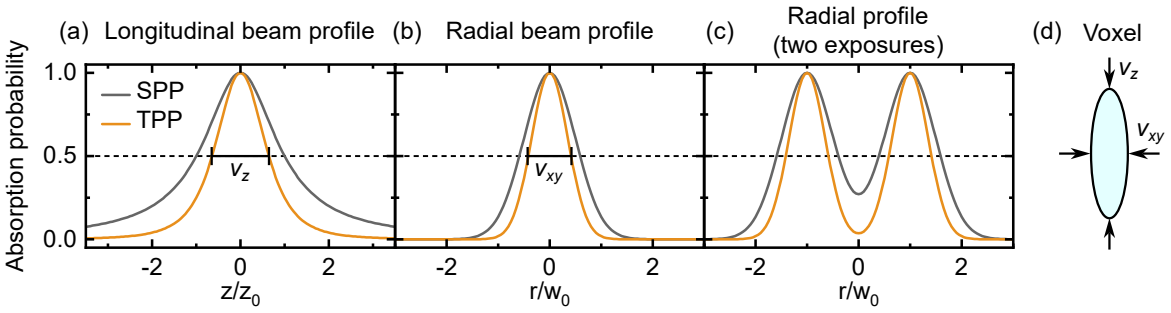

Figure 3.7: Normalized absorption probability in single-photon-polymerization (SPP) and two-photon-polymerization (TPP) in the focus of a Gaussian beam. (a,b) show profiles through the center of the focus. The profile in (c) describes two sequential point exposures separated in radial direction by $2w_0$. Due to the tighter confinement of the voxel in TPP, the overlap between features in close proximity to each other is reduced. (d) Sketch of the ellipsoidal voxel with lateral size v_{xy} and axial size v_z. z_0 and w_0 denote the Rayleigh length and beam waist, respectively. (a,b) adapted from Ref. [67].

Additionally, photopolymerization is subject to a **chemical nonlinearity**, i.e., a certain threshold concentration of the active photoinitiator needs to be reached before polymerization starts. Consequently, operating close to this polymerization threshold allows for the realization of arbitrarily small **feature sizes** - both with single- and two-photon absorption [200]. In practice, this regime can be reached by increasing the **scanning speed** of the beam, reducing the **laser power**, or by adding a polymerization inhibitor to the resist [200]. Employing this approach, suspended wires with sub-100 nm lateral feature size have been successfully fabricated [201], with the record achieving a width of 23 nm [202].

However, these small voxel sizes come at the cost of decreased **mechanical stability** and higher susceptibility to laser power fluctuations because the degree of crosslinking in the polymer is low near the threshold [203]. More complex structures require minimal lateral voxel sizes of at least 200 nm [199].

The main advantage of two-photon absorption lies in a more technical aspect: Once the photoinitiator is activated, it remains in this state for prolonged times if the threshold concentration is not yet reached, resulting in a buildup of active photoinitiator along the complete beam path [203]. This **memory effect** is especially detrimental in single-photon-polymerization as 100 out-of-focus exposures with 1% of the threshold intensity would already be enough to create unwanted artifacts [196]. Two-photon-polymerization, on the other hand, can tolerate up to 10,000 of such exposure giving the photoinitiator time to return to its inactive state.

Due to the memory effect, the achievable **lateral and axial resolution** (i.e., the smallest achievable spacing between features such that they can still be distinguished) is given by a version of Abbe's diffraction limit [203]:

$$\boxed{d_{\text{lateral}} = \frac{\lambda}{2\sqrt{2}\text{NA}} = 197 \text{ nm}, \qquad d_{\text{axial}} \approx \frac{\lambda A}{2\sqrt{2}\text{NA}} = 689 \text{ nm},} \tag{3.10}$$

where A is the aspect ratio of the voxel. Compared to single-photon-polymerization, the resolution in a two-photon-polymerization process is better by a factor of $\sqrt{2}$ as illustrated in Fig. 3.7(c). The calculated values correspond to the 3D nanoprinting system used in this thesis, assuming $A = 3.5$. An experimental demonstration for a simular system reached $d_{\text{lateral}} = 375$ nm and $d_{\text{axial}} = 509$ nm [204]. Further improvements in the resolution can be achieved by shrinking the polymer structures in a heat treatment allowing up to 5-fold reduction in side lengths [205].

Overall 3D nanoprinting by two-photon-polymerization offers the best combination of high printing speed (voxels/s) and high resolution within the group of **3D additive manufacturing techniques** (for a good overview see [206] and continuously updated version online [207]). Higher resolution is only achievable at orders of magnitude longer fabrication times, e.g., with electron beam induced deposition of gaseous precursors [208] or the emerging aerosol jet 3D nanoprinting technique [209].

3.3 Optical Transmission Measurements

To determine the optical properties of the fabricated samples, the transmission of white light through the waveguides was measured as shown in Fig. 3.8. The setups consist of a broadband supercontinuum laser source (SuperK Fianium, NKT Photonics, wavelength range: 390 nm - 2400 nm, repetition rate: 152 kHz - 80 MHz, output power: 5-15 mW in a 10 nm window), in- and outcoupling objectives mounted on 3D translation stages (Olympus, 20 x, NA = 0.4; Olympus, 10 x, NA = 0.25), a CCD camera (Thorlabs DCU223C) for imaging the waveguide mode, and a spectrometer (Princeton Instruments Acton MicroSpec

2500i, grating period: 300 g/mm, blaze angle: 750 nm, spectral resolution: $\Delta\lambda = 0.13$ nm, detector: Princeton Instruments Acton Pixis 100) connected to a multimode-fiber (M15L05, core size: 105 µm). Light is coupled to the fundamental mode of the waveguide, which is optimized by beam steering and shifting the objective on a 3D translation stage (Elliot Martock MDE122). The process is monitored by imaging the core mode onto the camera and optimizing for highest pixel intensity while preserving the shape of the fundamental mode. In a second step, the power coupled to the fiber of the spectrometer is maximized. For measurements of wavelength ranges beyond 1100 nm, an optical spectrum analyzer (Ando AQ-6315A) is used, which needs to be combined with a notch filter to block the pump laser of the supercontinuum source at 1060 nm. All recorded spectra are normalized to a reference spectrum taken without a sample and the objectives moved closer together to compensate for the missing length of the waveguide. Mode images at different wavelengths were recorded using the wavelength selector of the supercontinuum source (SuperK SELECT, smallest transmission bandwidth: 10 nm).

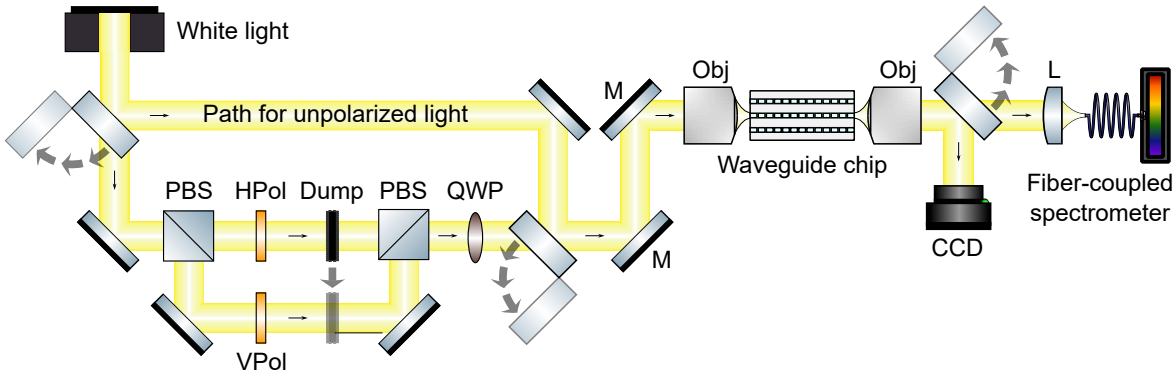

Figure 3.8: Setup for transmission and circular dichroism measurements. White light: supercontinuum laser source, PBS: polarizing beamsplitter, HPol/VPol: horizontal/vertical linear polarizer, QWP: quarter waveplate, Qbj: objective, CCD: camera, L: lens, M: mirror pair for beam steering. Flip mirrors determine whether polarized or unpolarized light is sent to the waveguide chip, and a beam dump is used for selecting a specific polarization. Component library from Ref. [210] was used.

The setup allows light of several polarization states to be used, in particular unpolarized, linearly polarized (horizontal/vertical with respect to the plane of the sample substrate), and circularly polarized (LCP/RPC) light. To generate polarized light, linear polarizers (Thorlabs LPVIS100, 550 - 1500 nm), and a quarter waveplate (Thorlabs AHWP05M-980, 690 - 1200 nm) with its optical axis oriented at a 45° angle with respect to the axis of the polarizers were used.

Circularly polarized light was needed specifically to determine the circular dichroism of twisted waveguides (i.e., a difference in transmission of LCP/RPC light) which is discussed in Chapter 6. Measurements of circular dichroism pose additional requirements on the setup because reflections and refractions on any surface reduce the degree of circularity

of the polarization state, thus creating elliptically polarized light (because the Fresnel reflection coefficients are generally different for TE and TM incidence [137]). To avoid this, the quarter waveplate is the last optical element before the light is coupled to the waveguide. Furthermore, any shifts of the beam need to be avoided when switching between LCP and RCP light as such shifts would change the amount of light that is coupled to the waveguide, thus leading to false positive CD measurements. To avoid any mechanical movement, the two linear polarizers are placed in the arms of a Mach Zehnder interferometer beam path. By blocking one arm of the beam path, a specific linear polarization (horizontal or vertical) is selected, which translates to a specific circular polarization after the quarter waveplate. The beam path is created using two polarizing beamsplitters (Thorlabs PBS252, 620 - 1000 nm) to avoid the 75% loss that would occur for non-polarizing beamsplitters. For accurate measurements, a precise overlap of the two beams created in the interferometer is essential, which is achieved by ensuring that the beam positions match at two points that are about 1.5 m apart: an iris at the output of the interferometer and the pinhole represented by the multimode fiber.

Chapter 4

3D-Nanoprinted Antiresonant Hollow-Core Waveguides

As mentioned in Chapter 1, 3D nanoprinting is a promising fabrication technique for realizing chip-integrated hollow-core waveguides. A unique advantage of this approach is the ability to realize structures with **high structural openness**, allowing any medium of interest to enter the waveguide passively via diffusion. As such, the presented works are a step towards realizing compact, cost-efficient, and mass-producible photonic devices and sensors such as infrared and Raman spectrometers, integrated quantum optical circuits, optofluidic setups, or point-of-care diagnostics.

Two types of hollow-core waveguides will be discussed, the microgap waveguide consisting of square-shaped waveguide segments separated by micrometer-sized gaps for analyte exchange, and the light cage featuring a freely suspended hexagonal array of polymer strands with side-wise access to the core. Light guidance in both waveguides is provided by the **antiresonance effect**, i.e., by a mismatch between the effective index of the core and cladding modes. The specific implementation of this guidance mechanism in both waveguides will be explained.

In Section 4.1, all relevant optical properties of **microgap waveguides**, such as propagation loss, tunability of the resonances, and influence of the gaps on transmission are experimentally revealed and simulated. Furthermore, two analytical models for light guidance in square-core antiresonant waveguides are developed that correctly describe the experimental behavior. To demonstrate the sensing capabilities, absorption spectroscopy of ammonia gas and aqueous solutions of Rhodamine 6G (R6G) dye was performed.

Light cages were previously introduced in Refs. [66, 81, 82] and the fundamental aspects of light guidance covered in these works will be summarized in Section 4.2. Building on these works, we study the repeatability and accuracy of the fabrication method and demonstrate that waveguide lengths of up to 3 cm can be reached. Additionally, possible applications of light cages in fluorescence spectroscopy will be covered. Overall, the study of light cages serves as a basis for Chapter 6, where twisted variants of these waveguides will be studied.

4.1 Microgap Waveguides

The results presented in this chapter are published in Ref. [211]:

J. Bürger, V. Schalles, J. Kim, B. Jang, M. Zeisberger, J. Gargiulo, L. S. Menezes, M. A. Schmidt, and S. A. Maier

"*3D-nanoprinted antiresonant hollow-core microgap waveguide - an on-chip platform for integrated photonic devices and sensors*"

 Note that results from the Master's thesis of the author [67] are used in this chapter as they are required to introduce the topic. Specifically, the transmission measurements and theoretical modeling of the waveguides are part of [67]. All work related to the gas sensing experiment and writing of the manuscript [211] was carried out during the doctorate.

The concept of microgap waveguides was motivated by the desire to create a 3D-nanoprinted hollow-core waveguide with a straightforward design, simplifying reproduction and allowing complete analytical modeling of its optical properties. The design features two elements that alternate on the micrometer scale as shown in Fig. 4.1: (1) a square-shaped hollow waveguide segment of length L responsible for confining light via the antiresonance effect, and (2) an open gap region of length G allowing fast diffusive access to the core. The light confining segment consists of the hollow core with edge length D, surrounded by a polymer wall of thickness W and refractive index n_W.

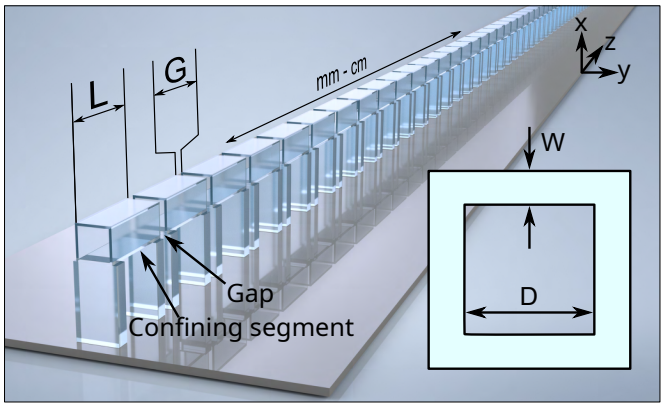

Figure 4.1: Illustration of the on-chip hollow-core microgap waveguide fabricated via 3D nanoprinting. The main parameters are gap size G, segment length L, wall thickness W, and core size D. Inset: Square-shaped cross section.

4.1.1 Light Guidance in Square-shaped Hollow-core Waveguides

As the refractive index of the used polymer is on the order of $n_W = 1.5$ (Fig. 3.3), modes in the lower-index core are not bound by total internal reflection. To understand why the formation of stable modes is still possible, it is insightful to study the optical properties

of a single waveguide segment of infinite length, i.e., neglecting the gaps. In the following, we describe the optical properties of this segment using FEM simulations and develop two analytical models for the effective index and propagation loss of the fundamental core modes.

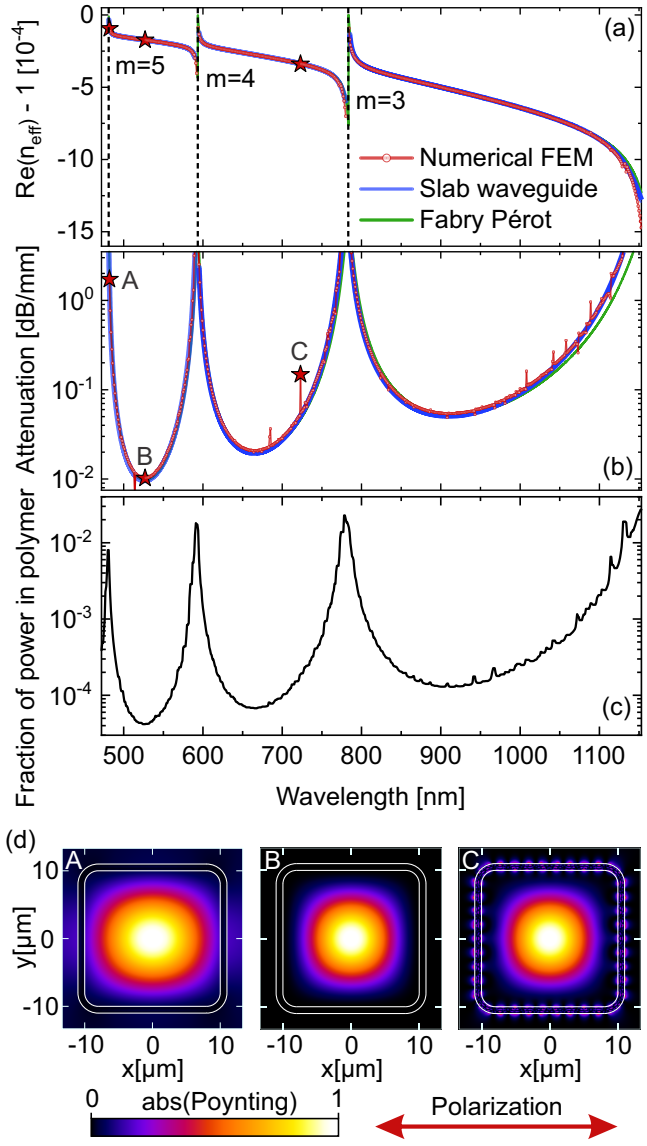

Figure 4.2: Optical properties of microgap waveguides (theory). (a,b) Spectral distribution of the real part of the effective index and the attenuation of the fundamental core mode (red: 2D FEM simulation of a rounded cross section of the waveguide, green: Fabry-Pérot model, blue: leaky slab waveguide model). The vertical black dashed lines in (a) denote the position of the cladding resonances (Eq. 4.5). All calculations include the material dispersion of the polymer. (c) Median-filtered spectral distribution of the optical power located in the polymer walls normalized to the total power of the mode integrated over the complete simulation region (square with length of 34 µm). (d) Simulated Poynting vector distribution of the core mode at the wavelengths indicated in (a,b) by the red stars (A: Close to resonance, B: Off-resonance, C: Azimuthal sub-resonance). Red arrow denotes the polarization of the propagating mode. The calculations were performed for D = 20 µm and W = 1 µm.

Numerical simulations were conducted for a 2D cross section of the waveguide following the description in Section 3.1. To reduce the computation time, we leveraged the Cartesian symmetry of the waveguide allowing the simulation region to be limited to one quarter of the cross section. For this approach, perfect-electrical conductor and perfect magnetic conductor boundary conditions were applied along the vertical and horizontal symmetry lines, respectively. The simulations reveal the formation of a fundamental mode in the core with broad spectral bands of high transmission, which are delimited by sharp

resonances with orders of magnitude higher loss (Fig. 4.2(b)). For practical applications, the waveguide will be operated in the off-resonance domains, in which losses of about 0.01 dB/mm for visible light are theoretically achievable ($D = 20$ µm, $W = 1$ µm). Simulations of the shape of the fundamental mode show that in these low-loss regions, the shape of the mode nearly follows the C_{4z} symmetry of the cross section and most of the optical power is located inside the core (Fig. 4.2(d), image B). Only a small fraction of the power of well below 10^{-3} remains inside the polymer wall (Fig. 4.2(c)), similar to the previously investigated light cage geometry [83]. Closer to the resonance, the mode spreads out along the polarization direction, transforming to an elliptical shape (Fig. 4.2(d), image A). This asymmetric shape arises due to the polarization dependence of the reflections on the confining walls.

The fundamental idea why stable modes can exist in the low-index medium can be understood based on a ray model. According to Fresnel's equations [128], even low-index dielectrics become highly reflective under near-grazing incidence, effectively turning the waveguide walls into mirrors. However, due to the finite thickness of the walls, interference of waves inside the material needs to be taken into account. At certain wavelengths, this interference leads to Fabry-Pérot resonances where the confining material becomes completely transparent. In the wavelength intervals between these resonances, light can be guided with low loss.

The derivation of this **Fabry-Pérot model** can be seen as the counterpart to a previously reported analytical description of tube-type hollow-core waveguides [212]. The analysis starts by initially assuming perfect reflectivity, resulting in field nodes on the surfaces of the wall. In this case, the wavevector of the fundamental mode (i.e., the direction of the ray) is given by:

$$\mathbf{k} = \begin{pmatrix} \kappa \\ \kappa \\ \beta \end{pmatrix}, \tag{4.1}$$

where $\kappa = \pi/D$ is the transverse wavevector component, $\beta = \sqrt{k_0^2 - 2\kappa^2}$ is the propagation constant, and k_0 is the free space wavevector. This step fixes the angle of incidence $(\pi/2 - \Theta)$ at the core-cladding boundary. A posteriori, we now find that the assumption of grazing incidence $(\Theta \ll \pi/2)$ is justified if the core size is much larger than the wavelength $(D \gg \lambda)$,

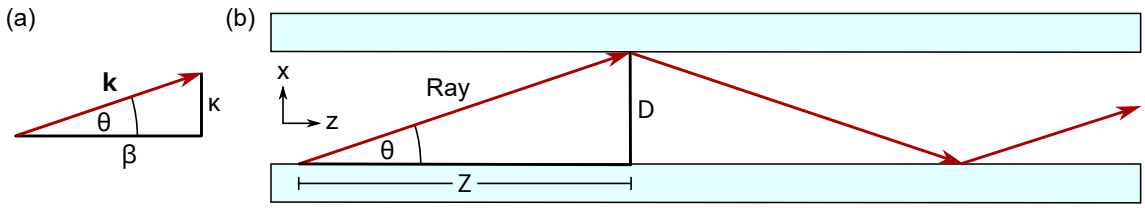

Figure 4.3: Sketch of the wavevector components (a) and zig-zag length Z (b) for the Fabry-Pérot model. Only the horizontal walls are shown. Light is propagating along the z direction with propagation constant β. When taking the vertical wall pair into account, two reflections occur over the distance Z. θ is the inclination angle of the ray.

which is the case in the fabricated structures. In the next step, we take into account the finite reflectivity of the walls, describing them as Fabry-Perot resonators yielding reflection coefficients $r^{\mathrm{FP}}_{\mathrm{TE/TM}}$ for transverse electric (TE) and transverse magnetic (TM) polarized waves as [213]:

$$r^{\mathrm{FP}}_{\mathrm{TE/TM}} = \frac{r_{\mathrm{TE/TM}}(1-\mathrm{e}^{2\mathrm{i}\phi})}{1-r^2_{\mathrm{TE/TM}}\mathrm{e}^{2\mathrm{i}\phi}}, \qquad r_{\mathrm{TE}} = \frac{\kappa-\kappa_W}{\kappa+\kappa_W}, \qquad r_{\mathrm{TM}} = \frac{\kappa-\frac{\kappa_W}{n_W^2}}{\kappa+\frac{\kappa_W}{n_W^2}}, \tag{4.2}$$

$$\kappa_W^2 = k_0^2 n_W^2 - \beta^2, \qquad \phi = W\kappa_W, \tag{4.3}$$

$$T^{\mathrm{FP}}_{\mathrm{TE/TM}} = 1 - \left|r^{\mathrm{FP}}_{\mathrm{TE/TM}}\right|^2, \tag{4.4}$$

where r_{TE} and r_{TM} are the reflection coefficients at a single air-dielectric interface obtained from Fresnel's equations, κ_W is the transverse wavevector component in the wall, ϕ is the phase acquired by the waveguide mode in a single pass through the wall and $T^{\mathrm{FP}}_{\mathrm{TE/TM}}$ is the transmission through the Fabry-Pérot slab. Eq. 4.2 directly allows calculation of the resonances, which correspond to the wavelengths λ_{Res} where the reflectivity of the Fabry-Perot slab vanishes ($r^{\mathrm{FP}}_{\mathrm{TE/TM}} = 0$):

$$\boxed{\lambda_{\mathrm{Res}} = \frac{2W}{m}\sqrt{n_W^2-1} \quad \forall\, m \in \mathbb{N},} \tag{4.5}$$

where m is the order of the resonance, which is equal to the number of field oscillations in the polymer layer. To estimate the real and imaginary parts of the effective index of the fundamental mode in the off-resonance regions, we define the zig-zag length Z along the waveguide axis over which the fundamental mode undergoes two reflections, one on a horizontal wall and one on a vertical wall (Fig. 4.3):

$$Z = \frac{\beta D}{\kappa} \approx \frac{k_0 D}{\kappa} \qquad \text{for D} \gg \lambda. \tag{4.6}$$

With this lengthscale, the attenuation coefficient α or - alternatively - the imaginary part of the effective index can be calculated as[1]:

$$\alpha = \frac{2T_{av}}{Z}, \qquad \boxed{\mathrm{Im}(n_{\mathrm{eff}}) = \frac{\lambda^2 T_{av}}{4\pi D^2},} \tag{4.7}$$

with $T_{av} = (T_{\mathrm{TE}} + T_{\mathrm{TM}})/2$ describing the polarization averaged transmission coefficient of the Fabry-Pérot slab. Lastly, the effect of the resonances on the real part of the effective index is addressed. To this end, we calculate the additional phase shift $\Delta\phi$ due to the imperfect reflections on the walls resulting in a modification $\Delta\beta$ of the propagation constant compared to the perfectly reflecting waveguide:

$$\Delta\phi = \arg\left(-\frac{r^{FP}_{\mathrm{TE}} + r^{FP}_{\mathrm{TM}}}{2}\right), \qquad \Delta\beta = \frac{2\Delta\phi}{Z}. \tag{4.8}$$

[1] Over a length z, the transmission follows $T = \exp(-\alpha z) = \exp(-2\,\mathrm{Im}(n_{\mathrm{eff}})k_0 z)$.

With this modification, the real part of the effective index can be expressed as:

$$\boxed{\mathrm{Re}(\mathrm{n_{eff}}) = \frac{\beta + \Delta\beta}{\mathrm{k_0}} = \sqrt{1 - \frac{\lambda^2}{2\mathrm{D}^2}} + \frac{\lambda^2 \Delta\phi}{2\pi \mathrm{D}^2}.} \tag{4.9}$$

In **summary**, the Fabry-Pérot model yields closed-form expressions for the dispersion and the propagation loss of the fundamental core mode, which matches well with the results of the FEM simulation shown in Fig. 4.2(a,b), with small deviations occurring towards longer wavelengths. Most relevant from a practical point of view is Eq. 4.5, which shows that the spectral positions of the resonances solely depend on the thickness of the wall W for a given refractive index n_W of the polymer.

In a broader context, the Fabry-Pérot model reveals that the mechanism of light guidance in microgap waveguides is based on the **antiresonance effect** [214] - a phenomenon observed in all hollow-core waveguides studied in this thesis. At certain wavelengths, the core mode is phase-matched to a cladding mode of the Fabry-Pérot cavity (vertical dashed black lines in Fig. 4.2(a)), leading to large propagation losses due to the removal of power from the core mode. Away from the resonances, the wavevector mismatch grows which prevents mode coupling to occur, resulting in transmission bands with low loss (cf. discussion on mode coupling in Section 2.1.3). Using Eq. 4.7, these off-resonance losses can be shown to scale as $\mathrm{Im}(n_{\mathrm{eff}}) \sim D^{-4}$ [67], which is in line with previous findings for tube waveguides [212]. Therefore, the losses can be made arbitrarily small by choosing larger core diameters as the incidence angle on the core-cladding interface gets more and more shallow. However, antiresonantly confined modes always dissipate energy during propagation and are therefore referred to as tunneling leaky modes or leaky modes [215]. Such leaky modes are common to many waveguides where light is not guided via total internal reflection, such as ARROWs [53], hollow-core photonic-crystal fibers [216, 217] or revolver hollow-core fibers [218].

As a separate step, we investigated a model that describes the square core as an independent superposition of two infinitely extended slab waveguides [135] corresponding to the horizontal and vertical wall pair, respectively (details can be found in Appendix A). For this **leaky slab waveguide model**, the effective indices of the fundamental TE and TM modes of a single slab waveguide were calculated numerically by solving Maxwell's equations with suitable boundary conditions. These were then combined to obtain the complex effective index n_{eff} of the square-shaped waveguide while neglecting the fields in the corners (Fig. A.1). Note that this approximation is particularly valid in situations where the core extent is substantially larger than the wavelength λ as it is the case for the fabricated samples. Furthermore, simulations showed that the exact shape of the corners is irrelevant, both for the position of the resonances and the off-resonance loss [67]. The results of this model (blue lines in Fig. 4.2(a,b)) yield virtually complete overlap with the full electromagnetic simulation (red lines).

None of the two models accounts for azimuthal resonances (Fig. 4.2(d), image C), visible through field oscillations along the long axis of the rectangular cladding elements, which has a length of $D + 2W$. The spectral positions of these azimuthal resonances strongly

depend on the shape of the corners, where the approximation of having two independent slab waveguides breaks down [67]. As shown in Ref. [219] these azimuthal resonances do not notably impact the modal characteristics and thus can be neglected for the microgap waveguide.

4.1.2 Implementation of Microgap Waveguides

The microgap waveguides were fabricated directly on silicon chips in a single pass of 3D nanoprinting using liquid IP-Dip photoresist with the procedure described in Section 3.2. The entire waveguide is supported from below by a chain of supporting blocks, which makes fabrication independent of potentially rough or tilted substrate surfaces. The maximum spacing between blocks in order for the structure to be stable was determined to be 60 µm. This design allows quick and reproducible fabrication, with a typical manufacturing time of 10 minutes per millimeter waveguide length. SEM and transmission microscopy images of the resulting waveguides are shown in Fig. 4.4.

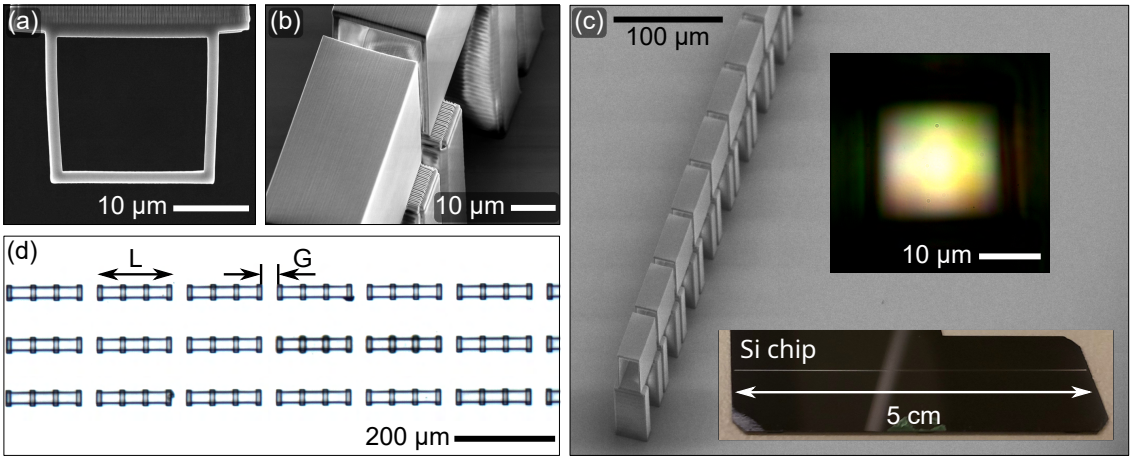

Figure 4.4: Fabrication of microgap waveguides. (a,b,c) Scanning electron microscope (SEM) images of a fabricated structure showing the cross section (a), the gap between adjacent elements (b), and an overview (c). Note that the dimensions in (b) and (c) are affected by the tilt of the chip during SEM imaging. Insets in (c): Photographic image of a 5 cm long microgap waveguide nanoprinted onto a silicon chip; CCD image of the core mode. (d) Transmission microscopy image of three waveguides (top view).

The degree of reproducibility of the printing method is verified for light cages in Section 4.2 - showing low chip-to-chip variations of the printed dimensions of about 15 nm. An overview of fabrication inaccuracies is provided in Table 4.10.

Combined with the accessibility of all three spatial dimensions offered by 3D nanoprinting, the parameters of microgap waveguides can be straightforwardly adapted to the requirements of a certain application. This flexibility was used in Ref. [67] to investigate the impact of changing wall thickness W (600 nm - 2 µm), core size D (10 µm - 20 µm), gap

length G (2 µm - 40 µm) and segment length L (45 µm - 1 mm). The maximum waveguide length reached is 5 cm (see inset image in Fig. 4.4(c)). These experimental results will be summarized in the next subsection.

In order to quantify the amount of open space for side-wise accessing the core, we calculated the **structural openness factor (SOF)** for all fabricated devices. The SOF is defined here as the fraction of the surface area of the waveguide that is open to the environment [66] which in this case is given by SOF $= G/(L+G)$. Fully functional samples with SOFs ranging from 0.2% to 18% were fabricated.

4.1.3 Characterization of Transmission Loss, Resonance Tunability and Gaps

The fabricated waveguides were characterized optically by measuring their transmission spectrum and mode profile using an unpolarized supercontinuum white light source. Details of the setup are described in Section 3.3.

All investigated samples show a core mode formation from the blue to the near-infrared, matching the shape predicted by the numerical simulations (Fig. 4.2(d)). The recorded spectra show bands with high transmission delimited by resonance dips, reaching contrasts of more than 60 dB for the sample with 5 cm length. Repeatability of the fabrication is high as indicated by the light-colored lines in Fig. 4.5 which represent transmission spectra of identical copies of the waveguide located on the same chip.

Based on the idea of the cut-back method, we determined the **propagation loss** of samples with a core size of $D = 20$ µm and SOF of 1 % ($L = 176$ µm, $G = 2$ µm) by measuring the transmission spectrum of samples with different length ranging from 0.5 cm to 5 cm (Fig. 4.5(a)). The results were fitted with the expected transmission for an ideal waveguide:

$$T(z) = A\exp(-\alpha z), \qquad \text{Attenuation}\,[\text{dB/length}] = \frac{10\,\text{dB}}{\ln(10)}\alpha, \tag{4.10}$$

where $A < 1$ describes the coupling loss arising from a mismatch between the field of the focused laser beam and the profile of the fundamental mode. A is also referred to as butt coupling coefficient and was introduced as c_{pq} in the section on coupled mode theory (Eq. 2.16). From this fit, the modal attenuation within the transmission bands in the visible is obtained as 0.38 - 0.72 dB/mm increasing to 1.25 dB/mm in the IR (1400 nm) for this specific core size and gap length. The coupling loss for the used setup was on the order of 3 - 4 dB.

According to Eq. 4.5, the **resonance wavelengths** can be tuned by varying the thickness of the polymer walls W. This relationship was experimentally verified by changing the thicknesses of the vertical walls between 600 nm and 2 µm with step sizes down to 60 nm (circles in Fig. 4.5(b)). Using Eq. 4.5 we calculated the experimentally realized wall thicknesses and verified that the designed step sizes (i.e., thickness increments) were successfully implemented as 62 nm and 67 nm (samples with wall thicknesses of 1670 nm, 1737 nm,

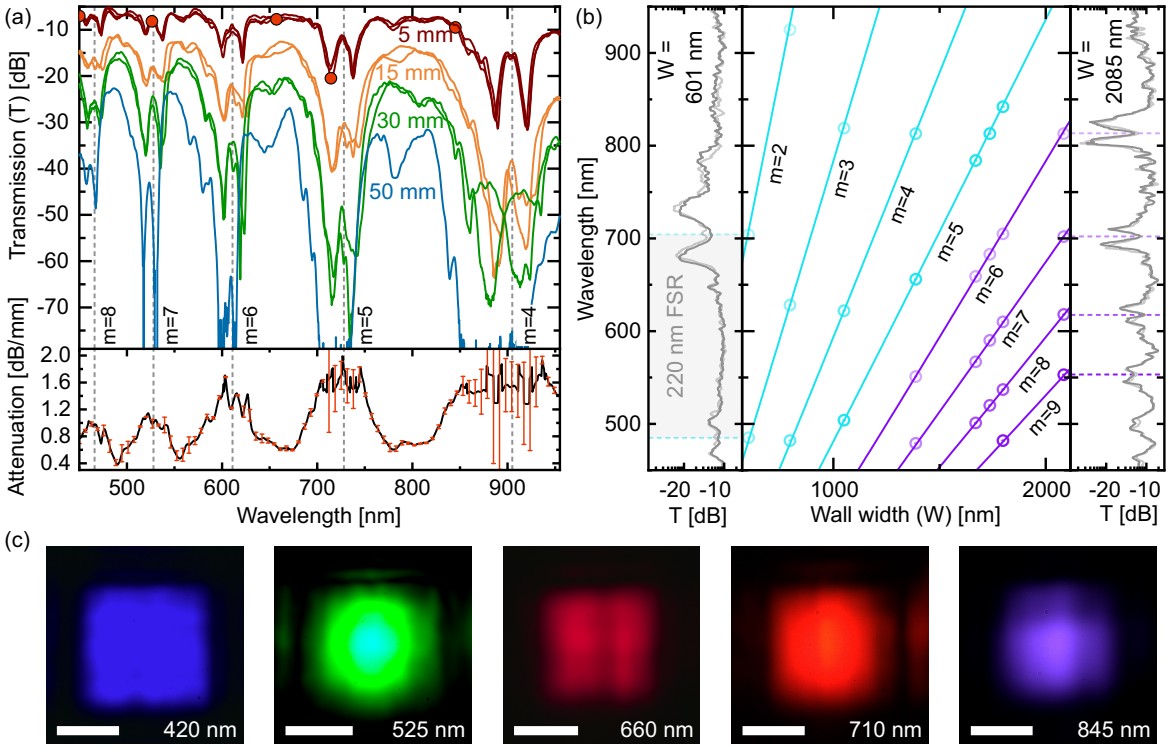

Figure 4.5: Optical properties of microgap waveguides (experiment). (a) Transmission spectra of waveguide samples (G = 2 µm, L = 176 µm, D = 20 µm, W = 1.55 µm) with different total lengths (red: 0.5 cm, orange: 1.5 cm, green: 3 cm, blue: 5 cm). Vertical dashed lines: Theoretical resonance wavelengths of order m obtained from the Fabry-Pérot model. Bottom plot: Spectral distribution of the modal attenuation. Values of copies of a certain structure are shown as curves with lower degree of color saturation. (b) Measured dependence of resonance wavelengths (circles) on wall thickness. Lines show the relation expected from the Fabry-Pérot model (Eq. 4.5). Gray curves show transmission spectra for the lowest (W = 601 nm) and largest (W = 2085 nm) investigated wall widths. (c) Measured mode profiles at selected wavelengths indicated by red circles in (a). Modes between 420 nm and 710 nm are represented by their true colors as measured by the camera. Scale bars have a length of 10 µm.

and 1799 nm). The thickness of the horizontal walls was kept fixed to 1.7 µm because a separate experiment showed that resonances corresponding to the horizontal walls are not observable [67]. Evaluating the change of the resonance wavelengths with wall thickness yields tuning slopes between 1.13 nm/nm for the $m = 2$ resonance and 0.25 nm/nm for the $m = 9$ resonance. Remarkable is the large free spectral range of 220 nm in the visible of the sample with 600 nm wall thickness as shown in the left panel of Fig. 4.5(b). This thickness is close to the transverse size of the printed voxel which sets a fundamental size limit to the features realizable by 3D nanoprinting. By calculating the difference between the measured wall thickness and the designed wall thickness, we determined the lateral voxel size v_{xy} to be (358 ± 23) nm for the used printing parameters [67].

Furthermore, the impact of the **gaps** on the transmission characteristics was studied by comparing samples with a fixed SOF of 18 % but different distributions of gaps to a reference sample which is nearly completely closed (SOF = 1 %, $G = 2$ µm) [67]. For a fixed SOF, the losses decrease when a large number of small gaps is used instead of a few long gaps. Assuming that the gap loss of the reference sample is negligible, we determined a loss per gap of 0.003 dB for a gap size of $G = 5$ µm increasing to 0.22 dB per gap for $G = 40$ µm.

In all recorded transmission spectra, a **double dip structure** is visible, which most likely arises due to fabrication-related inhomogeneities in the wall thickness. Numerical simulations reveal that surface roughness in the cross section of the waveguide can lead to a splitting of the resonances, especially towards shorter wavelengths [67]. Another reason might be a slight difference in the wall width between the left and right side of the square-shaped cross section. By fitting a sample spectrum with a two-width model, this difference was determined to be on the order of 50 nm for a wall thickness of 1.55 µm [67].

4.1.4 Discussion of Optical Properties

The two presented **analytical models** are in good agreement with the numerical simulations, with the leaky slab waveguide model showing the best overlap, especially at IR wavelengths, all of which confirm that antiresonance guidance is the relevant light guidance effect. Note that Eq. 4.5 accurately predicts the spectral positions of the resonances (Fig. 4.5(b)), providing a straightforward pathway to design samples with desired optical properties.

Numerical investigations showed that **fabrication inaccuracies** such as a rounding of the corners or surface roughness that is uniform along the waveguide axis (e.g., parallel stripes running along the waveguide axis) does not have a strong impact on the waveguide transmission [67]. This is in line with previous findings that the exact shape of the corners of polygonal hollow-core waveguides is irrelevant for its optical properties [220]. **Loss** due to the introduction of gaps was investigated experimentally and also found to be low with about 10^{-2} dB per gap for gaps shorter than 10 µm. However, the experimentally observed off-resonance loss is about one order of magnitude higher than predicted by theory. This could be explained by surface roughness that is non-uniform along the waveguide axis therefore acting as a grating that leads to scattering losses. Preliminary AFM measurements of the waveguide walls showed that such roughness is present in the fabricated samples. Future work will target improving the wall uniformity and quality to reach higher levels of transmission, particularly at IR wavelengths. Furthermore, the theoretical modeling indicates that an increased core size D substantially reduces modal attenuation, as losses were found to scale as $1/D^4$ [67]. This phenomenon is also found in antiresonant fibers [212] and is different from waveguides that operate on total internal reflection, where the modal losses are defined by scattering and material absorption. As the reflectivity of the waveguide walls increases with the refractive index contrast, a further reduction of the loss of the waveguide could principally be achieved by using materials with higher refractive index during the printing process like ceramics or crystalline materials provided

that the strong shrinkage of the typically used hybrid organic-inorganic resists during the heat-induced curing can be substantially reduced [221, 222, 223, 224, 225]. On the other hand, materials with lower refractive indices like quartz glass might also be beneficial because the losses from surface roughness could be lower [226, 227] and the resonances shift less with a varying wall thickness (see Eq. 4.5). However, the optical properties of the waveguides also depend to a great extent on the mechanical stability of the resist and the ability to create optically smooth surfaces, making it hard to judge a priori which type of resist is best suited. Overall, the use of inorganic materials would provide better stability of the microgap waveguides against harsh environmental conditions. As shown for light cages, protection against corrosive chemicals can also be provided by coating the nanoprinted structures with alumina nanofilms via low-temperature atomic layer deposition (ALD) [82, 57].

The experiments indicate that the introduction of **gaps** into the waveguide system does not influence the position of the transmission bands but only the magnitude of the overall transmission. For reaching a certain SOF, it seems beneficial to distribute many small gaps along the waveguide axis instead of a few long gaps. Here, we want to point out that beam diffraction of the waveguide mode in the gaps is low since the Rayleigh length of a comparable Gaussian-shaped mode is on the order of 200 µm which is much longer than the investigated gap sizes. Imperfect terminations of the segments or a manufacturing-induced offset between segments perpendicular to the beam axis could further contribute to the gap loss.

The high degree of **reproducibility** of the transmission spectra of copies of the same waveguide within one chip shows that the 3D nanoprinting process is a highly precise method for manufacturing waveguides. A quantitative study of the reproducibility is provided in Section 4.2 for light cages. Despite the fact that the voxel size is approximately half the wavelength of the femtosecond laser, sub-wavelength control of the wall thickness down to 60 nm is possible using 3D nanoprinting (Fig. 4.5(b)).

Compared to ARROW waveguides, microgap waveguides achieve similar propagation loss and total sample lengths [228, 54] while offering simplified fabrication and transverse access to the core region through the gaps. In addition, square-core waveguides are intentionally independent of the polarization direction of the light, which is an advantage over ARROW waveguides which often have rectangular cross sections [229, 230, 231, 232]. One particular advantage of microgap waveguides is their large structural openness factor: Waveguide architectures that contain holes that are introduced in a post-processing step, often reach SOFs of only $0.001\ \% - 0.005\ \%$ [60, 61, 62], while in contrast, the fabricated microgap waveguides reach SOFs of up to 18 %. Such high openness is especially important for experiments relying on passive diffusion of a medium into the core, such as low vapor pressure quantum optics [57], nanoparticle tracking analysis [233], or the sensing of gases and liquids presented in the next two subsections.

4.1.5 Sensing Applications

The large structural openness and the ability to precisely tune the wavelengths of the transmission bands, make microgap waveguides interesting for on-chip sensing applications, both for liquid and gaseous samples. As proof-of-principle, we use microgap waveguides to demonstrate **refractive index sensing** of isopropanol/water mixtures, and **absorption spectroscopy** of ammonia (gas) and Rhodamine 6G dye solution (liquid).

Quantitative analysis is possible by relating the measured absorbance A and the molar concentration c of the analyte via **Lambert-Beer's law** [234]:

$$A = \log_{10}\left(\frac{P_0}{P}\right) = \epsilon c l, \tag{4.11}$$

with the incident power P_0, the transmitted Power P, the molecular absorption coefficient ϵ, and the absorption path length l. It is important to note that Lambert-Beer's law is only valid if the modal field is entirely present inside the analyte. As shown in Fig. 4.2(c) this assumption is justified in microgap waveguides as the fraction of power inside the material of the waveguide is well below 10^{-3} within the transmission bands. This provides a clear advantage over solid-core waveguides, where a non-negligible part of the field is guided in the material and only the evanescent field interacts with the analyte. Since the extent of this evanescent field is wavelength-dependent, solid-core waveguides require complex modal calculations that precisely consider the waveguide geometry to modify Lambert-Beer's law for quantitative sensing applications [235].

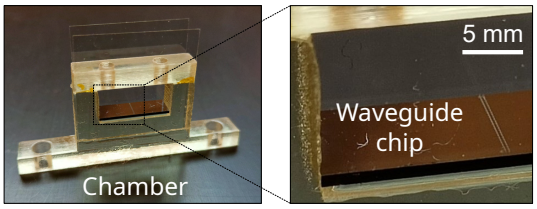

Figure 4.6: Example of an experimental chamber used in the sensing experiments. This specific chamber was used in gas sensing of ammonia and includes gas in- and outlets (two holes on the top side).

To define a specific interaction volume, the waveguides are placed in **3D-printed chambers** made by a conventional 3D-printer (Agilista from Keyence Corp., method: PolyJet technology, photopolymer: AR-M2, see Fig. 4.6). Laser light can enter and exit the chamber through borosilicate glass windows with a thickness of 0.15 mm each. Analytes are introduced into the chamber and passively diffuse into the waveguide. A key aspect of the study involves determining the timescale for this process, i.e., the **analyte exchange time**. We investigate how this time depends on the gap size and compare it to the diffusion speed in bulk media, and in capillaries without side-wise openings (SOF = 0).

Sensing of Gases

Gas sensing in microgap waveguides is demonstrated on the example of ammonia, which features a strong absorption line at a wavelength of $\lambda_0 = 1501.74$ nm [236, 237]. The employed setup consists of a tunable diode laser (TUNICS 1550, Photonetics), two microscope objectives for in- and outcoupling (Edmund, 20 x, NA= 0.4; Olympus, 10 x, NA = 0.25), a short-wave infrared camera (ABS, IK1513), and an infrared photodiode (Thorlabs, S122C) to monitor the outgoing power (Fig. 4.7). Gas mixtures of nitrogen with varying concentrations of ammonia ranging from 10 % to 100 % were prepared using a computer-controlled gas mixer (Qcal, GMS_4CH_HP). From there the gas mixture flows through a tube to the inlet of the experimental chamber while the outlet is open to ambient air. Further details on the experiment and data analysis are reported at the end of this section.

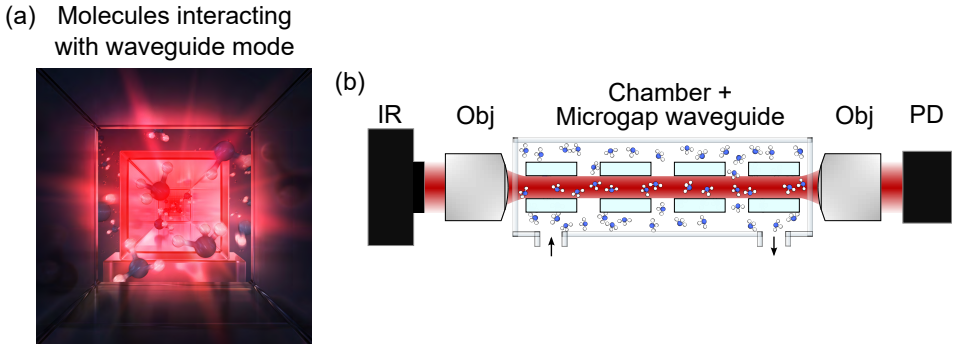

Figure 4.7: IR gas absorption spectroscopy with microgap waveguides. (a) Illustration of the inside of the waveguide filled with ammonia molecules (light is propagating towards the reader's eye). Artwork was created by Vera Hiendl, e-conversion (DFG cluster of excellence). (b) Schematic of experimental setup illustrating the diffusion of ammonia molecules into the waveguide core (IR: tunable infrared laser, Obj: microscope objective, PD: IR photodetector, arrows: gas in- and outlets).

To ensure that the targeted wavelength lies within a transmission band of the microgap waveguides, we implemented samples with a wall width of $W = 1.67$ µm. The corresponding transmission spectrum of one of the used waveguides is depicted in Fig. 4.8. All samples feature a waveguide length of 5 mm.

First, we determined the transmission through a microgap waveguide with a SOF of 5.4 % ($G = 10$ µm, L = 176 µm) as a function of the ammonia concentration. As expected, a clear dip in the transmission centered around the absorption line at λ_0 can be observed, reducing the transmitted power by about 15 % if the chamber is filled entirely with ammonia (Fig. 4.9(a)). For low ammonia concentrations between 10 % and 50 %, we find that the absorbance increases linearly with concentration (Fig. 4.9)(b)) in line with Lambert Beer's law (Eq. 4.11). On the other hand, the absorbance saturates for higher concentrations. This trend is also observed in a reference measurement conducted through the same gas chamber but without coupling light to the waveguide, eliminating any influence from the waveguide itself. As reported elsewhere [238, 239], this saturation can be attributed

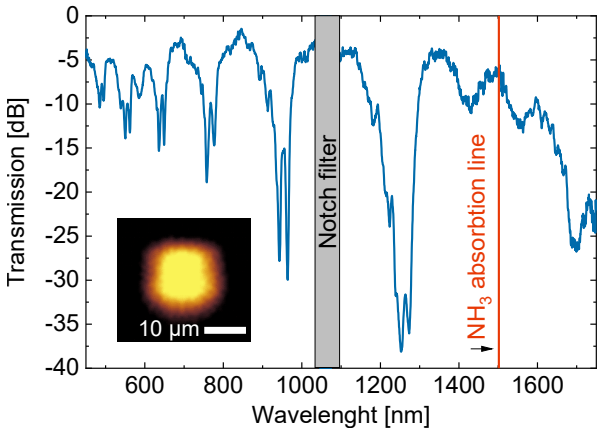

Figure 4.8: Optical properties of the micro-gap waveguide sample used for ammonia gas sensing. Normalized transmission spectrum recorded in air (G = 10 µm, L = 176 µm, D = 20 µm, W = 1.67 µm, total length: 5 mm). Targeted ammonia absorption line at λ_0 = 1501.74 nm is shown in red. Gray region could not be investigated because a notch filter was required to block the pump laser of the white light source. Inset: Recorded mode profile at λ_0.

to collisional broadening of the lineshape with increasing ammonia concentration, which results in an increase in the area of the absorption dip but a reduction in amplitude.

To determine the **limit of detection (LoD)** - the lowest concentration of ammonia that can be detected with our setup - we use the absorbance data for concentrations between 10 % and 50 % to obtain a linear calibration curve (Fig. 4.9(b)) in accordance with Eq. 4.11:

$$A = a \cdot c_r + b, \tag{4.12}$$

where c_r is the volume concentration of ammonia in percent. The values of the coefficients a and b are listed in Table 4.1 and agree with the reference measurement without the waveguide within one standard deviation. The data points from the two measurements are expected to overlap since light travels the same distance through the ammonia gas.

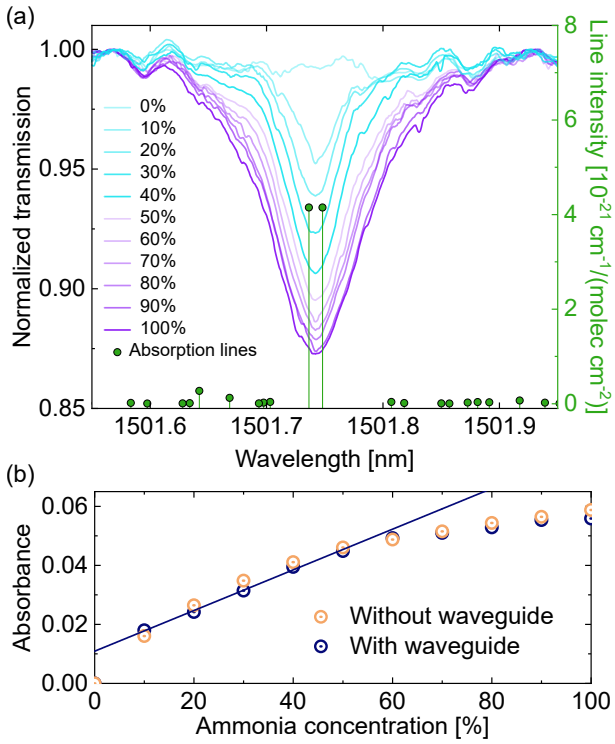

Figure 4.9: Results of gas sensing. (a) Waveguide transmission spectra for varying concentrations of ammonia mixed with nitrogen, recorded around a strong ammonia absorption line (λ_0 = 1501.74 nm, green dots: absorption data according to HITRAN database [236, 237]). Transmission values larger than one are caused by laser power fluctuations. (b) Corresponding absorbance at λ_0 (blue: measurement from (a), orange: reference measurement without waveguide, blue line: calibration curve).

Table 4.1: Coefficients of linear calibration curves for the ammonia absorbance measurements with and without waveguide.

Coefficients	a	σ_a	b	σ_b
With waveguide	6.89×10^{-4}	0.23×10^{-4}	1.09×10^{-2}	0.08×10^{-2}
Without waveguide	7.46×10^{-4}	0.64×10^{-4}	1.05×10^{-2}	0.22×10^{-2}

From the calibration curve, the LoD can be obtained as [234]:

$$\text{LoD} = \frac{3\sigma}{s}, \tag{4.13}$$

where, σ is the standard deviation of the residuals of the fit, and s is the slope of the calibration curve. For the specific configuration used here, we determined a limit of detection of LoD = 3.1 %.

To further assess the diffusion capabilities, the gas **filling time** into the core has been determined through time-resolved measurements. Specifically, the transmission through waveguides with different gap sizes ($G = 2$ µm - 20 µm, Fig. 4.10) was continuously monitored at the center of the absorption line at λ_0. Each measurement started by switching the incoming gas from 100 % nitrogen to 100 % ammonia.

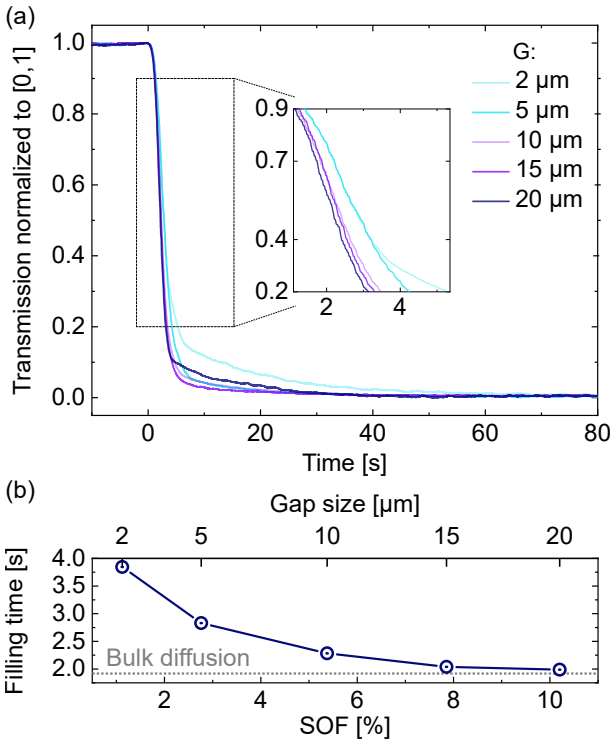

Figure 4.10: Dynamic measurements of ammonia absorption. (a) Time-resolved decay of the transmission for different gap sizes G when filling the chamber with 100 % ammonia (recorded at λ_0). (b) Filling time of the waveguides shown in (a) as a function of SOF (dotted gray line: filling time of the chamber measured without any waveguide).

The initial plateau ($t < 0$, $T = 1$ in Fig. 4.10(b)) appears due to the time the gas needs to flow from the gas mixing unit into the gas chamber. After the waveguide is reached,

the transmission shows a rapid decay, indicating diffusion into the different waveguide segments. Note that no further decrease in transmission was observed at any longer time, indicating no further diffusion. The filling times for different gap sizes, defined by the time difference between 90 % and 20 % of the originally transmitted power (see end of this section for the choice of these values), are shown in Fig. 4.10(b). Here, larger gaps lead to a faster decay of the transmission and reach 2.0 s for a gap size of 20 µm (corresponding to a SOF of 10 %). This value is nearly identical to the filling time of the gas chamber itself, which was determined in a separate measurement to be 1.92 s. Note that for the smallest gap size (G = 2 µm, SOF = 1.1 %) twice that time is required (all measured values are listed in Table 4.2). The shoulder in the transmission data, which is visible after the initial decay, results from mechanical compression and decompression of the waveguide, leading to size modulation of the core section and thus the core mode.

Further experimental details:

All measurements were performed with a fixed gas flow rate of 75 sccm provided by the gas mixer. Each measurement was started two minutes after changing the concentration to ensure that the gas inside the chamber was replaced completely. For the spectroscopic measurement, the laser wavelength was swept through the wavelength region of 1501.55 nm to 1501.95 nm with a step size of 1 pm. The bandwidth of the laser is 100 kHz which is well below the used step size. Each spectrum was normalized to an individual linear baseline, that connects the transmission values at the border of the region of interest (1501.57 nm and 1501.93 nm). A single measurement took around three minutes, which is limited by the scanning speed of the tunable laser.

Since we did not record the ingoing laser power with a separate photodiode, power fluctuations are present in the raw data between measurements of different ammonia concentrations. Therefore each spectrum was normalized to an individual linear baseline, that connects the transmission values at the border of the region of interest (1501.57 - 1501.93 nm). This explains why some values in the transmission spectra exceed one and might be the reason for the deviation of the linear calibration curve from the measurement with 0 % ammonia (Fig. 4.9(b)). Oscillations in the spectra are caused by the coupling objectives.

For the time-resolved measurement, the transmission wavelength remained constant at the center of the absorption line at λ_0. To compare the filling times of the waveguides with different gap sizes, all transmission data was individually normalized to the interval [0,1]. The original data shows a transmission drop of around 15 % as expected from the static measurements for an ammonia concentration of 100 % (dark purple curve in Fig. 4.9(a)). The filling times were then determined as the time difference between reaching 90 % and 20 % of the normalized transmitted power. Those limits were chosen to suppress the effect of fluctuations at the beginning of the measurement and the shoulder after the initial decay.

The specifications of the waveguides used in the time-resolved measurements are listed in Table 4.2. To achieve waveguides with different SOFs, the segment length was held constant at L = 176 µm while the gap size G was changed with the number of segments being adjusted to reach a similar length of the waveguides (second column of Table 4.2). As

Table 4.2: Geometric parameters of the waveguides used in the dynamic experiments.

Gap size [µm]	Waveguide length [µm]	Total # of gaps	Confined space [µm]	Unconfined space[a][µm]	Unconfined space[b][µm]	Filling time [s]
2	4448	24	4400	48	800	3.84
5	4520	24	4400	120	800	2.83
10	4454	23	4224	230	976	2.28
15	4569	23	4224	345	976	2.04
20	4488	22	4048	440	1152	1.98

[a] Due to gaps within the waveguide.
[b] Due to gap between glass walls of chamber and waveguide.

an overview, we decompose the length that the light travels through the chamber into three contributions (columns 4-6 of Table 4.2) : (1) the length over which the light is confined, which is determined by the number and length of the segments, (2) the unconfined space due to the gaps (sum of the length of the gaps), and (3) the space between the glass windows and the first/last waveguide segment.

Even without using microgap waveguides for the gas absorption experiment, the transmission through the gas chamber does not change instantaneously when it is filled with ammonia because some time is required for the gas previously present inside the chamber to be replaced. To determine this filling time, a bulk measurement was performed in the same chamber without coupling light to the waveguide. Since the light travels the same distance through the gas as in the waveguide experiments, this measurement allows the bulk filling time to be determined. The measurement started by changing the incoming gas from 100 % nitrogen to 100% ammonia, revealing a bulk filling time of 1.92 s.

Sensing of Liquids

The results presented in this section are published in Ref. [240]:

J. Kim, J. Bürger, B. Jang, M. Zeisberger, J. Gargiulo, L. S. Menezes, S. A. Maier, and M. A. Schmidt

"*3D-nanoprinted on-chip antiresonant waveguide with hollow core and microgaps for integrated optofluidic spectroscopy*"

Optics Express 31, 2833-2845 (2023), https://doi.org/10.1364/OE.475794

To demonstrate the applicability of microgap waveguides to liquid-based sensing and optofluidics, absorption spectroscopy of an aqueous solution of R6G dye is performed, as well as refractive index sensing of a mixture of water and isopropanol.

For the studies in the previous chapters, where the core of the waveguide was filled with air or gases, the refractive index of the medium was simply assumed to be 1, independent of the actual gas. For liquid environments on the other hand, the refractive index depends on the specific medium, leading to the following **modified equation for the resonance wavelengths** [241]:

$$\boxed{\lambda_{\mathrm{Res}} = \frac{2W}{m}\sqrt{n_W^2 - n_L^2} \quad \forall\, m \in \mathbb{N},} \tag{4.14}$$

where, W is the wall thickness, while n_W and n_L refer to the refractive index of the polymer and liquid, respectively. Light guidance via the antiresonance effect is possible as long as $n_L < n_W \approx 1.5$, which is the case for common liquid analytes (aqueous solutions, saliva, blood). For analytes with higher refractive indices, light would be guided via total internal reflection, as in conventional solid-core guidance.

To verify the **refractive index dependence** of the resonance wavelengths, six refractive index scenarios were established by different mixtures of water and isopropanol (IPA) covering a ranging from n = 1.33 - 1.38 at λ = 527 nm (Fig. 4.11(b)). The mixtures were filled into a waveguide chamber hosting a microgap waveguide of 15 mm length and a wall thickness of W = 1.468 µm. Next, the transmission spectrum through the waveguide was determined using the setup described in Section 3.3. The measurements reveal an increasing blue shift of the transmission dips for higher IPA concentrations (i.e., higher refractive indices) reaching values of up to 80 nm for a difference in refractive index of 0.05 (Fig. 4.11). Overall, the results are in high agreement with the analytical prediction of Eq. 4.14, proving that light is guided in the liquid by the antiresonance effect. The resulting **sensitivity on the refractive index** amounts to $\sim$ 1600 nm/RIU at a wavelength of 750 nm, which is comparable to other refractive index sensors based on cavity resonances [242] but below that of surface plasmon resonance sensors [243]. In addition, we note that no degradation of the optofluidic waveguide was observed over time, neither in water or IPA, nor in harsher environments (e.g., water/ethanol [244]), presumably because the structure is fully polymerized after development. Combined with the high fringe contrast of 40 dB in the spectral region 700 nm $< \lambda <$ 780 nm, microgap waveguides are well suited for applications as refractive index sensor in integrated devices.

Next, we turn to the application of **absorption spectroscopy**, demonstrated here for aqueous solutions of Rhodamine 6G (R6G) dye. The waveguide is customized for this purpose with the wall width set to W = 1.55 µm, ensuring that the absorption peak of the dye at 527 nm falls within a transmission band of the water-filled waveguide (cf. Eq. 4.14). To enable fast diffusion of the dye into the waveguide core, the SOF of the waveguide is chosen to be 10 % (G = 20 µm, L = 176 µm). Generally, absorption spectroscopy benefits from large interaction lengths between liquid and light as this increases the contrast of the transmission dip. To determine, which maximal length can be practically achieved, we determined the **transmission loss** of the chosen microgap waveguide in water. Analogous

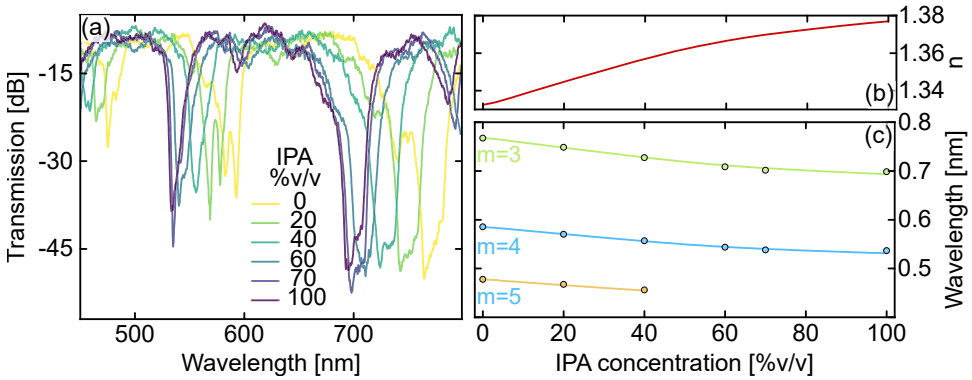

Figure 4.11: Refractive index sensing in microgap waveguides. (a) Spectral distribution of transmission for different mixture ratios of water/IPA (indicated in the legend). (b) Refractive index of water/IPA mixture as a function of IPA concentration at $\lambda = 527$ nm. (c) Spectral locations of measured transmission dips as a function of IPA concentration (points). Solid lines denote the expected dependence on the refractive index according to Eq. 4.14. A waveguide with G = 20 µm, L = 176 µm, D = 20 µm, W = 1.468 µm and total length of 15 mm was used.

to Section 4.1.3, the transmission through 5 samples with different lengths ranging from 5 mm to 15 mm was measured and the loss was determined by Eq. 4.10. Here, we would expect slightly higher losses compared to the air-filled waveguide as a lower index contrast between medium and wall results in lower reflectivity of the wall according to Fresnel's equations [128]. Yet, at the wavelength of maximum absorption of R6G ($\lambda = 527$ nm), the losses amount to 0.4 dB/mm - a value that is nearly identical to the loss of air-filled microgap waveguides shown in Fig. 4.5. Most likely, the lower reflectivity of the walls is compensated for by lower scattering losses, given that the perturbation of the waveguide due to surface roughness scales proportionally to the index contrast and is therefore reduced. Moreover, filling the waveguide with water results in fewer resonances within the same wavelength range (cf. Eq. 4.14). The primary reason behind this is that the reduced index contrast leads to a lower number of modes in the polymer walls.

For the **absorption spectroscopic experiments**, a waveguide length of 15 mm is chosen resulting in manageable transmission losses of 6 dB. Inside the chamber, the waveguide was exposed to aqueous solutions of different concentrations of R6G, and spectrally resolved power transmission measurements were performed (Fig. 4.12(a)). A clear reduction in light transmission in the region of the dye absorption is visible, increasing for higher dye concentrations as expected. A key observation is the excellent overlap of the molar attenuation coefficient between the waveguide measurements and a reference measurement in a cuvette almost across the entire relevant spectral range (Fig. 4.12(b)). Note that the measured values of the molar attenuation coefficient both lie within the range of those reported in literature [245]. This agreement is also an a posteriori evidence for the direct application of the Beer-Lambert law, resulting from the high fraction of power in the waveguide core. Another key feature is the spectrally wide transmission bands covering almost

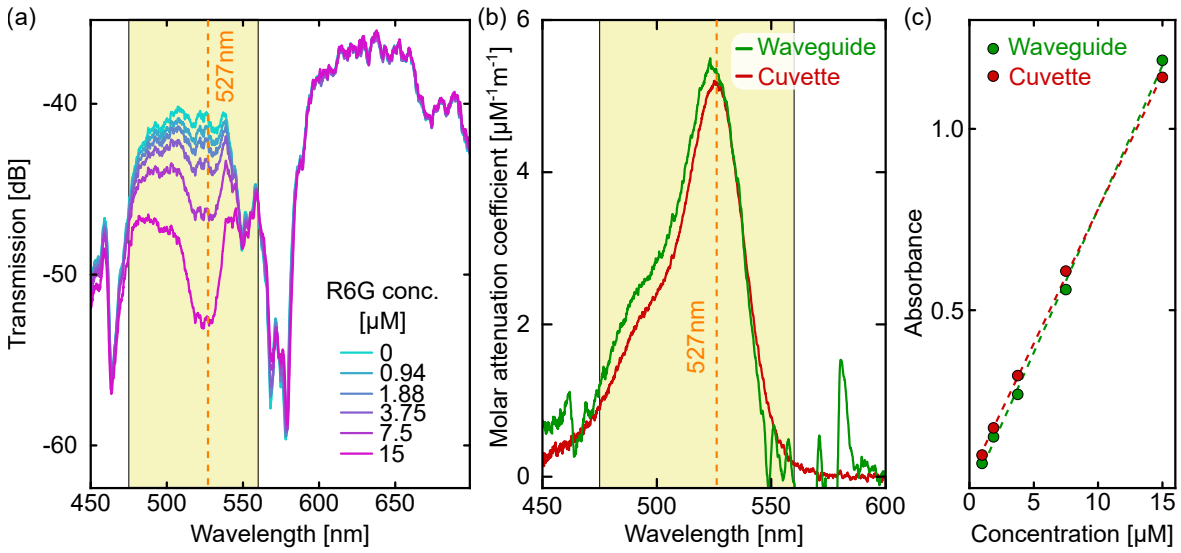

Figure 4.12: Liquid sensing in microgap waveguides via absorption spectroscopy. (a) Spectral distribution of transmission of the waveguide in case the concentration of R6G in water is varied (as indicated in the legend). Note that the raw data is shown, i.e., the transmission is not normalized to the spectrum of the supercontinuum source here. (b) Spectral distributions of the molar attenuation coefficient of R6G measured at a concentration of 15 µM, using the waveguide (green) in comparison to the corresponding reference obtained with a cuvette (red). The orange dashed lines in (a) and (b) refer to the main absorption wavelength of R6G, while the light yellow areas indicate the spectral interval of the main absorption of the R6G molecules. (c) Calibration curve at the main absorption wavelength of the dye (λ = 527 nm). A waveguide with G = 20 µm, L = 176 µm, D = 20 µm, W = 1.55 µm and total length of 15 mm was used.

the entire absorption range of the dye (light yellow areas in Fig. 4.12(a,b)). It should be mentioned that the fine spectral features of the microgap waveguide are imprinted on the absorption spectrum, which, however, do not influence the result, i.e., the determination of the molar attenuation coefficient in any way.

The **limit of detection** (LoD) of the absorption spectroscopic measurements is again determined by Eq. 4.13. To this end, the slope s of the measured linear dependence of the absorbance on the concentration (evaluated at the main absorption wavelength of the dye λ = 527 nm), dashed lines in Fig. 4.12(c)) is used. The fluctuations of the measured absorbance σ were here determined as the standard deviation of a series of 20 blank transmission measurements without analytes (microgap waveguide and reference with water only) following the procedure described in Ref. [234]. The resulting data is summarized in Table 4.3, which allows a direct comparison to the cuvette-based reference measurements. The results show nearly equal LoD values for microgap waveguide (75 nM) and reference measurements (72 nM), emphasizing the quality of the nanoprinted structure and the applicability of the microgap waveguide concept within the context of spectroscopic

applications. Note that the LoD depends not only on the waveguide itself but also on the employed detection system. Thus, it can be expected that improved diagnostics can further reduce the LoD. The minimum measured concentration in the experiments is $c = 0.939$ µM for both waveguide and reference.

Table 4.3: Comparison of spectroscopic properties of microgap waveguide and cuvette.

	Microgap waveguide	Cuvette
Slope of calibration curve s [µM^{-1}]	0.0791	0.0741
Standard deviation of absorbance (blank) σ	0.00198	0.00178
Limit of detection [nM]	75	72
Molar attenuation coefficient ϵ [µM^{-1}m^{-1}]	5.28	5.07

To reveal the **influence of the gaps on the diffusion properties** of the microgap waveguide from the experimental side, additional time-resolved experiments were performed. As described at the end of this section, a defined amount of R6G was introduced into the water-filled chamber and the change of the transmitted power at the main absorption line of R6G was determined over time (Fig. 4.13). The benchmark figure chosen here was the time after which the transmitted power dropped to 10 % of the power before the addition of the dye ($t_{10\%}$). In the case of the microgap waveguide this time was $t_{10\%} = 2.4$ min, which is much shorter than the filling time of a capillary having a comparable inner diameter ($t_{10\%} = 13.5$ min, diameter: 20 µm). Note that even a capillary with a much larger diameter of 224 µm showed a longer diffusion time ($t_{10\%} = 6.9$ min). Thus, the results clearly show improved diffusion properties of the microgap waveguide compared to conventional systems that allow accessing the core only via the waveguide ports.

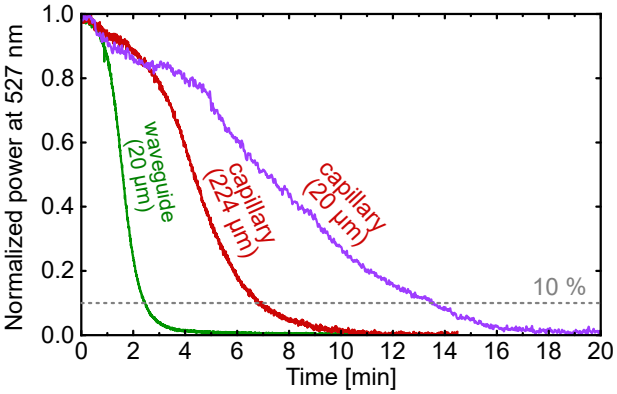

Figure 4.13: Diffusion-related properties of the microgap waveguide in liquids. Transmitted power through the waveguide (green, core size: $D = 20$ µm), and two capillaries (red: core size: $D = 224$ µm, purple $D = 20$ µm) as a function of time after injection of R6G. All curves have been normalized to the transmitted power at $t = 0$. Sample lengths were 5 mm and $\lambda = 527$ nm.

Further experimental details:

To establish different refractive index environments, various mixtures of **isopropanol** (isopropyl alcohol, IPA, 99.9 % Carl Roth GmbH) and distilled water were prepared (IPA/water volume fractions: 0, 20, 40, 60, 70, 100 % v/v). The refractive index of the composite

liquid can be found in one of our previous works [84]. Solutions containing defined concentrations of **R6G** (R4127 from Sigma-Aldrich, Inc.) were made with distilled water by diluting a highly concentrated solution (30 µM) to 15, 7.5, 3.75, 1.875, and 0.938 µM. These solutions were also used in the reference experiments. The absorption spectrum of each solution was controlled before the measurements using a UV-VIS spectrophotometer (V-666 from JASCO, Deutschland GmbH).

The dimensions of the used 3D-printed **chamber** were as follows: width: 2.0 cm, height: 1.0 cm, length: 1.5 cm and a liquid volume of $\sim$ 1 mL was used.

During the **measurements**, the liquids were exposed to broadband white light from the supercontinuum laser source. Preliminary temperature measurements have shown that the infrared part of the spectrum does not lead to any heating of the liquid and has no influence on the results. For normalization of the transmitted power, reference measurements have been performed by moving the beam 500 µm above the waveguides. This procedure results in exactly the same interaction length as in the experiments with waveguides.

To find the **spectral locations of the transmission dips**, the measured spectra were fitted by Gaussian functions within the vicinity of each individual resonance, allowing to extract the wavelength of minimal transmission.

For the **time-resolved experiments** monochromatic light at the main absorption line of R6G (λ = 527 nm) was coupled into a microgap waveguide located in distilled water. In the next step, a defined amount of 15 µM R6G solution was introduced into the chamber and the transmitted power was acquired every 300 ms using a power meter. Thus, the temporal evolution of the diffusion of the dye into the waveguide core was measured by following the decrease in transmission resulting from the filling of the core with the absorbing species. The results were compared to reference measurements using capillaries of different core diameters. Note that compared to the absorption spectroscopic measurements, shorter samples of 5 mm length were considered, as otherwise, the diffusion time of the capillary sample can exceed practically feasible values.

4.1.6 Discussion of Sensing Applications

The agreement of the measured absorbance between the waveguide and the reference measurements verifies that microgap waveguides are well suited for absorption spectroscopy in gases (Fig. 4.9(b)) and liquids (Fig. 4.12(b)).

Of particular interest from the application perspective are the time-resolved measurements of the absorbance, which show a strong reduction in the **analyte exchange time** when microgap waveguides are used instead of waveguides without gaps (i.e., capillaries) of the same length (shown for liquid sensing in Fig. 4.13), and when the structural openness factor (gap size) of microgap waveguides is increased (shown for gas sensing in Fig. 4.10(b)). The measured exchange time is generally composed of three contributions: (i) filling time of the chamber, (ii) bulk diffusion into the free areas between the segments and (iii) restricted diffusion into the cores of the segments themselves. Due to the latter, the samples with small SOF show a slower diffusion in the gas sensing experiments, with a delay of 2 s compared to the chamber itself. This is in contrast to the samples with the largest SOF

(about 10 %), filling up nearly as fast as the gas chamber. Therefore, we attribute the decrease in filling time for larger gap sizes G to the fact that these samples allow more bulk-type diffusion. A further reduction of the filling time can be achieved by using even more gaps or by local modification of the microgap waveguide (e.g., perforation or partial opening of the segments), which can be easily realized by means of 3D nanoprinting. Such a reduction in the exchange time is especially relevant for passive sensing of liquids (i.e., without stirring or pumping), as the measured exchange time is on the order of minutes in these experiments instead of seconds. This difference results from the about 4 orders of magnitude lower diffusion coefficients in liquids compared to gases due to the difference in density and the different magnitude of intermolecular forces [246]. In general, fast exchange times are desirable in any application demanding high throughput (e.g., devices in commercial analytical laboratories), or fast response times (e.g., breath analysis).

Apart from response time, the **limit of detection** is a crucial performance parameter of sensing devices. For example, relevant ammonia concentrations in environmental gas sensing, are on the order of parts per billion (ppb) [247]. In this regard, we would like to point out that in our system, the measured LoD for ammonia of 3.1 % is predominantly limited by the detection system and not by the waveguide itself. As reported for instance in Ref. [248, 249], more advanced detection methods such as wavelength-modulation spectroscopy, lock-in detection, monitoring of the incident laser power or chemical methods (e.g., spectrophotometric ammonia detection) can be employed to measure ammonia concentrations in the ppb range.

A comparison of the achievable detection limits for liquid-based absorption spectroscopy in waveguides is shown in Table 4.4. A first category of comparable systems are evanescent field-based **slab and ridge waveguides** [250, 38, 251, 252], which overall exhibit similar performance parameters compared to the microgap waveguide. Note that a key advantage of the microgap waveguide is that the light-matter interaction occurs within a hollow core. In contrast, in evanescent field-based systems, the interaction takes place near a surface, which can lead to undesirable effects. For example, unwanted absorption features were measured in Ref. [250], resulting from dimer formation near a surface. Such an effect was not observed in the experiments for microgap waveguides, which renders additional surface treatment unnecessary.

Optical fibers with liquid cores are a further class of systems the microgap waveguide should be compared to. For example, Teflon can be used as a cladding material to guide light directly in water due to its very low refractive index [253]. However, the high intrinsic surface roughness necessitates very large core diameters in the millimeter range to compensate for the scattering losses. Another relevant type of fiber with greater structural complexity are antiresonant hollow-core fibers, which are used, for example, to detect pharmaceuticals in water through UV spectroscopy [39]. As the length of hollow fibers used in these experiments is on the order of meters, the fringe contrast resulting from the absorbing species is much larger than in centimeter-scale microgap waveguides. The increased interaction length therefore results in orders of magnitude lower detection limits, both in liquids [253] and gases [254]. However, the associated filling times of such fibers may exceed practically feasible limits. Instead, microgap waveguides can be directly

Table 4.4: Comparison of the performance of microgap waveguides with other waveguide systems used for absorption spectroscopy of liquids (yellow: on-chip slab waveguides, orange: on-chip solid-core waveguides, brown: fibers with hollow core). Molar concentrations c and LoD correspond to R6G unless specified otherwise by footnotes.

Waveguide type	Length [mm]	Cross section [µm ×µm]	Minimal c [nM]	LoD [nM]	Wavelength	Ref.
Microgap waveguide	15	20 × 20	988	75	VIS	This work
Slab waveguide	30	16,700 × 10,000	1,000	n/a	VIS	[250]
Slab waveguide	5	20,000 × 10,000	2,200	10[a]	VIS	[38]
Planar nanoribbon	1.5	0.15 × n/a	6,000	300,000[b]	VIS	[251]
Polymer-core waveguide	110	40 × 50	n/a	n/a	VIS	[252]
Liquid-core fiber	1,300	1,000 ×1,000	0.13	n/a	VIS	[253]
Hollow-core fiber	1,000	30 ×30	100[c]	50[c]	UV-VIS	[39]

[a] for TNT (trinitrotoluene, explosive)
[b] for EITC (eosin-5-isothiocyanate, photosensitizer)
[c] for SMX (sulfamethoxazole, antibiotic)

immersed in the analyte, which can transversely enter the core region.

Learning from these examples, the LoD of microgap waveguides could be further reduced by increasing the waveguide length. An increase from the current length of 5 mm to the maximally investigated length of 5 cm would principally allow measuring ten times lower concentrations.

4.1.7 Conclusion

In summary, we introduced a novel type of integrated on-chip hollow-core waveguide that shows strong light-analyte interaction over centimeter distances with fast analyte exchange times. Microgap waveguides with lengths of up to 5 cm were realized on silicon chips through 3D nanoprinting, avoiding time-consuming multi-step fabrication procedures. As confirmed by two mathematical models and numerical simulations, light guidance in this type of waveguide is based on the antiresonance effect, which is reflected by characteristic dips in the transmission spectrum. Our study included full optical characterization, revealing modal loss, impact of gap size, and spectral tuning potential. Examples of highlights include operation from visible to near-infrared wavelengths with an off-resonance loss of 0.4 - 0.7 dB/mm, extremely broadband transmission windows (> 200 nm), clear resonance dips with exceptionally high fringe contrasts (> 60 dB), low loss per gap (0.003 dB), and controlling resonance wavelengths through precise nanoprinting with successfully implemented step sizes (i.e., increments) in wall thickness of 60 nm. Particularly noteworthy is the exceptionally large structural openness factor of 18 %, exceeding those of perforated

waveguides by more than a thousand.

The application potential was demonstrated in the context of absorption spectroscopy of both gaseous and liquid analytes. Experiments with aqueous solutions of R6G dye revealed a reduction in analyte exchange time from 14 min to 2 min when microgap waveguides are used instead of capillaries of the same length and diameter. For ammonia gas, the measured filling time of the waveguide was nearly indistinguishable from bulk type diffusion in cuvettes. Due to the extremely high fraction of the modal power present in the core (> 99 %), quantitative measurements of the analyte concentration are possible by direct application of Lambert-Beer's law without any modification. The determined detection limits are in the range of comparable systems and could be improved by using more sophisticated detection techniques or increasing the waveguide length.

Due to these unique properties, application of the on-chip antiresonant hollow-core microgap waveguide can be expected in a variety of fields related to integrated spectroscopy, including bioanalytics (e.g., detection of contamination), environmental sciences (e.g., gas analysis) and life sciences (e.g., nanoparticle tracking analysis, Raman spectroscopy). Future work will focus on extending the transmission windows of microgap waveguides to the highly relevant fingerprint region in the mid-infrared (MIR) spectral range, allowing specific detection of biomolecules in common biomedical analytes such as blood or saliva via MIR-spectroscopy.

4.2 Light Cages

The results presented in this chapter are published in Ref. [255]:

J. Bürger, J. Kim, B. Jang, J. Gargiulo, M. A. Schmidt, and S. A. Maier

"*Ultrahigh-aspect-ratio light cages: fabrication limits and tolerances of free-standing 3D nanoprinted waveguides* "

Optical Materials Express 11, 1046-1057 (2021), https://doi.org/10.1364/OME.419398

Moving to a more complex 3D-nanoprinted hollow-core waveguide, this chapter discusses recent results on the light cage. Light cages consist of a hexagonal array of freely suspended polymer strands, allowing lateral access to the core volume without the addition of gaps along the waveguide axis as shown in Fig. 4.14. Light cages were previously introduced in Ref. [66] with subsequent studies reported in Refs. [81, 82, 83, 84].

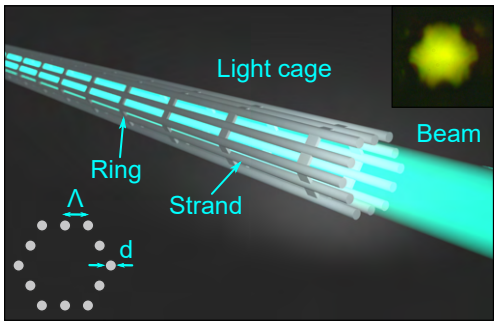

Figure 4.14: Geometry of the light cage. Bottom-left inset: Cross section of the waveguide indicating the pitch distance Λ and diameter of the polymer strands d. Top-right inset: CCD image of the core mode under white light excitation.

Here, we discuss the fabrication characteristics of these waveguides arising from the used two-photon polymerization lithography. The current limits of achievable waveguide length (3 cm), single strand aspect ratio (8200), and modal attenuation are revealed. Furthermore, we unlock the fabrication accuracy of the 3D nanoprinting method from optical measurements. Very high reproducibility for light cages on the same chip is found, while different conditions in fabrication cycles impose chip-to-chip variations. We also highlight the relevance of including reinforcement rings to prevent structural collapse during the development step of the fabrication. The results presented uncover key issues resulting from the 3D nanoprinting fabrication process, which can be transferred to other nanoprinted waveguides like the microgap waveguides reported in Section 4.1.

Additionally, we report a further application of light cages in fluorescence spectroscopy on the example of Rhodamine B dye in Section 4.2.5.

4.2.1 Design and Implementation

The design of the light cage has similarities with revolver-type antiresonant fibers [256] - both consisting of dielectric elements in the micrometer range, which surround a hollow core (cf. Fig. 1.1(b)). In the case of the light cage, these elements are solid polymer strands that are distributed in a hexagonal arrangement. Unlike fibers, these strands are not surrounded by a closed tubular cladding but are freely suspended, with mechanical stability being ensured by support rings connecting adjacent strands laterally at preselected distances. At the bottom of the hexagon, the waveguide structure is supported by a chain of solid polymer blocks elevating the structure from the substrate (Fig. 4.15).

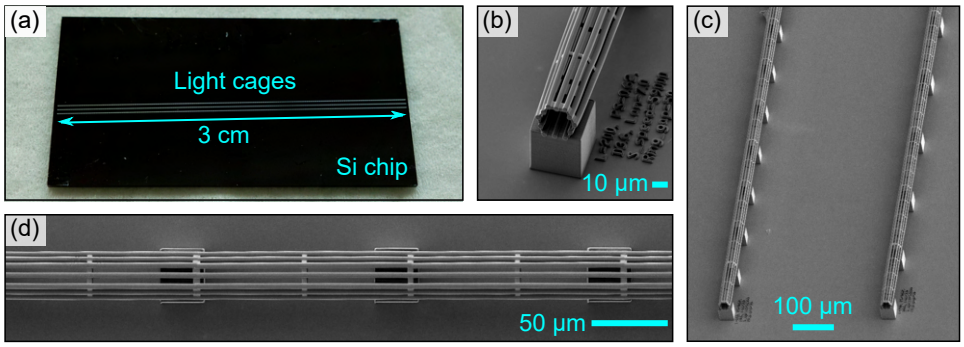

Figure 4.15: Fabricated light cage samples. (a) Photographic image of three light cages nanoprinted onto a silicon chip (length: 3 cm). (b,c,d) SEM images showing an oblique view of the end facet of a light cage (b), an oblique view of two light cages on one chip (c), and a top view (d). Note that the dimensions indicated in the images with oblique view are impacted by the tilt of the sample.

In this work, we specifically studied light cage geometries consisting of twelve strands, all with a common strand diameter ($d \approx 3.6$ µm), pitch (center-to-center distance, $\Lambda = 7$ µm), common dimensions of the support rings (width along waveguide axis: 3 µm, thickness: 1 µm), and support block spacing ($L_{\mathrm{Block}} = 178$ µm). These values result in a large structural openness factor (SOF) of $(\Lambda - d)/\Lambda = 0.49$. We investigated the transmission and mechanical stability of the waveguides as a function of the support ring spacing ($L_{\mathrm{Supp}} = 45$ µm) and total waveguide length L_{LC} with the values in brackets corresponding to the standard geometry shown in Fig. 4.15. Furthermore, the variations in the optical properties of light cages located on the same chip (i.e., within one fabrication run), and between different chips (i.e., fabrication on different days) were analyzed.

The light cages were fabricated on polished silicon substrates by 3D nanoprinting using liquid IP-Dip photoresist with the procedure described in Section 3.2. The used printing parameters are summarized in Table 4.5. These settings were chosen to ensure high accuracy of the printed structures and result in a manufacturing time of 18 minutes per millimeter waveguide length.

Table 4.5: Parameters for fabrication of light cages.

Parameter	Value
Slicing distance	150 nm
Hatching distance	100 nm
Acceleration of galvanometric mirror	1 V/ms^2
Scanning speed	55,000 µm/s
Laser power	31 mW (setting in Describe: 62%)

4.2.2 Light Guidance Mechanism

Similar to microgap waveguides, light guidance in light cages is enabled by the **anti-resonance effect** allowing light to be guided in a low-index medium filling the core (air or liquids) despite the cladding consisting of polymer strands with a higher refractive index. In light cages, this effect is based on the hybridization of the individual strand modes leading to the formation of ring-like cladding supermodes. In certain wavelength ranges, the mode in the central hollow core cannot couple to these supermodes due to a large wavevector mismatch (inhibited coupling) leading to transmission bands with low optical attenuation as shown in Fig. 4.16. In between these transmission bands, light couples from the core to the lossy cladding supermodes resulting in a characteristic distribution

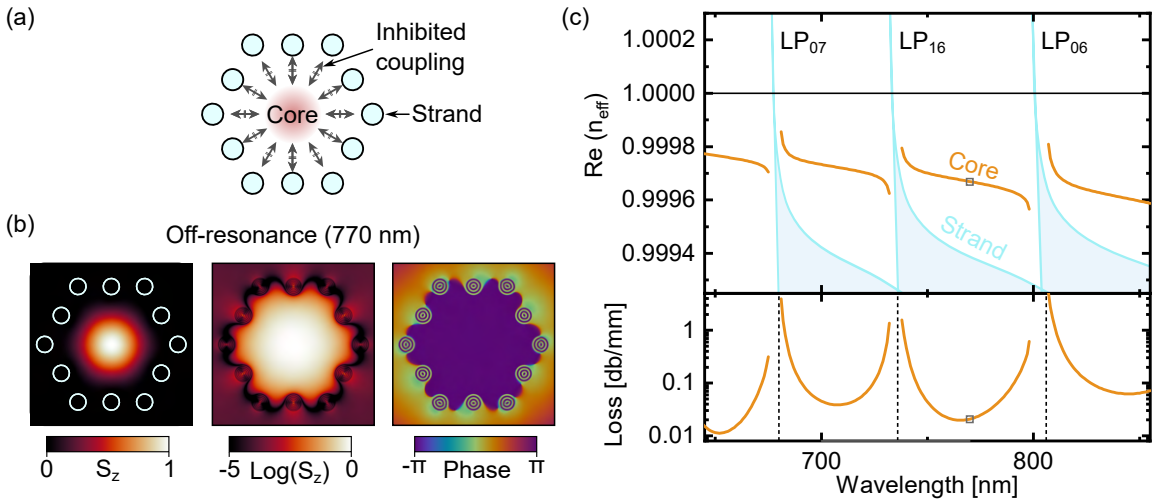

Figure 4.16: Light guidance mechanism in light cages. (a) Light is guided due to an antiresonance between the core mode and the strand supermode. (b) Poynting vector (S_z) and phase of the electric field of the core mode. LP-like modes of the strands are visible in the logarithmic plot. (c) Spectral distribution of the real part of the effective index and the attenuation of the core mode (orange). A qualitative sketch of the dispersion of the coupled strand modes is added in blue based on Ref. [66]. Gray square at 770 nm lies within an off-resonance band, where a phase mismatch between core and strand modes prevents coupling resulting in low propagation loss. Vertical dashed lines correspond to the cut-off wavelengths of the isolated strand modes. The strand diameter is $d = 3.6$ µm.

of spectral resonances. This behavior has been experimentally confirmed in a series of works [66, 82, 81] and an example of such a transmission spectrum is shown in Fig. 4.18.

In order to better understand why light is not able to "escape" in between the strands, it is crucial to understand the **coupling of strand modes** that gives rise to the confining ring-like supermode. While a detailed description is available in Ref. [66], we provide a qualitative explanation to outline the key characteristics. In this 2D model, we assume that the strand mode can be represented by a single wavevector, dissected into the propagation constant β and a radial component k_r such that[2]:

$$nk_0 = \sqrt{\beta^2 + k_r^2}. \tag{4.15}$$

This allows three cases to be distinguished as depicted in Fig. 4.17. If the wavelength is much smaller than the strand diameter, the effective index of the strand mode $n_{\text{eff}} = \beta/k_0$ is larger than the index of air ($n = 1$). Since Maxwell's boundary conditions require that β is identical in air and within the material of the strand, the radial wavevector component in air needs to be purely imaginary in order to fulfill Eq. 4.15. Consequently, the mode is bound to the strand and its field in air decays fast $\sim \exp(-\operatorname{Im}(k_r^{\text{air}})r)$. In this case, the overlap between the strand modes is limited and no coupling occurs.

For longer wavelengths, n_{eff} decreases and approaches 1, meaning that the imaginary part of k_r^{air} is reduced. The field is still evanescent in air but now extends further towards the other strands resulting in stronger coupling.

The wavelength at which $n_{\text{eff}} = 1$ is referred to as **cut-off wavelength $\boldsymbol{\lambda_{\text{co}}}$** because the mode in the strand is no longer guided by total internal reflection as the wavelength increases further because the imaginary component of k_r^{air} vanishes. Instead, the strand mode exists as a leaky mode (cf. Section 2.1.2), with an oscillating field in air carrying away power from the strand (k_r^{air} becomes real). As the field no longer decays exponentially in air, the modal fields of the strands overlap and couple strongly forming the sought-after ring-like supermode (Fig. 4.17(c)).

To analyze the **formation of resonances** in light cages, it is important to note that the effective index of the mode in the hollow core is always close to 1 in air (see simulation results in Fig. 4.16(c)). Therefore, coupling between core and strand modes must occur close to the cut-off of the strand modes to ensure phase matching (cf. Section 2.1.3 on coupled mode theory). To predict the cut-off wavelengths, the strand modes can be approximated as LP modes in the weak guidance approximation (introduced in Section 2.1.2) with the modal fields being described by Bessel functions. This approximation allows to calculate the corresponding cut-off wavelength λ_{co} of an isolated strand mode located in air by [131]:

$$\boxed{\lambda_{\text{co}} = \frac{\pi d\,\text{NA}}{u_{l-1,m}}, \quad \text{NA}(\lambda) = \sqrt{n_p^2(\lambda_{\text{co}}) - 1},} \tag{4.16}$$

where $u_{l-1,m}$ is the m^{th} root of the Bessel function of order $l-1$, NA is the numerical aperture, $n_p(\lambda)$ is the refractive index of the polymer, and l and m refer to the azimuthal

[2] n is the refractive index and k_0 is the vacuum wavevector.

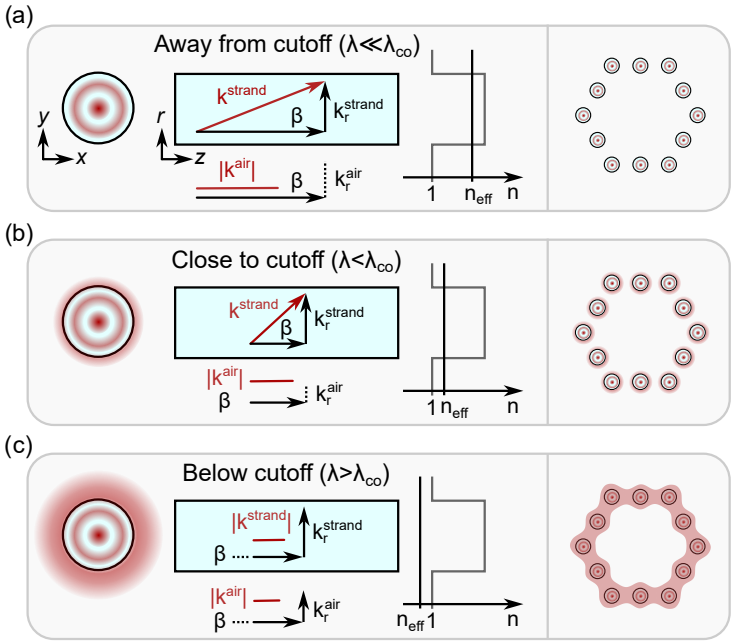

Figure 4.17: Qualitative sketch of the cut-off behavior of the strand modes on the example of the LP_{02} mode. The relevant wavevector components of the strand mode are shown (a) at a wavelength λ far away from the cut-off wavelength λ_{co}, (b) near the cut-off, and (c) below the cut-off. Blue rectangle represents a side view of the strand (propagation direction is along the z axis). The wavevectors in the strand k^{strand} and in air k^{air} are shown in red. Both wavevectors are dissected into the propagation constant β and the radial component k_r (shown in black). Real parts of the wavevectors are represented as arrows, imaginary parts as dashed lines, and absolute values as solid lines. For simplicity the radial component in the strand k_r^{strand} is assumed to be identical in all cases. A qualitative sketch of the intensity distribution is shown for an isolated strand on the left and for the strand supermode on the right. Furthermore, the refractive index profile along the radial direction is shown with n_{eff} being the effective index of the isolated strand mode.

and radial order of the LP mode, respectively. As expected from the simple model - and proven experimentally in Refs. [66, 82] - the spectral positions of the resonances λ_R are described accurately by these cut-off wavelengths: $\lambda_R \approx \lambda_{co}$. In particular, the LP modes of low order in l ($l = 0$, $l = 1$) were found to be most relevant [66].

What is left, is to understand why light can be guided in the core with low loss in the spectral regions between the resonances. In these **off-resonance transmission bands**, the loss is determined by the wavevector mismatch between the core mode and the strand supermode. To this end, the **dispersion of the supermodes** was analyzed in Ref. [66] using a nearest-neighbor coupling model developed by Birks et. al [257] in the context of photonic bandgap fibers. To avoid calculating all possible strand mode combinations, the model analyzes two "edge" supermodes which limit the effective index region of all possible supermodes. Results of this calculation are shown in Ref. [66] and are sketched

qualitatively in Fig. 4.16(c). As the phase mismatch between the core mode and the supermodes grows quickly away from the resonances, the coupling is strongly reduced and only a small fraction of power remains in the strands (Fig. 4.16(b)).

More intuitively, the existence of the supermodes divides the **state space** in such a way that the core mode is only surrounded by ring-like supermodes of the strands. If coupling to the strand modes is inhibited, the only other path for losses would require tunneling to the next available free-space radiation mode, which is an unlikely process. In particular, the off-resonance loss can be further reduced by adding more strands, making the tunneling barrier wider. This approach has for example been used to create "dual-ring" light cages with lower propagation loss in Ref. [81]. To note here is that the exact location of the strands is irrelevant for the spectral position of the resonances, as these are solely determined by the strand diameter and the refractive index (cf. Eq. 4.16), making the light cage geometry relatively robust against fabrication inaccuracies. In the context of fibers, it was shown that even arbitrary arrangements of strands surrounding a hollow core can enable low-loss light guidance [258].

Furthermore, we show in Section 6.5, that the dispersion of the fundamental mode of light cages is very similar to that of a **tube waveguide** (i.e., the cross section is a solid ring) made out of the same polymer material with a thickness that is slightly smaller than the strand diameter. This result further corroborates the fact that the ring-like supermode of the strand modes acts like a tube for confining light inside the light cage.

4.2.3 Statistical Analysis of Fabrication Accuracy

The optical properties of the samples were determined by measuring the transmission T across the visible spectral range using the setup and procedure described in Section 3.3. The off-resonance modal attenuation was calculated by fitting the transmission values with the expected exponential decay (Eq. 4.10).

In order to allow for statistically analyzing geometry variations of the structure induced by the fabrication, we determine the spectral positions of the transmission dips (i.e., resonance wavelengths λ_R) from the experimental data of light cages of identical length and fabrication parameters. Then we identify the order of the LP mode of the strand that is causing the resonance by using the list of cut-off wavelengths of various LP modes in Table 4.9. Next, the corresponding mean wavelength $\overline{\lambda_R} = 1/N \sum \lambda_{R,i}$ and standard deviation $\sigma_{\lambda_R} = (1/(N-1) \sum (\lambda_{R,i} - \overline{\lambda_R})^2)^{1/2}$ is determined, where i is the sample number, N is the number of light cages of identical length and $\lambda_{R,i}$ is the corresponding resonance wavelength. The associated values of the mean strand diameter $\overline{d}$ and standard deviation σ_d can then be straightforwardly calculated via Eq. 4.16:

$$\overline{d} = \frac{u_{l-1,m}}{\pi \, \mathrm{NA}(\overline{\lambda_R})} \, \overline{\lambda_R}, \tag{4.17}$$

$$\sigma_d = \left| \frac{\partial d}{\partial \lambda_R} \right| \sigma_{\lambda_R} \approx \frac{u_{l-1,m}}{\pi \, \mathrm{NA}(\overline{\lambda_R})} \, \sigma_{\lambda_R}. \tag{4.18}$$

Note that in Eq. 4.18 we assume that the dispersion of the NA is negligible allowing to use the respective value at $\overline{\lambda_R}$. Furthermore, we neglect refractive index variations resulting from two-photon polymerization of the resist because these only occur between different fabrication runs and are extremely small with absolute deviations of below 0.005 [194].

4.2.4 Optical Characterization and Discussion

The maximum sample length that has been achieved here was $L_{\mathrm{LC}} = 3$ cm, representing the current state-of-the-art in light cage length and constituting a factor of three improvement to previous experiments ($L_{\mathrm{LC}} = 10.5$ mm reported in Ref. [66]). This leads to an **aspect ratio** (length-to-diameter) of a single strand of approximately AR = 8200 which to our knowledge represents the largest AR of a 3D-nanoprinted structure that is partially suspended. Examples of freely suspended nanoprinted structures from other groups are presented in Table 4.6 showing aspect ratios < 500, which is more than ten times smaller than the light cage structure shown here.

Table 4.6: Comparison of different 3D-nanoprinted structures that include suspended-type elements. Examples of non-free-standing waveguides are also shown (gray).

Structure type	Free-standing	Smallest width [nm]	Aspect ratio	Reference
Light cage	yes	3,600	8,200	This work
Woodpile	partially	350	357	[259]
Microtube	yes (vertical)	600	100	[260]
Single nanopillar	yes (vertical)	9,000	50	[261]
Taper on fiber	yes	15,100	16	[262]
Microneedles	yes (vertical)	630	10	[263]
Freeform lens	yes (vertical)	105,000	1.1	[264]
Step-index waveguide	no (fixed to substrate)	600	33,000	[265]
Bragg grating waveguide	no	1,500	66.7	[266]

The spectral characterization of the 3 cm long light cage in Fig. 4.18 shows an alternating sequence of regions of low and high loss, with the resonance wavelengths being correctly predicted by the cut-off of the LP_{0m} and LP_{1m} modes via Eq. 4.16. These results confirm that light is guided by an antiresonance between the core mode and the strand supermodes. On closer inspection, the resonances feature a double-dip substructure (e.g., around $\lambda = 800$ nm), which might arise from LP mode splitting as discussed later in the section.

Similar to the study on microgap waveguides (cf. Section 4.1.3), we determine the **off-resonance modal attenuation** of the light cage by measuring the transmission through samples of different lengths (5 mm - 20 mm, Fig. 4.19(a-d)). The resulting transmission

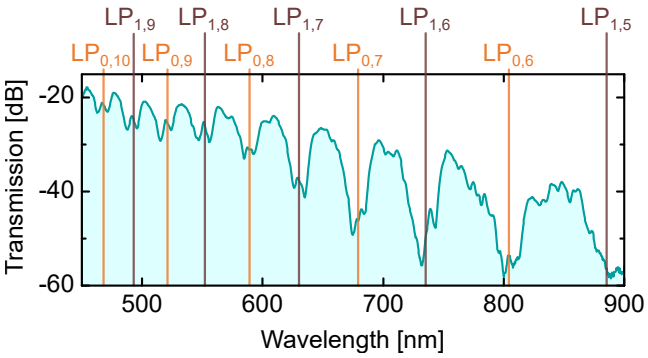

Figure 4.18: Spectral distribution of the measured transmission through a 3 cm long light cage. Vertical lines denote the cut-off wavelengths of the LP modes indicated on the top. Cut-off wavelengths were calculated via Eq. 4.16 using a strand diameter of $d = 3.592$ µm.

loss is close to 0.65 dB/mm at around $\lambda = 520$ nm increasing to about 1 dB/mm at near-infrared wavelengths. These values lie within the range of commonly used on-chip hollow core waveguides [54, 267] and high contrast photonic band gap fibers [268]. Furthermore, the measured losses agree with that of significantly shorter light cages previously reported [66], indicating that the fabrication accuracy is maintained over the increased distance. Therefore, even longer waveguide lengths can principally be realized. Here, it is important to note that long writing times lead to a higher probability of contamination and structural deformation. If the writing area is larger than the area where the immersion lens and chip are in contact with the resin, it is difficult to keep the entire writing area well

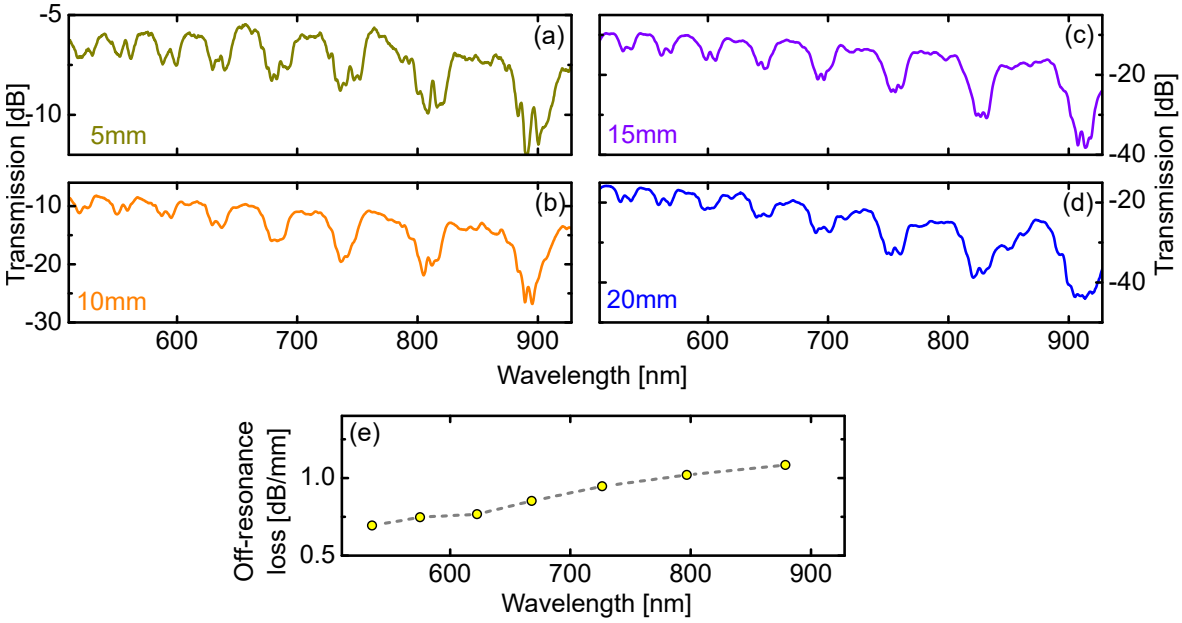

Figure 4.19: Measured optical properties of light cages. (a-d) Spectral distribution of transmission through light cages samples with various lengths L_{LC} of 5 mm (a), 10 mm (b), 15 mm (c), and 20 mm (d). The propagation loss was calculated from exponential fitting of the transmitted power versus sample length at the spectral location of high transmission and is shown in (e). The gray dashed line in (e) is a guide to the eye.

covered with resin throughout the printing process. Future strategies to increase the length of the implemented light cages therefore target reducing the writing time by using other photoresins with a coarser voxel size. The magnitude of the losses leads to an attenuation of several tens of dB over the 3 cm, which indicates that longer light cages have practical limitations for the used core radius and on the basis of the current implementation scheme. Similar to microgap waveguides and other tube-like antiresonant waveguides, the losses can principally be reduced by increasing the core extent as modal attenuation scales approximately proportional to the inverse of the fourth power of the core diameter [212].

Generally, the measured loss values are about one to two orders of magnitude higher than predicted by simulations (Fig. 4.16(c)). In this context, it is important to reveal the **impact of the reinforcement rings** on modal attenuation from the experimental perspective. While the rings are required to hold the strands in their hexagonal arrangement, they introduce a non-uniformity along the waveguide axis that might lead to scattering losses. At the same time, the rings reduce the lateral openness of the cage structure and therefore their number should be kept to a minimum. To address this issue, a series of light cages of identical length ($L_{\mathrm{LC}} = 10$ mm) but different longitudinal spacing between the rings (10 µm, 30 µm, 50 µm, 70 µm) have been implemented on one chip and the spectral distribution of the transmission of the fundamental core mode has been determined. These measurements show neither a significant spectral shift of the resonances nor a substantial change of the transmission value (change of transmission values in the transmission bands throughout this measurement series is < 2.5 dB). Overall, no consistent trend is observable from these measurements, indicating that the impact of the reinforcement rings on the modes is minimal. This experimental observation is supported by simulations, which indicate that the fraction of modal power present inside the polymer is negligible [84]. Overall, these findings suggest that the main origin of the observed modal attenuation results from surface roughness of the strands.

The spectral bandwidth of the measured transmission bands is within the order of 20 nm - 40 nm in the visible spectrum. Larger spectral bandwidth can principally be achieved by implementing strands with smaller diameters, potentially allowing broadband applications for dispersion control in nonlinear optical devices or ultrafast spectroscopy.

To specify the **structural deviations induced by 3D nanoprinting** for identical light cages that are located on the same chip (**intra-chip**), we use the above-mentioned data analysis procedure for an ensemble of five identical light cages of length $L_{\mathrm{LC}} = 15$ mm ($\mathrm{N} = 5$, example of transmission spectrum is shown in Fig. 4.19(c)). Using an automated numerical procedure (Mathematica: FindPeaks), we determine the spectral positions of the transmission dips within the spectral interval 575 nm $< \lambda <$ 840 nm including five different orders of modes. Note that the fundamental mode (LP_{01} mode) of the strands has no cut-off and therefore cannot impose a resonance in the transmission spectrum of the light cage. Several dips include double-dip features, which presumably result from a lift of LP modal degeneration which is associated either with polarization mode splitting due to coupling to hybrid HE and EH modes (resulting from the large refractive index contrast between polymer and air) or from a slight ellipticity of the strands (leading to a lifting of the otherwise degenerate modes in the purely cylindrical case). In the anal-

ysis, we assign identical labels for the two sub-resonances within one transmission dip according to the LP mode nomenclature. The resulting values (Table 4.7) show that the implementation via 3D nanoprinting yields highly reproducible structures within one chip since the standard deviation of the determined resonance wavelengths is extremely small ($\sigma_\lambda < 1$ nm), which is supported by the value obtained by averaging over all standard deviations ($\overline{\sigma_\lambda} = 0.3$ nm). Note that due to the small absolute value of the deviations, a large sample length of $L_{\mathrm{LC}} = 15$ mm was chosen here in order to increase the fringe contrast of the dips and therefore allows for a more precise localization of the resonance wavelengths. A preliminary study has shown that samples with different lengths show deviations of a similar order of magnitude. Moreover, the calculated standard deviations of the strand diameter (determined by Eq. 4.18) yield values within the nanometer range including the corresponding mean value ($\overline{\sigma_d} = 2$ nm) additionally confirming the appropriateness of using 3D nanoprinting for implementing highly reproducible light cage structures. Note that the mean of the calculated mean diameter ($\overline{\overline{d}} = 3665$ nm) is close to the diameter used in the corresponding dispersion simulations ($d = 3.6$ µm in Fig. 4.16(c)). The small standard deviations overall show extremely small structural variations for light cages located on the same chip, indicating excellent reproducibility, which is close to values known from fiber optics. Note that for microstructured optical fibers, fiber drawing within a single drawing process is highly reproducible [269], while fiber structures can vary significantly between different runs.

Table 4.7: Result of the statistical analysis for uncovering the intra-chip reproducibility of the light cage ($L_{\mathrm{LC}} = 15$ mm).

Resonance order	λ_R [nm]	σ_λ [nm]	$\overline{d}$ [nm]	σ_d [nm]
LP08	596.3	0.3	3641	2
LP08	603.4	0.2	3687	1
LP17	638.8	0.4	3647	2
LP17	645.5	0.3	3687	2
LP07	688.1	0.4	3643	2
LP07	695.0	0.6	3681	3
LP16	746.3	0.1	3650	1
LP16	754.2	0.1	3689	1
LP06	818.8	0.4	3659	2

The chip-to-chip, i.e., **inter-chip variations** of the structural features of the light cages have been analyzed in a similar way to the intra-chip analysis presented in the previous paragraph. Here, we investigated the spectral positions of five resonances of three light cages located on different chips (details can be found in Table 4.8, $L_{\mathrm{LC}} = 5$ mm). An approximately ten times larger variation of the spectral positions of the resonance wavelengths σ_λ was observed (mean standard deviation $\overline{\sigma}_\lambda = 2.9$ nm), which is reflected in correspondingly higher variations of the strand diameter (mean standard deviation $\overline{\sigma_d} = 15$ nm).

This value is reasonable given the current experimental circumstances: The dimensions of 3D-nanoprinted polymer structures are subject to strong shrinkage during the development process with rates of up to 26 % per dimension [270]. Therefore, the actual dimensions of a 3D-nanoprinted structure strongly react to fluctuations in the development process (e.g., exact timing, temperature, final concentration of photoresist in developer, humidity), potentially imposing structural changes from sample to sample. Therefore the measured larger chip-to-chip variations appear realistic on the basis of the experimental circumstances, which will be improved in future studies. Note that the inter-chip measurement uses a different version of light cages which have a larger mean diameter ($\overline{\overline{d}} = 3841$ nm) and were performed with a broadband optical spectrum analyzer (cf. Section 3.3). The latter has the consequence that only a single dip per resonance could be resolved, leading to a single value of λ_R per strand mode (Table 4.8).

Table 4.8: Result of the statistical analysis for uncovering the inter-chip reproducibility of the light cage ($L_{\mathrm{LC}} = 5$ mm).

Mode	λ_R [nm]	σ_λ [nm]	$\overline{d}$ [nm]	σ_d [nm]
LP08	626.2	2.1	3832	13
LP17	670.8	2.5	3837	14
LP07	722.8	3.5	3833	19
LP16	787.2	2.9	3856	14
LP06	859.5	3.5	3845	15

An important issue needing consideration is the structural collapse of the light cage during the drying stage of the development process. When the used solvent evaporates a meniscus is formed between adjacent strands which results in a deformation of the high aspect ratio strands if the **capillary forces** exceed the elastic restoring force of the polymer. To understand the collapsing effect from the experimental perspective, we fabricated another series of light cages with the same pitch ($\Lambda = 7$ µm) and length ($L_{\mathrm{LC}} = 2$ mm) but with different spacing between reinforcement rings. Increasing the spacing from 30 µm to 70 µm does not lead to a visible difference between the light cages (Fig. 4.20(b-d)), while for a spacing of 100 µm a deformation of the light cage cross section in the middle between two rings is observed (Fig. 4.20(e)). We attribute this phenomenon to radially inward capillary forces (red arrows in Fig. 4.20(a)) that the strands experience during the drying process.

The results presented clearly indicate the necessity of including reinforcement rings, which distribute the stress from the capillary forces more evenly during the transition from the liquid to the air environment. This consideration applies in particular to situations where the liquid has a high surface tension, such as aqueous solutions. A further improvement of the mechanical stability or conversely, a larger spacing between support rings might be obtained by using photoresists with a higher Youngs modulus such as IP-L780 [271] or by improving the polymerization through an additional curing procedure [270].

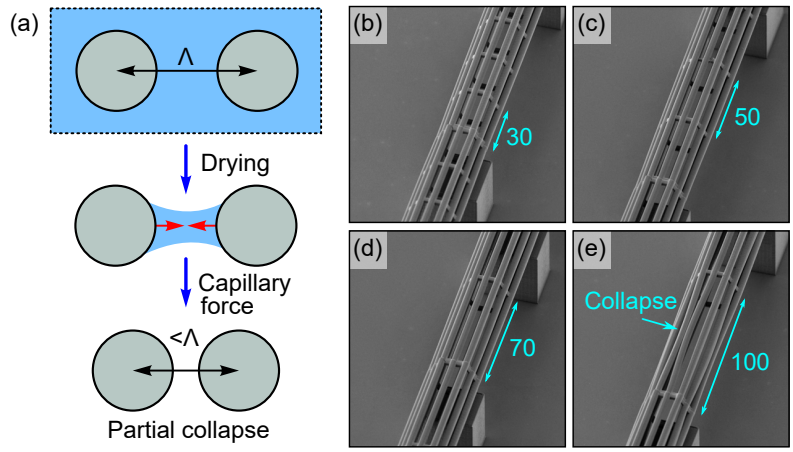

Figure 4.20: Study of the mechanical stability of the light cage, showing the necessity to include reinforcement rings to support the cage. (a) Sketch showing the capillary force induced collapsing process emerging during the drying process. SEM images on the right side show light cages of same pitch and length ($\Lambda = 7$ µm, $L_{\mathrm{LC}} = 2$ mm) but with different distance between the reinforcement rings ((b) 30 µm, (c) 50 µm, (d) 70 µm, (e) 100 µm).

Further details of the study:

The cut-off wavelengths of the LP modes that are relevant for this section have been calculated using the material dispersion of the polymer from Eq. 3.9. The resulting wavelengths for the LP modes with $l = 0$ and $l = 1$ are shown in Table 4.9.

Table 4.9: Calculated cut-off wavelengths of the LP modes for a strand of diameter $d = 3.64$ µm located in air.

l=0	λ_{co} [µm]	l=1	λ_{co} [µm]
LP02	3.460	LP11	5.511
LP03	1.893	LP12	2.404
LP04	1.309	LP13	1.536
LP05	1.003	LP14	1.131
LP06	0.815	LP15	0.897
LP07	0.688	LP16	0.744
LP08	0.596	LP17	0.638

4.2.5 Sensing Applications

Light cages can generally be used for the same application scenarios as microgap waveguides as both feature a large structural openness factor allowing liquids or gases to freely enter the core volume to interact with the guided light. In this context, light cages have been successfully employed in waveguide-integrated absorption spectroscopy of gases [83]

and liquids [84], and integrated quantum optical experiments (electromagnetically induced transparency in cesium vapor) [57]. Here, we summarize the results of a further application, namely **fluorescence spectroscopy** of an aqueous Rhodamine B dye solution. Additionally, light cages were applied for **nanoparticle tracking analysis** during the course of this thesis, the results of which are reported in Ref. [244].

Fluorescence Spectroscopy

The results presented in this chapter are published in Ref. [272]:
J. Kim, B. Jang, T. Wieduwilt, S. C. Warren-Smith, J. Bürger, S. A. Maier, and M. A. Schmidt
"*On-chip fluorescence detection using photonic bandgap guiding optofluidic hollow-core light cage*"

The on-chip detection of fluorescent light is essential for many bioanalytical and life-science related applications, such as medical diagnostics [273], quantitative polymerase chain reaction (qPCR) tests (e.g., for detection of SARS-CoV-2 RNA) [274], fluorescence enzyme-linked immunosorbent assays (ELISA) [275], or fluorescence resonance energy transfer (FRET) assays [276]. In this section, we show that fluorescence light from R6G dye generated in the core of a water-filled light cage can be efficiently captured and guided to the waveguide ports. Two aspects of light cages make them particularly interesting for this application: (1) light is guided almost exclusively in the analyte, which minimizes background signals from fluorescence or Raman scattering of the waveguide material, and (2) the analyte can be quickly exchanged through the open space between the strands within an on-chip environment.

The detection of fluorescence is in general more difficult than measuring an absorbing material in a waveguide. As described in Section 4.1.1 for microgap waveguides, antiresonant waveguides can only confine light rays incident on the cladding under grazing angles. While this condition is well satisfied for the waveguide mode propagating nearly parallel to the waveguide axis, fluorescence light emanates from a molecule in all spatial directions. Therefore, we decided to add a second ring of confining strands to the light cage, increasing the total strand number from 12 to 18 (Fig. 4.21). As explained in Section 4.2.2, a larger number of strands decreases the propagation loss and allows for a more efficient capturing of the fluorescence light. This **dual ring light cage** geometry was previously introduced in Ref. [81] and a sketch of the geometry is shown in Fig. 4.21.

For the **experimental demonstration**, we choose Rhodamine B dye (RhoB, molar mass: 479.01 g/mol) dissolved in water and use a light cage length of $L_{\mathrm{LC}} = 4.5$ mm. Two concentration ranges corresponding to a low ($0.075\ \mu\mathrm{M} < c < 2.4\ \mu\mathrm{M}$) and a high ($3.75\ \mu\mathrm{M} < c < 30\ \mu\mathrm{M}$) dye concentration were prepared. The solutions were characterized using a separate spectrometer (F550B, Perkin Elmer), which showed that the maximum excitation

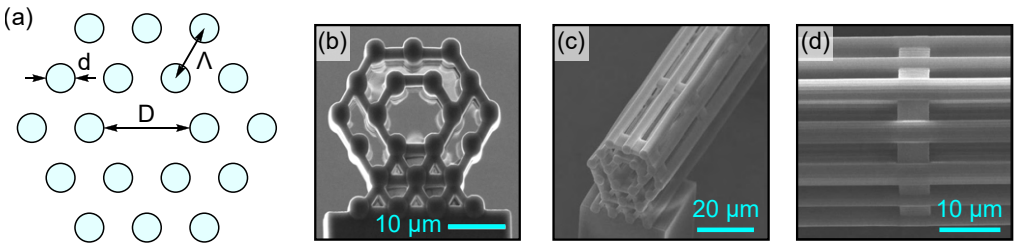

Figure 4.21: Dual ring light cages used in the fluorescence spectroscopy experiment. (a) Schematic of the geometry indicating the pitch Λ, strand diameter d, and core size D. SEM images on the right depict fabricated structures, including (b) a view of the end face, (c) an oblique view, and (d) a top view. Note that the dimension indicated in (c) is affected by the tilt of the sample during imaging.

and emission (for $c = 1$ µM) occurs at λ= 552.6 nm and $\lambda = 576.5$ nm, respectively. Here, another advantage of the fabrication via 3D nanoprinting comes into play: as we can precisely adjust the diameter of the strands, it is possible to tune the spectral locations of the transmission bands such that both excitation and emission wavelengths lie within high transmission domains (cf. Eq. 4.16). Therefore, the light cage allows for both guiding the excitation light to the fluorescent molecules and efficiently capturing the uniformly emitted fluorescence light. For the measurements, the fundamental core mode was excited with a narrowband diode laser (W532-50FS, Pavilion Integration Corp., $\lambda = 532$ nm, maximal power 50 mW) and the output light was detected using a fast spectrometer (USB2000, Ocean insight, 450 nm $< \lambda <$ 800 nm, $\Delta\lambda = 0.32$ nm), while a notch filter (blocking range 523 nm $< \lambda <$ 544 nm, extinction ratio $<$ 20 dB, OD = 6 @ 533 nm) was inserted into the beam path to prevent the residual excitation light reaching the detection system. Two fixed integration times were used at the spectrometer, one optimized for the low concentration range and another for the high concentration range, to be able to compare the measured fluorescence power within each range. As described in Section 4.1.5, the light cage chips are placed in a chamber which is then filled with the dye solution.

Imaging the **intensity distribution of the fluorescence light** at the output facet of the waveguide reveals the clear hexagonal symmetry of the fundamental mode of the light cage, proving that the fluorescence light is captured by the waveguide (Fig. 4.22(c)). Only a negligible fraction of the guided power is present in the strands completely vanishing in a reference measurement without dye at the same integration time. Any fluorescence background from the material of the strands can therefore be neglected for the investigated concentrations.

The **fluorescence power** guided to the output increases with dye concentration, with the emission peaking at roughly $\lambda = 579$ nm as expected (Fig. 4.22(a,b)). Note that for the high concentrations, a spectral red-shift of the fluorescence maximum is observed, which is in accordance with bulk measurements and can be explained by dimer formation [277, 278]. As the raw data captured by the spectrometer is shown, the spectral fingerprint of the light cage is visible in the emission spectra, leading to a reduction of the recorded power around

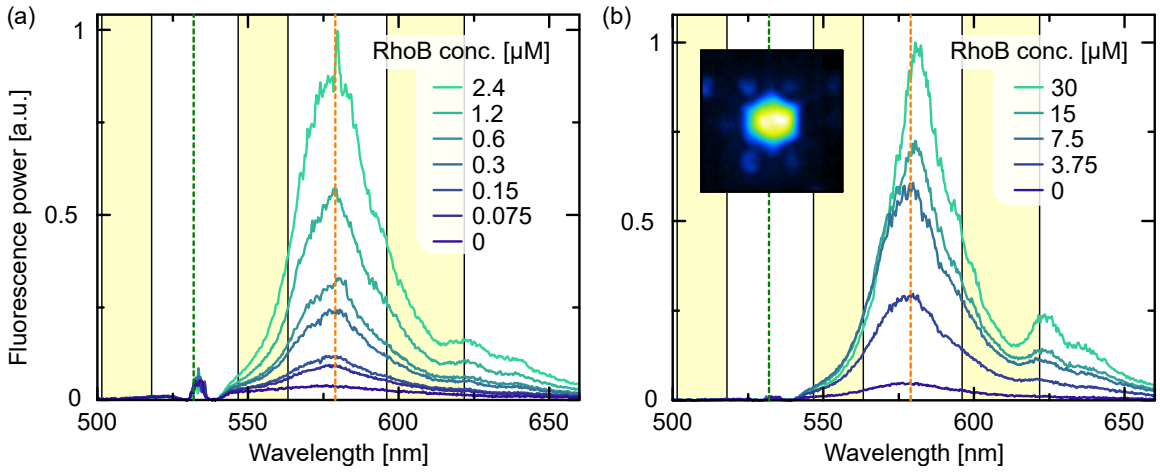

Figure 4.22: Measured fluorescence collection properties of the dual ring light cage demonstrated on the example of RhoB dissolved in water. Spectral distribution of the collected fluorescence power is shown for (a) the low concentration regime ($0 < c < 2.4$ µM), and (b) the high concentration regime ($0 < c < 30$ µM). The yellow areas denote the location of resonances of the light cage. Each set of curves was normalized to the range [0,1]. Inset in (b): Measured output mode in case the excitation light at 532 nm is filtered out, thus solely corresponding to the collected fluorescence light ($c = 30$ µM).

the resonances of the light cage (yellow areas in Fig. 4.22). Furthermore, we note that the small peaks for 530 nm $< \lambda <$ 535 nm result from the residual excitation light passing through the notch filter and not from the residual fluoresce of the dye, which is evident from the fact that the amplitude of this peak does not change with dye concentration.

For a **quantitative assessment** of the light cage properties, we analyzed the fluorescence power (normalized to the power at $c = 2.4$ µM) as a function of concentration at the main fluorescence wavelength ($\lambda = 579$ nm) for both the light cage and a cuvette-based reference measurement (Fig. 4.23). As for the absorption spectroscopic experiments with microgap waveguides, we determine the limit of detection (LoD) from these calibration curves using Eq. 4.13.

The resulting LoD in the case of the light cage is LoD = 8 nM, matching the value from the bulk cuvette measurements (LoD = 10 nM). Similar to the experiments on microgap waveguides, achieving lower detection limits requires the use of more sophisticated detection techniques, or the use of fibers of much longer lengths but without the possibility for passive analyte exchange. For example, a LoD of 0.1 nM has been demonstrated in a 10 cm long hollow-core photonic crystal fiber [25].

In analogy to the experiments on microgap waveguides, we perform **time-resolved experiments** to monitor the diffusion of the dye into the core after adding a certain amount of dye to the water-filled chamber. To this end, we track the fluorescence power at the main fluorescence wavelength ($\lambda = 527$ nm) and compare the results to a fiber-type capillary of similar core diameter and length. As a benchmark, we use the elapsed time $t_{99\%}$

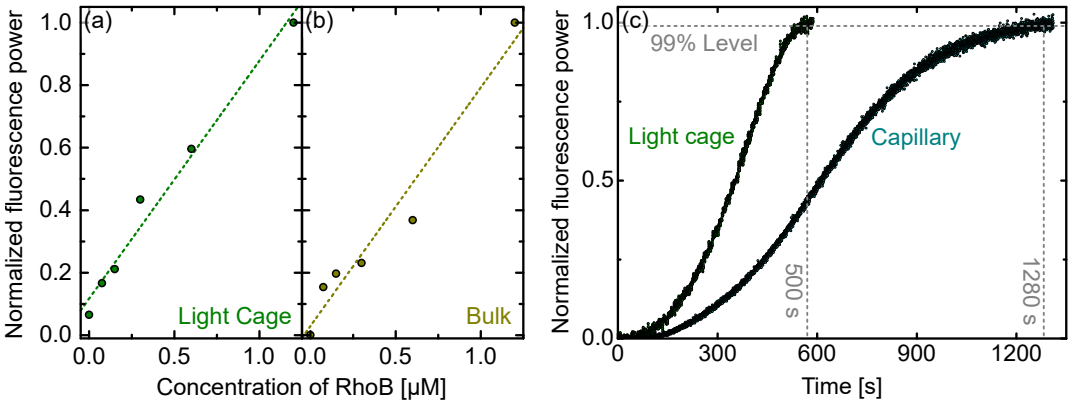

Figure 4.23: Quantitative analysis of the fluorescence properties. Measured fluorescence power/concentration relation for (a) dual-ring light cage and (b) cuvette-based reference measurement. The dots correspond to the measured data, while the dashed lines are linear fits. (c) Time-resolved increase of the fluorescence power after injection of the dye into the chamber. Dual-ring light cage (green) is compared to a fiber-type capillary with comparable core diameter (cyan, core diameter $D = 15$ µm). Identical chambers and lengths ($L = 5$ mm) are used. The horizontal gray dashed line refers to 99 % of the saturated power. Data in (a,b,c) was evaluated at the main fluorescence line ($\lambda = 579$ nm, orange dashed line in Fig. 4.22).

until 99 % of the maximal fluorescence power is reached on saturation of the waveguide with the dye solution. The results shown in Fig. 4.23(c) reveal that the use of light cages reduces the filling time 2.6-fold from $t_{99\%} = 1280$ s for the capillary to $t_{99\%} = 500$ s for the light cage. This difference would grow even larger if longer waveguides are considered as the filling time of light cages is in principle independent of sample length but would increase for capillaries, which can only be accessed from the end faces.

4.2.6 Conclusion

As previously reported, the light cage represents a novel type of hollow core on-chip optical waveguide with unique properties such as diffraction-less light guidance over centimeter distances, side-wide access to the core, and a high fraction of optical power inside the core region [66]. As such it is well suited for future integrated sensing applications [279] that demand fast response times and minimal background signal originating from the material of the waveguide. In this chapter, we demonstrated the highest so far achieved waveguide length for light cages of 3 cm, corresponding to a single-strand aspect ratio of 8200. The measured modal attenuation lies in the range of 0.5 - 1 dB/mm in the visible, suggesting that realizing even longer waveguide lengths requires strategies to reduce the propagation loss.

The investigation of structural intra-chip variations shows extremely small variations ($\overline{\sigma_d} = 2$ nm) yielding a very high level of reproducibility that is essential from the application perspective. About ten times larger chip-to-chip variations have been observed

($\overline{\sigma_d} = 15$ nm), which mainly result from fluctuations in the development processes, which can be improved by exerting more rigorous control over the sample treatment conditions. Finally, the importance of including reinforcement rings to mechanically support the suspended structures particularly during exposure of light cages to a liquid environment has been uncovered. Particularly the conducted study on reproducibility is not only relevant for light cages but can also be translated to other 3D-nanoprinted waveguides, especially to nanoprinted geometries with suspended structures. As an overview, the fabrication inaccuracies encountered in the study on light cages and microgap waveguides are summarized in Table 4.10.

Table 4.10: Overview of the different types of fabrication inaccuracies and the impact on the fabricated dimensions.

Type of inaccuracy	Effect	Magnitude
Surface roughness (constant average dimensions)	Broadening of resonances, increased loss	Not studied, 30 - 40 nm reported in other works [101, 75]
Differences in the dimension within one structure (e.g., different thickness of left and right wall in microgap waveguides, or between different strands of light cages)	Splitting of resonances	50 nm in microgap waveguides
Intra-chip variations (different average dimension between two structures on the same chip)	Shifting of resonances	2 nm in light cages [255]
Inter-chip (i.e., batch-to-batch) variations (different average dimensions on different chips)	Shifting of resonances	15 nm in light cages [255]

In terms of sensing applications, we showed that by using dual-ring light cages, fluorescence light from a dye-doped aqueous solution can be efficiently captured and guided to the waveguide ports. As experimentally demonstrated, the flexibility of the light cage design and of the 3D nanoprinting process allows for localization of both the excitation and emission within the high transmission domains of the fundamental core mode. Detection limits for Rhodamine B that match bulk measurements and fast dye diffusion into the waveguide core were revealed experimentally.

Similar to microgap waveguides, applications of light cages in areas such as bioanalytics and environmental sciences are conceivable, while more sophisticated applications such as Raman spectroscopy could be targets of future research. As the light cage concept is not limited to liquids of a specific refractive index, the acquisition of fluorescence signals from

a variety of analytes is possible, as well as from multiple emitting species. Therefore, light cages offer a promising new direction for the use of hollow-core waveguides in laboratory-on-a-chip applications, combining high-efficiency fluorescence detection with integrated microfluidics.

4.3 Comparison between Microgap Waveguides and Light Cages

Microgap waveguides and light cages target similar applications as both are on-chip hollow-core waveguides with a large structural openness enabling fast analyte exchange. In comparison, the design of light cages allows for a larger structural openness factor of currently 49 %, while the realized microgap waveguides samples feature a maximal SOF of 20 %. Therefore, light cages are generally preferable for applications requiring the fastest response times, particularly if diffusion speeds are low as it is the case for liquid analytes.

For gas sensing, on the other hand, even the SOF of 20 % in microgap waveguides proved sufficient to approach filling times near the limit of bulk diffusion. In this case, microgap waveguides might be more relevant, as their simplified design allows shorter manufacturing times (10 min/mm vs. 18 min/mm for light cages), and lower propagation losses, especially in the infrared spectral range (1.25 dB/mm vs. 3 dB/mm @ 1400 nm). As a result, longer waveguide lengths are feasible using microgap waveguides before the attenuation becomes impracticably high (samples with 5 cm vs. 3 cm were realized). In turn, the contrast of the core-strand resonances is larger in microgap waveguides (> 60 dB for the 5 cm long sample vs. 25 dB for the 3 cm long light cage), which is, for example, relevant for the accurate determination of the resonance wavelength in refractive index sensing.

Another advantage of microgap waveguides is an exceptional mechanical stability, which allows the realization of wall widths as narrow as 600 nm. In contrast, the strand diameter of light cages currently stands at 3.6 µm, with preliminary experiments suggesting that strand diameters below 2 µm are not feasible due to the strong capillary forces acting on the strands during development. Presumably, the continuous walls of microgap waveguides allow for a more even distribution of capillary forces, while they are concentrated on the smaller strands in light cages, explaining the different mechanical properties. Due to the smaller feature sizes of the cladding elements, the number of cladding modes can be reduced in microgap waveguides, resulting in much wider spectral transmission windows (> 200 nm vs. ~ 50 nm in light cages).

In comparison to ARROWs, both microgap waveguides and the light cages have decisive advantages, such as lateral access and thus significantly faster diffusion, and the avoidance of costly and time-consuming multi-step manufacturing processes by using 3D nanoprinting - while all three waveguides offer similar losses on the order of 1 dB/mm.

It is important to note that a substantially enhanced level of integration can be reached through interfacing 3D-nanoprinted waveguides with optical fibers using V-grooves on sili-

con chips, an approach that has been demonstrated for light cages [83] but can also be applied to microgap waveguides. Another appealing approach is to nanoprint structures directly on the end face of optical fibers, which has been realized both for conventional hollow-core waveguide geometries [101], and microgap waveguides [280].

Chapter 5

Off-axis twisted waveguides

The results presented in this chapter are currently under review for publication in a journal. A preprint is available on arXiv [281]:

J. Bürger, A. C. Valero, T. Weiss, S. A. Maier, and M. A. Schmidt

"*Impact of coordinate frames on mode formation in twisted waveguides*"

The journal allows reproduction of the work in dissertations without requesting permission.

As a preparation for the study on twisted light cages presented in Chapter 6, we investigated the optical properties of modes inside the solid core of a single off-axis twisted strand.

The interest in such off-axis twisted waveguides started emerging in the 1980s due to the observation that single-mode fibers helically coiled around a cylinder exhibit **circular birefringence**, manifested by the rotation of the polarization state of linearly polarized light as it propagates along the waveguide [117, 109, 282, 283]. The rotation was initially understood based on the transversality of light [117], which means that the polarization vector is constrained to the surface of the **k**-sphere. As the wavevector **k** changes direction when light propagates along the helix, the polarization vector is parallel transported on the surface of the sphere [161] - a concept well known from differential geometry [284]. Due to the curvature of this surface, it was found that the polarization vector does not necessarily return to its original state after the light completes a closed loop on the **k**-sphere. More specifically, the polarization vector rotates relative to the laboratory frame whenever the light's trajectory features a nonzero torsion[1]. This conceptual framework initially served well in explaining the observed circular birefringence in helical fibers[2].

Among many other fields in physics, the identification of a quantum mechanical geometrical phase factor reported by Michael Berry in 1984 [288] - now widely known as the

[1]Torsion refers here to a purely geometrical quantity and is not related to any torsional stress in the material.

[2]Note that we always use the term "helical waveguide" to refer to an off-axis twisted waveguide, in distinction to on-axis twisted waveguides [92, 97, 124, 96] or two-dimensional spiraling waveguides [285, 286, 287].

Berry phase - sparked new insights into the physics of light traveling along curved trajectories. In fact, the first observation of this seminal theoretical work was accomplished in such a helically coiled fiber in 1986 [289, 290]. Building on the previous works, it was found that the angle by which linearly polarized light is rotated in one turn of the helical waveguide corresponds to the Berry phase.

The theory evolved further in the years thereafter, in particular, it was realized that light traveling along curved trajectories experiences a **spin-orbit and orbit-orbit interaction** coupling the spin or orbital angular momentum (OAM) of a beam of light to its orbital motion [177, 161, 183, 174]. The emergence of circular and OAM birefringence in helically coiled fibers could now be explained as a direct consequence of these couplings. Conversely, spin-orbit and orbit-orbit interactions were found to act back on the trajectory of light splitting the beam depending on its spin and OAM. These effects are now known as the photonic spin Hall [178, 174] and orbital Hall effects [182, 183] (introduced in Section 2.4).

In all of these early works, the cross-sectional shape of the helical waveguides is assumed to be circular in the plane perpendicular to the helical path, which can be well described in the Frenet-Serret frame. On the other hand, more recent experimental works often use the helicoidal frame to perform simulations of fibers fabricated with off-axis twisted air holes or capillaries [98, 119, 115, 93, 110]. In this chapter, we point out that the resulting structures differ, both in their geometry and their optical properties - an important fact that has previously been overlooked. Furthermore, we compare the results to helical waveguides defined in a third coordinate system, the "Overfelt frame" [168], which is derived from a toroidal geometry. Given that virtually all works on twisted waveguides use one of these coordinate systems, the presented results could be of importance to a wide range of waveguide designs.

Another aspect frequently lacking in previous works is a comprehensive description of the **transformation of fields from the helicoidal frame back to the laboratory frame**. We describe this process in detail in Appendix B and explain under which conditions it is possible to define an effective refractive index for modes of on- and off-axis twisted waveguides in the lab frame. Such an effective index is needed for example when analyzing coupling to modes in straight waveguides or for comparison to experimental results.

We conducted simulations for both single-mode and multimode variants of the three off-axis twisted waveguide types and compared the results to an analytical model for the effective index [122] and loss [291] of modes in helical waveguides. The study investigates twist rates of up to 20 turns per mm, which are, to our knowledge, the highest investigated so far for off-axis twisted waveguides (an overview of such works can be found in Appendix C). Spin- and OAM-dependent splittings in the spatial properties of the modes were analyzed, as well as the emergence of superchiral fields on the surface of the waveguides (i.e., fields with a larger chiral asymmetry than circularly polarized plane waves, see Section 2.2.5 and Refs. [85, 121]).

5.1 Geometry of Helical Waveguides

Starting from a coordinate system that features a coordinate in which a helix is translation invariant, a natural way to define a helical waveguide is the following: set a circular refractive index profile with radius r_c in the plane spanned by the unit vectors of the remaining two coordinates and extend it infinitely in the direction of translation invariance. Using

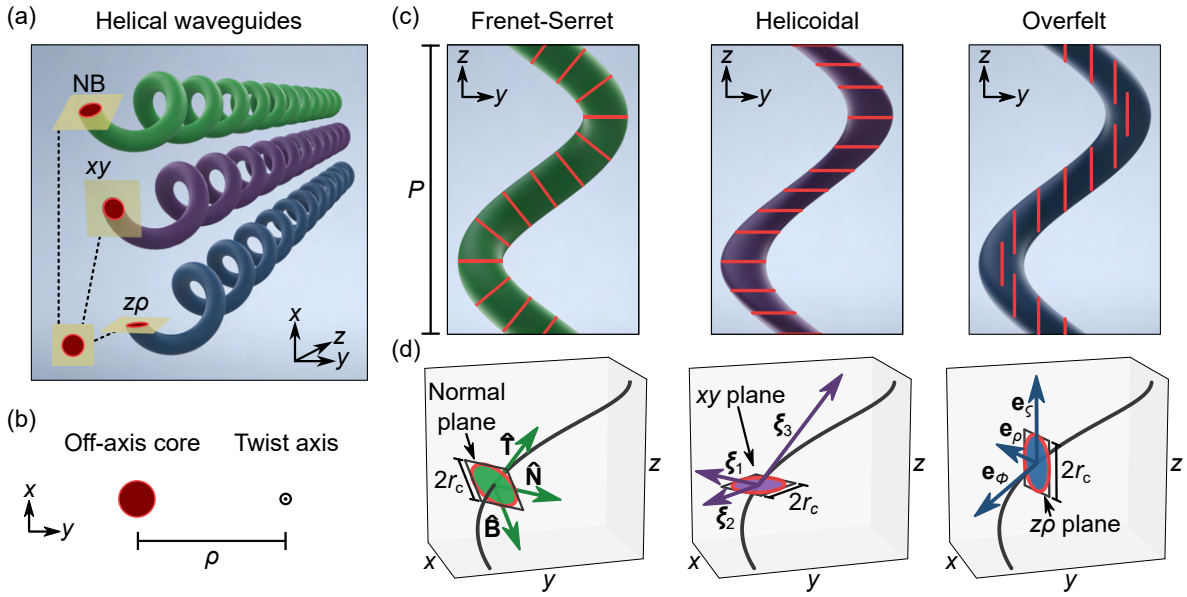

Figure 5.1: Helical waveguide geometries. (a) Illustration of the three waveguide types investigated in this chapter. (b) In these off-axis twisted waveguides, the core is located at a distance ρ from the twist axis. (c) Orthographic side views of the Frenet-Serret waveguide (green), the helicoidal waveguide (purple), and the Overfelt waveguide (blue). All helices are left-handed with a pitch distance P. (d) Basis vectors of the corresponding coordinate systems. The waveguides are defined to have a circular cross section with radius r_c in the plane spanned by the two basis vectors which are not tangential to the helical path (black curve). Red lines in (c) denote the orientation of the circular cross section. Note that only the Frenet-Serret system is orthogonal.

this procedure, the **Frenet-Serret, helicoidal, and Overfelt waveguide** were defined from their respective coordinate systems in Section 2.3. For comparison, the investigated waveguides are shown side-by-side in Fig. 5.1. For the study, we use an off-axis distance $\rho = 14$ µm (the radius of the helix), and a core radius of $r_c = 1.8$ µm or $r_c = 0.2$ µm for the multimode or single-mode variants of the waveguides, respectively.

To gain further insights into the differences in the geometry of the three waveguides, it is useful to determine their **cross sections in the *xy* plane**, which are depicted in Fig. 5.2. Interestingly, these cross sections can take on quite non-trivial shapes, and an exact analytical description is - to our knowledge - not available. When the twist rate tends to 0, the Frenet-Serret waveguide becomes more and more straight with $\hat{\mathbf{T}}$ pointing mostly

in the z direction. Therefore, the shape of the Frenet-Serret waveguide approaches that of the helicoidal waveguide for low twist rates. As the twist rate approaches infinity, the Frenet-Serret waveguide becomes more and more like a torus with $\hat{\mathbf{T}}$ lying mostly in the xy plane. This is precisely the shape to which an Overfelt waveguide collapses at infinite twist rate, which is why the cross sections of both waveguides approach each other at high twist rates.

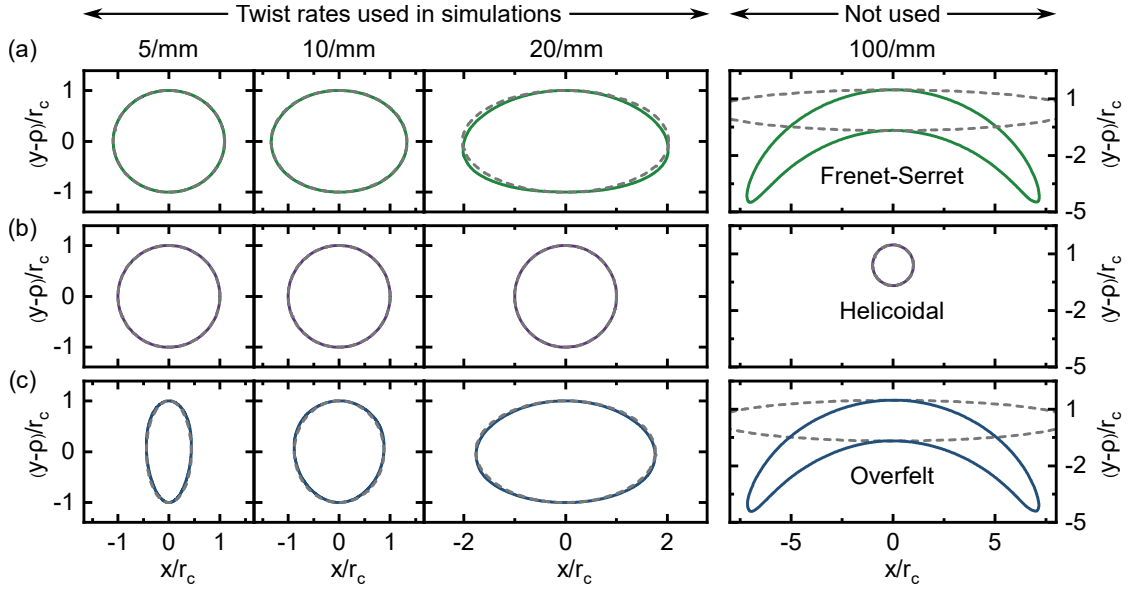

Figure 5.2: Cross sections of helical waveguides in the xy plane. Cross sections were calculated numerically for four different twist rates (noted on the top) using an off-axis distance of $\rho = 14$ µm and $r_c = 1.8$ µm. The center of the twist axis is located below the shown coordinate range at $x = y = 0$. The geometry of the Frenet-Serret waveguide (green) approaches that of the helicoidal waveguide (purple) for low twist rates and that of the Overfelt waveguide (blue) for high twist rates. Gray dashed lines show an analytical approximation of the cross section, which is valid in the limit of weak coiling ($\bar{\kappa} r_c \ll 1$) and if the extent of the ellipse in x direction is much smaller than $2\pi\rho$. Waveguide modes were simulated for twist rates up to 20/mm.

Knowing the cross sections of the three waveguides in the xy plane allows to perform all following **FEM simulations** in the helicoidal coordinate system because the shape of the cross sections merely rotates around the twist axis as the z coordinate is changed (i.e., a structure that is invariant along the helical trajectory in one of the coordinate systems is also invariant in the other two systems). Specifically, we calculate the modal properties using a commercial FEM solver (PropagatingMode module of JCMwave). JCMwave offers built-in support for the helicoidal coordinate system, along with appropriately defined perfectly matched layers.

To simplify the definition of the geometry in the simulations, we derive an analytical **approximation of the cross sections** describing the shape as an ellipse adapting an idea

from Ref. [106]: When imagining the helical waveguide to be wound around a cylinder, it is possible to "cut" the cylinder along the axial direction and "unroll" it onto a plane as shown in Fig. 5.3. We point out that this unrolling is only possible in the limit of weak coiling, i.e., if the radius of curvature of the helix is much larger than the radius of the core ($\bar{\kappa} r_c \ll 1$). Otherwise, the side of the waveguide facing away from the cylinder is much longer than the side facing towards the inside preventing the unrolling. The weak coiling approximation is valid for all investigated waveguides up to arbitrary twist rates since $\bar{\kappa} r_c < r_c/\rho < 0.13 \ll 1$.

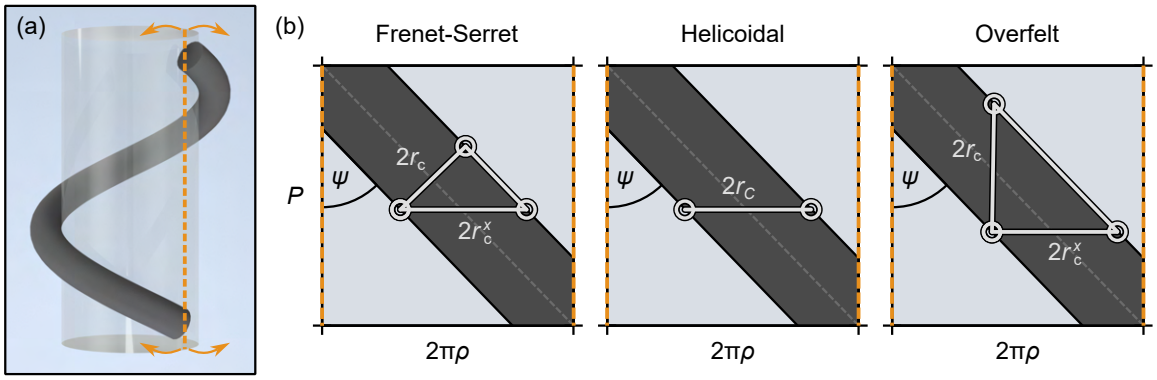

Figure 5.3: Approximation for the xy cross section of the investigated helical waveguides as ellipses. When imagining the waveguides to be placed on the surface of a cylinder (a), the surface can be cut along the orange dashed line and unrolled onto a plane (b), provided that the waveguides are weakly coiled ($\bar{\kappa} r_c \ll 1$). The waveguides are tilted by an angle ψ, giving rise to elliptical cross sections in the xy plane with semi-axes r_c^x and r_c^y, as long as $2r_c^x \ll 2\pi\rho$. r_c^y points into the plane and is equal to r_c for all three waveguides. In its defining coordinate systems, each waveguide has a circular cross section with radius r_c.

Noting that the waveguides are tilted by an angle $\psi = tan^{-1}(\alpha\rho)$ from the z axis after unrolling, it is possible to describe the cross sections of the waveguides in the xy plane by an ellipse. One axis of the ellipse is perpendicular to the surface of the cylinder and its length r_c^y is equal to the radius r_c of the circular cross section defined in the corresponding coordinate system. The length of the other axis r_c^x can be calculated by trigonometry from the sketches in Fig. 5.3(b), yielding the values listed in Table 5.1.

To be precise, the so-obtained cross section would now have to be "attached" back onto the cylinder which deforms the ellipse according to the curvature of the cylinder (see right panels in Fig. 5.2). However, this step would generate a more difficult shape and is not required as long as the length of the ellipse along the azimuthal direction (here $2r_c^x$) is much smaller than the circumference ($2r_c^x \ll 2\pi\rho$). In this thesis waveguides up to twist rates of 20/mm were simulated, where $2r_c^x < 7.3\ \mu\text{m} \ll 2\pi\rho \approx 88.0\ \mu\text{m}$, such that the approximation of the cross sections as ellipses is valid.

Table 5.1: Semi-major and semi-minor axes of the elliptical xy cross sections of the three helical waveguides in the weak-coiling approximation, and provided that $2r_c^x \ll 2\pi\rho$. r_c is the radius of the core defined within each of the coordinate systems.

Semi-axis	Frenet-Serret	Helicoidal	Overfelt
r_c^x	$\sqrt{1+(\alpha\rho)^2}\, r_c$	r_c	$\alpha\rho\, r_c$
r_c^y	r_c	r_c	r_c

5.2 Transformation of Effective Index to Lab Frame

The results returned by the mode solver are the fields in the xy plane at $z = 0$ and the effective index $n_{\text{eff}}^{\text{Helical}}$ such that the fields $\tilde{\mathbf{F}}$ in the helicoidal coordinate system satisfy [104]:

$$\tilde{\mathbf{F}}(\xi_{\mathbf{1}}, \xi_{\mathbf{2}}, \xi_{\mathbf{3}}) = \mathrm{e}^{\mathrm{i}k\xi_3\, n_{\text{eff}}^{\text{Helical}}} \mathbf{F}(\xi_{\mathbf{1}}, \xi_{\mathbf{2}}). \tag{5.1}$$

We apply a coordinate transformation to evaluate the fields in Cartesian coordinates at $z \neq 0$ which subsequently allows to display all modal quantities within the NB plane. Step-by-step instructions are available in Appendix B.

When transforming the fields to Cartesian coordinates, the fields develop an additional z dependent phase factor which we refer to as the **transformation phase** (cf. Appendix B.1.1). We show that the transformation phase only increases linearly in z under specific conditions. Most importantly, the following conditions have to be satisfied: (1) the electric field is circularly polarized with spin $s = \pm 1$, and (2) its spatial phase profile is flat or has an OAM profile with an $\mathrm{e}^{\mathrm{i}l\phi}$ phase dependence. In this case it is possible to define an effective index $n_{\text{eff}}^{\text{Lab}}$, such that the phase of the fields measured in the lab frame increases as $\mathrm{e}^{\mathrm{i}kz\, n_{\text{eff}}^{\text{Lab}}}$ with:

$$\boxed{n_{\text{eff}}^{\text{Lab}} = n_{\text{eff}}^{\text{Helical}} + (s+l)\frac{\alpha\lambda}{2\pi}.} \tag{5.2}$$

This equation holds both for off-axis twisted waveguides and on-axis twisted waveguides and matches with earlier derivations valid for on-axis twisted waveguides [104] and off-axis twisted waveguides [122] that were derived based on different approaches. Compared to these earlier derivations, we can also treat cases where the modes feature a noncircular polarization state and find that the transformation phase does not increase linearly in z in this case. More intuitively, these phase changes are caused by the rotation of the polarization ellipse, following the twist of the waveguide. For example, if the short axis of the polarization ellipse points along the x direction at $z = 0$, it will point along the y direction at $z = P/4$. This effect is unique to modes in twisted waveguides as the polarization state of an eigenmode in a straight waveguide does not change during propagation. The definition of an effective index in the lab frame for such elliptically polarized modes might therefore give the wrong impression, that they could couple to a mode in a straight waveguide with the same effective index. Keeping these caveats in mind, we still apply Eq. 5.2 to all results for better comparability.

5.3 Analytical Description of Frenet-Serret Waveguides

To prepare for the interpretation of the FEM simulation results in Section 5.4, we first need to understand why off-axis twisting has an impact on the optical properties of a mode. To this end, we turn to a model that has been developed by Alexeyev and Yavorsky based on perturbation theory in 2008 [122]. Their theory describes the optical properties of Frenet-Serret waveguides - the simplest of the three waveguides types - and is based on three assumptions:

1. The radius of curvature of the helix is small compared to the radius of the core: $r_c\bar{\kappa} \ll 1$ (weak coiling approximation).
2. The fields are transverse in the Frenet-Serret frame and can be described by the scalar wave approximation. This approximation is valid for fibers with low index contrast: $\Delta = \frac{n^2_{\text{Core}} - n^2_{\text{Cladding}}}{2n^2_{\text{Core}}} \ll 1$.
3. The torsion τ of the helix can be treated as a small parameter.

Formulating the scalar wave equation in the Frenet-Serret frame introduces a new set of operators $\hat{V}_i$ compared to the operator $\hat{H}_0$ of the untwisted system:

$$(\hat{H}_0 + \hat{V}_0 + \hat{V}_1 + ...)\,|\Psi\rangle_{\text{FS}} = \beta^2_{\text{FS}}\,|\Psi\rangle_{\text{FS}}\,, \tag{5.3}$$

where $|\Psi\rangle_{\text{FS}}$ denotes the two transverse components of the field and β_{FS} the propagation constant, both given in the Frenet-Serret frame. Expression for the operators can be found in Ref. [122]. Under the assumptions given above, the additional operators $\hat{V}_i$ can be treated as small perturbations of the untwisted system. Using first-order perturbation theory, the twist-induced corrections to the propagation constant can be calculated. The dominant term is caused by the operator $\hat{V}_0$, which reads:

$$\boxed{\Delta\beta_{\text{FS}} = (s + l)\tau.} \tag{5.4}$$

This simple result implies that any waveguide forcing photons to move along a non-planar path (which therefore has torsion) results in a twist-induced splitting of the effective modal index proportional to the total angular momentum $s + l$. For helical trajectories, the effect is particularly simple due to the constant torsion of a helix.

The splitting can result in modes with different total angular momentum to have the same effective index at a certain twist rate. In this case, Alexeyev and Yavorsky showed that coupling between modes with a difference in total angular momentum of i can be provided by the higher-order operators $\hat{V}_i$. This coupling is of interest for mode conversion applications [292] but is not studied further here.

The result can be converted to the helicoidal coordinate frame by noting that the helix is parametrized by the arc length in the Frenet-Serret frame while it is parametrized by the z distance in the helicoidal frame:

$$n^{\text{Helical}}_{\text{eff}} = \left(n_0 + \frac{(s + l)\tau}{k_0}\right)\sqrt{1 + \alpha^2\rho^2}, \tag{5.5}$$

where n_0 is the effective index of the mode in the untwisted waveguide. Note that the sign of τ is negative for a left-handed helix. To get a better understanding of the magnitude of the twist-induced splitting, the result can further be converted to the lab frame using Eq. B.26:

$$\boxed{n_{\text{eff}}^{\text{Lab}} = \underbrace{n_0\sqrt{1+\alpha^2\rho^2}}_{\substack{\text{Geometric increase}\\ \text{in path length}}} + \underbrace{(s+l)\frac{\alpha}{k_0}\left(1-\frac{1}{\sqrt{1+\alpha^2\rho^2}}\right)}_{\substack{\text{Spin-orbit } (s) \text{ and}\\ \text{orbit-orbit } (l) \text{ interaction}}}.} \tag{5.6}$$

This result is valid when the modal field is circularly polarized and has a flat or OAM phase profile (see Appendix B.1.3). The fact that the signs of τ and α are opposite was used. For small twist rates $\alpha\rho \ll 1$ the result can be simplified showing that the splitting of modes with different total angular momentum increases strongly with twist rate and helix radius:

$$\boxed{n_{\text{eff}}^{\text{Lab}} = n_0\sqrt{1+\alpha^2\rho^2} + (s+l)\frac{\rho^2\alpha^3\lambda}{4\pi} \qquad \text{for } \alpha\rho \ll 1.} \tag{5.7}$$

For high twist rates, the splitting increases linearly in α:

$$\boxed{n_{\text{eff}}^{\text{Lab}} = n_0\sqrt{1+\alpha^2\rho^2} + (s+l)\frac{\alpha\lambda}{2\pi} \qquad \text{for } \alpha\rho \gg 1.} \tag{5.8}$$

This important result shows that twisting a waveguide lifts the degeneracy between modes with the same magnitude of total angular momentum but different sign. In straight step-index fibers, these modes are degenerate (cf. Section 2.2.2) and therefore the spin and OAM state is not conserved during propagation (minor imperfections in any real-world waveguide lead to a coupling of the degenerate modes).

5.3.1 Berry Phase in Helical Waveguides

On a more fundamental level, the additional phase induced by the twist (Eq. 5.4) can be seen as a consequence of the spin-orbit and orbit-orbit interaction of light in the "semi-geometrical optics" approximation (cf. Section 2.4) [122]. As light propagates under the influence of these interactions, it acquires a spin- and OAM-dependent **Berry phase** Φ_B [290, 161, 183], the photonic equivalent of the Berry phase in quantum mechanics:

$$\Phi_B = (s+l)\int_C \mathbf{A}\cdot d\mathbf{k} = (s+l)\int_S \mathbf{F}\cdot d\mathbf{S} = (s+l)\Omega, \tag{5.9}$$

where C is the contour traced out by the light in momentum space, $\mathbf{F} = \boldsymbol{\nabla}_{\mathbf{k}} \times \mathbf{A} = \frac{\mathbf{k}}{k^3}$ is the Berry curvature for $s = +1$ and $l = 0$, and $\mathbf{A}$ is the Berry connection for $s = +1$ and $l = 0$ (defined in Ref. [161]). The second and third equalities hold if C is a loop such that S is its enclosed surface on the $\mathbf{k}$-sphere ($\partial S = C$). In this case, the Berry phase is solely determined by the solid angle Ω of the loop that the light traces out on the $\mathbf{k}$-sphere.

For off-axis twisted waveguides, $\mathbf{k}$ points along the tangent $\hat{\mathbf{T}}$ of the helix which is tilted from the z axis by a fixed angle θ with $\cos(\theta) = 1/\sqrt{1+\alpha^2\rho^2}$ (cf. Section 2.3.1). Therefore, the trajectory of the light traces out a solid angle $\Omega = 2\pi(1-\cos(\theta))$ after propagating one turn in the helix. Plugging these terms into Eq. 5.9 yields the Berry phase shift after propagating a distance z along the helix axis:

$$\boxed{\Phi_B = (s+l)\,2\pi\left(1-\frac{1}{\sqrt{1+\alpha^2\rho^2}}\right)\frac{z}{P} \quad \text{(Berry phase in a helical waveguide).}} \tag{5.10}$$

The resulting correction to the effective index of the modes δn can be calculated from $\delta n = \Phi_B/(zk_0)$ and coincides with the lab frame result obtained earlier (second term in Eq. 5.6).

5.4 Simulation Results for Optical Properties of Helical Waveguide Geometries

With these preparations, we start analyzing the twist-rate-dependent optical properties of the three helical waveguides. Modes were calculated numerically using a commercial FEM solver (JCMwave) which directly supports calculations in the helicoidal coordinate system. To this end, the approximation of the xy cross sections as ellipses with the parameters of Table 5.1 was used.

Based on the 3D-nanoprinted waveguides reported in Chapters 4 and 6, and a recent realization of helical waveguides with this technique [102], we chose the refractive index n of the waveguides as that of the photoresist defined in Eq. 3.9. Specifically, the simulations were conducted at a wavelength of $\lambda = 770$ nm, and a refractive index of the core of $n_{\text{co}} = 1.5423$ with a cladding made out of air ($n = 1$). First, we analyze multimode variants of the three waveguides ($r_c = 1.8$ µm), for which the resulting V number is 17.25 (number of guided modes: $V^2/2 \approx 149$).

5.4.1 Fundamental Modes in Multimode Waveguides

The optical properties of the twisted multimode waveguides are very similar across a large range of investigated twist rates (5/mm - 20/mm) since the cross sections of the waveguides are so wide that the specific shape plays a minor role. The two fundamental modes are circularly polarized with the **wavefronts lying in the NB plane** as shown in Figs. D.1 and D.3.

The real part of the effective index and the circular birefringence (difference in the real part of the effective index between the LCP and RCP mode, evaluated in the lab frame) match well with the analytical model of Eq. 5.6 for all waveguide types. Off-axis twisting has two immediate consequences: (1) the effective index of the mode increases due to the longer path that the light is traveling along the helix to reach a certain distance z (first term in Eq. 5.6 and Fig. 5.4(a)), and (2) a splitting occurs between modes with different

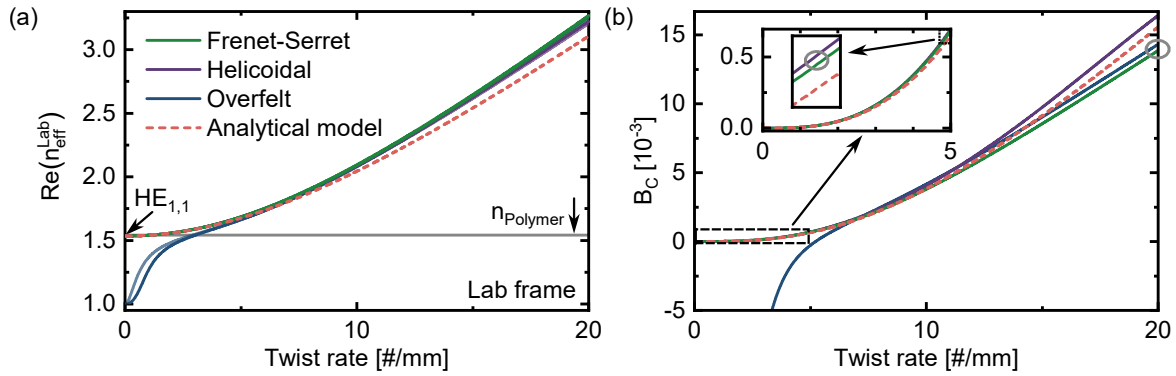

Figure 5.4: Optical properties of multimode helical waveguides (r_c = 1.8 µm). (a) Twist rate dependence of the real part of the effective mode index of the two fundamental modes calculated in the lab frame. A darker color shade denotes the LCP mode, a lighter shade the RCP mode. (b) Circular birefringence B_C (i.e., difference between the effective index of the two lowest-order modes). Note that for low twist rates (< 5/mm) the modes of the Overfelt waveguide become elliptically polarized. Red dashed lines in (a,b) represent an analytical prediction for the Frenet-Serret waveguide (Eq. 5.6).

total angular momentum (second term in Eq. 5.6 and Fig. 5.4(b)). Compared to typical values of birefringence found in polarization-maintaining fibers (10^{-3} - 10^{-4}), much higher birefringence on the order of 10^{-2} can be reached at the highest investigated twist rate of 20/mm ($\alpha\rho = 1.8$).

Since the cross section of the Overfelt waveguide becomes infinitely narrow along the B direction for $\alpha \to 0$ (see Fig. D.3), its optical properties deviate from those of the other two waveguides for twist rates below 5/mm. Due to the narrowing of the cross section, the two fundamental modes change from being circularly polarized to linearly polarized at low twist rates, resulting in a larger (linear) birefringence. As the modes are more and more localized in air, the effective index approaches 1 for $\alpha \to 0$.

5.4.2 OAM Modes in Multimode Waveguides

Next, we investigated the four OAM modes with $|l| = 6$ in the multimode Frenet-Serret waveguide. The modes are organized in two groups, one originating from the $EH_{5,1}$ mode pair of the untwisted waveguide with a total angular momentum (TAM) of ±5 and the other one from the $HE_{7,1}$ mode pair with a TAM of ±7 [158]. As the twist rate rises, the effective index of the modes overall increases with the same geometrical factor as the fundamental modes (first term in Eq. 5.6 and Fig. 5.5(a)). On the other hand, the birefringence within each mode pair is 5 or 7 times larger than for the fundamental modes, respectively, as expected from the second term in Eq. 5.6. This larger splitting for OAM modes is a consequence of the photonic orbit-orbit interaction term being l times as large as the spin-orbit interaction term. Off-axis twisting therefore lifts the degeneracy of OAM modes with the same total angular momentum, resulting in **OAM birefringence**. This

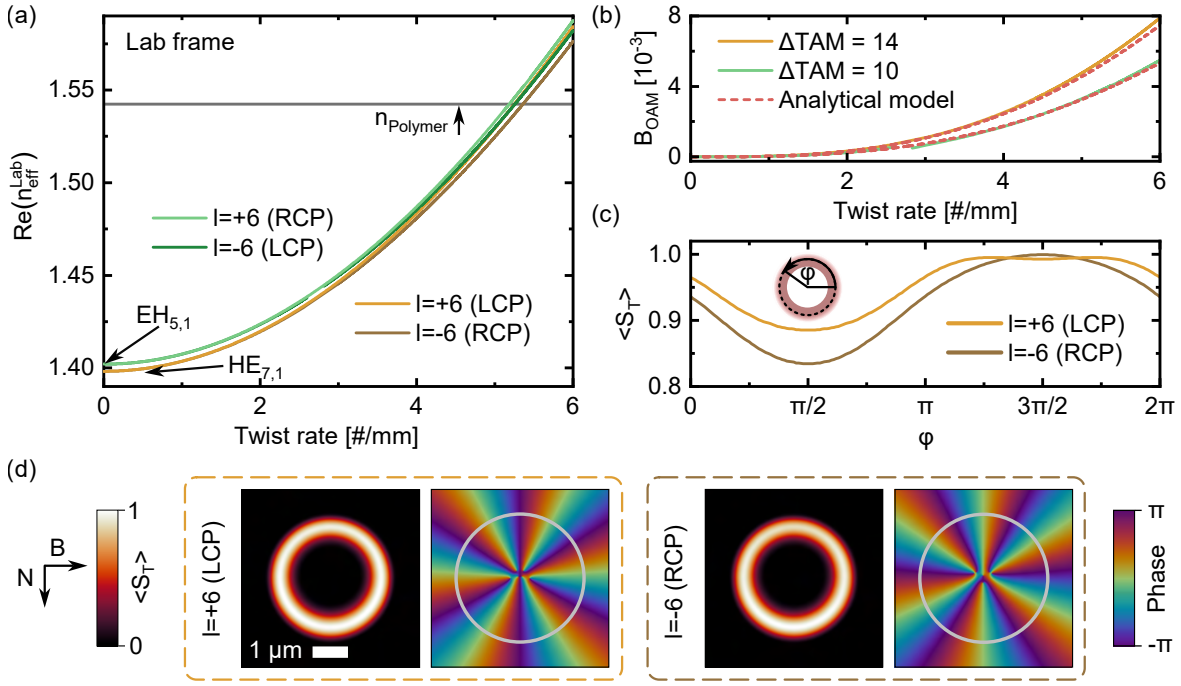

Figure 5.5: OAM modes in Frenet-Serret waveguide geometry ($r_c = 1.8$ µm). (a) Twist rate dependence of the real part of the effective mode index in the lab frame for the four modes with $|l| = 6$. The two modes with total angular momentum (TAM) of ± 5 (green) stem from the even and odd $EH_{5,1}$ modes of the untwisted waveguide, while the two modes with TAM of ± 7 (orange) originate in the $HE_{7,1}$ modes. (b) OAM birefringence between these mode pairs. Note that the other pairings (+5/-7 and -7/+5) are already nondegenerate in the untwisted case. The simulated splitting matches well with the analytical prediction (red dashed line, Eq. 5.6). (c,d) Longitudinal component of the Poynting vector of the modes with TAM of ± 7 for a twist rate of 5/mm. Evaluating the azimuthal distribution of the Poynting vector along a selected circle shows an increase in the intensity at the side of the waveguide that points towards the central twist axis. This asymmetry is different for the two modes, which might be a result of the photonic orbit-orbit interaction. Panel (d) additionally displays the phase of the B component of the electric field with the cross section of the waveguides shown as gray line.

effect can be used to create fibers, which preserve the OAM state during propagation. Furthermore, twisting can induce coupling between modes, which enables twist-based mode converters [122]. While not explored further in this study, such a coupling can be observed for the mode pair with a TAM of ± 5 at a twist rate of 2.7/mm, explaining the discontinuity in the green curves in Fig. 5.5(a,b).

5.4.3 Fundamental Modes in Single-mode Waveguides

To study single-mode variants of the three waveguide types, the core radius was reduced to $r_c = 0.2$ µm, resulting in a V number of 1.92. Contrary to the multimode case, the optical properties of these waveguides differ strongly from each other. As the cross section is much narrower, any change in the cross section from a circular profile affects the polarization of the mode as shown in Fig. 5.6(d). The resulting mix of linear and circular birefringence in the fundamental modes of the helicoidal and Overfelt waveguide can be much larger and of opposite sign than that of the Frenet-Serret waveguide (Fig. 5.6(b)). As the cross section of the Frenet-Serret waveguide is circular in the NB plane at all twist rates, its modes remain circularly polarized and their effective indices are accurately described by Eq. 5.6. Another aspect to consider is that the fraction of power located in air is also dependent

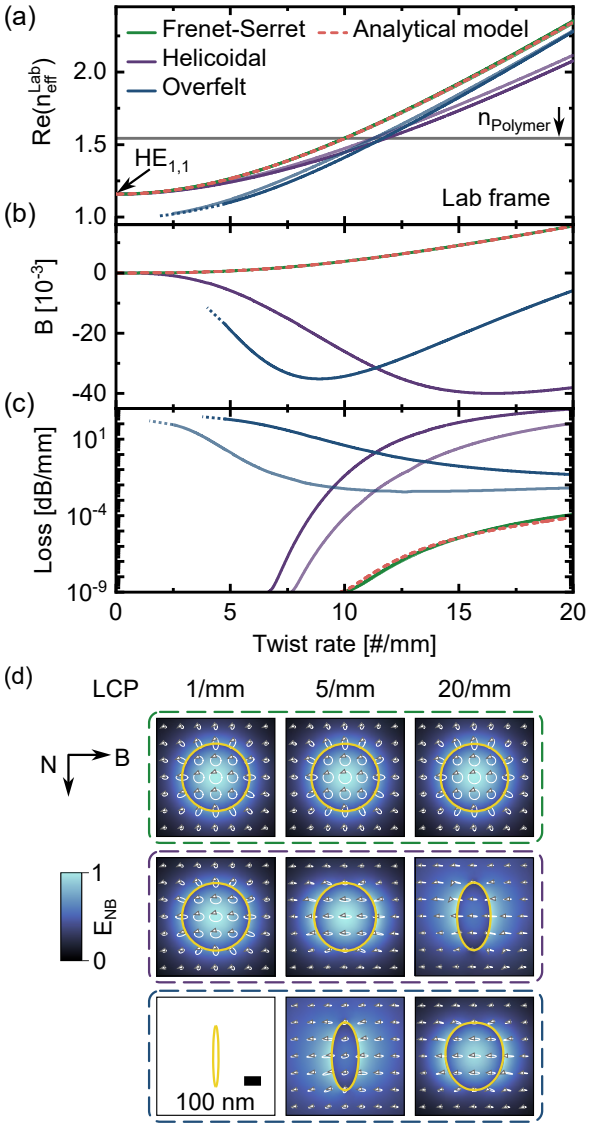

Figure 5.6: Optical properties of single-mode helical waveguides ($r_c = 0.2$ µm). (a,b,c) Twist rate dependence of the real part of the effective mode index, the birefringence, and the attenuation of the two fundamental modes calculated in the lab frame. A darker color shade denotes the LCP mode, a lighter shade the RCP mode. Red dashed lines in (a,b,c) represent an analytical prediction for the Frenet-Serret waveguide (Eqs. 5.6 and 5.12). (d) Spatial distribution of the transverse (NB) component of the electric field of the LCP mode at three different twist rates. Polarization ellipses show that the field of the Frenet-Serret waveguide (green box) remains circularly polarized at all twist rates. Helicoidal waveguide (purple box) and Overfelt waveguide (blue box) feature elliptically polarized eigenmodes at high or low twist rate, respectively. The cross section of the waveguides is highlighted as yellow line. Note that the modes of the Overfelt waveguide could not be calculated for twist rates below 5/mm due to very high loss and low confinement in the core (blue dots in a,b,c and blank field in d).

on the shape of the cross section. For example, the fraction of power in air is increased at small twist rates ($\alpha\rho \ll 1$) for the Overfelt waveguide, and at large twist rates ($\alpha\rho > 1$) for the helicoidal waveguide, which results in a reduction of the effective index (Fig. 5.7 and Fig. 5.6(a)).

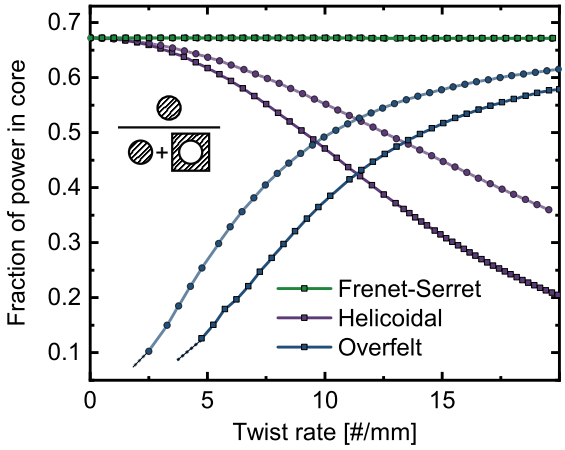

Figure 5.7: Twist rate dependence of the fraction of power present inside the core calculated for the single-mode helical waveguides geometries indicated in the legend. The power inside the core was calculated by integrating the T component of the Poynting vector over the area of the core in the NB plane. It was normalized by the integral over the complete simulation region as shown in the inset. A darker color shade denotes the LCP mode, a lighter shade the RCP mode. Note that the modes of the Overfelt waveguide could not be calculated for twist rates below 5/mm due to very high loss and low confinement in the core (blue dots).

As expected from the analytical formula for the cross sections of the waveguides (Table 5.1), the properties of the Frenet-Serret waveguide converge with those of the helicoidal waveguide for low twist rates and with those of the Overfelt waveguide for high twist rates. The propagation loss of the waveguides will be discussed below in Section 5.6.

5.5 Effects of Bending on Modes in Helical Waveguides

5.5.1 Fundamental Modes in Multimode Waveguides

Next, we studied the spatial properties of the modes in more detail with an overview available in Appendix D. Regarding the intensity distributions of the fundamental modes in the multimode waveguides, twisting has two effects: (1) the mode profile becomes narrower and (2) it shifts away from the twist axis. These effects are shown in Fig. 5.8(a,b) for the Frenet-Serret waveguide and in Fig. D.3 for the helicoidal and Overfelt waveguides. Both effects are well known from fiber bends in a two-dimensional plane as the radius of curvature decreases [293]. If the bent waveguide is approximated as a circle with a radius of curvature R, it can be mapped to a straight waveguide using a conformal transformation [294]. This mapping results in a modified refractive index profile that increases approximately linear (for $R \gg r_c$) across the waveguide and cladding: $n \approx n_0\,(1 + x/R)$, where $x = 0$ corresponds to the center of the waveguide and n_0 is the refractive index profile of the waveguide before bending [295] (see Fig. 5.9). More intuitively, as the mode has

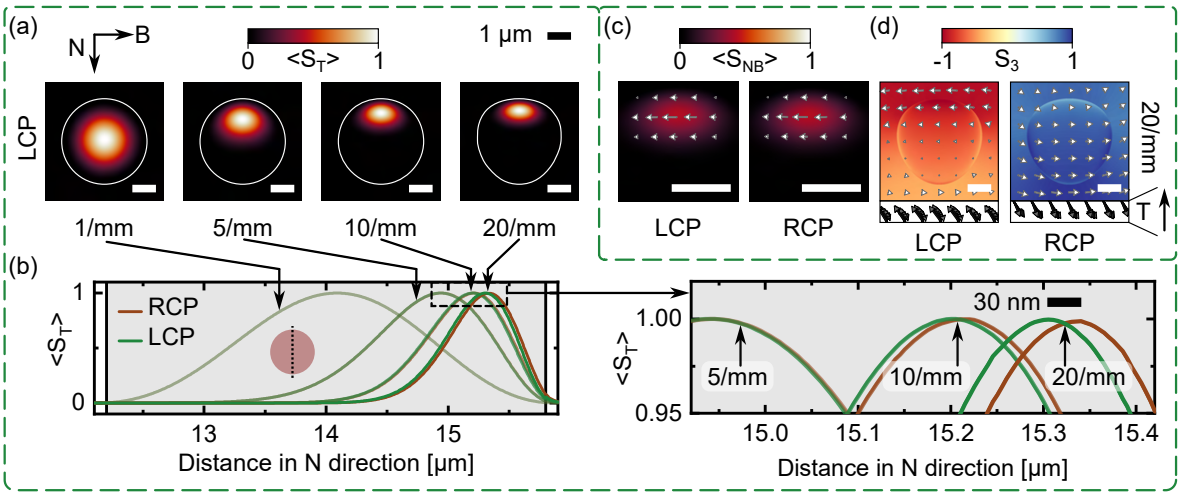

Figure 5.8: Spatial properties of modes in the multimode Frenet-Serret waveguide depicted in the TNB frame. (a) Distribution of the T component of the Poynting vector (i.e., tangential to the helix) of the LCP mode at four different twist rates. At increasing twist rate, the waveguide becomes bent such that the center of the mode moves to larger radii, i.e., away from the twist axis. A line cut of these distributions along the N direction through the center of the waveguide is shown in (b). The zoomed inset shows that the RCP mode (brown) moves further outwards than the LCP mode (green), potentially a consequence of the photonic spin Hall effect. (c) At a high twist rate of 20/mm, the Poynting vector develops a transverse component pointing in the negative B direction for both LCP and RCP modes. (d) The spin vector of the electric field $\mathbf{s_E}$ also develops a transverse component that points in opposite directions for the two polarizations. The magnitude of $\mathbf{s_E}$ is equal to the third component of the Stokes vector S_3.

to propagate a larger distance on the outside of the bend than on the inside, the mapped refractive index increases away from the center of curvature. The reason for the observed shift of the modal patterns towards the region of higher index can be seen when noting that

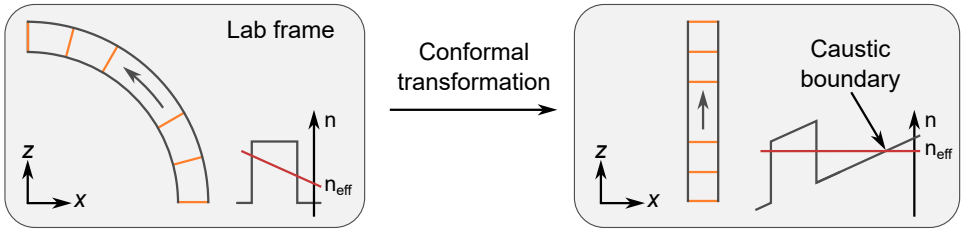

Figure 5.9: Description of bent waveguides. The wavefronts in the bent waveguide (orange) are perpendicular to the propagation direction (gray arrow) resulting in the effective index (red) decreasing towards the outside of the bend. Equivalently, the waveguide can be described as a straight waveguide (right panel) with a refractive index profile that increases away from the center of curvature. Idea for figure is taken from Ref. [296].

the scalar wave equation is equivalent to the time-independent Schrödinger equation [133] for a potential equal to $-n^2$. Consequently, the mode moves to larger radii to minimize its "energy". For helical waveguides, the radius of curvature of the bend is given by $R = 1/\bar{\kappa}$, which decreases with increasing twist rate.

5.5.2 OAM Modes in Multimode Waveguides

While twisting strongly impacts the effective index of OAM modes, its impact on the mode profile is much weaker than for the fundamental mode. Contrary to the fundamental modes, the center of the modes with $|l| = 6$ does not shift away from the twist axis as shown in Fig. 5.5(d). This is to be expected since the effect of bending on the mode profile is known to decline as the mode order increases [293, 297]. What is typically observed for OAM modes in bent fibers is that the angular intensity distribution is slightly nonuniform with a peak on the side facing away from the center of curvature [293, 297, 298]. However, the OAM modes in the twisted Frenet-Serret waveguide peak on the side facing towards the twist axis as shown in Fig. 5.5(c). This asymmetry must therefore be purely related to the twist.

5.5.3 Fundamental Modes in Single-mode Waveguides

The intensity distribution of the modes in the single-mode Frenet-Serret waveguide remains virtually unaffected by twisting due to the confinement provided by the high index contrast as shown in Fig. 5.10(a). For systems with a lower index contrast, a shift of the center of the mode would be expected [293] similar to what has been discussed above for the multimode system.

5.6 Loss in Helical Waveguides

Propagation loss in off-axis twisted waveguides is different from the loss of the corresponding untwisted waveguide for two reasons: (1) The geometric path length to reach a certain axial distance z is increased because the light is traveling along a helical trajectory, and (2) additional loss arises from bending. The geometric factor effectively increases the intrinsic loss γ_0 of the untwisted waveguide, which might be present due to surface roughness or material absorption. We denote the associated attenuation coefficien[3] for the twisted waveguide as γ_{geo}:

$$\gamma_{\text{geo}} = \gamma_0 \frac{\sqrt{P^2 + (2\pi\rho)^2}}{P} = \gamma_0 \sqrt{1 + \alpha^2 \rho^2}. \tag{5.11}$$

Bend loss of optical fibers has been studied extensively for situations where the weak guidance approximation is satisfied ($\Delta \ll 1$), the modal field inside the twisted core is the

[3]The attenuation coefficient is defined via the relation $I(z) = I(0)\exp(-\gamma z)$, where I denotes the optical power.

same as in the straight fiber, and the radius of curvature is much larger than the radius of the core ($R \gg r_c$) [131, 299]. More advanced models exist if one or more of these assumptions are not satisfied [293, 300, 301]. Here, we use the model from Ref. [131] that is valid when all three assumptions are met and includes a correction factor taking into account that the bends do not lie within a flat plane but occur along a helical path. In this case, the attenuation coefficient γ_{bend} is given by [291]:

$$\gamma_{\text{bend}} = \frac{\sqrt{\pi}}{2r_c}\frac{V^2\sqrt{W}}{U^2}\sqrt{\frac{r_c}{R}}\,\mathrm{e}^{-\frac{4}{3}\frac{R}{r_c}\frac{W^3\Delta}{V^2}}\underbrace{\left(1-\frac{1}{2}(\alpha\rho)^2+\frac{3}{32}(\alpha\rho)^4\right)}_{\text{correction for helical bend}}, \tag{5.12}$$

where $V = 2\pi(n_{\text{co}}^2 - n_{\text{cl}}^2)r_c/\lambda$ is the V number, $\Delta = (n_{\text{co}}^2 - n_{\text{cl}}^2)/(2n_{\text{co}}^2) = 0.29$ is the refractive index contrast and $R = 1/\bar{\kappa}$ is the radius of curvature of the helix. $U(V)$ and $W(V)$ are numerical solutions to a transcendental equation characterizing the mode and can be obtained from Ref. [131]. For the single-mode Frenet-Serret waveguide, one has $V = 1.92$, $U = 1.50$, and $W = 1.20$ and for its multimode version $V = 17.25$, $U = 2.27$, and $W = 17.10$. Note that the mode profile of the multimode waveguide changes as the twist rate increases, thus Eq. 5.12 is only approximately valid.

The resulting bend loss γ_{bend} is shown for the Frenet-Serret waveguide in Fig. 5.6(c), matching well with the simulated data. Interestingly, bending strongly affects the loss of the single-mode waveguide as the twist rate increases while it remains negligibly low for the multimode variant (below 2×10^{-24}dB/mm at the highest investigated twist rate). As the simulated loss of the multimode waveguides is below the noise level of the solver, it is not shown. This difference in bend loss can be understood based on the conformal transformation method described above. Since the mapped refractive index profile increases away from the center of curvature, at some distance from the waveguide - the caustic boundary - the mapped index of the cladding is higher than that of the core mode and the field becomes radiative due to the absence of total internal reflection [295]. As the field of the multimode waveguide remains well confined within the core, its amplitude at the caustic boundary is very low. In the single-mode waveguide on the other hand, a much larger fraction of the field is present inside the cladding, thus explaining the notable difference in bend loss.

The geometric contribution to the loss γ_{geo} was not analyzed in this study because the material of the waveguide was assumed to be lossless ($\gamma_0 = 0$). Preliminary simulations with lossy materials showed that the total loss is well described as the sum $\gamma_{\text{geo}} + \gamma_{\text{bend}}$ in this case.

5.7 Twist-induced Effects on Spatial Mode Properties

5.7.1 Spin- and OAM-dependent Effects

Apart from the large shift of the center of the modes induced by bending, we also observe several spin- and OAM-dependent splittings in the spatial properties of the modes,

summarized here for the Frenet-Serret waveguide: (1) For the multimode waveguide, the center of the LCP and RCP modes (evaluated on the T component of the Poynting vector) are split along the N direction as shown in Fig. 5.8(b). The splitting increases with twist rate and reaches 30 nm (about 1 % of the core diameter) for a twist rate of 20/mm. (2) In the single-mode case, such a splitting occurs for the transverse component of the Poynting vector $\mathbf{S}_{\mathrm{NB}}$ while a splitting cannot be observed in its longitudinal component. The splitting reaches 50 nm (12.5 % of the core diameter) for a twist rate of 20/mm as shown in Fig. 5.10(b). (3) For the OAM modes in the multimode variant, we observe that the difference between the intensity on the top and bottom side of the vortex depends on the sign of the total angular momentum. Bottom and top refers to the side facing towards and away from the twist axis, respectively as shown in Fig. 5.5(c,d).

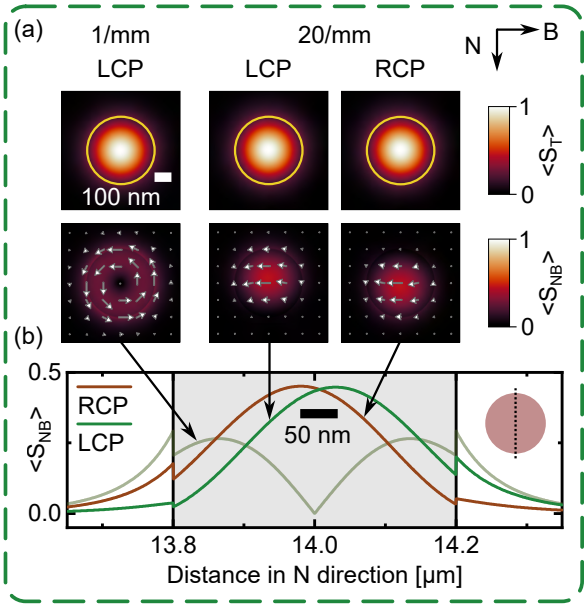

Figure 5.10: Spatial properties of modes in the single-mode Frenet-Serret waveguide. (a) Distribution of the longitudinal (T) and transverse (NB) component of the Poynting vector at low (1/mm) and high (20/mm) twist rates. The longitudinal component remains unchanged when the twist rate increases while the transverse component shifts in opposite directions along the N axis. (b) Line cut of S_{NB} along the N direction through the center of the waveguide. The splitting might be a consequence of the photonic spin Hall effect. Yellow circles in (a) highlight the cross section of the waveguides.

As a result, we hypothesize that these spin- and OAM-dependent splittings arise due to an interplay between the confinement provided by the waveguiding structure, and the photonic spin Hall [177, 174] and photonic orbital Hall [182, 183] effects. When light propagates along a curved trajectory that changes on lengthscales much larger than the wavelength, its movement can be characterized by equations of motion for the center of gravity of the mode. These equations contain a spin-orbit [177, 161] and an orbit-orbit [183] interaction term, that results in spatial splittings between modes with distinct total angular momenta as described in Section 2.4. In fact, these photonic spin Hall and orbital Hall effects are just another consequence of the spin-orbit and orbit-orbit interaction of light [161], which so accurately describes the circular birefringence of the helical waveguides (cf. Section 5.3.1). Therefore it is likely that these effects are at the origin of the observed spatial splitting, although they do not apply directly to modes confined in waveguides.

5.7.2 Transverse Components of the Poynting and Spin Vectors

At high twist rates (> 10/mm), the fundamental modes of all investigated waveguide types (single-mode and multimode) develop an increasingly large transverse component of the Poynting vector $\mathbf{S}_{\mathrm{NB}}$, shown exemplarily for the Frenet-Serret waveguide in Fig. 5.8(c) and Fig. 5.10(a). The direction of this additional component is along the negative B direction regardless of polarization. Similarly, the spin vector $\mathbf{s_E}$ of the electric field contains a transverse component along the B direction for high twist rates, pointing in opposite directions for the two spin states (Fig. 5.8(d)). The evolution of these properties at different twist rates can be found for all waveguide types in Appendix D. Transverse spin is well known to occur in evanescent waves where its direction is independent of polarization and led to applications involving spin-momentum locking [150, 302, 303]. The origin of transverse spin and momentum in helical waveguides remains to be studied.

5.7.3 Elliptically Polarized Eigenmodes and Superchiral Fields

Lastly, we want to point out an effect that becomes apparent when the cross section of the twisted single-mode waveguide is elliptical in the NB plane as it is the case for the helicoidal waveguide. As discussed, the interplay of the linear birefringence of the core and the circular birefringence caused by the twist results in elliptically polarized eigenmodes. Similar to a linearly polarized mode, the modal fields are enhanced in the direction of the long axis of the polarization ellipse. These locations differ for the electric and magnetic field as shown in Fig. 5.11(a). In this example, the magnetic field is enhanced at the top and bottom surface of the core, while the electric field is reduced. Combined with the fact that the fields are still circularly polarized to a sufficient degree, such a configuration is ideal for creating superchiral fields.

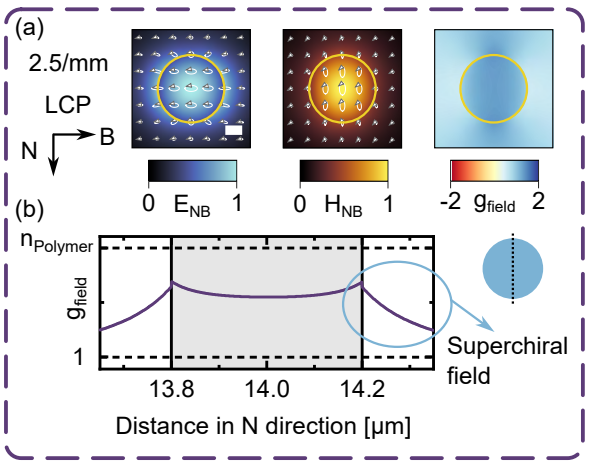

Figure 5.11: Spatial properties of modes in single-mode helicoidal waveguides. (a) The elliptically polarized eigenmodes of the helicoidal waveguide feature a reduced electric field on the top and bottom surface of the waveguide (left panel) while the magnetic field is enhanced (middle panel). This difference results in a superchiral field with g_{field} being larger than the refractive index on the outside of the core (right panel). (b) Line cut of g_{field} along the N direction through the center of the waveguide. Yellow circles in (a) highlight the cross section of the waveguides.

We quantify the superchirality in terms of the factor g_{field} (defined and explained in Section 2.2.5), with $|g_{\mathrm{field}}| > n$ indicating a superchiral field. In brief, g_{field} is the enhancement

factor of the molecular g-factor, which is typically measured in chiral sensing experiments. Here, we found an enhancement factor of ≈ 1.4 on the surface of the waveguide. Values of g_{field} for other twist rates can be found in Fig. D.4. We note that this value is lower than in the pioneering experiment for superchiral fields, where an enhancement of around 11 was measured [85, 121]. However, our enhancement occurs in a region of space where the field has an appreciable intensity while the pioneering experiment was carried out in the node of a standing wave where the intensity is low. Further research is required to optimize the superchirality in helical waveguides (e.g., by increasing both the twist rate and the linear birefringence), and to find a method to place molecules precisely in the regions of superchiral field.

5.8 Discussion

The numerical results for the effective index of all three multimode helical waveguides are in high agreement with the analytical prediction, underpinning the fact that the cause of the circular birefringence and OAM birefringence is a purely geometrical effect inherent to the helical path. As such, the phase difference between modes with different total angular momentum $\delta n_{\text{eff}}^{\text{Lab}} k_0 z$ does not depend on wavelength, material, and core size (cf. Eq. 5.6). Helical waveguides can therefore find applications as broadband spin- and OAM-preserving waveguides. More generally, any waveguide with nonzero torsion at each point of its trajectory will be able to preserve the angular momentum state of the light.

A typical example of a Frenet-Serret waveguide is a piece of fiber helically coiled around a cylinder, as it was used in the first experiments on helical waveguides [282, 117, 304, 289]. Helical waveguides can also be created by twisting a fiber with an off-axis core [109, 115]. Such fibers are fabricated by either spinning the preform while drawing the fiber or in a thermal post-processing step [106]. In this situation, it is conceivable that both helicoidal or Frenet-Serret type waveguides can in principle be created depending on the fabrication conditions. Since both types converge to the same shape at low twist rates, a difference would only be observable at high twist rates ($\alpha\rho \gg 1$) where fabrication inaccuracies might play an additional role. Finally, the Overfelt waveguide might be relevant for situations where a helical waveguide is constructed by extending a toroidal shape in the z direction or to describe Frenet-Serret waveguides at large twist rates.

All waveguides created with planar fabrication techniques on the other hand, necessarily have zero torsion and can therefore not exhibit circular or OAM birefringence based on geometric effects. Chip-integration of helical waveguides therefore requires three-dimensional fabrication techniques such as 3D nanoprinting. This technique can be used to realize all three discussed waveguide types and even provides the ability to freely choose the cross section within the NB plane. A first realization of a 3D-nanoprinted helical waveguide was reported in Ref. [102], albeit without providing a detailed study of the optical properties or the geometry. While the twist rate achievable in fibers is inherently limited by the properties of the glass, 3D nanoprinting can potentially realize higher twist rates with pitch distances down to the core diameter. With our simulations, we explored waveguides with

pitch distances as low as 14 times the core diameter, but even lower pitch distances seem theoretically feasible given the low bend loss in the multimode versions of the waveguides. The study on twisted light cages following in Chapter 6 showed that twist rates of 10/mm can be achieved experimentally, corresponding to $\alpha\rho = 0.9$ while a value of $\alpha\rho \approx 0.5$ was reported in Ref. [102]. Another technique that allows realizing helical waveguides on a chip is direct laser writing, where a small refractive index modification is created in glass by scanning of a focused femtosecond laser beam [305, 306, 307]. However, precise control over the cross section of the waveguide proved to be challenging due to aberrations of the focal spot inside the glass that need to be compensated [308, 309].

The study of the polarization properties of modes in helical waveguides revealed that the shape of the cross section in the NB plane strongly impacts their optical properties if the waveguides are single-mode. Any deviation from a circular cross section can induce linear birefringence, thus creating elliptically polarized eigenmodes. The simple analytical formula by Alexeyev and Yavorsky [122] is therefore not sufficient to describe the effective index in this specific case. Instead, a recently developed theoretical model for off-axis twisted waveguides with elliptical cross sections in the Frenet-Serret frame [103] could be applied to predict the birefringence and polarization of the helicoidal and Overfelt waveguide. This would require prior knowledge of the modes of an untwisted waveguide with the same elliptical cross section.

Elliptically polarized eigenmodes also occur in on-axis twisted waveguides with an elliptical cross section and were applied in creating ultranarrow (sub-megahertz) spectral dips in stimulated Brillouin scattering [310]. The authors used that the polarization state of elliptically polarized modes depends on the wavelength, which is another intriguing effect that is unique to twisted waveguides.

5.9 Conclusion

In summary, this theoretical study presented comprehensive insights into mode formation in three types of helical waveguides, named Frenet-Serret, helicoidal, and Overfelt waveguides. The comparison of numerical simulations and theoretical analysis revealed that the effective index of Frenet-Serret waveguides can be accurately described by an analytical formula by Alexeyev and Yavorsky [122] (Eq. 5.6) even if (1) the index contrast is large ($n = 1.54$ to air, $\Delta = 0.29$), (2) the mode is not entirely transversely polarized, (3) the mode profile changes from that of the untwisted waveguide, and (4) the twist rate approaches relatively high values. Furthermore, we discussed the propagation loss in helical waveguides, describing it as a sum of bend loss [291] and intrinsic loss. We also provided a novel derivation of an equation to transform the effective index from the helicoidal to the lab frame that is valid for both on- and off-axis twisted waveguides up to arbitrary twist rates, provided that the spatial properties of the modes fulfill certain conditions. It is worth noting that there are cases where it is not advisable to assign such a lab frame effective index, e.g., when the modes are elliptically polarized.

The wavefronts of the modes in the three types of helical waveguides were found to lie transverse to the tangent of the helix (i.e., in the NB plane), up to the highest investigated twist rates of 20/mm. While the Frenet-Serret waveguide maintains a circular cross section in the NB plane at all twist rates, the helicoidal and Overfelt waveguides can exhibit elliptical cross sections, leading to non-circular polarization if the core size is small. These elliptically polarized modes were found to generate superchiral fields on the surface of the waveguides. Lastly, the study explored spin- and OAM-dependent splittings in the spatial intensity distribution of the modes, showing potential links to the photonic spin Hall and orbital Hall effects.

While the investigated waveguide geometries were determined by the properties of the underlying coordinate systems, helical off-axis waveguides with arbitrary cross sections can be simulated with the technique described in this work. The larger parameter space can be used to precisely control the polarization states of the eigenmodes and optimize the generation of superchiral fields, which could lead to novel types of waveguide-based chiral sensing devices. In the past, helical waveguides were realized by twisting glass fibers since an implementation via planar fabrication techniques is not possible. Such helical waveguides were mostly used for their circular birefringence, which prevents linearly polarized light from becoming elliptically polarized in the presence of mechanical stress. This robustness against environmental fluctuations is employed in applications such as fiber optic current and magnetic field sensors based on the Faraday effect [311, 312, 304], or optical twist and tension sensors [117]. However, with the potential for modern on-chip integration through 3D nanoprinting [102, 66, 211] or direct laser writing [305, 306, 307], these waveguides hold promise for accessing new applications, including chiral spectroscopy, integrated Brillouin lasing for ultrahigh-resolution optical sensing [310], and OAM-maintaining transport of optical signals on a chip. On a fundamental level, exploring ultrahigh twist rates with pitch distances close to the diameter of the off-axis core may offer insights into complex physical effects such as strong spin-orbit and orbit-orbit interactions.

Chapter 6

Twisted Light Cages

The results presented in this chapter will soon be submitted for publication in a peer-reviewed journal. Figures and text passages will appear in similar or identical form in this publication.

With the working principle of light cages explained in Section 4.2 and the foundations of twisted waveguides detailed in Chapter 5, this section presents theoretical and experimental results on twisted light cages - the culmination of this thesis.

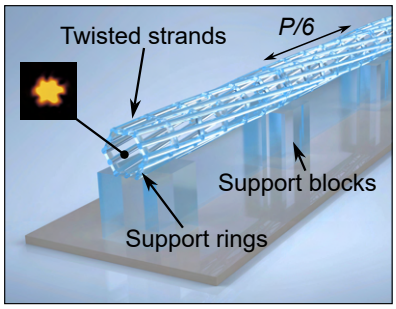

Figure 6.1: Illustration of a twisted light cage. P: helical pitch distance. Inset: CCD image of the core mode at $\lambda = 600$ nm.

Twisted light cages are on-axis twisted waveguides and differ in two key points from the off-axis twisted solid-core waveguides presented earlier:

1. Light cages are hollow-core waveguides and host lossy higher-order modes. At first, this might seem a disadvantage compared to the low loss of high-contrast solid-core waveguides. However, the absence of loss also excludes the presence of circular dichroism, i.e., a difference in loss between the LCP and RCP mode. Twisted light cages, on the other hand, were found to possess strong circular dichroism by chirally selective coupling of the fundamental core mode with a lossy higher-order core mode.

2. As explained in Chapter 4, light is guided inside the hollow core with only a very small fraction of optical power being present inside the (potentially absorbing) material of the waveguide. This allows high-power applications and access to wavelength ranges where a material platform is considered too lossy for solid-core guidance, e.g., in the technically relevant extreme ultraviolet (XUV) range [313].

Previous works on twisted waveguides (see Table C.1 for an overview) almost exclusively concern fibers (i.e., waveguides drawn from a glass preform). Here, the highest values of circular dichroism are found in **chiral fiber gratings**, i.e., on-axis twisted solid-core fibers with a non-circular cross section [91, 92, 95, 96, 97] reaching values of up to 3 dB/mm [92]. Loss in these fibers stems from the coupling of the core mode to lossy cladding modes. Due to the simple geometry of these fibers (a single core embedded in a homogeneous cladding), very high twist rates can be achieved, typically implemented by spinning the fiber in a thermal post-processing step. The highest reported twist rate corresponds to a helical pitch distance of 24 µm [91].

However, based on the advantages of hollow-core fibers outlined above in point 2, ways were sought to fabricate twisted fibers with more complex geometries. Using thermal post-processing or spinning of the preform during fiber drawing, several variants of **twisted photonic crystal fibers (PCF)** were demonstrated, albeit usually with solid cores and without analyzing their circular dichroism [93, 94, 99, 110, 105, 106, 107, 114, 111]. A notable exception is a study by Roth et al. from 2018, which reported a twisted hollow-core PCF reaching a circular dichroism of 8.3 db/m [119]. However, twisting the more complex PCF geometries proved to be challenging and achievable twist rates are limited to about 340 µm (reported in Ref. [98]).

We show that this limitation in twist rate can be overcome by using 3D nanoprinting and present the first comprehensive study on twisted hollow-core waveguides fabricated by this method, attaining pitch distances down to 88 µm. (One similar work exists where a 3D-nanoprinted twisted coreless PCF segment was demonstrated (pitch distance: 200 µm) but optical properties were not analyzed beyond imaging the intensity distribution of the mode [101].) The measured circular dichroism in **twisted light cages** reached values of up to 0.8 dB/mm - a significant improvement over the twisted hollow-core PCF of Ref. [119], albeit at the expense of an overall higher propagation loss.

As explained in Chapter 4, a further drawback of the fiber-based twisted waveguides is the lack of methods for automated large-scale **chip integration**, therefore restricting their potential use cases. Twisted light cages, on the other hand, can be fabricated directly on an existing photonic chip adding functionalities such as circular polarization filtering or OAM conversion. Furthermore, applications in chiral spectroscopy or as microscopic twist- and tension sensor can be foreseen.

6.1 Geometry and Fabrication

Fabrication via 3D nanoprinting allows the twist to be implemented already in the design step, i.e., in the computer-aided design (CAD) file that is processed by the printer. Therefore no additional processing steps are required compared to untwisted waveguides (these steps are described in Section 3.2). 5 mm long light cages with four different twist rates ranging from 0/mm to 11.4/mm were realized in this way. The fabrication parameters are listed below in Table 6.1 while SEM and photographic images of the waveguides are shown in Fig. 6.2(a,b).

Table 6.1: Parameters for fabrication of twisted light cages.

Parameter	Value
Slicing distance	200 nm
Hatching distance	100 nm
Acceleration of galvanometric mirror	3 V/ms^2
Scanning speed	15,000 µm/s
Laser power	29 mW (setting in Describe: 58%)

The fabricated waveguides are referred to as **multimode strand light cages** in the following to emphasize, that resonances between the core and strand modes can be observed in their transmission spectra (which were investigated for untwisted light cages in Section 4.2.4). As explained in the next section, twisting the waveguide induces additional resonances between two core modes. To better investigate the origin of these resonances, most simulations were performed for twisted light cages with single-mode strands (single-mode strand diameter: $2r_c = 0.4$ µm, multimode strand diameter: $2r_c = 3.6$ µm). For these **single-mode strand light cages**, the strand mode does not have a cut-off such that no core-strand resonances are present at the investigated wavelength of λ=770 nm

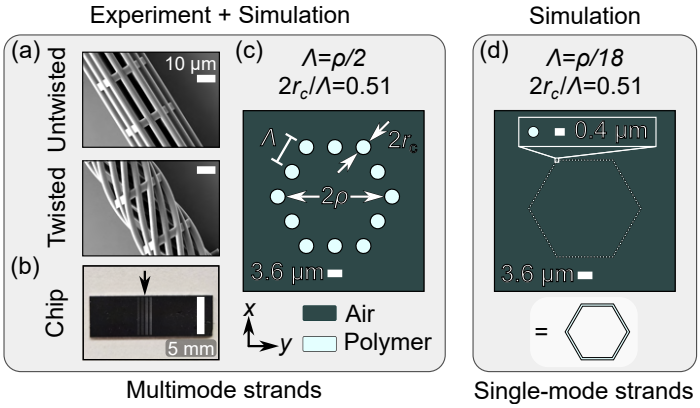

Figure 6.2: Geometry of twisted light cages. (a) SEM images of fabricated structures viewed from the top. (b) Photographic image of a twisted light cage sample fabricated on a Si-chip via 3D nanoprinting (arrow indicates position of the waveguides). (c) Cross-sectional geometry of the multimode strand light cage including the relevant parameters (lateral pitch distance $\Lambda = 7$ µm, strand offset $\rho = 14$ µm, and strand diameter $2r_c = 3.6$ µm). (d) Single-mode strand light cages (used in simulations only) feature a smaller strand diameter of $2r_c = 0.4$ µm, which prevents any resonances between core and strand modes. For better readability, the sketch at the bottom of (d) is used throughout the chapter to refer to this geometry. Both geometries feature the same values of ρ and $2r_c/\Lambda$ but differ in the number of strands (12 for the multimode strand variant, 108 for the single-mode strand variant).

(see Fig. 6.3). To compensate for the smaller strand diameter, the number of strands was increased from 12 to 108, such that the ratio of strand diameter to lateral pitch distance[1] $2r_c/\Lambda$ remains the same (see Fig. 6.2(d)). This ensures that both variants feature a comparable propagation loss as the fraction of open space between the strands is identical (see Fig. 6.3). Note that all simulations concern left-handed waveguides with the strand diameters stated above, except when comparing the results to the experimental data presented in Section 6.6.

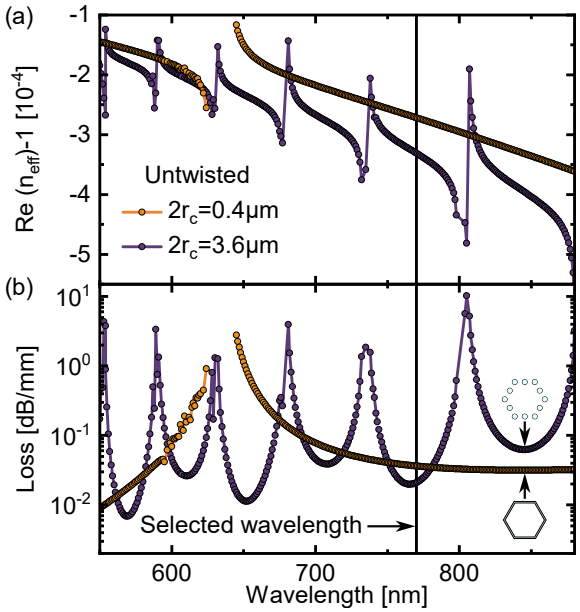

Figure 6.3: Comparison between multimode and single-mode strand light cages. Spectral distribution of the real part of the effective index (a) and attenuation (b) of the fundamental mode of the untwisted waveguides. The single-mode strand light cage (orange) does not feature any core-strand resonances for wavelengths larger than 650 nm. Subsequent simulations use a wavelength of 770 nm, which is located in a transmission band of the multimode strand light cage (purple). Insets in (b) depict the geometries (individual strands are not shown for the single-mode strand geometry to improve readability).

Regarding the specific **geometry**, twisted light cages are on-axis twisted waveguides, i.e., the hollow light-guiding core is centered on the twist axis. The polymer strands that form the cladding, on the other hand, are off-axis twisted waveguides providing a link to the results obtained in Chapter 5. Of the three analyzed off-axis twisted waveguide geometries, the Frenet-Serret type seems the best choice at first. This would ensure that the cross section of the strand modes is circular in the plane perpendicular to their propagation direction (i.e., the tangent of the helical path). However, we chose the strands to be of the helicoidal type, meaning that their cross section is defined to be circular in the xy plane (see Fig. 6.2(c)). Two thoughts guided this choice:

1. 3D nanoprinting of a geometry containing several circles in the xy plane is most robust against fabrication inaccuracies as the printer operates on a Cartesian grid (i.e., the variation of the cross section between individual strands is minimal). Implementing strands of the Frenet-Serret type would require the cross sections to be elliptical

[1]The ratio $2r_c/\Lambda$ (usually referred to as d/Λ) is an important structural parameter in PCFs since it remains constant during the fiber drawing process (it is the same in the preform as in the finished fiber). More importantly, the parameter has been shown to determine the maximal number of modes present in a solid-core PCF [314].

in the xy plane, be tilted with respect to each other, and feature a twist-rate dependent ellipticity (cf. Table 5.1). Keeping in mind that the shape of the 3D-nanoprinted voxel is also elliptical[2], it is more challenging to ensure that all strands have identical properties with this geometry - an open task for future works.

2. Fabricated samples feature strand diameters corresponding closely to the multimode strands analyzed in Section 5.4.1. In this case, the difference in optical properties between the helicoidal and Frenet-Serret waveguides was found to be minimal.

6.2 Origin of Circular Dichroism

The untwisted single-mode strand light cage does not allow resonances between the core and strands to form. Yet, when twisting the structure and simulating the optical properties at a fixed wavelength, resonances appear at certain twist rates as shown in Fig. 6.4(a,b). Some of these resonances are **achiral resonances**, i.e., they affect the RCP and LCP fundamental mode in the same way. Others are **chiral resonances** such that only one of the two modes features an increased loss while the mode of the opposite handedness is unaffected, thus giving rise to circular dichroism.

By analyzing the real part of the effective index we find that the resonances are caused by coupling of the fundamental core mode with a lossy higher-order core mode and occur whenever:

1. The effective refractive indices $n_{\mathrm{eff}}^{\mathrm{Helical}}$ of the two modes match.

2. The total angular momentum j of the modes differs by an integer multiple of n, where n is the order of the rotational symmetry of the waveguide cross section C_{nz} ($n = 6$ for light cages).

To note here is that the analysis is performed in the helicoidal coordinate frame. The strong splitting in $n_{\mathrm{eff}}^{\mathrm{Helical}}$ between modes of the same OAM order $|l|$ is therefore not a physical effect but merely caused by the rotation of this coordinate frame relative to the lab frame (see Ref. [104] and Appendix B). The splitting that remains when transforming the results to the lab frame is about three orders of magnitude smaller as shown later in Section 6.4. When neglecting these marginal deviations (i.e., assuming that the effective index evaluated in the lab frame does not depend on twist rate), Eq. B.16 can be used to describe the index of the modes in the twisted frame:

$$n_{\mathrm{eff}}^{\mathrm{Helical}} \approx n_{\mathrm{eff}}^{l,m}\Big|_{\alpha=0} - (s+l)\frac{\alpha\lambda}{2\pi}, \tag{6.1}$$

where $n_{\mathrm{eff}}^{l,m}\Big|_{\alpha=0}$ is the effective index of a mode with azimuthal order l and radial order m in the straight waveguide. Eq. 6.1 is shown as gray dashed line in Fig. 6.4(a) and allows to predict the twist rates (or wavelengths) at which the indices of two modes intersect based

[2] A voxel is the volume polymerized by a point exposure (cf. Section 3.2). In the xy plane it has an elliptical cross section with the half-axes aligned along the x and y axis.

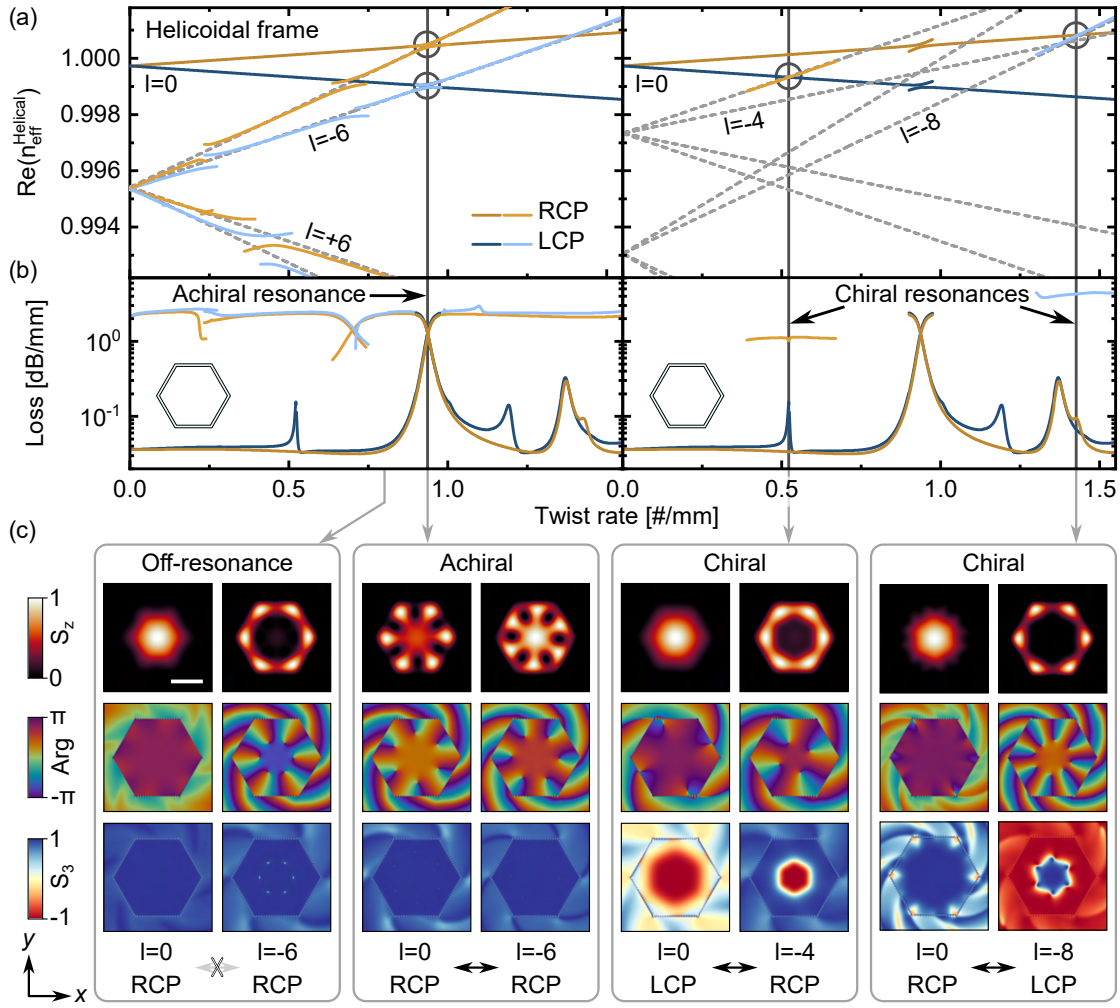

Figure 6.4: Theory of twist induced resonances in single-mode strand light cages. (a) The real part of the effective index of the fundamental core modes ($l = 0$) intersects with that of higher-order core modes ($l \neq 0$) at certain twist rates. Coupling occurs if the difference in total angular momentum between the modes $\Delta j = \Delta s + \Delta l$ is equal to $6q$, $q \in \mathbb{Z}$. The first achiral resonance ($\Delta s = 0$, $\Delta l = 6$) is shown on the left panel, while the right panel depicts the modes involved in the first chiral LCP resonance ($\Delta s = +2$, $\Delta l = 4$), and first chiral RCP resonance ($\Delta s = -2$, $\Delta l = 8$). The analysis is performed in the helicoidal frame which causes a splitting between modes along the gray dashed lines given by Eq. 6.1. The results for the fundamental modes are identical in the right and left panel of (a,b). Curves for the higher-order modes in (b) are only shown near the resonance to improve clarity. (c) Distributions of Poynting vector S_z, phase of E_x, and third component of Stokes vector S_3 for four pairs of the fundamental mode and the relevant higher-order mode at twist rates indicated by the gray arrows. At chiral resonances, the spin state of the oppositely polarized modes mixes to allow coupling (four panels in bottom right corner). As a side note, the spiraling features in the phase patterns are explained in Appendix E.1. The wavelength is 770 nm and scale bar in (c) denotes 10 µm. The two remaining resonances between twist rates of 1 - 1.5/mm are analyzed in Fig. E.2.

purely on the knowledge of the modes in the untwisted waveguide. Therefore, resonances between the fundamental modes ($l = 0$, $s = \pm 1$, $m = 1$, $j = l + s$) and higher-order modes ($\tilde{l}$, $\tilde{s}$, $\tilde{m}$, $\tilde{j}$) can be calculated by the two conditions:

$$\alpha\,\Delta j = k_0(n_{\mathrm{eff}}^{0,1} - n_{\mathrm{eff}}^{\tilde{l},\tilde{m}}), \tag{6.2a}$$

$$\Delta j = 6q \text{ for } q \in \mathbb{Z}, \tag{6.2b}$$

where $\Delta j = j - \tilde{j}$ is the difference in total angular momentum between the modes. Note that the right-hand side of the Eq. 6.2a is always positive, which imposes a condition on the sign of q. For left-handed waveguides α and q are positive, such that the resonances are caused by higher-order modes with $\tilde{j} < 0$.

Eq. 6.2a effectively describes a **diffraction grating** as used in the context of fiber gratings [315]. This is to be expected since twisting introduces a periodic modulation along the propagation direction, thus acting as a grating. The left side of the equation is the grating wavevector for a period length $P/6$ and diffraction order q, and the right side describes the wavevector mismatch between the modes (see Fig. 6.5). This **transfer of linear momentum** can occur both in twisted waveguides and untwisted waveguides with a periodic index modulation. Eq. 6.2b, on the other hand, describes a **transfer of angular momentum** mediated by the twisted structure, which does not occur in untwisted waveguides.

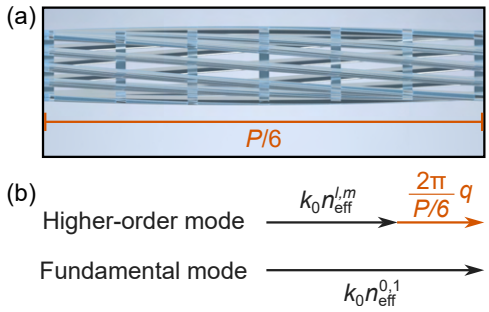

Figure 6.5: Interpretation of twisted waveguides as gratings. (a) Side view of a twisted light cage with 6-fold rotational symmetry. Its cross section repeats after a distance $P/6$ although each individual strand features a helical pitch distance P. (b) Wavevectors involved in coupling of two core modes. The grating vector of the twisted waveguide (orange) mediates the phase matching. Note that the spin- and OAM-selectivity is hidden in the order q, as the grating can only couple modes with $\Delta j = 6q$.

The origin of the **selection rule** $\Delta j = 6q$ (Eq. 6.2b) can be understood based on the symmetry of the modes of the untwisted waveguide [104]. For circularly symmetric systems (e.g., round step-index fibers), modes are eigenstates of the angular momentum operator with the eigenvalue j being an integer. However, the rotational invariance is broken in light cages due to their hexagonal cross section. In general, a lower C_{nz} rotational symmetry implies that modes need to be constructed as a superposition of eigenstates of the angular momentum operator with integer eigenvalues $j_0 + nq \;\forall\; q \in \mathbb{Z}$ [104]. These angular momentum harmonics therefore allow a mode with a certain dominant angular momentum j_0 (in previous equations simply referred to as j) to couple to all modes with a dominant angular momentum of $j_0 + nq$. Without these harmonics, such a coupling would

not be possible because the eigenstates of the angular momentum operator are mutually orthogonal. To further corroborate this argument, the fundamental mode of the light cage will be decomposed into its OAM eigenstates in Section 6.3.

With this model in place, we can answer the question why some of the twist-induced resonances are achiral and others are chiral. The required condition $\Delta j = \Delta s + \Delta l = 6q$ can be achieved in two ways. For $\Delta s = 0$, $\Delta l = 6q$, both the LCP and RCP fundamental mode couple to the corresponding higher-order modes with $\tilde{l} = -6q$ at the same twist rate, thus resulting in an achiral resonance. When a fundamental mode couples to a higher-order mode of opposite spin ($\Delta s = -2$, $\Delta l = 6q + 2$ or $\Delta s = +2$, $\Delta l = 6q - 2$), the resonances of the LCP and RCP fundamental mode occur at different twist rates resulting in chiral resonances (see Fig. 6.4(a)).

One might now ask, why modes of different spin angular momentum s are allowed to couple as these states are mutually orthogonal in free space. This can be resolved when noting that each eigenstate of the angular momentum operator with eigenvalue j does not necessarily contain just one spin state. In fact, even in round step-index fibers, the fundamental $\mathrm{HE}_{1,1}$ mode with angular momentum $j = 1$ is a superposition of three states: a dominant contribution with $s = 1$ and OAM $l = 0$, and two minor contributions[3] with ($s = -1$, $l = 2$) and ($s = 0$, $l = 1$) [316]. The letters s and l used throughout the manuscript refer to the dominant contribution, while the weaker contributions enable the coupling between modes carrying different labels s. Near chiral resonances, hybrid modes containing both spin states form as shown in the lower row of Fig. 6.4(c).

The coupling conditions Eqs. 6.2a and 6.2b have first been derived for $q = 1$ in the context of chiral fiber gratings (i.e., on-axis twisted solid-core fibers) using first-order perturbation theory [292, 123]. While our derivation can successfully predict the spectral locations of twist-induced resonances, a perturbative approach would give access to additional details like the hybridization of modes and the formation of anti-crossings in the real part of the effective index. To our knowledge, Eqs. 6.2a and 6.2b have not yet been derived in the context of higher-order perturbation theory (i.e., for arbitrary values of q) for on-axis twisted waveguides. Nevertheless, a conceptual outline for the use of higher-order perturbation theory was developed for off-axis twisted waveguides [122]. As an alternative, the details of mode coupling in twisted waveguides could potentially be analyzed using coupled mode theory, which was introduced for straight waveguides in Section 2.1.3. However, the stated mode coupling equations in Cartesian coordinates (Eq. 2.14) are not directly applicable to twisted waveguides, as the differential operators take on a different form in helicoidal coordinates since the system is not orthogonal [173], which complicates the derivation. An attempt without taking these changes into account can be found in Ref. [317] but is likely only applicable at low twist rates. Lastly, we note that Eqs. 6.2a and 6.2b have previously been validated for resonances occurring in on-axis twisted PCFs, that are caused by a coupling between core and cladding modes [318]. Our work additionally demonstrates the applicability to resonances caused by coupling between two core modes.

[3] The contribution with $s = 0$ arises from the field component along the longitudinal direction.

6.3 Angular Momentum Selection Rule

As stated in the previous section, modes in light cages contain angular momentum harmonics of the form $j_0 + 6q \; \forall \; q \in \mathbb{Z}$, where j_0 is the dominant angular momentum [104]. To confirm this theoretical statement, we analyze the **OAM distribution** of the RCP fundamental mode of an untwisted light cage with $j_0 = -1$. To this end, the mode is decomposed into Bessel beams of radial order p and azimuthal order l, where l corresponds to the (integer) OAM order of the Bessel beam as explained in Section 2.2.2. Some relevant Bessel beam basis functions are shown in Fig. 6.6(a). The result of this analysis is a probability distribution $|a_{l,p}|^2$, that - when summed over the radial order p - denotes the probability for finding a photon with angular momentum l in the analyzed mode of the light cage. This distribution is expected to contain OAM harmonics of the form $l = 6q$ with $s = -1$, and $l = 6q-2$ with an opposite spin $s = +1$. While polarization was not analyzed here, the distribution of OAM harmonics shown in Fig. 6.6(d) matches this expected pattern. Furthermore, the decomposition shows that contributions with $l = 6q - 2$ feature relatively weak amplitudes explaining why the **coupling strength** in chiral resonances is lower than in achiral resonances. Looking at the effective modal index shown in Fig. 6.4, it is clear that chiral resonances arise from weak coupling (on resonance the real part of the two modes is identical while there is a gap in the loss), while modes are strongly coupled in achiral resonances (on resonance, a gap opens in the real part of the effective index while the loss is identical for both modes). Weak and strong coupling are differentiated based on whether the coupling strength is smaller or larger than the losses, respectively, as described in Section 2.1.3.

Convergence of the decomposition was checked by computing the sum of all probabilities, yielding $\sum_l \sum_p |a_{l,p}|^2 = 1 - 3.5 \times 10^{-5}$. The maximal order of p was chosen such that any further rise in p would increase the sum of probabilities by about the same amount as a further rise in the maximal value of $|l|$ (see Fig. 6.6(c,d)). A further choice that has to be made is the value of R_0, which is the radius of the circle, on which the Bessel functions are defined. Changing R_0 mostly changes the amplitude distribution among the different radial orders p but has little impact on the OAM distribution $\sum_p |a_{l,p}|^2$. To minimize the impact of this ambiguous choice, all further OAM decompositions are performed for 10 different values of R_0 ranging from 13 to 16 µm. The resulting standard deviations are shown as error bars in Fig. 6.7 and indicate an increasing error for larger values of $|l|$.

The - now verified - angular momentum selection rule (Eq. 6.2b) provides a direct link between the **rotational symmetry of the waveguide** and the number of allowed resonances. To emphasize this point, additional simulations were performed for a geometry where the 108 strands of the single-mode light cage are arranged in a circle instead of a hexagon, resulting in a C_{108z} rotational symmetry. Indeed, the OAM decomposition of the fundamental LCP and RCP modes shown in Fig. 6.7(b) indicates that the first OAM harmonics occur only for $|l| = 108$ and $|l| = 108 \pm 2$ (for the respective contributions of opposite spin). The lower number of OAM harmonics in the untwisted structure directly translates into a reduction in the number of twist-induced resonances. In fact, resonances are completely absent for the round structure in the range of investigated twist rates of

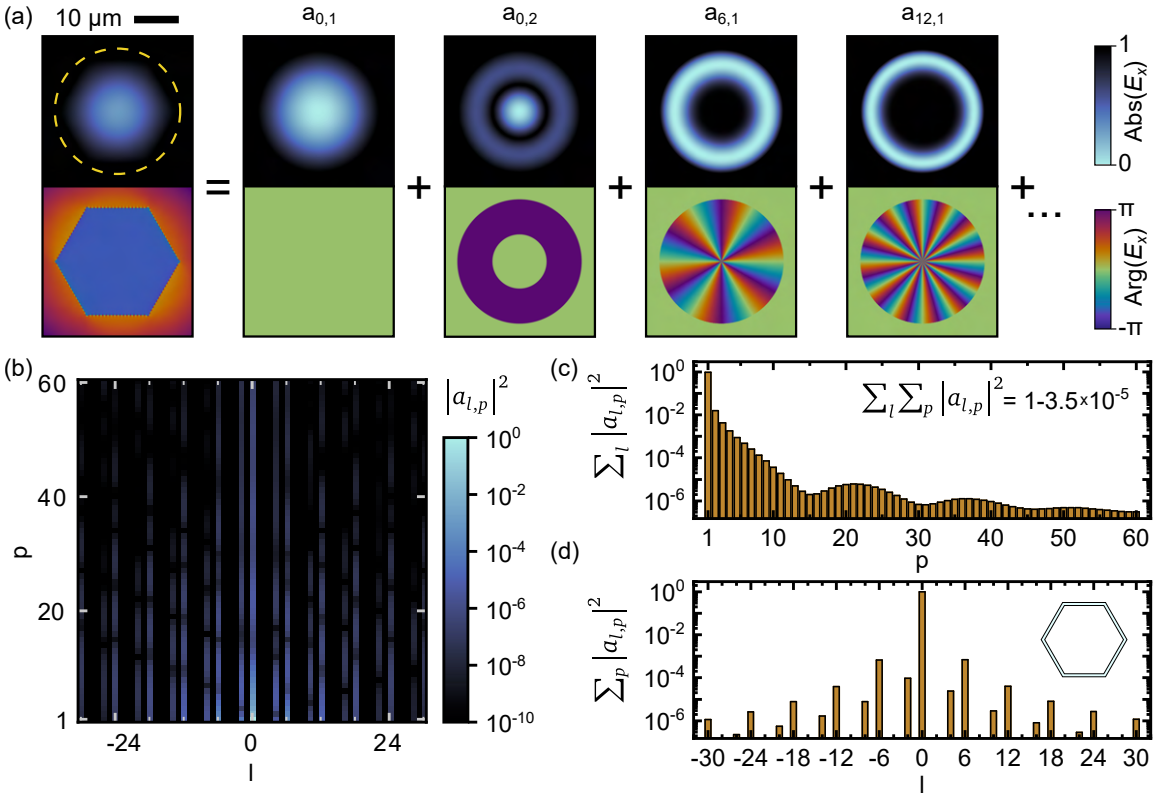

Figure 6.6: Decomposition of a mode into Bessel beams for analyzing its OAM content. (a) The electric field E_x of the RCP fundamental mode of an untwisted single-mode strand light cage (left panel) can be decomposed into a series of Bessel beams Ψ_{lp} with amplitudes $a_{l,p}$ according to Eq. 2.32 (right panels). Ψ_{lp} is defined within a circle of radius R_0 (yellow dashed line) with values on the boundary being 0. Field values outside of this circle are not analyzed. (b) Distribution of $|a_{l,p}|^2$ up to $|l| = 30$ and $p = 60$ for the mode shown in (a). (c,d) Summing $|a_{l,p}|^2$ over l or p shows the convergence of the decomposition procedure. The sum over all squared amplitudes is close to 1 indicating a good fit (c).

0-3.5/mm (see Fig. 6.8(c)). Next, we analyzed the **effect of twisting on the OAM distribution** (so far only untwisted waveguides were discussed). For left-handed twisted waveguides, the amplitudes of the negative OAM orders increase, both for the hexagonal and round light cage (see lower row in Fig. 6.7(b)). Calculating the average OAM of the RCP modes based on the OAM distribution yields $\bar{l} = -1.9 \times 10^{-6}$ for the untwisted hexagonal light cage and $\bar{l} = -3.6 \times 10^{-4}$ for a twist rate of 3.5/mm. A possible explanation for this relatively small effect might lie in modal hybridization. As previously discussed and shown in Fig. 6.4, only modes with negative OAM are able to couple to the fundamental mode for left-handed twist, while the index difference to the modes with positive OAM increases. Therefore, even away from resonances, the fundamental mode will always be - to a small extent - hybridized with modes carrying negative OAM, thus explaining the shift of the OAM distribution.

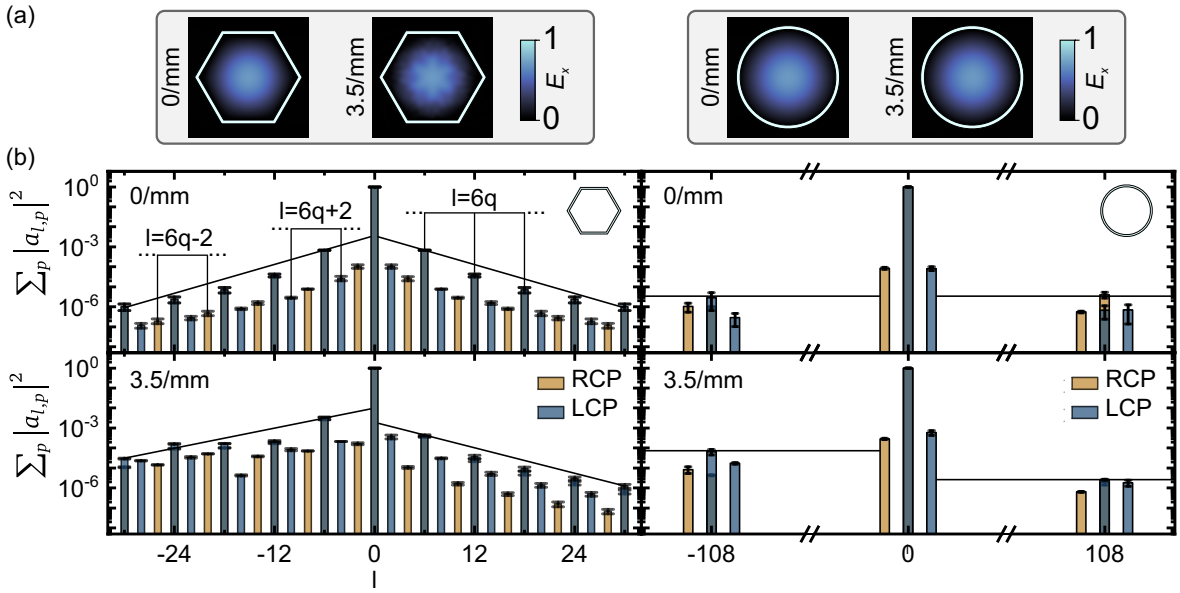

Figure 6.7: OAM decomposition of modes in a hexagonal (left panels) and a round (right panels) single-mode strand light cage. (a) Electric field of fundamental RCP modes at the indicated twist rates. Light blue lines denote the geometries, both including 108 strands (strands are not shown individually for readability). (b) OAM decomposition for the RCP (brown) and LCP (blue) fundamental modes. Both LCP and RCP modes contain dominant OAM contributions equal to integer multiples q of 6 (hexagonal geometry, left panels) or 108 (round geometry, right panels). Overlapping bars from RCP and LCP modes result in gray color. Smaller contributions of $l = 6q \pm 2$ are also present, which are likely of the opposite polarization, such that $j = 6q$ in all cases. Twisting shifts the average of the OAM distribution towards negative values for a left-handed twist (lower panels in b).

6.4 Origin of Circular Birefringence

Apart from circular dichroism, on-axis twisted waveguides are known to be circularly birefringent, although typically weaker than the previously discussed off-axis twisted waveguides (cf. Section 5.4.1). To **evaluate the measurable circular birefringence**, the real part of the effective index is transformed back to the laboratory frame by Eq. B.16 using the dominant values of s and l. As the amplitudes of the OAM harmonics are several orders of magnitude smaller, they can be neglected in this transformation. Circular birefringence B_C is then calculated as the difference in effective index $n_{\mathrm{eff}}^{\mathrm{Lab}}$ between the LCP and RCP mode. B_C increases from 0 in the untwisted waveguide to 7.5×10^{-6} at a twist rate of 3.5/mm (Fig. 6.8). This value is similar to circular birefringence in commercially available spun optical fibers [112] and is therefore sufficient to ensure robust propagation of circularly polarized light. The polarization direction of linearly polarized light would be rotated by an angle $\theta = B_C\, \pi z/\lambda \approx 9°$ for a waveguide length of $z = 5$ mm.

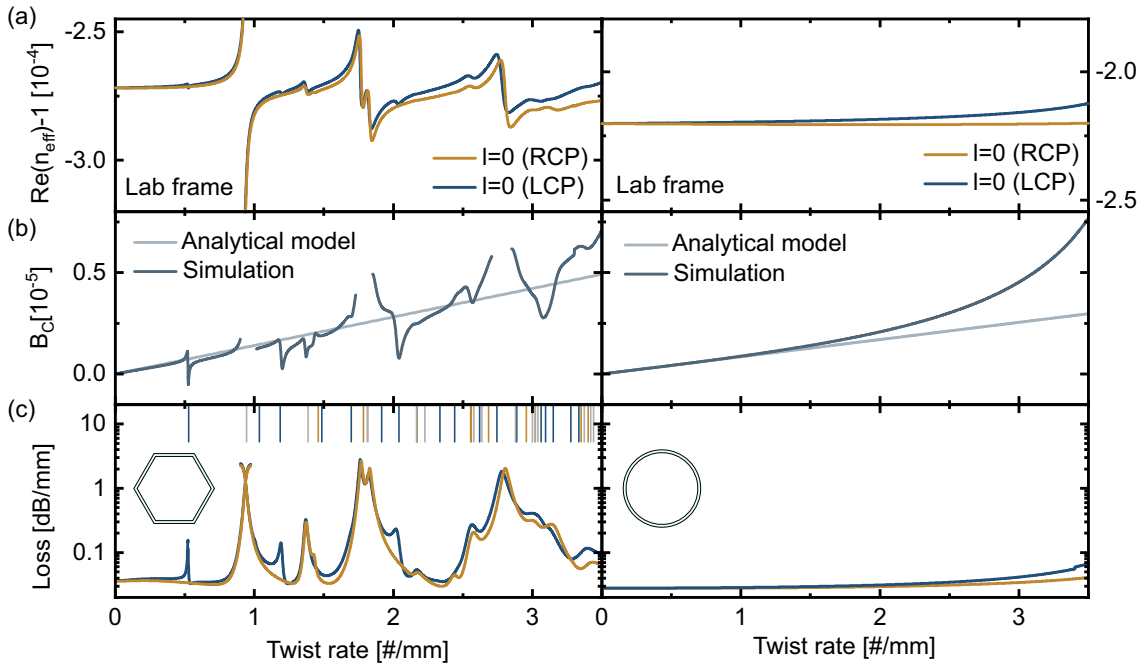

Figure 6.8: Optical properties of twisted single-mode strand light cages in the lab frame. Left panels show the hexagonal, right panels the round geometry. (a) Real part of the effective index of the RCP and LCP fundamental mode. (b) Circular birefringence (i.e., difference between the effective index of the LCP and RCP mode). Light gray line is an analytical prediction based on the properties of the untwisted waveguide (Eq. 6.3). (c) Attenuation of the fundamental core modes. Vertical lines are predictions for the resonances according to Eq. 6.6 (blue: LCP, brown: RCP, gray: LCP and RCP). Insets in (c) depict the geometries.

The **physical origin of circular birefringence** in on-axis twisted waveguides is again related to the angular momentum of the modes. It turns out that even in an untwisted waveguide the angular momentum distribution is not symmetric if the rotational invariance is broken, i.e., the amplitudes of the contributions with $j_0 + 6q$ are different from those with $j_0 - 6q$ [104]. Using a perturbative approach, this small asymmetry has been shown to be the cause of circular birefringence in on-axis twisted waveguides [99, 104]:

$$\boxed{B_C = \alpha(\langle j \rangle - j_0)\frac{\lambda}{\pi},} \tag{6.3}$$

where $\langle j \rangle$ denotes the angular momentum flux of the RCP mode in the untwisted waveguide and is calculated as the sum of spin angular momentum flux $\langle s \rangle$ and orbital angular momentum flux $\langle l \rangle$ defined in Eq. 2.36. For the RCP mode in the hexagonal light cage, $\langle s \rangle = -0.99947$, $\langle l \rangle = 3.8 \times 10^{-4}$, and $\langle j \rangle = -0.99909 = j_0 + 9.1 \times 10^{-4}$. We note that the value of $\langle l \rangle$ differs from the average $\bar{l}$ obtained in the OAM decomposition. This discrepancy likely arises because in the OAM decomposition, only the electric field component E_x was

analyzed while the calculation of $\langle l \rangle$ involves all transverse electric and magnetic field components. Nevertheless, both $\bar{l}$ and $\langle l \rangle$ decrease with increasing twist rate confirming the earlier result.

The outcome of Eq. 6.3 is shown as gray line in Fig. 6.8(b) matching well with the simulated values in the absence of resonances. Circular birefringence is found to be lower in the round light cage than in the hexagonal version because the C_{108z} symmetry of the round light cage is close to complete rotational invariance where B_C would be 0. For OAM modes, the circular birefringence is about one order of magnitude larger than for the fundamental modes and a description via Eq. 6.3 is less reliable due to the large number of resonances (see Fig. 6.9).

Interestingly, any intersections in the effective indices of the fundamental modes and the OAM modes are absent after the results are transformed to the **lab frame** using Eq. B.16 (see Fig. 6.9(a)). This is to be expected since only the index of the dominant angular momentum contribution was transformed, while the coupling is provided by the angular momentum harmonics. As these harmonics feature a different angular momentum of $j_0 + 6q$, their index is transformed differently by Eq. B.16 which would result in the expected intersections with the dominant contribution of the other mode. Therefore, it is generally best to describe on-axis twisted waveguides in the helicoidal frame where all angular momentum harmonics feature the same effective index.

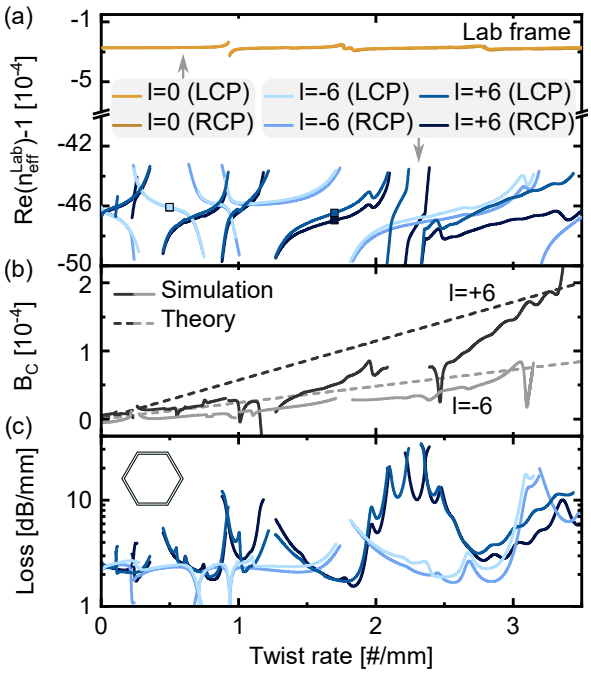

Figure 6.9: Optical properties of OAM modes with $|l| = 6$ in twisted single-mode strand light cages in the lab frame. (a) Real part of the effective index of the OAM and fundamental modes. (b) Circular birefringence including analytical prediction of Eq. 6.3 (gray dashed lines). Since the formula is not valid near resonances, the fields have been evaluated at the twist rates indicated in (a) by the small square boxes. (c) Attenuation of the OAM modes.

6.5 Resonance Prediction Based on Tube Model

Eqs. 6.2a and 6.2b allow to predict twist-induced resonance based on the effective indices of the higher-order modes in the untwisted waveguide. While these can be obtained from simulations, it is insightful to apply a recently reported model for tube-type hollow-core

fibers [212], which allows to calculate the indices of higher-order modes based on the dispersion of the fundamental mode.

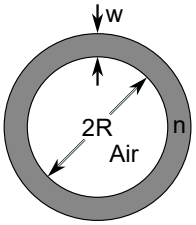

Figure 6.10: Geometry of the tube waveguide model of Ref. [212]. The model applies to waveguides where the cross section is a ring with inner radius R, thickness w, and refractive index n.

The model approximates the cladding surface to be locally flat[4], which is a good approximation if $R \gg \lambda$. If the core is filled with air, the effective index of its modes can be described as [212]:

$$n_{\text{eff}}^{l,m} = 1 - \frac{u_{l,m}^2}{2}(k_0 R)^{-2} - \frac{u_{l,m}^2}{2}\frac{n^2+1}{\sqrt{n^2-1}}(k_0 R)^{-3}\cot\left(k_0 w\sqrt{n^2-1}\right) + \mathcal{O}\left((k_0 R)^{-4}\right), \tag{6.4}$$

where $u_{l,m}$ is the m$^{\text{th}}$ root of the l$^{\text{th}}$ order Bessel function of the first kind. $l = ..., -1, 0, 1, ...$ and $m = 1, 2, ...$ refer to the azimuthal and radial order of the modes, respectively, akin to the definition of LP modes. HE and EH vector modes are grouped together in this equation by neglecting contributions of $\mathcal{O}\left((k_0 R)^4\right)$. The equation also holds for TE and TM modes if the refractive index contrast is low ($n \approx 1$). Since the following analysis is based on modes with $|l| \neq 1$, TE and TM modes can be neglected entirely.

The model is verified using the fundamental modes of the multimode and single-mode strand light cage. As shown in Fig. 6.11, the model is in good agreement with the simulated effective index with small deviations occurring around the resonances. The fitted

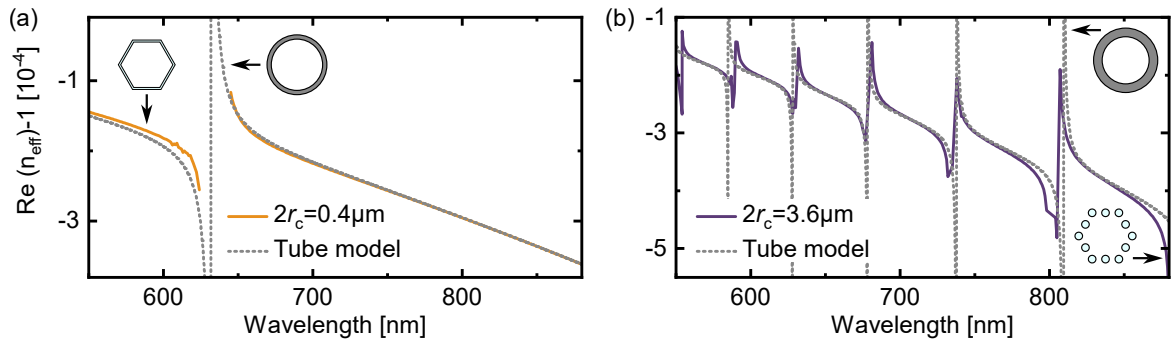

Figure 6.11: Application of the tube waveguide model [212] to light cages. The model (gray dotted line) accurately describes the dispersion of untwisted light cages with single-mode strands of diameter $2r_c$ of 0.4 µm (a) and multimode strands of diameter 3.6 µm (b). The fitted parameters were: $R = 12.37$ µm; $w = 0.267$ µm for (a), and $R = 11.5$ µm; $w = 3.448$ µm for (b).

[4]The model is similar to the one used for microgap waveguides in Section 4.1.1.

parameters R and w are remarkably close to the hexagon radius $\rho = 14$ µm and strand diameter $2r_c$ of the light cage, showing that the strand supermodes of the light cage indeed behave like a tube that confines the light inside the core.

Having determined the parameters of the model, Eq. 6.4 can be used to estimate the index of all higher-order modes, which only depends on $u_{l,m}$ for a fixed wavelength:

$$n_{\text{eff}}^{l,m} \approx 1 - A\, u_{l,m}^2, \tag{6.5}$$

where $A(\lambda)$ does not depend on the order of the mode. The quadratic dependence of the indices on $u_{l,m}$ matches well with the simulated modal indices as shown in Fig. 6.12. Plugging this relation into Eq. 6.2a then allows to determine the twist rates at which resonances may occur:

$$\boxed{\alpha\, \Delta j \approx A\, k_0 (u_{\tilde{l},\tilde{m}}^2 - u_{0,1}^2).} \tag{6.6}$$

Note that for large values of l or m, the function $u_{l,m}$ grows approximately linearly in m and l. The twist rates of the chiral and achiral resonances obtained with this model are shown as vertical lines in Fig. 6.8(c) matching well with the simulated resonances at low twist rates. At higher twist rates, the model projects that more and more resonances occur but the prediction of the exact twist rates becomes less reliable.

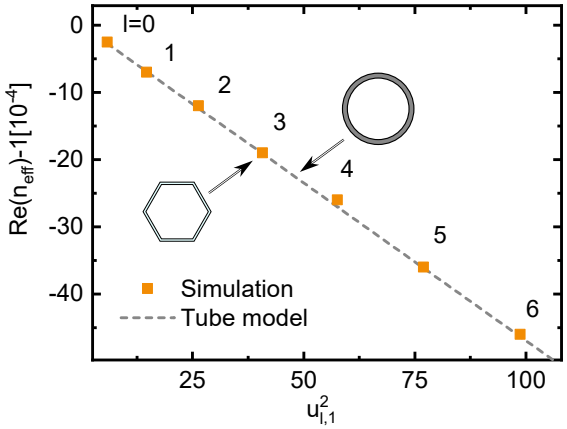

Figure 6.12: Effective index of higher-order modes in untwisted single-mode strand light cages. Indices of modes of radial order $m = 1$ and azimuthal orders l ranging from 0 to 6 were simulated (orange squares). Gray dashed line corresponds to the tube model (Eq. 6.5) with parameters obtained from the dispersion of the fundamental mode ($m = 1$, $l = 0$).

6.6 Experimental Results

The experimentally realized **twisted multimode strand light cages** are right-handed and feature a strand diameter of $2r_c = 3.814$ µm, which was determined from the measured spectral resonances of the untwisted waveguide via Eq. 4.16. Four different twist rates ranging from 0/mm to 11.4/mm were realized with the corresponding SEM images shown in Fig. 6.13(b).

As a first verification of the theoretical modeling, the LCP fundamental mode was excited in one of the twisted waveguides and **mode images** were recorded at different distances from the end face of the waveguide. Since the mode is invariant in the helicoidal

frame, its intensity distribution is supposed to follow the right-handed twist of the waveguide in the lab frame. This rotation could be confirmed in the measurement[5] as shown in Fig. 6.13.

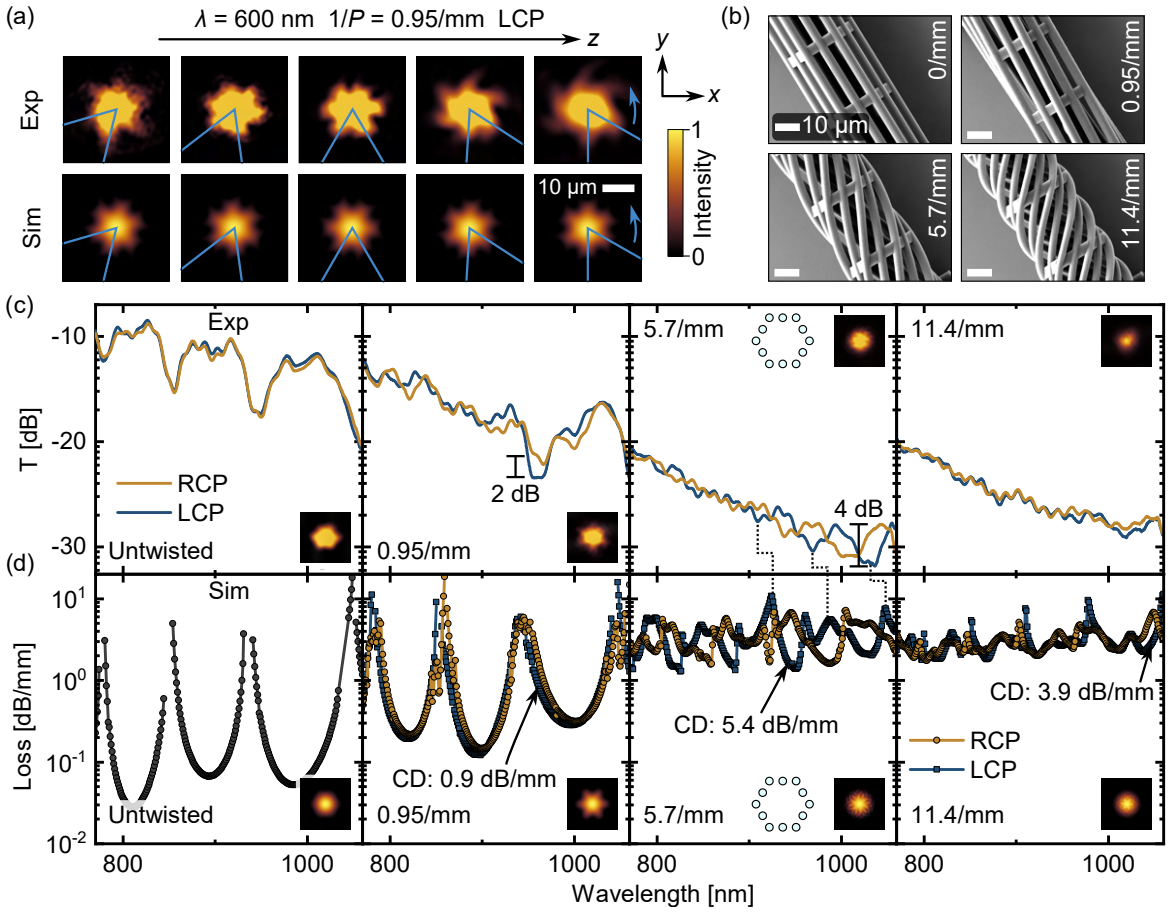

Figure 6.13: Experimental results for twisted multimode strand light cages with strand diameter $2r_c = 3.814$ μm. (a) CCD images of the LCP core mode along different axial positions recorded by moving the focal plane of the objective into (left) or out of (right) the waveguide. As expected, the intensity distribution follows the rotation of the right-handed twisted structure as z is changed (blue lines). Images were overexposed to better show this effect. Aberrations arise due to the presence of the strands when imaging inside the waveguide (left image) or due to diffraction once the mode leaves the waveguide (right image). (b) SEM images of the four studied light cages with twist rates up to 11.4/mm. (c) Normalized transmission spectra of RCP (orange) and LCP (blue) light through 5 mm long waveguide samples. (d) Simulated loss spectra of the same waveguides. Arrows indicate the wavelength of largest circular dichroism (difference in loss between modes of opposite circular polarization). Insets in (c,d) show the core mode at 770 nm.

[5]A video of the rotation of the mode will likely be made available in the Supporting Information of the manuscript that is being prepared.

Next, the **circular dichroism (CD)** was determined using the white light transmission setup described in Section 3.3. CD is here defined as the absolute value of the difference in loss between the LCP and RCP mode. In Fig. 6.13(c,d) the results are compared to numerical simulations of the modal attenuation of waveguides with identical properties. Three different regimes can be distinguished: (1) In the untwisted waveguide only core-strand resonances are present and the transmission is identical for LCP and RCP light. (2) At intermediate twist rates (0 - 1.3/mm), first twist-induced core-core resonances form, shown in more detail in Fig. E.3. For the twist rate of 0.95/mm depicted in Fig. 6.13(c,d) such a resonance is not present in the investigated wavelength range. The core-strand resonances can still be clearly distinguished and remain nearly unaffected by twisting, except for small spin-dependent shifts (for more detail see Fig. E.4). These shifts give rise to weak CD but were not investigated further. (3) At high twist rates (1.5 - 10/mm) more and more twist-induced resonances appear which result in strong CD and overall higher loss (more details in Fig. E.5). Due to the large number of resonances, core-strand resonances cannot be distinguished anymore in the loss spectra.

Overall, the experimental results clearly confirm the presence of CD in twisted light cages, reaching values of up to 0.8 dB/mm at a twist rate of 5.7/mm. The CD is about two orders of magnitude larger than in the previously reported twisted hollow-core fiber [119]. Nevertheless, we note that the overall loss at which this CD is achieved is very high in the current realization. To reach a 10 dB discrimination between LCP and RCP light, the two modes would be attenuated by 58 dB and 68 dB, respectively as shown in Table 6.2. On the other hand, the associated simulations indicate that the optical properties can be considerably improved given the current dimensions of the waveguide. Specifically, a CD of 5.4 dB/mm can potentially be reached, translating to losses of 2.9 dB and 12.9 dB for the two polarizations after a propagation distance of 1.9 mm (see Fig. 6.13(d) and Table 6.2).

Table 6.2: Comparison of measured (exp.) and simulated (sim.) CD to fiber-based twisted hollow-core waveguide of Ref. [119].

Waveguide	CD	Loss (-)[a]	Loss (+)[a]	Length for 10 dB CD[b]	Loss (-) at this length[b]
This work (exp.)	0.8 dB/mm	4.6 dB/mm[c]	5.4 dB/mm[c]	12.5 mm	58 dB
This work (sim.)	5.4 dB/mm	1.5 dB/mm	6.9 dB/mm	1.9 mm	2.9 dB
Fiber of [119]	8.3 dB/m	1.4 dB/m	9.7 dB/m	1.2 m	1.7 dB

[a] Loss (+/-) corresponds to the circular polarization state with highest or lowest loss, respectively.

[b] The length to reach a 10 dB discrimination between the two polarization states and loss (-) corresponding to this length are shown.

[c] The attenuation was calculated by assuming a coupling loss of 5 dB determined in earlier measurements of untwisted light cages discussed in Section 4.2.4.

There are two possible **explanations for the higher loss in the fabricated waveguides**: (1) Surface roughness of the strands leads to additional scattering loss explaining why the off-resonance loss in the untwisted waveguide is about one order of magnitude larger than in simulations (cf. Section 4.2.4). (2) The cross section of the twisted strands varies with the axial position in the waveguide, which results in a broadening of the core-strand resonances leading to higher losses. This would explain the absence of clear core-strand resonances in the sample with the intermediate twist rate of 0.95/mm (see Fig. 6.13(c,d)).

6.7 Discussion and Applications

The simulations clearly indicate the potential of twisted light cages as on-chip elements providing circular dichroism via chiral resonances. Provided that fabrication quality can be increased, waveguides of the currently achieved dimensions are able to provide comparable discrimination between LCP and RCP light and comparable loss as a 1.2 m long piece of the recently reported twisted hollow-core fiber [119] but at a length of only 1.9 mm (cf. Table 6.2). Furthermore, 3D nanoprinting allows interfacing with other on-chip waveguides by photonic wire bonding [76] without any additional processing steps. To this end, tapered structures can be used for maximizing the modal overlap between the small core of a step-index waveguide and the larger mode area of the hollow-core waveguide [319]. Integration with fibers has been successfully demonstrated using V-grooves on silicon chips [83, 244] or fabrication directly onto fiber-end faces [101].

Future work will focus on solving the fabrication-related challenges, e.g., by analyzing the cross section of the waveguide at different locations using a focused ion beam (FIB) system and precompensating any deviations during the design step. Further improvements may be reached by changing the fabrication direction from horizontal to vertical such that the axis of the waveguide is aligned perpendicular to the substrate. With this adjustment, the shape of the voxel within the cross-sectional plane of the waveguide changes from elliptical to circular, thus enhancing the accuracy of the fabrication. Furthermore, strategies to reduce the overall propagation loss will be explored, e.g., by reducing the spacing between strands, adding a second ring of strands as demonstrated in Ref. [81], or applying techniques for reducing the surface roughness of the polymer described in Ref. [320].

Possible **applications** of twisted light cages are demonstrated in Fig. 6.14 on the example of the single-mode strand light cage. The CD of chiral resonances shown in Fig. 6.14(a) allows twisted light cages to act as a **circular polarization filter** that can be placed in line with existing waveguides in devices where a pure circular polarization state is required, e.g., in areas such as optical communication, chiral sensing, or quantum optics. As light cages are 3D chiral structures (as opposed to planar structures with 2D chirality[6]), they suppress polarization of a specific handedness both for forward- and

[6]Difference between 2D and 3D chirality is discussed in Refs. [321, 322]. Planar structures of a single height (metasurfaces) can only provide 2D chirality, which reverses under change of propagation direction, unless the material itself is chiral (e.g., chiral dye molecules [323] or cholesteric liquid crystals [324]).

backward propagating light. Improved designs with lower propagation loss would therefore be of high relevance for the realization of single-handedness chiral cavities which require spin-dependent loss [325, 326]. Chiral cavities can enhance the weak chiroptical signals from chiral biomolecules [327, 328, 329], generate circularly polarized laser emission [330], and are of interest in quantum optics for their chiral vacuum states [331, 326]. The use of light cages in this context would be particularly beneficial as they allow direct access to the cavity mode through the open space between the strands for introducing atoms or molecules into the cavity.

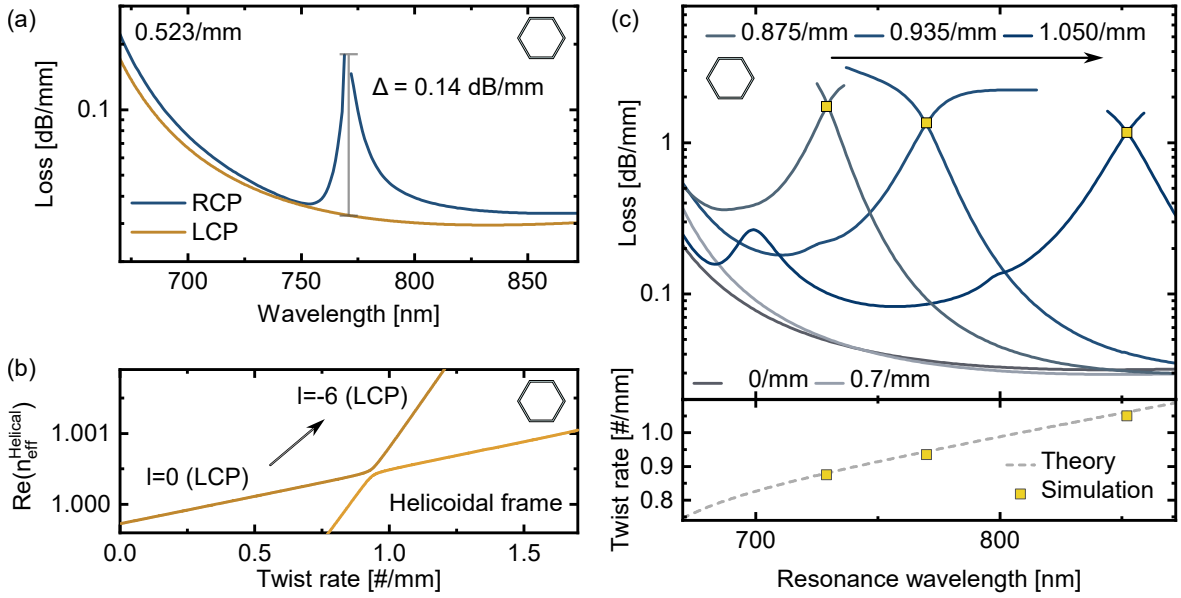

Figure 6.14: Potential on-chip applications of twisted light cages. (a) Spectral distribution of the attenuation around a chiral resonance enabling strong circular dichroism in a centimeter-scale waveguide. (b) Real part of the effective index in the lab frame around an achiral resonance. A waveguide with adiabatically increasing twist rate could convert the fundamental core mode to a mode carrying OAM (here: $l = -6$). (c) Spectral distribution of the attenuation around an achiral resonance. Increasing the twist rate results in a shift of the resonance towards longer wavelengths (bottom panel). This effect can be applied for twist and tension sensing. Dashed gray line denotes the analytical model of Eqs. 6.2a and 6.4. All subfigures (a-c) show simulation results for the single-mode strand light cage.

Another frequently explored application of on- and off-axis twisted waveguides is **OAM generation** [122, 123, 124]. However, in the case of twisted PCFs, the OAM is carried by a lossy cladding mode in most works [106, 119, 98, 94], which limits their use as mode converters. An exception is Ref. [107], where OAM beams were generated in the core of the twisted fiber but used an additional fiber Bragg grating for mode coupling. Twisted light cages, on the other hand, offer two advantages in this regard: (1) OAM modes can be generated directly in the light-guiding core, and (2) 3D nanoprinting provides a straightforward path to implement adiabatic mode conversion by enabling fabrication of

structures with spatially varying twist rates. Fig. 6.14(b) shows an example where an adiabatically increasing twist rate would result in conversion of a mode with $l = 0$ to a mode with $l = -6$. Such adiabatic coupling yields a broad operating bandwidth, which is an advantage over resonant coupling at a fixed twist rate. Preferably, adiabatic mode coupling should be implemented for an achiral resonance as their larger coupling strength allow for shorter device lengths[7].

In terms of **sensing applications**, twisted light cages are sensitive to **torsion and tension**, which both affect the helical pitch P. According to Eq. 6.2a, the wavelength λ_r at which resonances occur is equal to $\lambda_r = P\,\Delta n/\Delta j$, where $\Delta n(\lambda)$ and Δj are the mismatch in effective index and angular momentum of the modes in the untwisted waveguide. The wavelength dependence of Δn can be described by the tube waveguide model of Eq. 6.4, which predicts a shift of the resonances to longer wavelengths as the twist rate increases, matching well with the simulated values in Fig. 6.14(c). As Δn grows approximately quadratically in l, while Δj grows linearly in l, higher-order resonances generally feature a higher sensitivity to changes in P. For the first achiral resonace ($\Delta j = 6$), we find a torsion sensitivity $\Delta\lambda_r/\Delta\alpha$ of 0.11 nm/(rad/m). In other words, the resonance wavelength increases by 1 nm if P decreases by 1.5 µm. This value lies within the range of sensitivities between 0.03 - 0.5 nm/(rad/m) reported for fiber-based measurements [334, 335, 93, 336].

We note that many of the above applications have already been realized using **chiral fiber gratings** which often perform better than twisted hollow-core waveguides. Examples include circular dichroism of 3 dB/mm over a bandwidth of more than 80 nm [92], a torsion sensitivity of 0.47 nm/(rad/m) for a 24 mm long grating with a resonance contrast of 32 dB [334], OAM generation with high coupling efficiency [96], and polarizers based on adiabatically twisted fibers [337].

However, chiral fiber gratings are solid-core fibers and suitable methods for large-scale chip integration are lacking. Advantages of hollow-core light cages therefore lie in applications where a strong interaction of gases or liquids with the light in the core is desired, such as in **nonlinear frequency conversion**. The benefit of using twisted waveguides in these applications is mostly related to their circular birefringence, which allows circularly polarized supercontinuum generation ($B_C = 1.1 \times 10^{-6}$) [125] or light sources with pressure-tunable polarization states based on Raman scattering ($B_C = 3 \times 10^{-8}$) [126]. For twisted light cages, simulations indicate that B_C is on the order of 10^{-6} - 10^{-5} and could be further increased by using larger twist rates (cf. Eq. 6.3). As a result, twisted light cages offer an opportunity for the chip integration of the aforementioned works, while also increasing the robustness of the polarization state against environmental fluctuations.

Regarding the **theoretical analysis of twist-induced resonances**, we observed a discrepancy between our findings and those presented in earlier works on twisted PCFs [98, 106], an issue previously addressed in Ref. [318]. We want to extend this discussion to the

[7]For mode coupling between two waveguides to be adiabatic the coefficient $\eta = \left|\frac{1}{2\Gamma}\frac{\partial\theta}{\partial z}\right| \ll 1$, where $\theta = \arctan(\kappa/\Delta)$, Δ is the wavevector mismatch between the modes, κ is the coupling coefficient, and $\Gamma = \sqrt{\Delta^2 + \kappa^2}$ [332, 333]. Assuming that Δ varies linearly along the waveguide with $\frac{\partial\Delta}{\partial z} \equiv g$, and κ is constant, then $\eta = \frac{g\kappa}{2(\Delta^2+\kappa^2)^{3/2}} < \frac{g}{2\kappa^2}$. Larger coupling strengths κ therefore allow larger values of g (i.e., quicker changes of the twist rate) while maintaining adiabaticity.

theoretical analysis in Ref. [119], which states that only modes of the same total angular momentum are allowed to couple. Yet, visual inspection of Fig. 6 of this work indicates the coupling of a core mode with angular momenta $s = +1$, $l = 0$, $j = +1$ with a cladding mode with $s = -1$, $l = +12$, $j = +11$, seemingly contradicting their claim. Using the angular momentum selection rule Eq. 6.2b for the 5-fold rotationally symmetric fiber, however, would explain this coupling correctly as a chiral resonance.

Finally, we want to address the question whether the **high twist rates** achievable with 3D nanoprinting offer an advantage over glass-based fabrication techniques. As evident from Eq. 6.2a, higher twist rates are generally beneficial as they enable coupling of the fundamental mode to modes of very high OAM order, which feature higher losses and can therefore result in stronger circular dichroism. However, the coupling strength to such modes is currently limited, as their amplitudes in the OAM decomposition of the fundamental mode are very low (cf. Fig. 6.7). Future work will focus on increasing the amplitudes of these higher-order OAM contributions by using non-polygonal arrangements of the strands providing a path for both, stronger circular dichroism, and stronger circular birefringence (via the factor $\langle j \rangle - j_0$ in Eq. 6.3). Furthermore, it is worth noting that the coupling of two core modes should generally lead to higher coupling strengths compared to core-cladding resonances, where the modes are spatially separated. Thus, the full potential of strongly twisted 3D-nanoprinted hollow-core light cages remains to be unlocked.

6.8 Conclusion

In summary, this chapter gave a detailed overview of the physics of twisted light cages and contains the first experimental demonstration of circular dichroism in an on-chip hollow-core waveguide. Building on previous works, the origin of circular dichroism [122, 292, 123, 318] and circular birefringence [104, 99] in these waveguides have been explained based on the presence of higher-order OAM states in the fundamental mode of the untwisted waveguide.

The presence of circular dichroism was found to be related to twist-induced chiral resonances, which result from coupling of a higher-order core mode with the fundamental mode of opposite spin. Furthermore, a selection rule applies, which only allows resonances to occur if the total angular momentum of the involved modes differs by multiples of the order of the rotational symmetry of the waveguide (= 6 for hexagonal light cages). In this context, we presented a straightforward derivation for the mode coupling condition based on the properties of the helicoidal coordinate frame, which is valid for core and cladding modes in on-axis twisted waveguides. The twist rate or spectral location, where these resonances occur, was shown to be determined by the properties of the untwisted waveguide and can be predicted analytically by approximating the geometry of light cages as a tube [212].

While large circular dichroism of 0.8 dB/mm was measured experimentally, high propagation losses currently limit the immediate applicability of twisted light cages in real-world scenarios. Yet, with improvements in fabrication quality, the novel implementation via

3D nanoprinting has the potential to translate years of research on twisted PCFs into on-chip devices. Such applications include waveguide-integrated and broadband generation of circular polarization and OAM beams, nonlinear frequency conversion with circularly polarized light [125, 126], twist- and tension sensing, and chiral spectroscopy.

Chapter 7

Summary and Outlook

This thesis presented the application of 3D nanoprinting as a powerful tool for the chip integration of straight and twisted hollow-core waveguides. Three waveguide types were fabricated, characterized by optical transmission measurements, and analyzed by simulation and analytical theory. In particular, we introduced a novel type of on-chip hollow-core waveguide, the microgap waveguide, which features a simplified fabrication procedure and improves the previously reported light cage in terms of propagation loss, transmission bandwidth, and fabrication time. Furthermore, we demonstrate the first twisted hollow-core waveguide realized on a chip, a twisted light cage.

A unique feature of all discussed waveguides is a large structural openness enabling fast passive analyte exchange in contrast to hollow-core fibers, which can be filled only via the end faces. This property is particularly appealing for real-time optical sensing devices, which require liquids or gases to interact with the guided light. Here, we conducted proof-of-principle experiments on absorption spectroscopy of ammonia gas and aqueous solutions of Rhodamine 6G dye, as well as fluorescence spectroscopy of Rhodamine B dye. The results indicate limits of detection matching those of cuvette-based reference measurements, and a strong reduction in the analyte exchange time compared to capillaries of the same length.

Furthermore, the reproducibility of the 3D nanoprinting approach was studied on the example of light cages by inferring the realized dimension from the characteristic resonances in the transmission spectrum. Waveguides produced within a single fabrication run on the same chip reveal low variations in the dimensions (2 nm), while batch-to-batch variations are about one order of magnitude larger (15 nm). This remarkable level of accuracy underscores the potential of 3D nanoprinting in the context of integrated waveguide optics.

The ability to access all three spatial dimensions is also intriguing for the fabrication of chiral photonic structures. Here, we demonstrated the implementation of twisted hollow-core waveguides with unprecedented twist rates overcoming those of similar twisted hollow-core fibers [119] by more than two orders of magnitude: twisted light cages.

Specific coordinate frames for the analysis of such waveguides were introduced in a theoretical study on off-axis twisted solid-core waveguides. In this context, we clarify that structures defined with a circular geometry in these coordinates are not identical and pos-

sess different optical properties in the single-mode regime. On the other hand, structures with larger core sizes, such as those obtainable with 3D nanoprinting, behave similarly from the optics perspective. These findings are relevant to many works on twisted waveguides as virtually all are using either the investigated Frenet-Serret, helicoidal, or Overfelt frame in their theoretical modeling. We investigated circular and OAM birefringence of these waveguides, confirming that their origin is a purely geometric effect related to the curved helical path. Additionally, we uncovered that superchiral fields can be created on the surface of off-axis twisted waveguides and found spin- and OAM-dependent spatial splittings in the intensity distribution of the modes. Potential origins of these observations were identified to be the photonic spin Hall and orbital Hall effects.

With these preparations, we conducted an experimental and theoretical study on twisted light cages - an on-axis twisted waveguide. The fabricated samples were found to possess strong circular dichroism (CD), enabled by twist-induced resonances between two of the core modes. We categorized these resonances into achiral (without CD) and chiral resonances (with CD), and provided an analytical theory for predicting their spectral locations based on the dispersion of the untwisted waveguide. Furthermore, we discuss the occurrence of circular birefringence based on the analysis of the angular momentum distribution of the fundamental mode. The simulated birefringence is on the same order as in commercially available spun optical fibers, indicating that twisted light cages can robustly guide circularly polarized light. Overall, this thesis presented the first detailed study of all relevant optical properties of 3D-nanoprinted twisted waveguides, which is - more generally - applicable to any high-index contrast twisted waveguide.

Looking ahead, the ongoing trend of device miniaturization presents exciting prospects for the application of both straight and twisted 3D-nanoprinted hollow-core waveguides. As an example, a recent work demonstrated the monolithic integration of a laser, a 100 µm long evanescent-field waveguide, and a spectrometer for mid-infrared spectroscopy [338]. This device could be considerably improved by using 3D-nanoprinted hollow-core waveguides, which offer longer interaction lengths, larger overlap of the field with the analyte, and lower background signals from the material of the waveguide. These advantages identically apply to other optical sensing techniques [339], such as Raman, fluorescence, or circular dichroism spectroscopy. Due to the fast analyte exchange times of the demonstrated waveguides, such compact sensors could find numerous applications in passive sensing devices, such as in environmental monitoring, point-of-care testing, and chemical analysis.

Another interesting application scenario are microfluidic lab-on-a-chip devices, where analytes can be mixed with reagents via piezoelectric micropumps [340]. Such devices are already commercially available for applications such as DNA and cell analysis, immunoassays, clinical and pharmaceutical analysis, microreactors, and fuel cells [341, 342, 343]. A relatively new development in this direction are organs-on-a-chip, which mimic the physiological response of human organs and are used in drug development [344]. All of these devices could benefit from the additional integration of optical sensing techniques using hollow-core waveguides for analyzing the reaction products.

An overall similar approach is targeted in lab-on-a-fiber sensors, where external fiber-coupled light sources and spectrometers are used, while the active region of the device lies on a fiber tip or exposed section of the fiber [345]. In this context, the integration of light cages with delivery and detection fibers was recently demonstrated [83], as well as 3D nanoprinting of square-shape hollow-core waveguides directly onto fiber end faces [280].

Applications outside of sensing technology could arise in nonlinear frequency conversion [313] and quantum optical experiments using low-pressure atomic vapors [57]. Specific applications of twisted 3D-nanoprinted waveguides include broadband generation and guidance of circular polarization and OAM beams, nonlinear frequency conversion with circularly polarized light [125, 126], integrated Brillouin lasing for ultrahigh-resolution optical sensing [310], twist- and tension sensing, and chiral spectroscopy.

One important issue that needs to be resolved before all of these applications can become reality is the still relatively high manufacturing cost of 3D nanoprinting considering investments on the order of several hundred thousand euros for a tool that can fabricate about 30 waveguides of 5 mm length per day. Two approaches exist to remedy this problem. First, the fabrication can be parallelized using so-called multi-focal arrays. In a recent demonstration of this approach, 2000 individually addressable focal spots were generated in the focal plane of a single objective via a digital micro-mirror device (DMD) [346] meaning that several foci can "work" on polymerizing a single structure. This approach reached high printing speeds of 2×10^6 voxels/s (for an up-to-date list of achievable printing speeds see [207]), while maintaining small lateral and axial feature sizes (90/140 nm). The second approach involves reducing the cost of the 3D nanoprinter. Currently, expensive femtosecond lasers are required to drive the two-photon polymerization process. A novel approach instead uses two-step absorption (i.e., a real intermediate excited state of the photoinitiator molecule instead of a virtual state), which strongly increases the likelihood of the process while maintaining the square dependence on the intensity [347]. Therefore, an orders of magnitude cheaper continuous-wave laser can be used, as demonstrated with a 405 nm laser diode at a power of 0.1 mW, while maintaining the high resolution known from two-photon polymerization (300/420 nm lateral/axial resolution).

Combining both approaches could result in significantly lower fabrication costs, opening avenues for future hollow-core waveguide based integrated optical devices. In more general terms, advances in 3D nanoprinting could lead to a new era of 3D photonic architectures, affecting applications as far as optical neural networks [348], optical analog computing [349, 350], or optical quantum computing [351].

Appendix A

Leaky Slab Waveguide Model for Microgap Waveguides

Here, we describe the second theoretical model for describing light guidance in microgap waveguides, which takes into account that the walls of the waveguide are not perfectly reflecting and therefore the field nodes of the fundamental mode do not occur exactly at the core-cladding boundary. Despite the relatively simple square-shaped geometry, a complete analytical model is still lacking. Here, we present an approximation by superposing the exact solutions for the TE_0 and TM_0 modes of an infinitely extended hollow slab waveguide. This corresponds to crossing two infinitely extended slab waveguides at a 90° angle and neglecting the interference of the solutions at the corners of the waveguide where the field intensity is low. Our analysis follows the argument in Ref. [135].

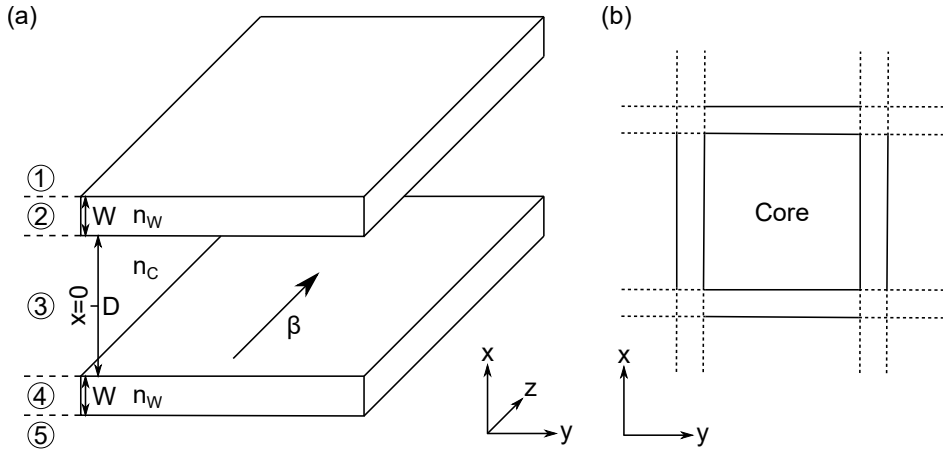

Figure A.1: Geometry for the slab waveguide model. (a) A single slab waveguide consists of two sheets (regions 2 and 4) of refractive index n_W and width W extending infinitely along the y and z direction. The core (region 3) and background (regions 1 and 5) have an index $n_C < n_W$. Light is propagating along the z direction with propagation constant β. (b) A microgap waveguide can be created by superimposing two slab waveguides.

We start with Maxwell's equations in linear media with refractive index n and make an **ansatz** for the electric and magnetic fields $\tilde{\mathbf{E}}$ and $\tilde{\mathbf{H}}$ propagating along the z direction:

$$\boldsymbol{\nabla} \times \begin{pmatrix} \tilde{E}_x \\ \tilde{E}_y \\ \tilde{E}_z \end{pmatrix} = -\mu_0 \frac{\partial}{\partial t} \begin{pmatrix} \tilde{H}_x \\ \tilde{H}_y \\ \tilde{H}_z \end{pmatrix}, \qquad \boldsymbol{\nabla} \times \begin{pmatrix} \tilde{H}_x \\ \tilde{H}_y \\ \tilde{H}_z \end{pmatrix} = \epsilon_0 n^2 \frac{\partial}{\partial t} \begin{pmatrix} \tilde{E}_x \\ \tilde{E}_y \\ \tilde{E}_z \end{pmatrix}, \tag{A.1}$$

$$\tilde{\mathbf{E}} = \mathbf{E}(x,y)\mathrm{e}^{\mathrm{i}(\omega \mathrm{t} - \beta \mathrm{z})}, \qquad \tilde{\mathbf{H}} = \mathbf{H}(\mathrm{x},\mathrm{y})\mathrm{e}^{\mathrm{i}(\omega \mathrm{t} - \beta \mathrm{z})}. \tag{A.2}$$

The ansatz is used to solve Maxwell's equations in each of the five regions of the slab waveguide individually and then impose boundary conditions to combine the solutions. Since the geometry is homogeneous along y, $\frac{\partial \mathbf{E}}{\partial y} = \frac{\partial \mathbf{H}}{\partial y} = 0$. Furthermore, we separate the solutions into two branches according to their polarization by setting $E_z = 0$ (TE modes) or $H_z = 0$ (TM modes). Plugging the ansatz Eq. A.2 in Eq. A.1 and using these conditions, we obtain the following set of equations:

$$\underline{\text{TE:}} \qquad E_x = E_z = H_y = 0, \qquad H_x = -\frac{\beta}{\omega \mu_0} E_y, \qquad H_z = \frac{\mathrm{i}}{\omega \mu_0} \frac{\partial E_y}{\partial x}, \tag{A.3}$$

$$\frac{\partial^2 E_y}{\partial x^2} + (k_0^2 n^2 - \beta^2) E_y = 0, \tag{A.4}$$

$$\underline{\text{TM:}} \qquad H_x = H_z = E_y = 0, \qquad E_x = \frac{\beta}{\omega \epsilon_0 n^2} H_y, \qquad E_z = -\frac{\mathrm{i}}{\omega \epsilon_0 n^2} \frac{\partial H_y}{\partial x}, \tag{A.5}$$

$$\frac{\partial^2 H_y}{\partial x^2} + (k_0^2 n^2 - \beta^2) H_y = 0. \tag{A.6}$$

According to Eqs. A.4 and A.6 both E_y and H_y are oscillatory functions of x and all other field components can be derived from them. Based on this observation we make the following ansatz for the TE solution:

$$E_y = \begin{cases} A_1 \exp(\mathrm{i}\kappa_C \mathrm{x}) & \text{for region } \textcircled{1} \\ A_2 \sin(\kappa_W x) + A_3 \cos(\kappa_W x) & \text{for region } \textcircled{2} \\ A_4 \cos(\kappa_C x) & \text{for region } \textcircled{3} \end{cases}, \tag{A.7}$$

with $\kappa_C = k_0 \sqrt{n_C^2 - n_{\text{eff}}^2}$, $\kappa_W = k_0 \sqrt{n_W^2 - n_{\text{eff}}^2}$, and $n_{\text{eff}} = \beta / k_0$. In the ansatz, we used the symmetry of the waveguide around its center line at $x = 0$, which allows to calculate the solution for regions $\textcircled{4}$ and $\textcircled{5}$ via $E_y(x) = E_y(-x)$.

The **boundary conditions** for the tangential components of $\tilde{\mathbf{E}}$ and $\tilde{\mathbf{H}}$ state that E_y and $H_z \propto \frac{\partial E_y}{\partial x}$ are continuous across the interfaces. Considering the two interfaces for $x > 0$, this condition yields four independent equations of which we consider the real part. This linear system can be written in the form of a matrix $\underline{\mathbf{M}}$ such that $\underline{\mathbf{M}}\,\mathbf{P} = \mathbf{0}$ with $\mathbf{P} = (A_1, A_2, A_3, A_4)$. For the solution to be nontrivial, it is required that $\det(\underline{\mathbf{M}}) = 0$ which yields the following analytical equation for the index n_{TE} of the **TE mode** that we

solved numerically:

$$\det\begin{pmatrix} \cos(\kappa_C b) & -\sin(\kappa_W b) & -\cos(\kappa_W b) & 0 \\ 0 & -\sin(\kappa_W a) & -\cos(\kappa_W a) & \cos(\kappa_C a) \\ -\kappa_C \sin(\kappa_C b) & -\kappa_W \cos(\kappa_W b) & \kappa_W \sin(\kappa_W b) & 0 \\ 0 & -\kappa_W \cos(\kappa_W a) & \kappa_W \sin(\kappa_W a) & -\kappa_C \sin(\kappa_C a) \end{pmatrix} = 0 \quad [\text{TE}], \tag{A.8}$$

where $a = D/2$ and $b = D/2 + W$ denote the interface locations. The TM solution n_{TM} can be obtained with a similar ansatz for H_y and the boundary condition that H_y and $E_z \propto \frac{\partial H_y}{\partial x}$ are continuous across the interface yielding the following equation:

$$\det\begin{pmatrix} \cos(\kappa_C b) & -\sin(\kappa_W b) & -\cos(\kappa_W b) & 0 \\ 0 & -\sin(\kappa_W a) & -\cos(\kappa_W a) & \cos(\kappa_C a) \\ -\frac{\kappa_C}{{n_C}^2} \sin(\kappa_C b) & -\frac{\kappa_W}{{n_W}^2} \cos(\kappa_W b) & \frac{\kappa_W}{{n_W}^2} \sin(\kappa_W b) & 0 \\ 0 & -\frac{\kappa_W}{{n_W}^2} \cos(\kappa_W a) & \frac{\kappa_W}{{n_W}^2} \sin(\kappa_W a) & -\frac{\kappa_C}{{n_C}^2} \sin(\kappa_C a) \end{pmatrix} = 0 \quad [\text{TM}]. \tag{A.9}$$

To obtain an approximation for the **real part** of the propagation constant β_{Square} and the effective index $n_{\text{eff}}^{\text{Square}}$ of the square waveguide, we calculate and combine the transverse wavevector components k_{TE} and k_{TM} of the TE and TM solution of the slab waveguide as shown in Fig. A.2.

$$k_{\text{TE/TM}}^2 = k_0^2 \left(1 - \text{Re}^2\{n_{\text{TE/TM}}\}\right), \tag{A.10}$$

$$\text{Re}^2\{\beta_{\text{Square}}\} = k_0^2 - k_{\text{TE}}^2 - k_{\text{TM}}^2, \tag{A.11}$$

$$\boxed{\text{Re}^2\{n_{\text{eff}}^{\text{Square}}\} = \text{Re}^2\{n_{\text{TE}}\} + \text{Re}^2\{n_{\text{TM}}\} - 1.} \tag{A.12}$$

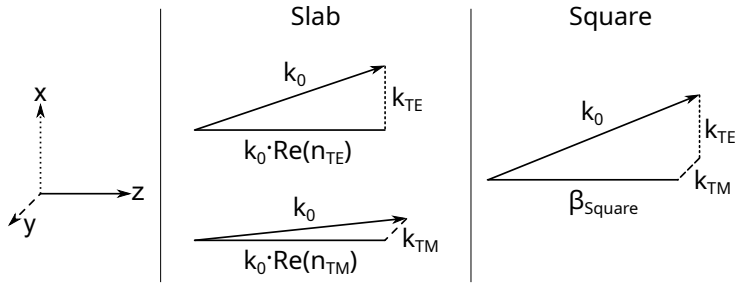

Figure A.2: Sketch of the wavevector components for the leaky slab waveguide model. Light is propagating along the z direction. The middle column shows the case for an infinitely extended slab waveguide with the two confining walls located perpendicular to the x axis (top) and y axis (bottom). Right column shows the situation for the square waveguide with four confining walls.

The **imaginary part** of the effective index is obtained by summing the imaginary parts of the effective indices of the TE and TM mode (by adding the second pair of walls to the slab waveguide the ray has to undergo twice as many reflections, thus the losses increase):

$$\boxed{\text{Im}\{n_{\text{eff}}^{Square}\} = \text{Im}\{n_{\text{TE}}\} + \text{Im}\{n_{\text{TM}}\}.} \tag{A.13}$$

Appendix B

Simulation of Twisted Waveguides

All simulations of twisted waveguides were performed using the helicoidal coordinate system, as implemented in a commercial FEM solver (PropagatingMode module of JCMwave). Due to the invariance of the waveguide along the ξ_3 coordinate, eigenmodes of helical waveguides can be separated into a phase factor and a modal field, which does not depend on ξ_3 [104]:

$$\tilde{\mathbf{F}}(\xi_{\mathbf{1}}, \xi_{\mathbf{2}}, \xi_{\mathbf{3}}) = \mathrm{e}^{\mathrm{i}\kappa\xi_3}\mathbf{F}(\xi_{\mathbf{1}}, \xi_{\mathbf{2}}), \tag{B.1}$$

where $\kappa/k_0 = n_{\mathrm{eff}}^{\mathrm{Helical}}$ is the eigenvalue of the mode returned by the mode solver. The resulting field needs to be transformed back to the Cartesian lab frame as described in detail in this section. Furthermore, we show under which conditions it is possible to define an effective mode index in the lab frame.

B.1 Transformation of Fields from Helicoidal Frame to Lab Frame

We assume that the solution of the field $\mathbf{E}$ is known for the plane $z = \xi_3 = 0$ and the field at an arbitrary point $(\tilde{x}, \tilde{y}, \tilde{z})$ is to be calculated in the lab frame. The field components are transformed from the helicoidal frame to the lab frame by the Jacobian of the coordinate transformation $\underline{\mathbf{T}}$:

$$\mathbf{E} = E_x\hat{\mathbf{x}} + E_y\hat{\mathbf{y}} + E_z\hat{\mathbf{z}} = E_{\xi_1}\xi_{\mathbf{1}} + E_{\xi_2}\xi_{\mathbf{2}} + E_{\xi_3}\xi_{\mathbf{3}}, \quad \text{with} \quad \underbrace{\begin{pmatrix} E_x \\ E_y \\ E_z \end{pmatrix}}_{\mathbf{E}^{\mathrm{Lab}}} = \underline{\mathbf{T}} \underbrace{\begin{pmatrix} E_{\xi_1} \\ E_{\xi_2} \\ E_{\xi_3} \end{pmatrix}}_{\mathbf{E}^{\mathrm{Helical}}}. \tag{B.2}$$

$\mathbf{E}_{\text{Helical}}$ and $\mathbf{E}_{\text{Lab}}$ were introduced to denote the coordinate vectors of $\mathbf{E}$ in the two frames. For the helicoidal coordinate system, the Jacobian and its inverse $\underline{\mathbf{T}}^{-1}$ read:

$$\begin{aligned}\underline{\mathbf{T}} = (\xi_1, \xi_2, \xi_3) &= \begin{pmatrix} \cos(\alpha\xi_3) & \sin(\alpha\xi_3) & \alpha(-\xi_1\sin(\alpha\xi_3) + \xi_2\cos(\alpha\xi_3)) \\ -\sin(\alpha\xi_3) & \cos(\alpha\xi_3) & -\alpha(\xi_1\cos(\alpha\xi_3) + \xi_2\sin(\alpha\xi_3)) \\ 0 & 0 & 1 \end{pmatrix} \\ &= \begin{pmatrix} \cos(\alpha z) & \sin(\alpha z) & \alpha y \\ -\sin(\alpha z) & \cos(\alpha z) & -\alpha x \\ 0 & 0 & 1 \end{pmatrix},\end{aligned} \tag{B.3}$$

$$\begin{aligned}\underline{\mathbf{T}}^{-1} &= \begin{pmatrix} \cos(\alpha\xi_3) & -\sin(\alpha\xi_3) & -\alpha\xi_2 \\ \sin(\alpha\xi_3) & \cos(\alpha\xi_3) & \alpha\xi_1 \\ 0 & 0 & 1 \end{pmatrix} \\ &= \begin{pmatrix} \cos(\alpha z) & -\sin(\alpha z) & -\alpha(x\sin(\alpha z) + y\cos(\alpha z)) \\ \sin(\alpha z) & \cos(\alpha z) & \alpha(x\cos(\alpha z) - y\sin(\alpha z)) \\ 0 & 0 & 1 \end{pmatrix}.\end{aligned} \tag{B.4}$$

Furthermore, it is useful to define the transformation matrices at the initial plane ($\xi_3 = z = 0$):

$$\underline{\mathbf{T_0}} = \begin{pmatrix} 1 & 0 & \alpha\xi_2 \\ 0 & 1 & -\alpha x\xi_1 \\ 0 & 0 & 1 \end{pmatrix}, \qquad \underline{\mathbf{T_0}}^{-1} = \begin{pmatrix} 1 & 0 & -\alpha\xi_2 \\ 0 & 1 & \alpha\xi_1 \\ 0 & 0 & 1 \end{pmatrix}. \tag{B.5}$$

In practice, the transformation between the coordinate systems is performed using the following steps:

1. The point $(\tilde{x}, \tilde{y}, \tilde{z})$ in the lab frame corresponds to a certain point $(\tilde{\xi_1}, \tilde{\xi_2}, \tilde{\xi_3})$ in the helicoidal frame, which is calculated by Eq. 2.48:

$$\begin{pmatrix} \tilde{\xi_1} \\ \tilde{\xi_2} \\ \tilde{\xi_3} \end{pmatrix} = \begin{pmatrix} \tilde{x}\cos(\alpha\tilde{z}) - \tilde{y}\sin(\alpha\tilde{z}) \\ \tilde{x}\sin(\alpha\tilde{z}) + \tilde{y}\cos(\alpha\tilde{z}) \\ \tilde{z} \end{pmatrix}. \tag{B.6}$$

2. Next, the field components in the helical frame $\mathbf{E}^{\text{Helical}}$ at the point $(\tilde{\xi_1}, \tilde{\xi_2}, \xi_3 = 0)$ are determined. Since JCMwave returns the field components in the lab frame $\mathbf{E}^{\text{Lab}}$ at $z = 0$, they need to be converted to the helical frame keeping $z = \xi_3 = 0$ using Eq. B.5:

$$\mathbf{E}^{\text{Helical}}(\tilde{\xi_1}, \tilde{\xi_2}, \xi_3 = 0) = \underline{\mathbf{T_0}}^{-1}\mathbf{E}^{\text{Lab}}(\tilde{x}\cos(\alpha\tilde{z}) - \tilde{y}\sin(\alpha\tilde{z}), \tilde{x}\sin(\alpha\tilde{z}) + \tilde{y}\cos(\alpha\tilde{z}), z = 0). \tag{B.7}$$

Here, we used that $\xi_1 = x$ and $\xi_2 = y$ for $\xi_3 = z = 0$ according to Eq. 2.48. Note that the point at which the solution $\mathbf{E}^{\text{Lab}}$ is evaluated depends on z due to the rotation of the two coordinate frames in relation to each other. Other solvers might directly return the field components in the helicoidal frame, in which case this step can be omitted.

3. The phase evolution factor from Eq. B.1 is introduced:

$$\mathbf{E}^{\text{Helical}}(\tilde{\xi_1}, \tilde{\xi_2}, \tilde{\xi_3}) = \mathrm{e}^{\mathrm{i}\kappa\tilde{\xi_3}}\mathbf{E}^{\text{Helical}}(\tilde{\xi_1}, \tilde{\xi_2}, \xi_3 = 0). \tag{B.8}$$

4. The field is transformed back to the lab frame using Eq. B.3:

$$\begin{aligned}&\mathbf{E}^{\text{Lab}}(\tilde{x}, \tilde{y}, \tilde{z}) = \underline{\mathbf{T}}\mathbf{E}^{\text{Helical}}(\tilde{\xi_1}, \tilde{\xi_2}, \tilde{\xi_3}) \\ &= \underbrace{\mathrm{e}^{\mathrm{i}\kappa\tilde{z}}}_{\text{phase}} \underbrace{\begin{pmatrix} \cos(\alpha\tilde{z}) & \sin(\alpha\tilde{z}) & 0 \\ -\sin(\alpha\tilde{z}) & \cos(\alpha\tilde{z}) & 0 \\ 0 & 0 & 1 \end{pmatrix}}_{\text{rotation of field}} \mathbf{E}^{\text{Lab}}(\underbrace{\tilde{x}\cos(\alpha\tilde{z}) - \tilde{y}\sin(\alpha\tilde{z}), \tilde{x}\sin(\alpha\tilde{z}) + \tilde{y}\cos(\alpha\tilde{z}), z = 0}_{\text{rotation of coordinates}}).\end{aligned} \tag{B.9}$$

The solution contains three contributions: (1) the phase evolution calculated in the helicoidal frame, (2) a rotation of the polarization ellipse around the z axis, and (3) the rotation of the coordinate frames with respect to each other.

An important observation is that the "shape" of the 3D polarization ellipse remains the same as the field propagates along the waveguide and merely rotates around the z axis. For fields where the polarization is the same at every point in the xy plane, one can therefore state that:

1. Transverse fields remain transverse.

$$E_z(x, y, 0) = 0 \iff E_z(x, y, z) = 0 \tag{B.10}$$

2. The degree of circularity as defined in Eq. 2.23 does not change.

$$\hat{S}_3(x, y, 0) = \hat{S}_3(x, y, z) \tag{B.11}$$

Eq. B.9 can be applied to calculate the phase evolution in the lab frame, which is important when studying mode coupling or other interference effects with structures that are not part of the twisted frame (e.g., a straight waveguide running parallel to a twisted waveguide). A necessary condition for mode coupling to occur is typically stated in the form that the effective index of the two modes needs to match. In the following sections, we show for a few relevant examples under which conditions it is possible to define an **effective index in the lab frame** - which is not always possible.

B.1.1 Fields Located On-axis

First, the possibility of defining an effective index in the lab frame is investigated for fields whose center is located on - or close to - the twist axis (as opposed to fields which are located in an off-axis core studied in Appendix B.1.2). For on-axis fields, it is possible to track the phase evolution of a fixed point (x, y) in the lab frame as the z coordinate is increased (see Fig. B.1).

Circularly Polarized Beams With OAM Phase Profile

The simplest case is a transverse field in the lab frame which is perfectly circularly polarized at every point in space at $z = 0$ and has an OAM phase profile with the singularity located on the twist axis.

$$\boxed{\mathbf{E}_{s,l}^{\mathrm{Lab}}(x, y, z = 0) = \frac{1}{\sqrt{2}} \begin{pmatrix} 1 \\ s\mathrm{i} \\ 0 \end{pmatrix} \mathrm{e}^{\mathrm{i}l\phi}}, \tag{B.12}$$

where $s = \pm 1$ denotes the spin, $l \in \mathbb{Z}$ the OAM order and $\phi = \tan^{-1}(y/x)$ the azimuthal angle. The field in the lab frame at $z \neq 0$ can be obtained by applying Eq. B.9, yielding:

$$\mathbf{E}_{s,l}^{\mathrm{Lab}}(x, y, z) = \frac{1}{\sqrt{2}} \begin{pmatrix} 1 \\ s\mathrm{i} \\ 0 \end{pmatrix} \mathrm{e}^{\mathrm{i}l \tan^{-1}\left(\frac{x \sin(\alpha z) + y \cos(\alpha z)}{x \cos(\alpha z) - y \sin(\alpha z)}\right)} \mathrm{e}^{\mathrm{i}s\alpha z} \mathrm{e}^{\mathrm{i}\kappa z}. \tag{B.13}$$

Using the addition theorem for tangens, $\tan(\gamma + \delta) = \frac{\tan(\gamma) + tan(\delta)}{1 - \tan(\gamma) tan(\delta)}$, the term in the exponential can be simplified as:

$$\tan^{-1}\left(\frac{x \sin(\alpha z) + y \cos(\alpha z)}{x \cos(\alpha z) - y \sin(\alpha z)}\right) = \tan^{-1}\underbrace{\left(\frac{\tan(\alpha z) + y/x}{1 - \tan(\alpha z) y/x}\right)}_{\tan(\alpha z + \tan^{-1}(y/x))} = \alpha z + \tan^{-1}(y/x). \tag{B.14}$$

The resulting equation for the evolution of the field in the lab frame is therefore:

$$\boxed{\mathbf{E}_{s,l}^{\mathrm{Lab}}(x, y, z) = \frac{1}{\sqrt{2}} \begin{pmatrix} 1 \\ s\mathrm{i} \\ 0 \end{pmatrix} \mathrm{e}^{\mathrm{i}l\phi} \mathrm{e}^{\mathrm{i}(s+l)\alpha z} \mathrm{e}^{\mathrm{i}\kappa z} = \mathbf{E}_{s,l}^{\mathrm{Lab}}(x, y, z = 0) \mathrm{e}^{\mathrm{i}(s+l)\alpha z} \mathrm{e}^{\mathrm{i}\kappa z}.} \tag{B.15}$$

We denote κz as the **helical propagation phase** and $(s + l)\alpha z$ as the **transformation phase**. For this example, both phases increase linearly in z which allows to define an effective index in the lab frame $n_{\mathrm{eff}}^{\mathrm{Lab}}$ as:

$$\boxed{n_{\mathrm{eff}}^{\mathrm{Lab}} = n_{\mathrm{eff}}^{\mathrm{Helical}} + (s + l)\frac{\alpha\lambda}{2\pi},} \tag{B.16}$$

where $n_{\mathrm{eff}}^{\mathrm{Helical}}(\alpha) = \kappa/k_0$ is the effective index in the helical frame. Note that this result does not contain approximations and holds for arbitrary twist rates as long as the fields have the structure defined in Eq. B.12.

The origin of the transformation phase is illustrated in Fig. B.1 for a circularly symmetric structure. According to Eq. B.9, a field that is invariant under changes of ξ_3 in the helicoidal frame rotates in the lab frame as z is increased, following the helical path of the structure. If the field carries OAM, the rotation of this phase profile results in the OAM contribution to the transformation phase $l\alpha z$. Eq. B.9 shows that apart from the phase

profile, the polarization ellipse is also rotated when z increases. This rotation results in the spin contribution to the transformation phase $s\alpha z$.

It is important to note that the helical propagation phase typically also carries a dependence on α. For the structure shown in Fig. B.1, it is straightforward to see that the transformation phase is exactly canceled by the twist rate dependence of the helical propagation phase: An on-axis structure with circular symmetry cannot be twisted (i.e., it does not change when twisted). For systems that are not circularly symmetric (e.g., hexagonal cores), the sum of the two phases remains dependent on the twist rate giving rise to circular birefringence.

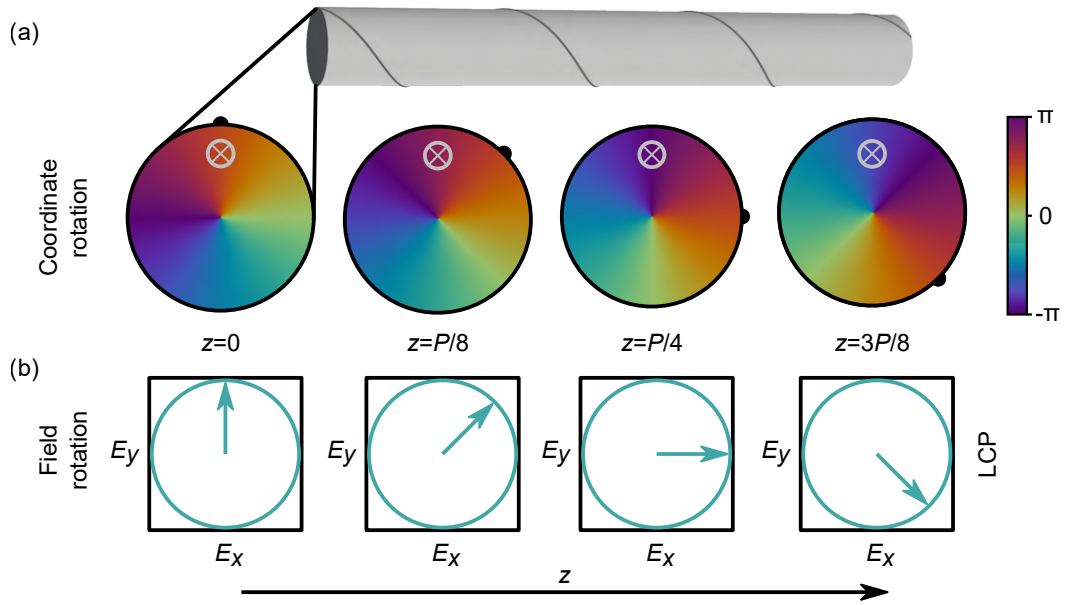

Figure B.1: Graphical explanation of the transformation phase for a circularly polarized transverse field with $s = l = 1$. For on-axis fields, the phase evolution is evaluated at fixed point (x, y) in the lab frame (gray crossed circle) as the z coordinate is increased. (a) shows the consequence of the rotation of the helical coordinate frame with respect to the lab frame. To isolate this effect, the phase of the x component of $\mathbf{E}^{\mathrm{Lab}}(x\cos(\alpha z) - y\sin(\alpha z), x\sin(\alpha z) + y\cos(\alpha z), 0)$ is evaluated (right hand side of Eq. B.9). As z increases, the phase at (x, y) grows resulting in the OAM contribution to the transformation phase: $l\alpha z$. The black bulge is a guide to the eye. (b) shows the isolated effect of the rotation of the field (middle term in Eq. B.9). As z increases the polarization ellipse is rotated with a period equal to the pitch length P of the helicoidal coordinate system, resulting in the spin contribution to the transformation phase: $s\alpha z$. Note that for the structure shown here, the sum of transformation phase and helical propagation phase does not depend on the twist rate due to its circular symmetry.

Elliptically Polarized Beams

Next, we study an example of eigenmodes which are transverse and elliptically polarized. For simplicity, the phase profile is assumed to be flat and the polarization is set to be constant across the beam cross section for $z = 0$:

$$\boxed{\mathbf{E}^{\mathrm{Lab}}_{\tilde{s},l}(x, y, z = 0) = \frac{1}{\sqrt{1 + (1 - \epsilon)^2}} \begin{pmatrix} 1 \\ \tilde{s}(1 - \epsilon)\mathrm{i} \\ 0 \end{pmatrix},} \tag{B.17}$$

where $\tilde{s} = \pm 1$ determines the direction of rotation of the polarization vector. Different values of the ellipticity of the polarization ellipse are investigated, which is defined as [135]:

$$\epsilon = \frac{a_x - a_y}{a_x}, \tag{B.18}$$

where a_x denotes the length of the major axis of the polarization ellipse and a_y the length of the minor axis. $\epsilon = 0$ corresponds to circular polarization and $\epsilon = 1$ to linear polarization. Applying Eq. B.9, yields the field at $z \neq 0$:

$$\boxed{\mathbf{E}^{\mathrm{Lab}}_{\tilde{s},l}(x, y, z) = \frac{1}{\sqrt{1 + (1 - \epsilon)^2}} \underbrace{\begin{pmatrix} \cos(\alpha z) + \tilde{s}\sin(\alpha z)(1 - \epsilon)\mathrm{i} \\ -\sin(\alpha z) + \tilde{s}\cos(\alpha z)(1 - \epsilon)\mathrm{i} \\ 0 \end{pmatrix}}_{\mathbf{E}^{\mathrm{Transformation}}} \mathrm{e}^{\mathrm{i}\kappa z}.} \tag{B.19}$$

While the helical propagation phase κz occurs in the same form as for circularly polarized fields, the transformation phase cannot be stated in a simplified form. Therefore, the transformation phase is determined numerically as the argument of $\mathbf{E}^{\mathrm{Transformation}}$. The increase of the transformation phase with z is shown for several values of ϵ below.

In untwisted waveguides, the propagation phase φ always increases linearly in z, even if the waveguide is filled with an anisotropic material due to the invariance of the structure in the z direction. This linearity is the basis for the definition of the effective refractive index n_{eff} via $\varphi = n_{\mathrm{eff}} k_0 z$. Twisted waveguides are however not invariant in the z direction of the lab frame. A peculiar consequence is that the propagation phase of non-circularly polarized eigenmodes of twisted waveguides can differ substantially from this linear increase such as in Fig. B.2(c). Therefore, it is generally not advisable to define an effective index in the lab frame via Eq. B.16. For example, a situation could arise where an eigenmode of a twisted waveguide would be assigned the same effective index as an eigenmode of an untwisted waveguide although their phases do not match locally at each z position.

More generally, the deviation from the linear increase in phase is a consequence of the rotation of the polarization ellipse as the field propagates along the twisted structure. For example, after propagating a quarter of the helix pitch the polarization ellipse shown in Fig. B.2(c) would be oriented vertically instead of horizontally. This is a fundamental difference to fields propagating in untwisted waveguides, where the orientation of the

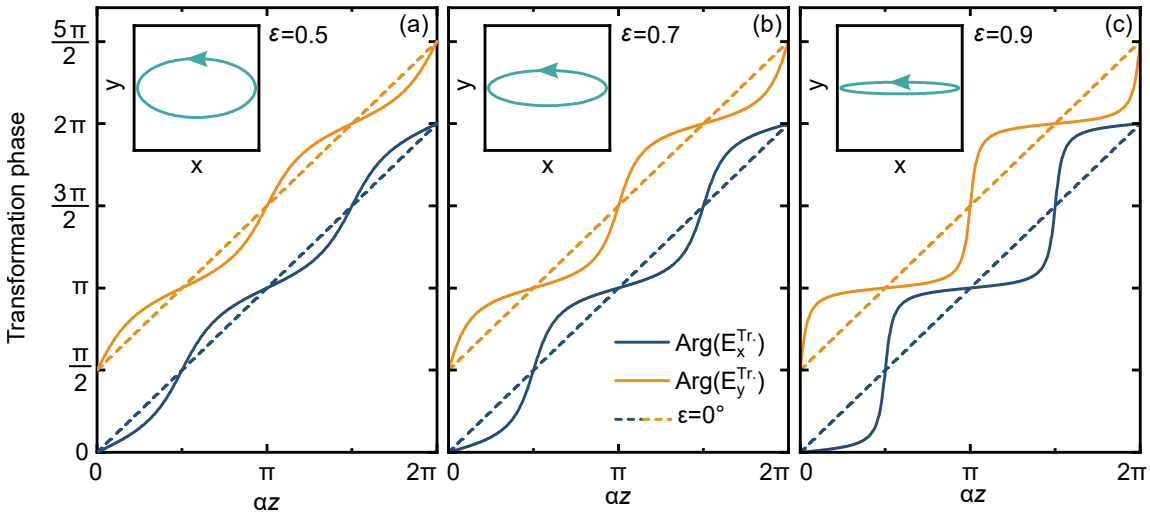

Figure B.2: Transformation phase for elliptically polarized transverse fields with $\tilde{s} = 1$. The phases of the x and y component of $\mathbf{E}^{\text{Transformation}}$ are shown as solid blue and orange lines, respectively. As the ellipticity of the polarization ellipse ϵ is increased, the differences to the phases of circular polarization (shown as dotted lines) grow larger. For ellipticities of $\epsilon = 0.5$ (a) and $\epsilon = 0.7$ (b), the phase difference to LCP ($\epsilon = 0$) remains below 0.2π. For a very high ellipticity of $\epsilon = 0.9$ (c) a strong deviation from the linear increase in z can be observed. Insets show the shape of the polarization ellipse.

polarization ellipse does not change. In this example, the overlap between the mode of a twisted and an untwisted waveguide would constantly change along the z direction, corroborating the fact that modes of structures with different twist rates cannot simply be compared by looking at the effective index.

Nonetheless, Eq. B.16 still correctly predicts the average phase increase over one twist period (dotted lines in Fig. B.2) and can therefore serve as guidance if the ellipticity of the field remains small enough such that the z dependence of the overlap integral can be neglected. In that case, the matching of effective indices defined by Eq. B.16 would give a necessary condition for quasi-phase-matching of two modes - similar to quasi-phase-matching in nonlinear optics.

Beams With Arbitrary Phase Profiles

A similar deviation from the linear phase increase occurs if the phase profile of the beam does not depend exactly linearly on ϕ, e.g., if the OAM phase profile is distorted due to coupling to other modes. For simplicity, we study a fictitious example, where the azimuthal phase increases only in one half of the beam and is constant in the other half. The field is

assumed to be transverse and circularly polarized:

$$\mathbf{E}_s^{\mathrm{Lab}}(x,y,z=0) = \frac{1}{\sqrt{2}}\begin{pmatrix}1\\ s\mathrm{i}\\ 0\end{pmatrix} \mathrm{e}^{\mathrm{i}f(\phi(x,y))} \qquad f(\phi) = \begin{cases} 2\phi & 0 \le \phi < \pi \\ 0 & \pi \le \phi < 2\pi \end{cases}, \tag{B.20}$$

where $s = \pm 1$ denotes the spin $\phi \in [0, 2\pi[$ is the azimuthal angle and $f(\phi)$ defines the phase profile. Again, we calculate the field for $z \neq 0$ using Eq. B.9, yielding:

$$\mathbf{E}_s^{\mathrm{Lab}}(x,y,z) = \frac{1}{\sqrt{2}} \underbrace{\begin{pmatrix}1\\ s\mathrm{i}\\ 0\end{pmatrix} \mathrm{e}^{\mathrm{i}f(\phi(x\cos(\alpha z) - y\sin(\alpha z), x\sin(\alpha z) + y\cos(\alpha z)))}}_{\mathbf{E}^{\mathrm{Transformation}}} \mathrm{e}^{\mathrm{i}s\alpha z}\, \mathrm{e}^{\mathrm{i}\kappa z}. \tag{B.21}$$

While the helical propagation phase κz occurs in the same form as in the previous examples, the transformation phase needs to be extracted as the argument of $\mathbf{E}^{\mathrm{Transformation}}$ shown below in Fig. B.3:

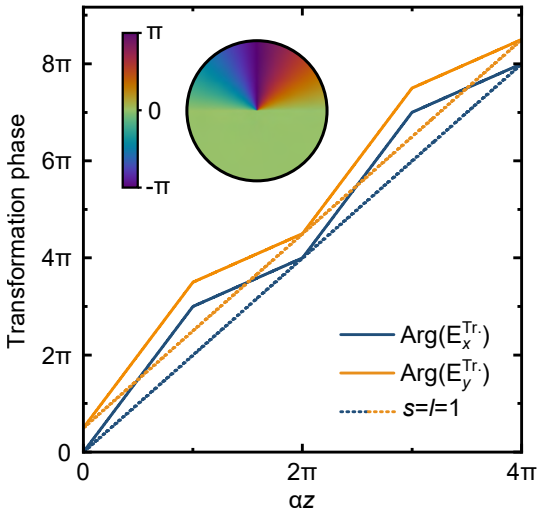

Figure B.3: Transformation phase for a beam whose phase profile differs from that of an OAM beam. As an example, a fictitious mode with $s = 1$ and the phase profile shown in the inset is assumed. The phases of the x and y component of $\mathbf{E}^{\mathrm{Transformation}}$ are shown as solid blue and orange lines, respectively. A strong deviation to the linear phase increase of a mode with perfect OAM phase profile with $s = l = 1$ (dotted lines) can be observed.

Fig. B.3 confirms that care should be taken when using Eq. B.16 to determine an effective index in the lab frame for eigenmodes of twisted structures. If the spatial phase of modes differs substantially from $\mathrm{e}^{\mathrm{i}l\phi}$, the propagation phase of the mode does not increase linearly in the z direction, which defeats the purpose of defining an effective index.

B.1.2 Fields Located Off-axis

This subsection deals with fields that are located in an off-axis region of space that winds around the twist axis. In this case, it is not possible to track the phase evolution of a fixed point (x, y) in the lab frame because as the z coordinate is changed, the core that is carrying the field moves away from this position (see Fig. B.4) Therefore we track the

phase evolution of a point that is located at a constant position relative to the center of the core as viewed in the lab frame.

Let's assume that the off-axis core is centered at a distance ρ from the twist axis. In the lab frame, this core moves along a helical trajectory $\mathbf{r}_0(z)$ according to Eq. 2.50. We now track a point that is placed at a constant (i.e., independent of z) offset $\mathbf{r}_1$ from this trajectory in the xy plane with local coordinates $\bar{x}$ and $\bar{y}$. Without loss of generality, the position of the core at $z = 0$ is chosen to be located on the positive part of the x axis:

$$\mathbf{r}_0(z) = \begin{pmatrix} \rho\cos(\alpha z) \\ -\rho\sin(\alpha z) \\ z \end{pmatrix}, \qquad \mathbf{r}_1 = \begin{pmatrix} \bar{x} \\ \bar{y} \\ 0 \end{pmatrix}, \qquad \mathbf{r}(\bar{x},\bar{y},z) = \mathbf{r}_0(z) + \mathbf{r}_1(\bar{x},\bar{y}) = \begin{pmatrix} \tilde{x} \\ \tilde{y} \\ \tilde{z} \end{pmatrix}. \tag{B.22}$$

Circularly Polarized Beams With OAM Phase Profile

As before, we first look at the simple case of a perfectly circularly polarized transverse field with a perfect OAM phase profile - now with the singularity located at the center of the off-axis core:

$$\boxed{\mathbf{E}^{\mathrm{Lab}}_{s,l}(x,y,z=0) = \frac{1}{\sqrt{2}}\begin{pmatrix} 1 \\ s\mathrm{i} \\ 0 \end{pmatrix} \mathrm{e}^{\mathrm{i}l\bar{\phi}},} \tag{B.23}$$

where $s = \pm 1$ denotes the spin, $l \in \mathbb{Z}$ the OAM order and $\bar{\phi} = \tan^{-1}(y/(x-\rho))$ the azimuthal angle relative to $\mathbf{r}_0(z=0)$. To calculate the field in the lab frame at $z \neq 0$, the field at $z = 0$ needs to be evaluated according to Eq. B.9:

$$\begin{aligned} &\mathbf{E}^{\mathrm{Lab}}_{s,l}(\tilde{x}\cos(\alpha\tilde{z}) - \tilde{y}\sin(\alpha\tilde{z}), \tilde{x}\sin(\alpha\tilde{z}) + \tilde{y}\cos(\alpha\tilde{z}), z=0) \\ =&\mathbf{E}^{\mathrm{Lab}}_{s,l}(\rho + \bar{x}\cos(\alpha\tilde{z}) - \bar{y}\sin(\alpha\tilde{z}), \bar{x}\sin(\alpha\tilde{z}) + \bar{y}\cos(\alpha\tilde{z}), z=0) \\ =&\frac{1}{\sqrt{2}}\begin{pmatrix} 1 \\ s\mathrm{i} \\ 0 \end{pmatrix} \mathrm{e}^{\mathrm{i}l\tan^{-1}\left(\frac{\bar{x}\sin(\alpha\tilde{z})+\bar{y}\cos(\alpha\tilde{z})}{\bar{x}\cos(\alpha\tilde{z})-\bar{y}\sin(\alpha\tilde{z})}\right)}. \end{aligned} \tag{B.24}$$

Following the same algebra as in the previous section one arrives at:

$$\boxed{\mathbf{E}^{\mathrm{Lab}}_{s,l}(\mathbf{r}(\bar{x},\bar{y},z)) = \frac{1}{\sqrt{2}}\begin{pmatrix} 1 \\ s\mathrm{i} \\ 0 \end{pmatrix} \mathrm{e}^{\mathrm{i}l\tan^{-1}(\bar{y}/\bar{x})}\mathrm{e}^{\mathrm{i}(s+l)\alpha z}\mathrm{e}^{\mathrm{i}\kappa z} = \mathbf{E}^{\mathrm{Lab}}_{s,l}(\mathbf{r}(\bar{x},\bar{y},z=0))\mathrm{e}^{\mathrm{i}(s+l)\alpha z}\mathrm{e}^{\mathrm{i}\kappa z}.} \tag{B.25}$$

This result has the same form as Eq. B.15 for on-axis fields. Therefore, we showed that it is also possible to define an effective index in the lab frame for off-axis fields - as long as the fields have the structure defined in Eq. B.23. The previously obtained formula for transforming the effective index Eq. B.16 also holds for these off-axis fields:

$$\boxed{n^{\mathrm{Lab}}_{\mathrm{eff}} = n^{\mathrm{Helical}}_{\mathrm{eff}} + (s+l)\frac{\alpha\lambda}{2\pi}.} \tag{B.26}$$

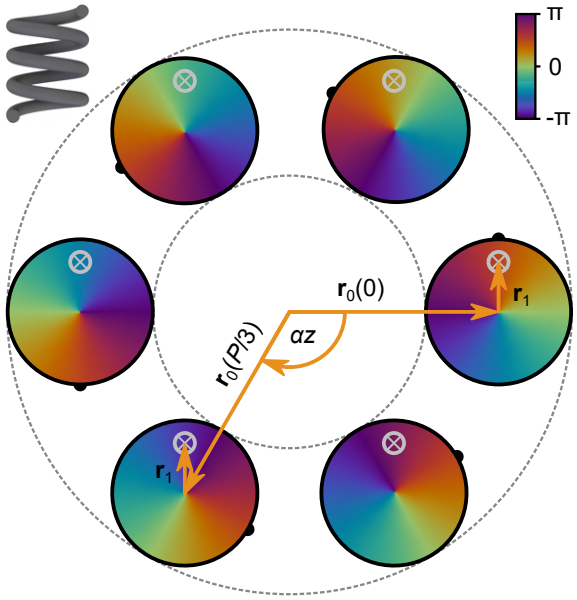

Figure B.4: Explanation of the OAM contribution to the transformation phase for fields located in an off-axis core. A circularly polarized transverse field with $s = l = 1$ is shown in the lab frame as z is increased in steps of 1/6 of the helical pitch. The phase is evaluated at a fixed point $\mathbf{r}_1$ relative to the center of the moving core $\mathbf{r}_0(z)$. Note that only the effect of the rotation of the helical coordinate frame with respect to the lab frame is shown. To isolate this effect, the phase of the x component of $\mathbf{E}^{\text{Lab}}(\tilde{x}\cos(\alpha z) - \tilde{y}\sin(\alpha z), \tilde{x}\sin(\alpha z) + \tilde{y}\cos(\alpha z), 0)$ is evaluated (right hand side of Eq. B.9). As z increases, the phase at the tracked point (gray crossed circle) increases resulting in the OAM contribution to the transformation phase: $l\alpha z$. The black bulge is a guide to the eye.

Non-transverse Beams

For a field in an off-axis core, its phase fronts are generally perpendicular to the helical trajectory of the core. Therefore, the field develops a z component and Eq. B.25 - derived for fields transverse to the z axis - does not apply anymore. In this case, the field is usually still circularly polarized (i.e., $\left|\hat{S}_3\right| = 1$) but the 3D polarization ellipse does not lie in the xy plane. As an example, we study a beam with uniform circular polarization where the polarization ellipse is tilted out of the xy plane by a tilt angle β:

$$\mathbf{E}_s^{\text{Lab}}(x, y, z = 0) = \frac{1}{\sqrt{2}} \begin{pmatrix} 1 & 0 & 0 \\ 0 & \cos(\beta) & -\sin(\beta) \\ 0 & \sin(\beta) & \cos(\beta) \end{pmatrix} \begin{pmatrix} 1 \\ s\mathrm{i} \\ 0 \end{pmatrix} = \frac{1}{\sqrt{2}} \begin{pmatrix} 1 \\ \mathrm{i}\cos(\beta) \\ \mathrm{i}\sin(\beta) \end{pmatrix}. \tag{B.27}$$

Again, Eq. B.9 is applied to calculate the field in the lab frame at $z \neq 0$. Since the field does not have a spatial dependence, the result is independent of the chosen trajectory

$\mathbf{r}(x, y, z)$ and applies to both off-axis and on-axis fields:

$$\mathbf{E}_s^{\mathrm{Lab}}(x, y, z) = \frac{1}{\sqrt{2}} \underbrace{\begin{pmatrix} \cos(\alpha z) + \mathrm{i}\cos(\beta)\sin(\alpha z) \\ -\sin(\alpha z) + \mathrm{i}\cos(\beta)\cos(\alpha z) \\ \mathrm{i}\sin(\beta) \end{pmatrix}}_{\mathbf{E}^{\mathrm{Transformation}}} \mathrm{e}^{\mathrm{i}\kappa z}. \tag{B.28}$$

The transformation phase is calculated as the argument of $\mathbf{E}^{\mathrm{Transformation}}$. Note that the phase of the z component of $\mathbf{E}^{\mathrm{Transformation}}$ does not change because the transformation includes a rotation of the polarization ellipse around the z axis.

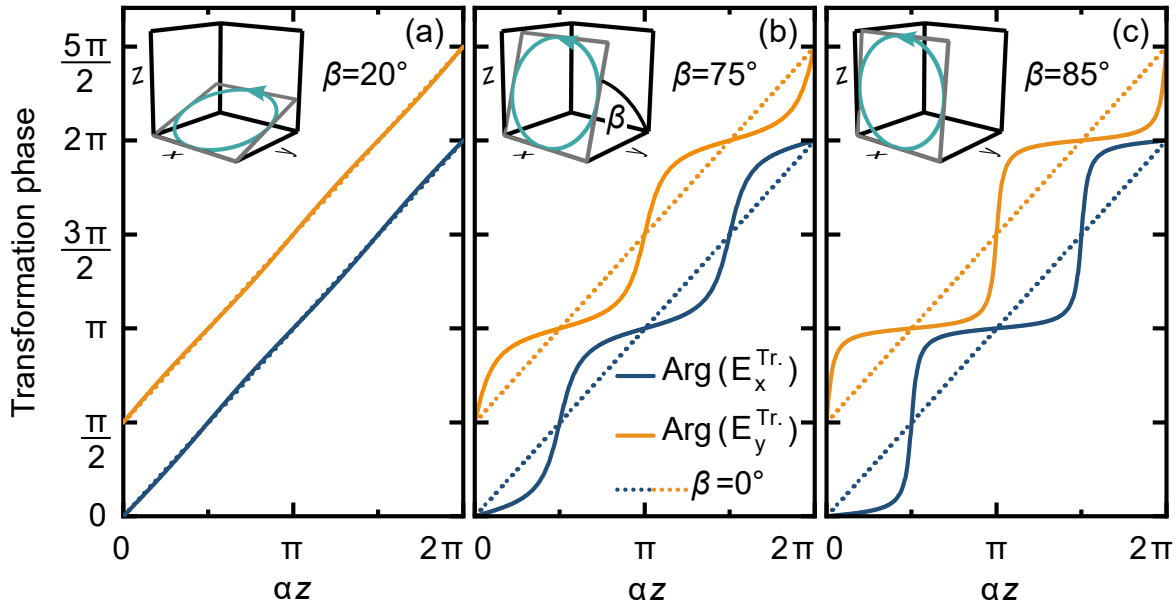

Figure B.5: Transformation phase for circularly polarized fields with $s = 1$ which are not transverse to the z axis. The polarization ellipse is tilted out of the xy plane by an angle β as indicated in the figure. The phases of the x and y component of $\mathbf{E}^{\mathrm{Transformation}}$ are shown as solid blue and orange lines, respectively. As the tilt angle is increased, the differences to the phases of an untilted polarization ellipse (shown as dotted lines) grow larger. For tilt angles of $\beta = 20°$ (a) and $\beta = 75°$ (b), the phase difference to the untilted ellipse remains below 0.2π. Only for very high tilt angles of $\beta = 85°$ (c) a strong deviation from the linear increase in z can be observed.

The transformation phase deviates from the linear increase in z if the field is not transverse. However, the phase difference to a transverse field with the same spin remains small even for high tilt angles of $\beta = 75°$ (Fig. B.5(b)). Therefore, Eq. B.16 can still be used as a guide to the phase evolution of the mode in the lab frame.

B.1.3 Summary

Eigenmodes of twisted waveguides have unique properties when it comes to their propagation. Since their field profile and their polarization ellipses rotate - following the twist of the structure - they can in general not be compared to a field propagating in an untwisted waveguide or a waveguide with a different twist rate. However, an exception exists if the field fulfills the following conditions:

- The field is transverse to the z axis.
- The field is circularly polarized with $s = \pm 1$.
- The spatial phase profile is flat or has an OAM profile with a $e^{il\phi}$ phase dependence.

Under these conditions, the propagation phase of the field increases linearly in the lab frame and an effective index in the lab frame can be defined using Eq. B.16:

$$\boxed{n_{\text{eff}}^{\text{Lab}} = n_{\text{eff}}^{\text{Helical}} + (s+l)\frac{\alpha\lambda}{2\pi}.} \tag{B.29}$$

This equation holds both for on-axis fields and fields located in an off-axis twisted core. An effective index in the lab frame can still be defined if the conditions are only slightly violated, especially if the polarization is still circular but the polarization ellipse is tilted out of the xy plane which is usually the case for off-axis twisted waveguides.

Appendix C

Overview of Works on Twisted Waveguides

Different types of on- and off-axis twisted waveguides are reported in the literature. Table C.1, shown on the next two pages, presents a broad selection of works in order of achieved (or theoretically analyzed) twist rate. Cross sections of these waveguide geometries are depicted in Fig. 1.5. A graphical overview of this table is available in Fig. 1.6.

To showcase the potential of 3D nanoprinting, a reference from 2009 on helical metasurfaces by Gansel et al. was included. This work reports the - to our knowledge - smallest pitch distance achieved so far with this technology: 1.8 µm [89]. However, as the total length of these helices is only about 5 µm, this result is not directly applicable in the context of the twisted waveguides presented in this thesis.

Table C.1: Comparison of works on twisted waveguides.

Type	Fabrication method	Twist period P [µm]	Radius ρ [µm]	$\alpha\rho$	Year	Ref.
On-axis twisted waveguides with off-axis rods						
Twisted light cage	3D nanoprinting	88	14[a]	1.00	2023	**This work**
Coreless PCF	3D nanoprinting	200	40[a]	1.26	2020	Bertoncini [101]
Solid-core PCF	Post-processing (CO2 laser)	341	16[a]	0.29	2012	Wong [98]
Solid-core PCF	Post-processing (CO2 laser)	435	16[a]	0.23	2013	Xi [93]
Solid-core PCF	Post-processing	456	16[a]	0.22	2015	Wong [94]
Solid-core PCF	Post-processing (CO2 laser)	622	16[a]	0.16	2013	Xi [99]
Coreless PCF	Preform spinning	2,000	41[a]		2016	Beravat [105]
Solid-core PCF (6 cores)	Preform spinning	2,200	6[b]/18[a]	0.02/0.05	2017	Russell[106]
Solid-core PCF (3 cores)	Preform spinning	2,500	2.5[a]	0.006	2020	Loranger [107]
Coreless PCF	Preform spinning	3,600	41[a]	0.07	2019	Roth [114]
Solid-core PCF (3 cores)	Post-processing (CO2 laser)	5,000	3[b]/16[a]	0.004/0.02	2014	Xi [110]
Solid-core PCF (3 cores)	Preform spinning	5,000	5.2[b]/16[a]	0.007/0.02	2022	Zeng [111]
Hollow-core PCF (single ring)	Preform spinning	11,900	48[a]	0.025	2018	Roth [119]
Hollow-core PCF (single ring)	Preform spinning	12,400	34[a]	0.017	2017	Edavalath [120]
On-axis twisted chiral fiber gratings						
Chiral intermediate period grating	Post-processing (open flame)	24	0		2021	Zou [91]
Chiral intermediate period grating	Post-processing (oven)	45	0		2004	Kopp [92]
Chiral long period grating	Post-processing (oven)	78	0		2004	Kopp [92]
Chiral long period grating	Post-processing (oven)	300	<1		2005	Ivanov [95]
Chiral long period grating	Post-processing (CO2 laser)	400	<1		2021	Ren [96]
Chiral long period grating	Post-processing (CO2 laser)	811	0		2004	Oh [97]

Type	Fabrication method	Twist period P [µm]	Radius ρ [µm]	$\alpha\rho$	Year	Ref.
Off-axis twisted waveguides						
Helix metasurface[c]	3D nanoprinting/electroplating	1.8	0.5	1.75	2009	Gansel [89]
Off-axis twisted waveguide	3D nanoprinting	500	40	0.5	2020	Gao [102]
Chiral long period grating	Post-processing (oven)	589	52	0.55	2010	Kopp [100]
Off-axis solid-core PCF	Preform spinning	1,880	95[b]	0.32	2009	Argyros [108]
Helical core fiber	Preform spinning	2,000	184	0.58	1985	Varnham [109]
Chirally-coupled-core fiber	Preform spinning	6,100	27	0.03	2011	Ma [115]
Helical waveguide array	Direct laser writing in glass	10,000	10	0.006	2018	Stutzer [116]
Fiber wound around cylinder	Macroscopic winding	12,000	48,000	25	1984	Ross [117]
Fiber wound around cylinder	Macroscopic winding	300,000	280,000	5.9	1986	Tomita [289]
On-axis spun optical fiber (commercially available)						
Bow-tie (SHB1250(7.3/80)-2.5mm)	Preform spinning	2,500	0			Fibercore [118]
Bow-tie (SHB1250)	Preform spinning	4,800	0			Thorlabs [112]
Polarization maintaining fiber (SH 1310_125-5/250)	Preform spinning	5,000	0			YOFC [113]
Theory & simulation						
Frenet-Serret, helicoidal, and Over-felt waveguide	-	50	14	1.76	2023	**This work**
Frenet-Serret waveguide	-	118[d]	3.5[d]	0.19	2021	Chen [103]
Twisted solid-core PCF	-	622	12[a]	0.12	2013	Weiss [104]

[a] Radius corresponding to outer rod.
[b] Radius corresponding to off-axis core.
[c] Not used as a waveguide because maximal achieved length is only about 5 µm.
[d] For a wavelength of 770 nm.

Appendix D

Additional Simulation Results for Off-axis Twisted Waveguides

To allow a better comparison of the modal properties across the three investigated off-axis twisted waveguide types, detailed plots for different twist rates are available on the next pages. Only the results for multimode waveguides are shown while identical plots are available for the single-mode variants in the Supplemental Material of the corresponding manuscript preprint [281]. The following optical properties (defined in Chapter 2) were evaluated:

- Longitudinal component of the Poynting vector S_{T}.
  - Corresponds to the intensity that would be measured at the output of the waveguide.
- Transverse component of the Poynting vector S_{NB}.
  - Both, the longitudinal and transverse components were scaled by the same value so that their magnitude can be compared.
  - If this component curls around the center of the waveguide in the azimuthal direction, the mode contains OAM. A small fraction of OAM is present in the fundamental modes because spin and OAM are only well separated as long as the paraxial approximation is strictly valid [302]. For the single-mode waveguides in particular, the paraxial approximation is not well satisfied and some of the spin angular momentum is converted to OAM while the total angular momentum is conserved [161].
- Transverse component of electric and magnetic field, $\mathbf{E}_{\mathrm{NB}}$ and $\mathbf{H}_{\mathrm{NB}}$, respectively.
  - White ellipses denote shape and orientation of the polarization ellipse within the NB plane (i.e., neglecting the longitudinal field component). Arrows indicate the direction of rotation of the polarization vector in time.

- Spin vector of electric and magnetic field, $\mathbf{s_E}$ and $\mathbf{s_H}$, respectively.
  - The magnitude of the spin vector corresponds to the Stokes parameter $\hat{S}_3$ of the respective field.
  - The transverse component of the spin vector is shown on top of $\hat{S}_3$ in the square-shaped plots.
  - The longitudinal component of the spin vector can be seen in the projection of the spin vector onto the TB plane shown in the rectangular box below. The height of the box corresponds to the maximal value of 1. The scaling of the arrows in the box and the rectangle is the same.
- Phase of one of the transverse components of the electric and magnetic field.
  - The phase of the B component is shown unless the N component is dominant. Labels in the plots indicate which component is shown.
  - The absolute value of the phase varies between plots.
- Characterization of the chirality of the fields in the form of g_{field}.
  - If $|g_{\text{field}}| > n$, the field is superchiral.
  - g_{field} is not shown for multimode waveguides since its magnitude is close to n at all twist rates.

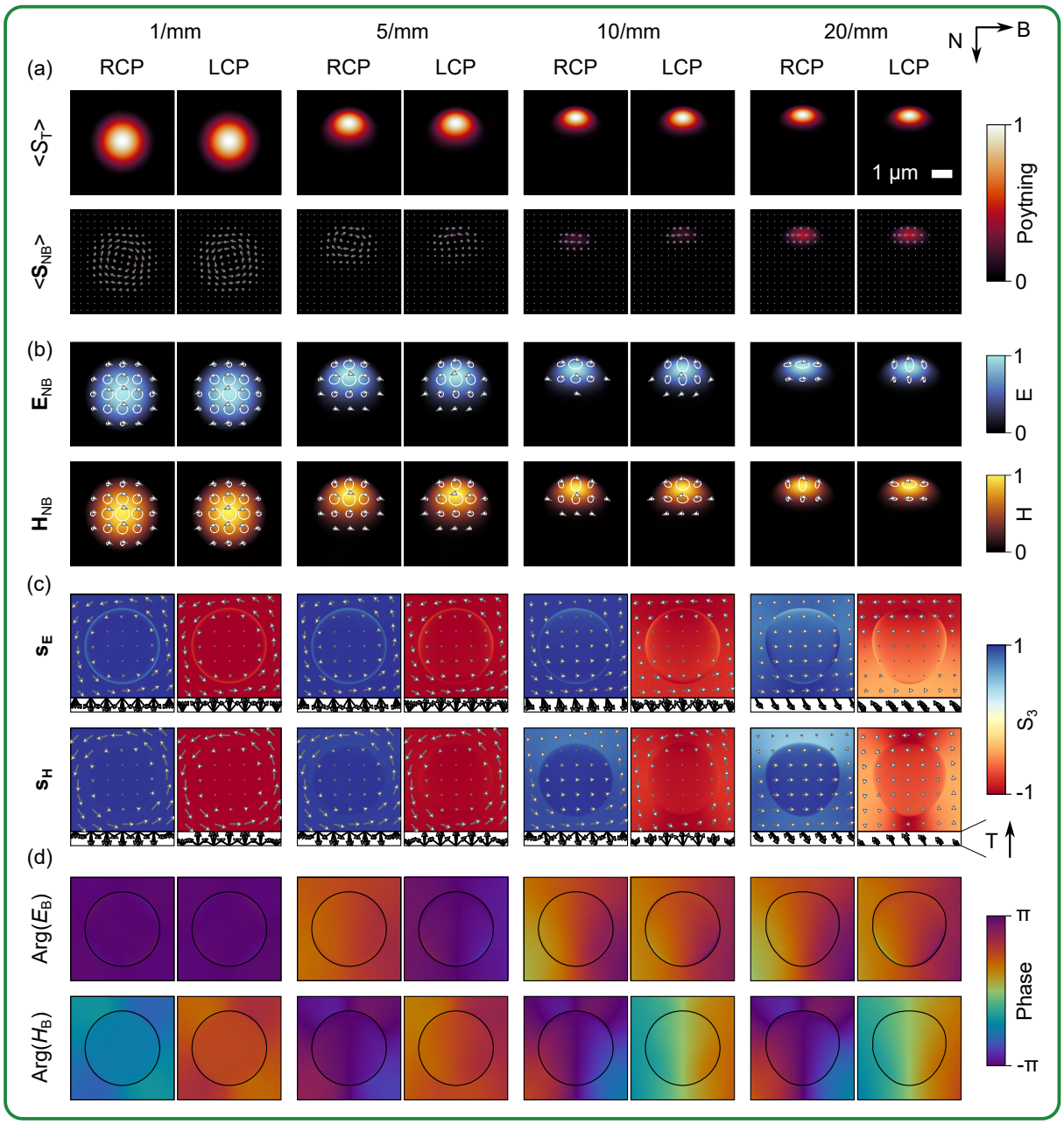

Figure D.1: Spatial properties of fundamental modes in the multimode Frenet-Serret waveguide ($V = 17.25$) depicted in the TNB frame. Four different twist rates from 1/mm to 20/mm are shown. Modes remain circularly polarized up to the highest twist rate. The cross sections of the waveguides are shown as black lines in (d). Since the cross section is approximated as an ellipse in the xy plane (cf. Section 5.1), the cross section in the TNB frame is not perfectly circular. Quantities depicted in (a-d) are explained at the beginning of this chapter.

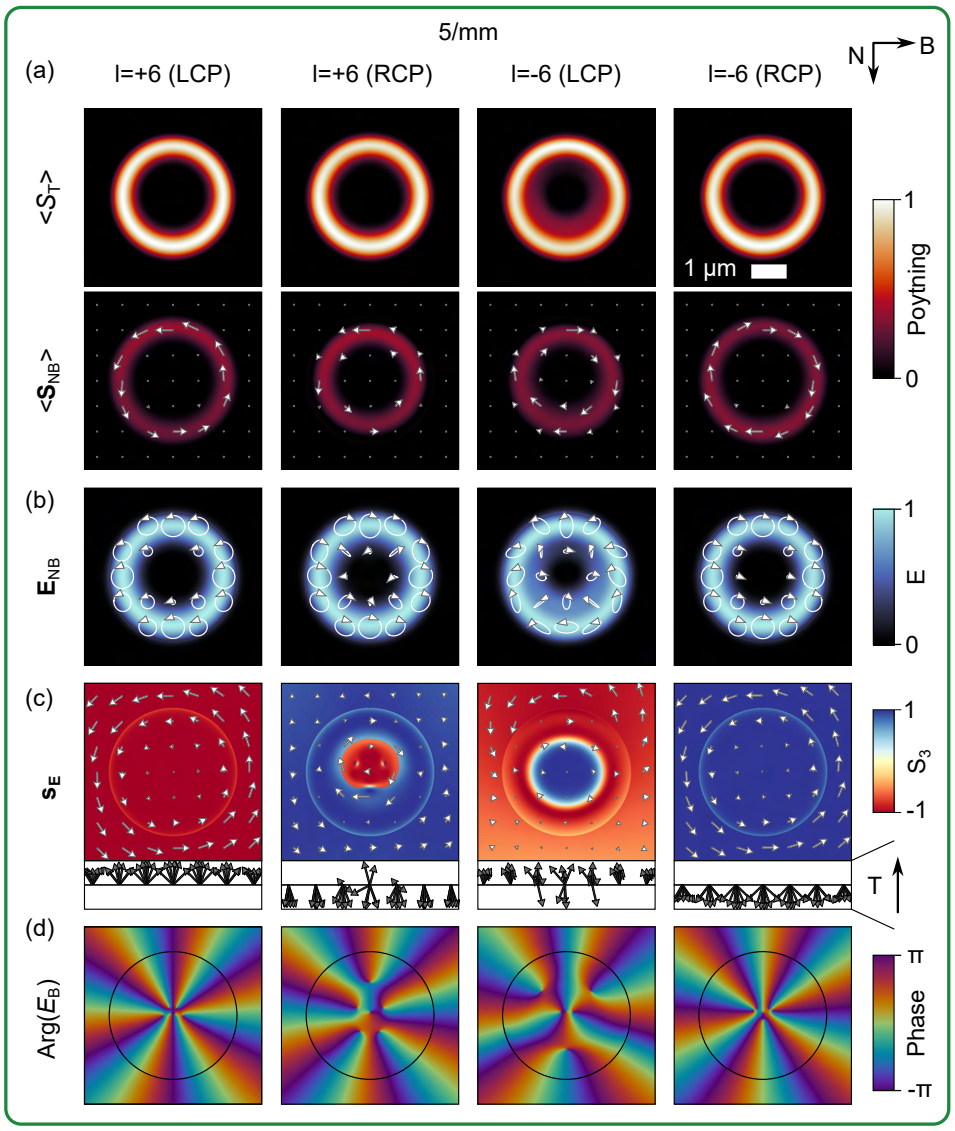

Figure D.2: Spatial properties of OAM modes ($|l| = 6$) in the multimode Frenet-Serret waveguide ($V = 17.25$) depicted in the TNB frame. Modes are evaluated at an intermediate twist rate of 5/mm. The cross sections of the waveguides are shown as black lines in (d). The two modes in the center ($l = +6$ (RCP), $l = -6$ (LCP)) are coupled to higher-order modes causing the changes in their phase and polarization properties (cf. Section 5.3). Quantities depicted in (a-d) are explained at the beginning of this chapter.

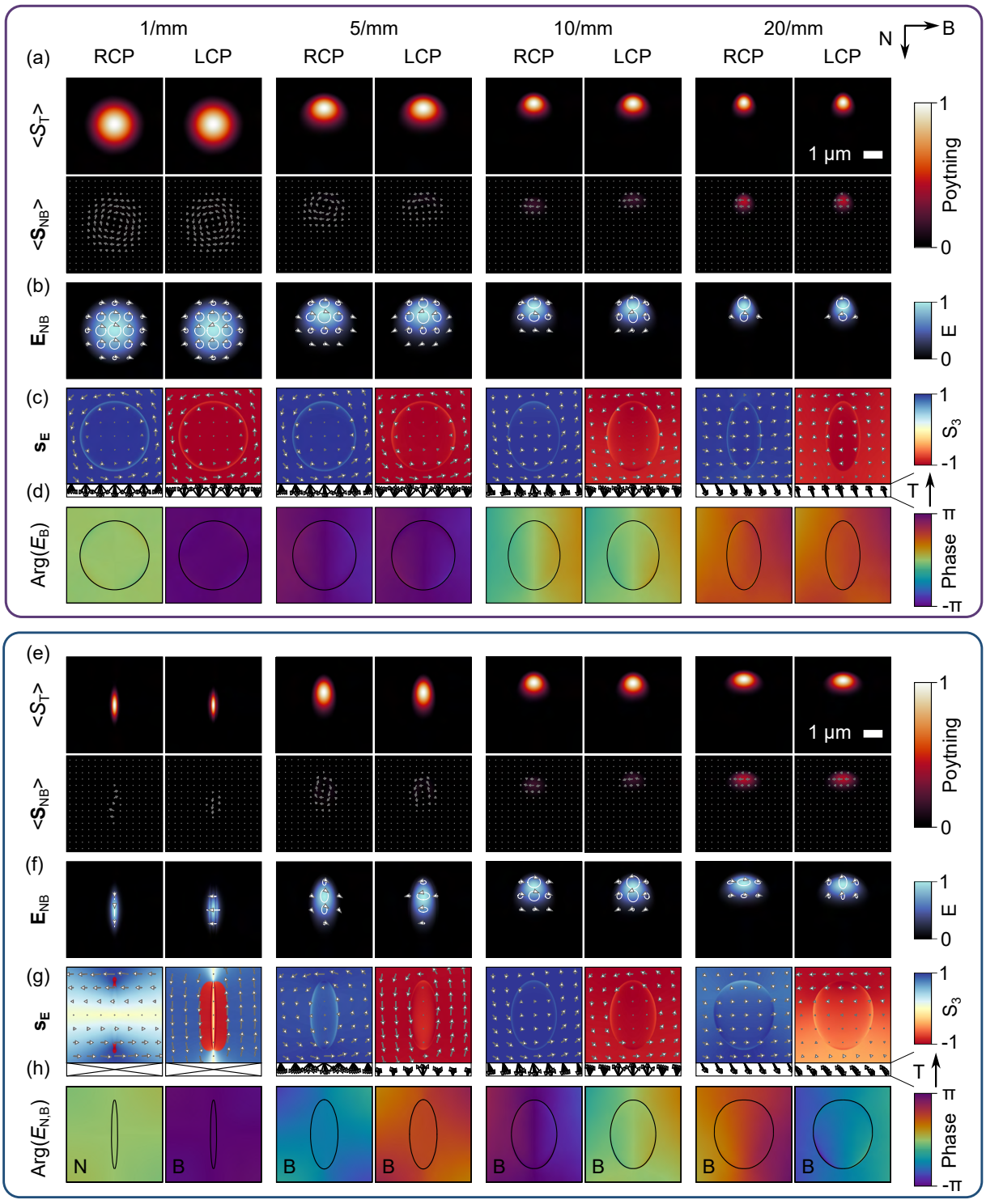

Figure D.3: Spatial properties of fundamental modes in the multimode helicoidal waveguide (a-d) and the multimode Overfelt waveguide (e-h) depicted in the TNB frame. Four different twist rates from 1/mm to 20/mm are shown. The cross sections of the waveguides are shown as black lines in (d,h). Longitudinal components of the spin vector in the first two entries in (g) are not shown because they are negligibly small. Quantities depicted in (a-h) are explained at the beginning of this chapter.

As shown in Fig. 5.11 of the main text, superchiral fields can occur on the surface of helicoidal waveguides. Concerning this figure, additional line cuts of g_{field} along the N direction for different twist rates can be found here in Fig. D.4.

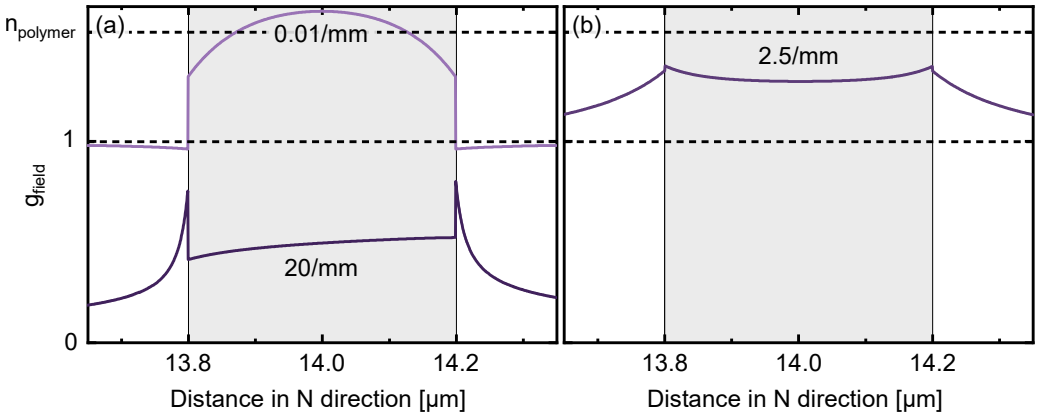

Figure D.4: Superchiral fields in helicoidal waveguides. g_{field} was evaluated for the LCP fundamental mode along the N direction through the center of the waveguide. This is an extension of Fig. 5.11(b) of the main text. (a) At low twist rates (0.01/mm), g_{field} is close to n like in a circularly polarized plane wave. At high twist rates (20/mm) the field becomes linearly polarized resulting in an overall lower value of g_{field}. (b) At an intermediate twist rate (2.5/mm) the field becomes superchiral on the surface of the waveguide ($g_{\text{field}}>1$).

Appendix E

Additional Simulation Results for Twisted Light Cages

E.1 Spiraling Phase Patterns in OAM Modes

Fig. 6.4(c) shows that modes carrying OAM feature a spiraling phase profile on the outside of the core, which is different from the OAM phase profile inside the core. The spiraling pattern arises as the sum of an OAM phase profile with that of a diverging lens whose focal length is found to be largely independent of twist rate and OAM order. The diverging field outside of the core might be related to the higher propagation loss of OAM modes compared to the fundamental modes, as energy is constantly carried away from the core.

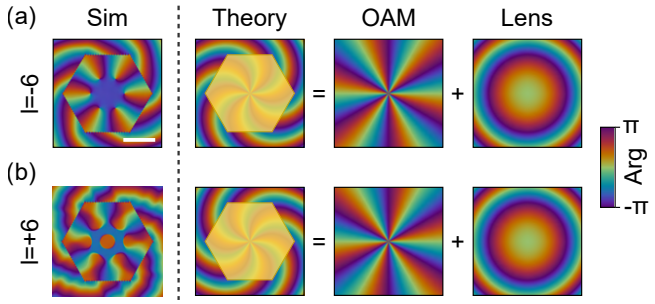

Figure E.1: Interpretation of "spiraling" phase profile of OAM modes shown in Fig. 6.4. For negative OAM (a), the phase profile twists counterclockwise outside of the core region, while it twists clockwise for positive OAM (b). Phase profiles on the left were simulated for a RCP mode at a twist rate of 0.8/mm. The twisting phase profile can be modeled as the sum of an $\exp(il\phi)$ phase profile and the phase of a diverging lens (focal length: -190 µm). Inside the core (yellow shaded area), the phase profile does not twist. Scale bar denotes 10 µm.

E.2 Additional Twist-induced Resonances

Here, two more resonances in twisted light cages are analyzed, completing the analysis presented in Fig. 6.4. The simulation results corroborate the explanation of twist-induced resonances in Section 6.2.

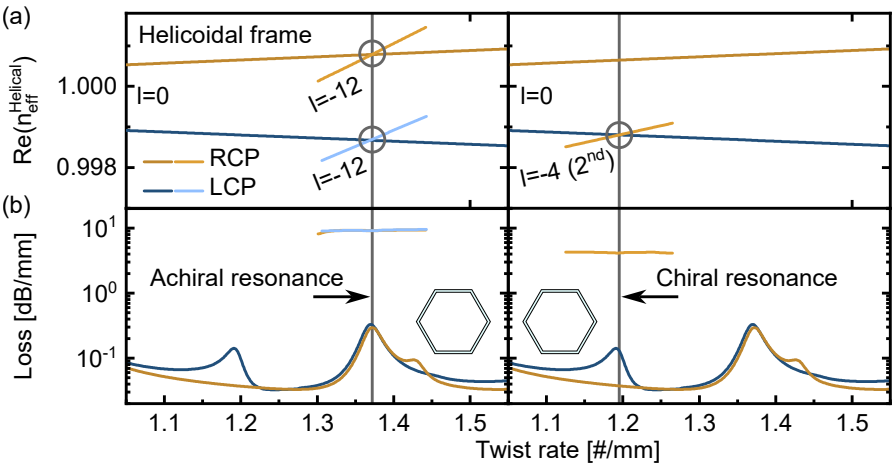

Figure E.2: Further twist induced resonances in single-mode strand light cages supplementing Fig. 6.4. (a) Real part of the effective index in the helicoidal frame and (b) attenuation of the fundamental core modes ($l = 0$) and relevant higher-order core modes. Left panel shows the second achiral resonance ($\Delta s = 0,\ \Delta l = 12$), and right panel a further chiral resonance ($\Delta s = +2,\ \Delta l = 4$). The OAM mode involved in the chiral resonance is of second radial order (i.e., $m = 2$ in the notation used for the tube model in Section 6.5).

E.3 Optical Properties of Multimode Strand Light Cages

The analysis of multimode strand light cages in the main part of the thesis was limited to the four twist rates of the fabricated samples. Here, additional results are presented for intermediate twist rates. Note that these results were calculated for a strand diameter of $2r_c = 3.6$ µm with left-handed twisting direction, while the results shown in Fig. 6.13 pertain to right-handed structures with $2r_c = 3.814$ µm.

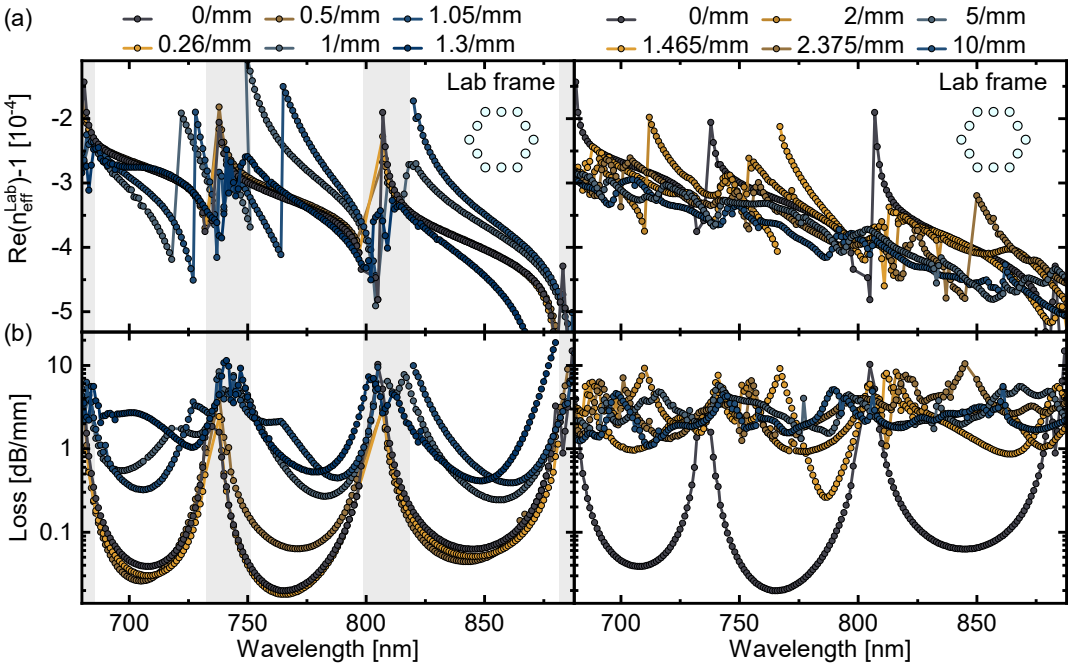

Figure E.3: Dispersion (a) and attenuation (b) of the RCP fundamental mode in multimode strand light cages at different twist rates. Dispersion was calculated in the lab frame using Eq. 5.2. Left panel: low twist rates (0 - 1.3/mm). Right panel: high twist rates (1.465 - 10/mm). Twisting induces resonances to higher-order core modes, e.g., at a wavelength of 770 nm for a twist rate of 1.05/mm.

The left panel of Fig. E.3 and Fig. E.4 indicate that the spectral position of core-strand resonances is nearly unaffected by twisting. This can be understood based on the analysis of off-axis twisted waveguides in Chapter 5. The strands of multimode strand twisted light cages correspond exactly to the multimode helicoidal waveguides analyzed earlier. Twisting was shown to increase the effective modal index of the strands due to the increased path that the light has to travel along the helical trajectory (cf. Eq. 5.6). However, light in the core remains on the twist axis and is therefore not forced to travel along an elongated path. Thus, the effective index of the core mode (evaluated in the lab frame) does not increase with twist rate as shown in Fig. 6.8. Since the index of the core is lower than that of the strands, twisting only increases this index difference further. Core-strand resonances therefore still only occur at the cut-offs of the strand modes (see more details in Section 4.2.2 on the untwisted light cages), which are apparently (mostly) unaffected by twisting.

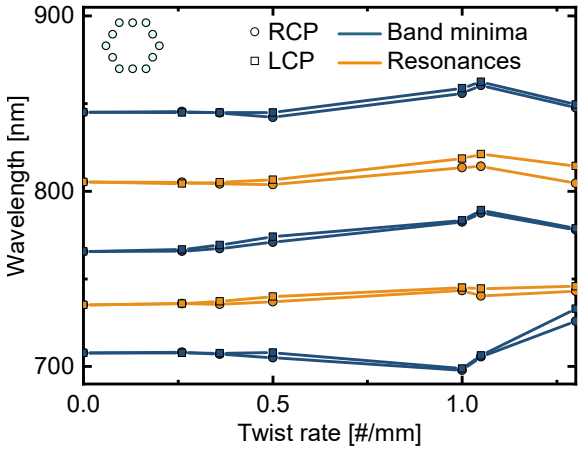

Figure E.4: Impact of twisting on the spectral position of core-strand resonances and transmission band minima. Analysis was performed for multimode strand light cages based on the data in Fig. E.3. Positions of core-strand resonances (orange) remain mostly unaffected by twisting while transmission band minima (blue) may shift due to twist-induced core-core resonances.

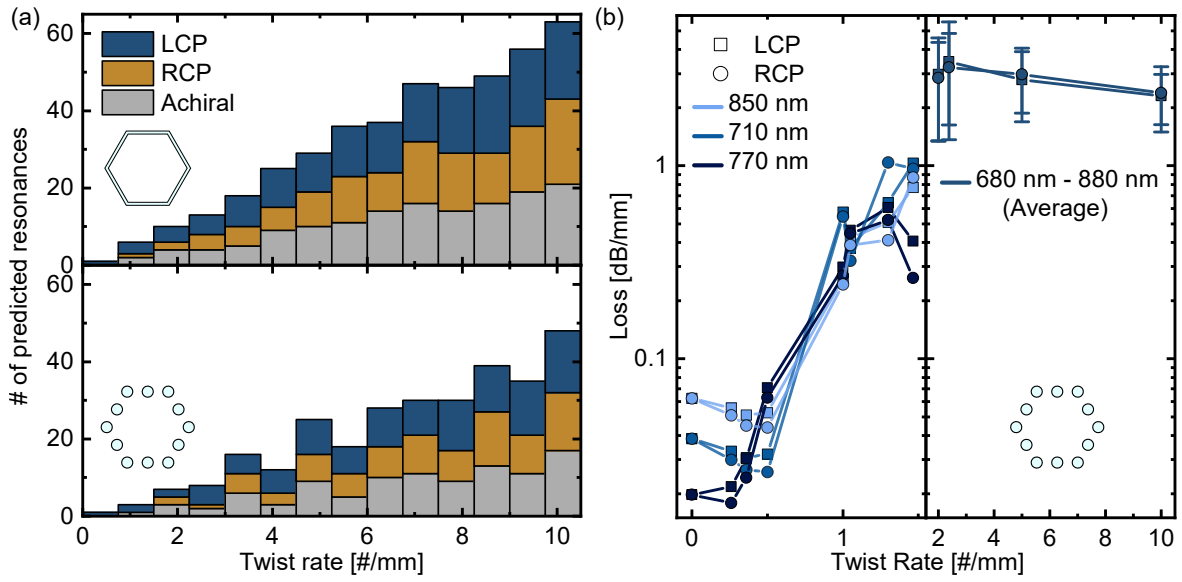

Figure E.5: Explanation for increased loss at high twist rates. (a) The number of allowed resonances (chiral: blue/brown, achiral: gray) increases with twist rate according to Eq. 6.6 both for the single-mode strand (top) and multimode strand variant (bottom). (b) The attenuation of the fundamental modes in the multimode strand light cage increases strongly with twist rate. For low twist rates (left side), the loss was evaluated at the off-resonance point of the three transmission bands indicated in the legend (data was taken from Fig. E.3). For high twist rates, individual transmission bands cannot be distinguished and the loss was averaged between 680 nm - 880 nm (right side). Error bars denote the corresponding standard deviation.

Bibliography

[1] T. H. Maiman. *Stimulated Optical Radiation in Ruby.* Nature **187** (1960), 493–494.

[2] M. Hentschel, R. Kienberger, C. Spielmann, G. A. Reider, N. Milosevic et al. *Attosecond metrology.* Nature **414** (2001), 509–513.

[3] B. P. Abbott, R. Abbott, T. D. Abbott, M. R. Abernathy, F. Acernese et al. *Observation of Gravitational Waves from a Binary Black Hole Merger.* Physical Review Letters **116** (2016), 061102.

[4] I. Bloch, J. Dalibard, W. Zwerger. *Many-body physics with ultracold gases.* Reviews of Modern Physics **80** (2008), 885–964.

[5] *The Nobel Prize in Physics 2017.* https://www.nobelprize.org/prizes/physics/2017/press-release/ [accessed 16-Dec-2023].

[6] *The Nobel Prize in Physics 2022.* https://www.nobelprize.org/prizes/physics/2022/summary/ [accessed 16-Dec-2023].

[7] *The Nobel Prize in Physics 2018.* https://www.nobelprize.org/prizes/physics/2018/summary/ [accessed 16-Dec-2023].

[8] *The Nobel Prize in Physics 2023.* https://www.nobelprize.org/prizes/physics/2023/press-release/ [accessed 16-Dec-2023].

[9] E. Sicard, L. Trojman. *Introducing 3-nm Nano-Sheet FET technology in Microwind.* Hyper Articles en Ligne (2021), hal–03377556.

[10] J. Hecht. *City of Light: The Story of Fiber Optics.* The Sloan Technology Series. Oxford Univ. Press (2009).

[11] J. Issa, Z. Yin, C. Polymeropoulos, Y. Jaluria. *Temperature distribution in an optical fiber draw tower furnace.* Journal of Materials Processing and Manufacturing Science **4** (1996), 221–232.

[12] K. Kao, G. Hockham. *Dielectric-fibre surface waveguides for optical frequencies.* Proceedings of the Institution of Electrical Engineers **113** (1966), 1151–1158.

[13] *The Nobel Prize in Physics 2009.* https://www.nobelprize.org/prizes/physics/2009/illustrated-information/ [accessed 16-Dec-2023].

[14] F. Couny, H. Sabert, P. J. Roberts, D. P. Williams, A. Tomlinson et al. *Visualizing the photonic band gap in hollow core photonic crystal fibers.* Optics Express **13** (2005), 558–563.

[15] B. Debord, A. Amsanpally, M. Chafer, A. Baz, M. Maurel et al. *Ultralow transmission loss in inhibited-coupling guiding hollow fibers.* Optica **4** (2017), 209–217.

[16] K. J. Rowland. *Guiding Light in Low-Index Media via Multilayer Waveguides.* Ph.D. thesis, University of Adelaide (2010).

[17] R. F. Cregan, B. J. Mangan, J. C. Knight, T. A. Birks, P. St. J. Russell et al. *Single-Mode Photonic Band Gap Guidance of Light in Air.* Science **285** (1999), 1537–1539.

[18] G. T. Jasion, H. Sakr, J. R. Hayes, S. R. Sandoghchi, L. Hooper et al. *0.174 dB/km Hollow Core Double Nested Antiresonant Nodeless Fiber (DNANF).* In: *Optical Fiber Communication Conference*, Th4C.7. Optica Publishing Group (2022).

[19] Y. Tamura, H. Sakuma, K. Morita, M. Suzuki, Y. Yamamoto et al. *Lowest-Ever 0.1419-dB/km Loss Optical Fiber.* In: *Optical Fiber Communication Conference*, Th5D.1. Optica Publishing Group (2017).

[20] H. Sakr, G. Jasion, T. Bradley, J. Hayes, H. C. Mulvad et al. *Hollow core optical fibres with comparable attenuation to silica fibres between 600 and 1100 nm.* Nature Communications **11** (2020), 6030.

[21] B. Debord, F. Amrani, L. Vincetti, F. Gérôme, F. Benabid. *Hollow-Core Fiber Technology: The Rising of "Gas Photonics".* Fibers **7** (2019), 16.

[22] A. M. Cubillas, S. Unterkofler, T. G. Euser, B. J. M. Etzold, A. C. Jones et al. *Photonic crystal fibres for chemical sensing and photochemistry.* Chemical Society Reviews **42** (2013), 8629–8648.

[23] A. M. Cubillas, M. Silva-Lopez, J. M. Lazaro, O. M. Conde, M. N. Petrovich et al. *Methane detection at 1670-nm band using a hollow-core photonic bandgap fiber and a multiline algorithm.* Optics Express **15** (2007), 17570–17576.

[24] P. Jaworski, P. Kozioł, K. Krzempek, D. Wu, F. Yu et al. *Antiresonant Hollow-Core Fiber-Based Dual Gas Sensor for Detection of Methane and Carbon Dioxide in the Near- and Mid-Infrared Regions.* Sensors **20** (2020), 3813.

[25] S. Smolka, M. Barth, O. Benson. *Highly efficient fluorescence sensing with hollow core photonic crystal fibers.* Optics Express **15** (2007), 12783–12791.

[26] G. O. S. Williams, T. G. Euser, P. S. J. Russell, A. C. Jones. *Spectrofluorimetry with attomole sensitivity in photonic crystal fibres.* Methods and Applications in Fluorescence **1** (2013), 015003.

[27] S. Hanf, R. Keiner, D. Yan, J. Popp, T. Frosch. *Fiber-Enhanced Raman Multigas Spectroscopy: A Versatile Tool for Environmental Gas Sensing and Breath Analysis.* Analytical Chemistry **86** (2014), 5278–5285.

[28] D. Yan, J. Popp, M. W. Pletz, T. Frosch. *Highly sensitive broadband raman sensing of antibiotics in step-index hollow-core photonic crystal fibers.* ACS Photonics **4** (2017), 138–145.

[29] A. Knebl, D. Yan, J. Popp, T. Frosch. *Fiber enhanced Raman gas spectroscopy.* Trends in Analytical Chemistry **103** (2018), 230–238.

[30] W. Reuter. *Ultra-Sensitive Method for the Detection of Illegal Dyes in Food Spices.* The Column **14** (2018), 21–24.

[31] C. Wu, A. B. Khanikaev, R. Adato, N. Arju, A. A. Yanik et al. *Fano-resonant asymmetric metamaterials for ultrasensitive spectroscopy and identification of molecular monolayers.* Nature Materials **11** (2012), 69–75.

[32] S. Nie, S. R. Emory. *Probing Single Molecules and Single Nanoparticles by Surface-Enhanced Raman Scattering.* Science **275** (1997), 1102–1106.

[33] K. Kneipp, Y. Wang, H. Kneipp, L. T. Perelman, I. Itzkan et al. *Single Molecule Detection Using Surface-Enhanced Raman Scattering (SERS).* Physical Review Letters **78** (1997), 1667–1670.

[34] J. B. Jensen, P. E. Hoiby, G. Emiliyanov, O. Bang, L. H. Pedersen et al. *Selective detection of antibodies in microstructured polymer optical fibers.* Optics Express **13** (2005), 5883–5889.

[35] P. Kumar, L. Morawska, C. Martani, G. Biskos, M. Neophytou et al. *The rise of low-cost sensing for managing air pollution in cities.* Environment International **75** (2015), 199–205.

[36] O. Lawal, W. M. Ahmed, T. M. E. Nijsen, R. Goodacre, S. J. Fowler. *Exhaled breath analysis: A review of 'breath-taking' methods for off-line analysis.* Metabolomics **13** (2017), 110.

[37] G. Wysocki, A. A. Kosterev, F. K. Tittel. *Spectroscopic trace-gas sensor with rapidly scanned wavelengths of a pulsed quantum cascade laser for in situ NO monitoring of industrial exhaust systems.* Applied Physics B **80** (2005), 617–625.

[38] P. Liu, Z. Li, B. Li, G. Shi, M. Li et al. *The analysis of time-resolved optical waveguide absorption spectroscopy based on positive matrix factorization.* Journal of Colloid and Interface Science **403** (2013), 134–141.

[39] M. Nissen, B. Doherty, J. Hamperl, J. Kobelke, K. Weber et al. *UV absorption spectroscopy in water-filled antiresonant hollow core fibers for pharmaceutical detection.* Sensors **18** (2018), 478.

[40] H. Schmidt, A. Hawkins. *Atomic spectroscopy and quantum optics in hollow-core waveguides.* Laser & Photonics Reviews **4** (2010), 720–737.

[41] J. P. Epping, T. Hellwig, M. Hoekman, R. Mateman, A. Leinse et al. *On-chip visible-to-infrared supercontinuum generation with more than 495 THz spectral bandwidth.* Optics Express **23** (2015), 19596–19604.

[42] B. Kuyken, T. Ideguchi, S. Holzner, M. Yan, T. Haensch et al. *An octave spanning mid-infrared frequency comb generated in a silicon nanophotonic wire waveguide.* Nature Communications **6** (2015), 6310.

[43] G. Roelkens, L. Liu, D. Liang, R. Jones, A. Fang et al. *III-V/silicon photonics for on-chip and intra-chip optical interconnects.* Laser & Photonics Reviews **4** (2010), 751–779.

[44] D. Pohl, M. Reig Escalé, M. Madi, F. Kaufmann, P. Brotzer et al. *An integrated broadband spectrometer on thin-film lithium niobate.* Nature Photonics **14** (2020), 1–6.

[45] D. Kita, B. Miranda, D. Favela, D. Bono, J. Michon et al. *High-performance and scalable on-chip digital Fourier transform spectroscopy.* Nature Communications **9** (2018), 4405.

[46] M. Souza, A. Grieco, N. Frateschi, Y. Fainman. *Fourier transform spectrometer on silicon with thermo-optic non-linearity and dispersion correction.* Nature Communications **9** (2018), 665.

[47] M. Chemnitz, G. Schmidl, A. Schwuchow, M. Zeisberger, U. Hübner et al. *Enhanced sensitivity in single-mode silicon nitride stadium resonators at visible wavelengths.* Optics Letters **41** (2016), 5377–5380.

[48] L. Tombez, E. J. Zhang, J. S. Orcutt, S. Kamlapurkar, W. M. J. Green. *Methane absorption spectroscopy on a silicon photonic chip.* Optica **4** (2017), 1322–1325.

[49] L. Stern, B. Desiatov, N. Mazurski, U. Levy. *Strong coupling and high contrast all optical modulation in atomic cladding waveguides.* Nature Communications **8** (2016), 14461.

[50] A. Säynätjoki, L. Karvonen, T. Alasaarela, X. Tu, T.-Y. Liow et al. *Low-loss silicon slot waveguides and couplers fabricated with optical lithography and atomic layer deposition.* Optics Express **19** (2011), 26275–82.

[51] C. A. Barrios, K. B. Gylfason, B. Sánchez, A. Griol, H. Sohlström et al. *Slot-waveguide biochemical sensor.* Optics Letters **32** (2007), 3080–3082.

[52] H. Sun, A. Chen, L. Dalton. *Enhanced evanescent confinement in multiple-slot waveguides and its application in biochemical sensing.* IEEE Photonics Journal **1** (2009), 48–57.

[53] M. A. Duguay, Y. Kokubun, T. L. Koch, L. Pfeiffer. *Antiresonant reflecting optical waveguides in SiO2-Si multilayer structures.* Applied Physics Letters **49** (1986), 13–15.

[54] D. Yin, H. Schmidt, J. Barber, A. Hawkins. *Integrated ARROW waveguides with hollow cores.* Optics Express **12** (2004), 2710–2715.

[55] D. Yin, J. P. Barber, A. R. Hawkins, H. Schmidt. *Waveguide loss optimization in hollow-core ARROW waveguides.* Optics Express **13** (2005), 9331–9336.

[56] B. M. Masum, S. M. Aminossadati, M. S. Kizil, C. R. Leonardi. *Numerical and experimental investigations of pressure-driven gas flow in hollow-core photonic crystal fibers.* Applied Optics **58** (2019), 963.

[57] F. Davidson-Marquis, J. Gargiulo, E. Gómez-López, B. Jang, T. Kroh et al. *Coherent interaction of atoms with a beam of light confined in a light cage.* Light: Science & Applications **10** (2021), 114.

[58] M. Sprague, P. Michelberger, T. Champion, D. England, J. Nunn et al. *Broadband single-photon-level memory in a hollow-core photonic crystal fibre.* Nature Photonics **8** (2014), 287–291.

[59] K. T. Kaczmarek, D. J. Saunders, M. R. Sprague, W. S. Kolthammer, A. Feizpour et al. *Ultrahigh and persistent optical depths of cesium in Kagomé-type hollow-core photonic crystal fibers.* Optics Letters **40** (2015), 5582–5585.

[60] Y. Hoo, Shujing Liu, Hoi Lut Ho, Wei Jin. *Fast Response Microstructured Optical Fiber Methane Sensor With Multiple Side-Openings.* IEEE Photonics Technology Letters **22** (2010), 296–298.

[61] C. Hensley, D. H. Broaddus, C. B. Schaffer, A. L. Gaeta. *Photonic band-gap fiber gas cell fabricated using femtosecond micromachining.* Optics Express **15** (2007), 6690.

[62] F. Yang, W. Jin, Y. Lin, C. Wang, H. Lut et al. *Hollow-Core Microstructured Optical Fiber Gas Sensors.* Journal of Lightwave Technology **35** (2017), 3413–3424.

[63] C. M. B. Cordeiro, E. M. Dos Santos, C. H. Brito Cruz, C. J. De Matos, D. S. Ferreiira. *Lateral access to the holes of photonic crystal fibers – selective filling and sensing applications.* Optics Express **14** (2006), 8403.

[64] M. Giraud-Carrier, C. Hill, T. Decker, J. A. Black, H. Schmidt et al. *Perforated hollow-core optical waveguides for on-chip atomic spectroscopy and gas sensing.* Applied Physics Letters **108** (2016), 131105.

[65] M. R. Holmes. *Micropore and nanopore fabrication in hollow antiresonant reflecting optical waveguides.* Journal of Micro/Nanolithography, MEMS, and MOEMS **9** (2010), 023004.

[66] C. Jain, A. Braun, J. Gargiulo, B. Jang, G. Li et al. *Hollow Core Light Cage: Trapping Light Behind Bars.* ACS Photonics **6** (2019), 649–658.

[67] J. Bürger. *3D Laser-Nanoprinted Hollow Core Waveguides for Real-Time Sensing.* Master's thesis, LMU Munich (2020).

[68] M. Göppert-Mayer. *Über Elementarakte mit zwei Quantensprüngen.* Annalen der Physik **401** (1931), 273–294.

[69] S. Maruo, O. Nakamura, S. Kawata. *Three-dimensional microfabrication with two-photon-absorbed photopolymerization.* Optics Letters **22** (1997), 132–134.

[70] H. Ren, X. Fang, J. Jang, J. Bürger, J. Rho et al. *Complex-amplitude metasurface-based orbital angular momentum holography in momentum space.* Nature Nanotechnology **15** (2020), 948–955.

[71] T. Frenzel, M. Kadic, M. Wegener. *Three-dimensional mechanical metamaterials with a twist.* Science **358** (2017), 1072–1074.

[72] M. Kadic, G. W. Milton, M. Van Hecke, M. Wegener. *3D metamaterials.* Nature Reviews Physics **1** (2019), 198–210.

[73] M. Deubel, G. von Freymann, M. Wegener, S. Pereira, K. Busch et al. *Direct laser writing of three-dimensional photonic-crystal templates for telecommunications.* Nature Materials **3** (2004), 444–447.

[74] T. Gissibl, S. Thiele, A. Herkommer, H. Giessen. *Two-photon direct laser writing of ultracompact multi-lens objectives.* Nature Photonics **10** (2016), 554–560.

[75] P.-I. Dietrich, M. Blaicher, I. Reuter, M. Billah, T. Hoose et al. *In-situ 3D nano-printing of freeform coupling elements for hybrid photonic integration.* Nature Photonics **12** (2018), 241–247.

[76] N. Lindenmann, G. Balthasar, D. Hillerkuss, R. Schmogrow, M. Jordan et al. *Photonic wire bonding: A novel concept for chip-scale interconnects.* Optics Express **20** (2012), 17667–17677.

[77] F. Klein, B. Richter, T. Striebel, C. M. Franz, G. von Freymann et al. *Two-Component Polymer Scaffolds for Controlled Three-Dimensional Cell Culture.* Advanced Materials **23** (2011), 1341–1345.

[78] V. Melissinaki, A. A. Gill, I. Ortega, M. Vamvakaki, A. Ranella et al. *Direct laser writing of 3D scaffolds for neural tissue engineering applications.* Biofabrication **3** (2011), 045005.

[79] A. Doraiswamy, C. Jin, R. J. Narayan, P. Mageswaran, P. Mente et al. *Two photon induced polymerization of organic–inorganic hybrid biomaterials for microstructured medical devices.* Acta Biomaterialia **2** (2006), 267–275.

[80] F. Mayer, S. Richter, J. Westhauser, E. Blasco, C. Barner-Kowollik et al. *Multimaterial 3D laser microprinting using an integrated microfluidic system.* Science Advances **5** (2019), eaau9160.

[81] B. Jang, J. Gargiulo, R. F. Ando, A. Lauri, S. A. Maier et al. *Light guidance in photonic band gap guiding dual-ring light cages implemented by direct laser writing.* Optics Letters **44** (2019), 4016.

[82] B. Jang, J. Gargiulo, M. Ziegler, R. F. Ando, U. Hübner et al. *Fine-tuning of the optical properties of hollow-core light cages using dielectric nanofilms.* Optics Letters **45** (2020), 196.

[83] B. Jang, J. Gargiulo, J. Kim, J. Bürger, S. Both et al. *Fiber-integrated hollow-core light cage for gas spectroscopy.* APL Photonics **6** (2021), 061301.

[84] J. Kim, B. Jang, J. Gargiulo, J. Bürger, J. Zhao et al. *The Optofluidic Light Cage – On-Chip Integrated Spectroscopy Using an Antiresonance Hollow Core Waveguide.* Analytical Chemistry **93** (2021), 752–760.

[85] Y. Tang, A. E. Cohen. *Optical Chirality and Its Interaction with Matter.* Physical Review Letters **104** (2010), 163901.

[86] K. Y. Bliokh, F. Nori. *Characterizing optical chirality.* Physical Review A **83** (2011), 021803.

[87] E. Hendry, T. Carpy, J. Johnston, M. Popland, R. V. Mikhaylovskiy et al. *Ultrasensitive detection and characterization of biomolecules using superchiral fields.* Nature Nanotechnology **5** (2010), 783–787.

[88] A. Kuzyk, R. Schreiber, Z. Fan, G. Pardatscher, E.-M. Roller et al. *DNA-based self-assembly of chiral plasmonic nanostructures with tailored optical response.* Nature **483** (2012), 311–314.

[89] J. K. Gansel, M. Thiel, M. S. Rill, M. Decker, K. Bade et al. *Gold Helix Photonic Metamaterial as Broadband Circular Polarizer.* Science **325** (2009), 1513–1515.

[90] L. A. Nguyen, H. He, C. Pham-Huy. *Chiral Drugs: An Overview.* International Journal of Biomedical Science **2** (2006), 85–100.

[91] T. Zou, J. Zhong, S. Liu, G. Zhu, Y. Zhao et al. *Helical Intermediate-Period Fiber Grating for Refractive Index Measurements With Low-Sensitive Temperature and Torsion Response.* Journal of Lightwave Technology **39** (2021), 6678–6685.

[92] V. I. Kopp, V. M. Churikov, J. Singer, N. Chao, D. Neugroschl et al. *Chiral Fiber Gratings.* Science **305** (2004), 74–75.

[93] X. Xi, G. K. L. Wong, T. Weiss, P. S. J. Russell. *Measuring mechanical strain and twist using helical photonic crystal fiber.* Optics Letters **38** (2013), 5401–5404.

[94] G. K. L. Wong, X. M. Xi, M. H. Frosz, P. St.J. Russell. *Enhanced optical activity and circular dichroism in twisted photonic crystal fiber.* Optics Letters **40** (2015), 4639.

[95] O. V. Ivanov. *Fabrication of long-period fiber gratings by twisting a standard single-mode fiber.* Optics Letters **30** (2005), 3290–3292.

[96] K. Ren, L. Ren, J. Liang, L. Yang, J. Xu et al. *Excitation of high-quality orbital angular momentum vortex beams in an adiabatically helical-twisted single-mode fiber.* Optics Express **29** (2021), 8441.

[97] S. Oh, K. R. Lee, U.-C. Paek, Y. Chung. *Fabrication of helical long-period fiber gratings by use of a CO_2 laser.* Optics Letters **29** (2004), 1464–1466.

[98] G. K. L. Wong, M. S. Kang, H. W. Lee, F. Biancalana, C. Conti et al. *Excitation of Orbital Angular Momentum Resonances in Helically Twisted Photonic Crystal Fiber.* Science **337** (2012), 446–449.

[99] X. M. Xi, T. Weiss, G. K. L. Wong, F. Biancalana, S. M. Barnett et al. *Optical Activity in Twisted Solid-Core Photonic Crystal Fibers.* Physical Review Letters **110** (2013), 143903.

[100] V. I. Kopp, V. M. Churikov, J. Singer, D. Neugroschl, A. Z. Genack. *Chiral fiber sensors.* In: *SPIE Defense, Security, and Sensing*, 76770U (2010).

[101] A. Bertoncini, C. Liberale. *3D printed waveguides based on photonic crystal fiber designs for complex fiber-end photonic devices.* Optica **7** (2020), 1487.

[102] H. Gao, G. F. R. Chen, P. Xing, J. W. Choi, H. Y. Low et al. *High-Resolution 3D Printed Photonic Waveguide Devices.* Advanced Optical Materials **8** (2020), 2000613.

[103] Y. Chen, P. St.J. Russell. *Frenet–Serret analysis of helical Bloch modes in N-fold rotationally symmetric rings of coupled spiraling optical waveguides.* Journal of the Optical Society of America B **38** (2021), 1173.

[104] T. Weiss, G. K. L. Wong, F. Biancalana, S. M. Barnett, X. M. Xi et al. *Topological Zeeman effect and circular birefringence in twisted photonic crystal fibers.* JOSA B **30** (2013), 2921–2927.

[105] R. Beravat, G. K. L. Wong, M. H. Frosz, X. M. Xi, P. S. Russell. *Twist-induced guidance in coreless photonic crystal fiber: A helical channel for light.* Science Advances **2** (2016), e1601421.

[106] P. St.J. Russell, R. Beravat, G. K. L. Wong. *Helically twisted photonic crystal fibres.* Philosophical Transactions of the Royal Society A: Mathematical, Physical and Engineering Sciences **375** (2017), 20150440.

[107] S. Loranger, Y. Chen, P. Roth, M. Frosz, G. K. L. Wong et al. *Bragg reflection and conversion between helical Bloch modes in chiral three-core photonic crystal fiber.* Journal of Lightwave Technology **38** (2020), 4100–4107.

[108] A. Argyros, J. Pla, F. Ladouceur, L. Poladian. *Circular and elliptical birefringence in spun microstructured optical fibres.* Optics Express **17** (2009), 15983–15990.

[109] M. P. Varnham. *Helical Core Circularly-Birefringent Fibers.* Proc. IOOC-ECOC (Venice) (1985), 135–138.

[110] X. M. Xi, G. K. L. Wong, M. H. Frosz, F. Babic, G. Ahmed et al. *Orbital-angular-momentum-preserving helical Bloch modes in twisted photonic crystal fiber.* Optica **1** (2014), 165.

[111] X. Zeng, P. S. Russell, C. Wolff, M. H. Frosz, G. K. L. Wong et al. *Nonreciprocal vortex isolator via topology-selective stimulated Brillouin scattering.* Science Advances **8** (2022), eabq6064.

[112] *Spec sheet of optical fiber (SHB1250, supplier: Thorlabs).* https://www.thorlabs.com/drawings/2c62d18a581c369c-8761DF56-CF0B-F53A-84FA2BB89FBAED44/SHB1250-SpecSheet.pdf [accessed 16-Dec-2023].

[113] *Spec sheet of optical fiber (SH1310_125-5/250, supplier: YOFC).* https://myphotos2020.oss-cn-beijing.aliyuncs.com/en/upload/20181219/1cv2mqsi9g1luh823.pdf [accessed 16-Dec-2023].

[114] P. Roth, G. K. L. Wong, M. H. Frosz, G. Ahmed, P. St.J. Russell. *Full-field characterization of helical Bloch modes guided in twisted coreless photonic crystal fiber.* Optics Letters **44** (2019), 5049.

[115] X. Ma, C.-H. Liu, G. Chang, A. Galvanauskas. *Angular-momentum coupled optical waves in chirally-coupled-core fibers.* Optics Express **19** (2011), 26515–26528.

[116] S. Stützer, Y. Plotnik, Y. Lumer, P. Titum, N. H. Lindner et al. *Photonic topological Anderson insulators.* Nature **560** (2018), 461–465.

[117] J. N. Ross. *The rotation of the polarization in low birefringence monomode optical fibres due to geometric effects.* Optical and Quantum Electronics **16** (1984), 455–461.

[118] *Spec sheet of optical fiber (SHB1250(7.3/80)-2.5mm, supplier: Fibercore).* https://www.lasercomponents.com/fileadmin/user_upload/home/Datasheets/fibercore/spun-fiber/spun_fiber.pdf [accessed 16-Dec-2023].

[119] P. Roth, Y. Chen, M. C. Günendi, R. Beravat, N. N. Edavalath et al. *Strong circular dichroism for the HE_{11} mode in twisted single-ring hollow-core photonic crystal fiber.* Optica **5** (2018), 1315.

[120] N. N. Edavalath, M. C. Günendi, R. Beravat, G. K. L. Wong, M. H. Frosz et al. *Higher-order mode suppression in twisted single-ring hollow-core photonic crystal fibers.* Optics Letters **42** (2017), 2074.

[121] Y. Tang, A. E. Cohen. *Enhanced Enantioselectivity in Excitation of Chiral Molecules by Superchiral Light.* Science **332** (2011), 333–336.

[122] C. N. Alexeyev, M. A. Yavorsky. *Generation and conversion of optical vortices in long-period helical core optical fibers.* Physical Review A **78** (2008), 043828.

[123] C. N. Alexeyev, A. N. Alexeyev, B. P. Lapin, G. Milione, M. A. Yavorsky. *Spin-orbit-interaction-induced generation of optical vortices in multihelicoidal fibers.* Physical Review A **88** (2013), 063814.

[124] H. Xu, L. Yang. *Conversion of orbital angular momentum of light in chiral fiber gratings.* Optics Letters **38** (2013), 1978.

[125] R. P. Sopalla, G. K. L. Wong, N. Y. Joly, M. H. Frosz, X. Jiang et al. *Generation of broadband circularly polarized supercontinuum light in twisted photonic crystal fibers.* Optics Letters **44** (2019), 3964–3967.

[126] S. Davtyan, D. Novoa, Y. Chen, M. H. Frosz, P. St. J. Russell. *Polarization-Tailored Raman Frequency Conversion in Chiral Gas-Filled Hollow-Core Photonic Crystal Fibers.* Physical Review Letters **122** (2019), 143902.

[127] D. J. Griffiths. *Introduction to Electrodynamics.* Cambridge University Press, 4th ed. (2017).

[128] L. Novotny, B. Hecht. *Principles of Nano-Optics.* Cambridge University Press, 2nd ed. (2012).

[129] S. A. Maier. *Plasmonics: Fundamentals and Applications.* Springer US (2007).

[130] R. W. Boyd. *Nonlinear Optics.* Elsevier, 3rd ed. (2008).

[131] A. W. Snyder, J. D. Love. *Optical Waveguide Theory.* Chapman and Hall (1983).

[132] A. K. Ghatak. *Leaky modes in optical waveguides.* Optical and Quantum Electronics **17** (1985), 311–321.

[133] D. J. Griffiths, D. F. Schroeter. *Introduction to Quantum Mechanics.* Cambridge University Press, 3rd ed. (2018).

[134] K. Yang, M. de Llano. *Simple variational proof that any two-dimensional potential well supports at least one bound state.* American Journal of Physics **57** (1989), 85–86.

[135] K. Okamoto. *Fundamentals of Optical Waveguides.* Elsevier, 2nd ed. (2006).

[136] R. Paschotta. *Field Guide to Optical Fiber Technology.* SPIE (2010).

[137] M. Born, E. Wolf. *Principles of Optics: 60th Anniversary Edition.* Cambridge University Press, 7th ed. (2019).

[138] R. E. Collin. *Field Theory of Guided Waves.* IEEE Press, 2nd ed. (1991).

[139] Z. Zhang, Y. Shi, B. Bian, J. Lu. *Dependence of leaky mode coupling on loss in photonic crystal fiber with hybrid cladding.* Optics Express **16** (2008), 1915.

[140] E. Kamenetskii, A. Sadreev, A. Miroshnichenko, eds. *Fano Resonances in Optics and Microwaves: Physics and Applications.* Springer International Publishing (2018).

[141] X. Xi. *Helically Twisted Solid-Core Photonic Crystal Fibers.* Ph.D. thesis, University of Erlangen–Nuremberg (FAU) (2015).

[142] J. Wiersig. *Review of exceptional point-based sensors.* Photonics Research **8** (2020), 1457–1467.

[143] N. B. Simpson, K. Dholakia, L. Allen, M. J. Padgett. *Mechanical equivalence of spin and orbital angular momentum of light: An optical spanner.* Optics Letters **22** (1997), 52–54.

[144] R. P. Feynman, R. B. Leighton, M. L. Sands. *The Feynman Lectures on Physics.* Basic Books, new millennium ed. (2011).

[145] L. Marrucci, C. Manzo, D. Paparo. *Optical Spin-to-Orbital Angular Momentum Conversion in Inhomogeneous Anisotropic Media.* Physical Review Letters **96** (2006), 163905.

[146] S. J. Orfanidis. *Electromagnetic Waves and Antennas.* Sophocles J. Orfanidis (2016).

[147] M. L. Degl'Innocenti, M. Landolfi. *Polarization in Spectral Lines.* Springer Science & Business Media (2006).

[148] H. G. Berry, G. Gabrielse, A. E. Livingston. *Measurement of the Stokes parameters of light.* Applied Optics **16** (1977), 3200–3205.

[149] B. Schaefer, E. Collett, R. Smyth, D. Barrett, B. Fraher. *Measuring the Stokes polarization parameters.* American Journal of Physics **75** (2007), 163–168.

[150] K. Y. Bliokh, A. Y. Bekshaev, F. Nori. *Extraordinary momentum and spin in evanescent waves.* Nature Communications **5** (2014), 3300.

[151] J. J. Gil, A. T. Friberg, A. Norrman, T. Setälä. *Effect of polarimetric nonregularity on the spin of three-dimensional polarization states.* New Journal of Physics **23** (2021), 063059.

[152] L. Allen, M. W. Beijersbergen, R. J. C. Spreeuw, J. P. Woerdman. *Orbital angular momentum of light and the transformation of Laguerre-Gaussian laser modes.* Physical Review A **45** (1992), 8185–8189.

[153] T. Doster, A. T. Watnik. *Laguerre–Gauss and Bessel–Gauss beams propagation through turbulence: Analysis of channel efficiency.* Applied Optics **55** (2016), 10239–10246.

[154] A. Rubano, F. Cardano, B. Piccirillo, L. Marrucci. *Q-plate technology: A progress review [Invited].* Journal of the Optical Society of America B **36** (2019), D70.

[155] H. He, M. E. J. Friese, N. R. Heckenberg, H. Rubinsztein-Dunlop. *Direct Observation of Transfer of Angular Momentum to Absorptive Particles from a Laser Beam with a Phase Singularity.* Physical Review Letters **75** (1995), 826–829.

[156] A. T. O'Neil, I. MacVicar, L. Allen, M. J. Padgett. *Intrinsic and Extrinsic Nature of the Orbital Angular Momentum of a Light Beam.* Physical Review Letters **88** (2002), 053601.

[157] A. M. Yao, M. J. Padgett. *Orbital angular momentum: Origins, behavior and applications.* Advances in Optics and Photonics **3** (2011), 161.

[158] S. Ramachandran, P. Kristensen. *Optical vortices in fiber.* Nanophotonics **2** (2013), 455–474.

[159] Qing Wang, O. Ronneberger, H. Burkhardt. *Rotational Invariance Based on Fourier Analysis in Polar and Spherical Coordinates.* IEEE Transactions on Pattern Analysis and Machine Intelligence **31** (2009), 1715–1722.

[160] M. V. Berry. *Paraxial beams of spinning light.* In: *International Conference on Singular Optics*, vol. 3487, 6–11. SPIE (1998).

[161] K. Y. Bliokh, F. J. Rodríguez-Fortuño, F. Nori, A. V. Zayats. *Spin–orbit interactions of light.* Nature Photonics **9** (2015), 796–808.

[162] J. W. Simmons, M. J. Guttmann. *States, Waves, and Photons: A Modern Introduction to Light.* Addison-Wesley Publishing Company (1970).

[163] J. D. Jackson. *Classical Electrodynamics.* Wiley, 3rd ed. (1999).

[164] S. M. Barnett. *Optical angular-momentum flux.* Journal of Optics B: Quantum and Semiclassical Optics **4** (2001), S7.

[165] J. E. Vázquez-Lozano, A. Martínez. *Optical Chirality in Dispersive and Lossy Media.* Physical Review Letters **121** (2018), 043901.

[166] L. D. Barron. *Molecular Light Scattering and Optical Activity.* Cambridge University Press, 2nd ed. (2004).

[167] Y. Inoue, V. Ramamurthy. *Chiral Photochemistry.* CRC Press, 1st ed. (2004).

[168] P. L. Overfelt. *Helical localized wave solutions of the scalar wave equation.* JOSA A **18** (2001), 1905–1911.

[169] W. Kühnel. *Differential Geometry: Curves, Surfaces, Manifolds.* American Mathematical Society, 3rd ed. (2015).

[170] *The right-hand grip rule (SVG graphic).* https://commons.wikimedia.org/wiki/File:Right-hand_grip_rule.svg [Wikimedia Commons, author: Schorschi2, part of public domain, accessed 16-Dec-2023].

[171] A. Nicolet, F. Zolla, Y. Ould Agha, S. Guenneau. *Geometrical transformations and equivalent materials in computational electromagnetism.* COMPEL - The international journal for computation and mathematics in electrical and electronic engineering **27** (2008), 806–819.

[172] A. Nicolet, F. Zolla, Y. O. Agha, S. Guenneau. *Leaky modes in twisted microstructured optical fibers.* Waves in Random and Complex Media **17** (2007), 559–570.

[173] R. S. Alassar, M. A. Abushoshah. *Divergence and Curl Operators in Skew Coordinates.* International Journal of Modeling and Optimization **5** (2015), 198–201.

[174] K. Y. Bliokh, A. Niv, V. Kleiner, E. Hasman. *Geometrodynamics of spinning light.* Nature Photonics **2** (2008), 748–753.

[175] Y. K. Kato, R. C. Myers, A. C. Gossard, D. D. Awschalom. *Observation of the Spin Hall Effect in Semiconductors.* Science **306** (2004), 1910–1913.

[176] J. Wunderlich, B. Kaestner, J. Sinova, T. Jungwirth. *Experimental Observation of the Spin-Hall Effect in a Two-Dimensional Spin-Orbit Coupled Semiconductor System.* Physical Review Letters **94** (2005), 047204.

[177] V. S. Liberman, B. Ya. Zel'dovich. *Spin-orbit interaction of a photon in an inhomogeneous medium.* Physical Review A **46** (1992), 5199–5207.

[178] K. Yu. Bliokh, Yu. P. Bliokh. *Topological spin transport of photons: The optical Magnus effect and Berry phase.* Physics Letters A **333** (2004), 181–186.

[179] M. Onoda, S. Murakami, N. Nagaosa. *Hall Effect of Light.* Physical Review Letters **93** (2004), 083901.

[180] X. Yin, Z. Ye, J. Rho, Y. Wang, X. Zhang. *Photonic Spin Hall Effect at Metasurfaces.* Science **339** (2013), 1405–1407.

[181] K. Yu. Bliokh, Yu. P. Bliokh. *Modified geometrical optics of a smoothly inhomogeneous isotropic medium: The anisotropy, Berry phase, and the optical Magnus effect.* Physical Review E **70** (2004), 026605.

[182] V. G. Fedoseyev. *Spin-independent transverse shift of the centre of gravity of a reflected and of a refracted light beam.* Optics Communications (2001).

[183] K. Y. Bliokh. *Geometrical Optics of Beams with Vortices: Berry Phase and Orbital Angular Momentum Hall Effect.* Physical Review Letters **97** (2006), 043901.

[184] K. Y. Bliokh, I. V. Shadrivov, Y. S. Kivshar. *Goos–Hänchen and Imbert–Fedorov shifts of polarized vortex beams.* Optics Letters **34** (2009), 389–391.

[185] V. G. Fedoseyev. *Transformation of the orbital angular momentum at the reflection and transmission of a light beam on a plane interface.* Journal of Physics A: Mathematical and Theoretical **41** (2008), 505202.

[186] S. Burger, J. Pomplun, F. Schmidt. *Finite Element Methods for Computational Nano-optics.* In: *Encyclopedia of Nanotechnology*, 837–843. Springer Netherlands, 1st ed. (2012).

[187] P. Gutsche. *Convergence Study of the Fourier Modal Method for Nano-optical Scattering Problems in Comparison with the Finite Element Method.* Diploma thesis, Eberhard Karl University of Tübingen (2014).

[188] J.-P. Berenger. *A perfectly matched layer for the absorption of electromagnetic waves.* Journal of Computational Physics **114** (1994), 185–200.

[189] F. Teixeira, W. Chew. *General closed-form PML constitutive tensors to match arbitrary bianisotropic and dispersive linear media.* IEEE Microwave and Guided Wave Letters **8** (1998), 223–225.

[190] W. C. Chew, W. H. Weedon. *A 3D perfectly matched medium from modified Maxwell's equations with stretched coordinates.* Microwave and Optical Technology Letters **7** (1994), 599–604.

[191] A. Taflove, S. C. Hagness, M. Piket-May. *9 - Computational Electromagnetics: The Finite-Difference Time-Domain Method.* In: *The Electrical Engineering Handbook*, 629–670. Academic Press, 1st ed. (2005).

[192] K. Yee. *Numerical solution of initial boundary value problems involving Maxwell's equations in isotropic media.* IEEE Transactions on Antennas and Propagation **14** (1966), 302–307.

[193] R. Rumpf. *Computational Electromagnetics.* https://empossible.net/academics/emp5337/ [accessed 16-Dec-2023].

[194] M. Schmid, D. Ludescher, H. Giessen. *Optical properties of photoresists for femtosecond 3D printing: Refractive index, extinction, luminescence-dose dependence, aging, heat treatment and comparison between 1-photon and 2-photon exposure.* Optical Materials Express **9** (2019), 4564.

[195] *Parameter Reference of JCMsuite.* https://jcmwave.com/docs/ParameterReference/fa3cd37e2f1089b31108925aa4fdea56.html?version=4.4.0 [accessed 16-Dec-2023].

[196] V. Hahn, F. Mayer, M. Thiel, M. Wegener. *3-D Laser Nanoprinting.* Optics and Photonics News **30** (2019), 28–35.

[197] L. Yang, F. Mayer, U. H. F. Bunz, E. Blasco, M. Wegener. *Multi-material multi-photon 3D laser micro- and nanoprinting.* Light: Advanced Manufacturing **2** (2021), 17.

[198] L. Jonušauskas, D. Gailevičius, S. Rekštytė, T. Baldacchini, S. Juodkazis et al. *Mesoscale laser 3D printing.* Optics Express **27** (2019), 15205.

[199] *NanoGuide (Knowledge database from Nanoscribe GmbH).* https://support.nanoscribe.com/hc/en-gb [accessed 16-Dec-2023].

[200] C. N. LaFratta, J. T. Fourkas, T. Baldacchini, R. A. Farrer. *Multiphoton Fabrication.* Angewandte Chemie International Edition **46** (2007), 6238–6258.

[201] V. F. Paz, M. Emons, K. Obata, A. Ovsianikov, S. Peterhänsel et al. *Development of functional sub-100 nm structures with 3D two-photon polymerization technique and optical methods for characterization.* Journal of Laser Applications **24** (2012), 042004.

[202] D. Tan, Y. Li, F. Qi, H. Yang, Q. Gong et al. *Reduction in feature size of two-photon polymerization using SCR500.* Applied Physics Letters **90** (2007), 071106.

[203] J. Fischer, M. Wegener. *Three-dimensional optical laser lithography beyond the diffraction limit.* Laser & Photonics Reviews **7** (2013), 22–44.

[204] J. Fischer, M. Wegener. *Three-dimensional direct laser writing inspired by stimulated-emission-depletion microscopy [Invited].* Optical Materials Express **1** (2011), 614–624.

[205] Y. Liu, H. Wang, J. Ho, R. C. Ng, R. J. H. Ng et al. *Structural color three-dimensional printing by shrinking photonic crystals.* Nature Communications **10** (2019), 4340.

[206] V. Hahn, P. Kiefer, T. Frenzel, J. Qu, E. Blasco et al. *Rapid Assembly of Small Materials Building Blocks (Voxels) into Large Functional 3D Metamaterials.* Advanced Functional Materials **30** (2020), 1907795.

[207] V. Hahn, P. Kiefer, T. Frenzel, J. Qu, E. Blasco et al. *Comparing 3D Printers.* https://3dprintingspeed.aph.kit.edu/ [accessed 16-Dec-2023].

[208] L. Keller, M. Huth. *Pattern generation for direct-write three-dimensional nanoscale structures via focused electron beam induced deposition.* Beilstein Journal of Nanotechnology **9** (2018), 2581–2598.

[209] W. Jung, Y.-H. Jung, P. V. Pikhitsa, J. Feng, Y. Yang et al. *Three-dimensional nanoprinting via charged aerosol jets.* Nature **592** (2021), 54–59.

[210] A. Franzen. *Gwoptics component library.* http://www.gwoptics.org/ComponentLibrary/ [licensed under Creative Commons Attribution-NonCommercial 3.0, accessed 16-Dec-2023] (2006).

[211] J. Bürger, V. Schalles, J. Kim, B. Jang, M. Zeisberger et al. *3D-Nanoprinted Antiresonant Hollow-Core Microgap Waveguide: An on-Chip Platform for Integrated Photonic Devices and Sensors.* ACS Photonics **9** (2022), 3012–3024.

[212] M. Zeisberger, M. A. Schmidt. *Analytic model for the complex effective index of the leaky modes of tube-type anti-resonant hollow core fibers.* Scientific Reports **7** (2017), 11761.

[213] P. Yariv, A; Yeh. *Optical Waves in Crystals: Propagation and Control of Laser Radiation.* Wiley, New York (1984).

[214] N. M. Litchinitser, A. K. Abeeluck, C. Headley, B. J. Eggleton. *Antiresonant reflecting photonic crystal optical waveguides.* Optics Letters **27** (2002), 1592–1594.

[215] A. Hartung, J. Kobelke, A. Schwuchow, K. Wondraczek, J. Bierlich et al. *Double antiresonant hollow core fiber – guidance in the deep ultraviolet by modified tunneling leaky modes.* Optics Express **22** (2014), 19131–19140.

[216] Philip Russell. *Photonic crystal fibers.* Science **299** (2003), 358–362.

[217] R. Sollapur, D. Kartashov, M. Zuerch, A. Hoffmann, T. Grigorova et al. *Resonance-enhanced multi-octave supercontinuum generation in antiresonant hollow-core fibers.* Light: Science & Applications **6** (2017), e17124.

[218] A. D. Pryamikov, A. S. Biriukov, A. F. Kosolapov, V. G. Plotnichenko, S. L. Semjonov et al. *Demonstration of a waveguide regime for a silica hollow - core microstructured optical fiber with a negative curvature of the core boundary in the spectral region > 3.5 μm.* Optics Express **19** (2011), 1441–1448.

[219] R. F. Ando, A. Hartung, B. Jang, M. A. Schmidt. *Approximate model for analyzing band structures of single-ring hollow-core anti-resonant fibers.* Optics Express **27** (2019), 10009–10021.

[220] A. D. Pryamikov, G. K. Alagashev, A. F. Kosolapov, A. S. Biriukov. *Impact of core-cladding boundary shape on the waveguide properties of hollow core microstructured fibers.* Laser Physics **26** (2016), 125104.

[221] G. Merkininkaitė, E. Aleksandravičius, M. Malinauskas, D. Gailevičius, S. Šakirzanovas et al. *Laser additive manufacturing of Si/ZrO_2 tunable crystalline phase 3D nanostructures.* Opto-Electronic Advances **5** (2022), 210077–210077.

[222] D. Gonzalez-Hernandez, S. Varapnickas, G. Merkininkaitė, A. Čiburys, D. Gailevičius et al. *Laser 3D Printing of Inorganic Free-Form Micro-Optics.* Photonics **8** (2021), 577.

[223] G. Konstantinou, E. Kakkava, L. Hagelüken, P. V. Warriam Sasikumar, J. Wang et al. *Additive micro-manufacturing of crack-free PDCs by two-photon polymerization of a single, low-shrinkage preceramic resin.* Additive Manufacturing **35** (2020), 101343.

[224] L. Brigo, J. E. M. Schmidt, A. Gandin, N. Michieli, P. Colombo et al. *3D nanofabrication of SiOC ceramic structures.* Advanced Science **5** (2018), 1800937.

[225] A. Vyatskikh, R. C. Ng, B. Edwards, R. M. Briggs, J. R. Greer. *Additive manufacturing of high-refractive-index, nanoarchitected titanium dioxide for 3D dielectric photonic crystals.* Nano Letters **20** (2020), 3513–3520.

[226] S. G. Johnson, M. L. Povinelli, M. Soljačić, A. Karalis, S. Jacobs et al. *Roughness losses and volume-current methods in photonic-crystal waveguides.* Applied Physics B **81** (2005), 283–293.

[227] E. N. Fokoua, F. Poletti, D. J. Richardson. *Analysis of light scattering from surface roughness in hollow-core photonic bandgap fibers.* Optics Express **20** (2012), 20980–20991.

[228] D. Yin, H. Schmidt, J. P. Barber, E. J. Lunt, A. R. Hawkins. *Optical characterization of arch-shaped ARROW waveguides with liquid cores.* Optics Express **13** (2005), 10564–10570.

[229] R. Bernini, E. Nuccio, A. Minardo, L. Zeni, P. Sarro. *Integrated silicon optical sensors based on hollow core waveguide.* Proc. SPIE 6477, Silicon Photonics II **6477** (2007), 647714.

[230] R. Bernini, S. Campopiano, L. Zeni, P. M. Sarro. *ARROW optical waveguides based sensors.* Sensors and Actuators, B: Chemical **100** (2004), 143–146.

[231] W. Yang, D. Conkey, B. Wu, D. Yin, A. Hawkins et al. *Atomic spectroscopy on a chip.* Nature Photonics **1** (2007), 331–335.

[232] H. Schmidt, A. R. Hawkins. *Optofluidic waveguides: I. Concepts and implementations.* Microfluidics and Nanofluidics **4** (2008), 3–16.

[233] R. Förster, S. Weidlich, M. Nissen, T. Wieduwilt, J. Kobelke et al. *Tracking and analyzing the brownian motion of nano-objects inside hollow core fibers.* ACS Sensors **5** (2020), 879–886.

[234] S. E. Braslavsky. *Glossary of terms used in photochemistry, (IUPAC Recommendations 2006).* Pure and Applied Chemistry **79** (2007), 293–465.

[235] H. Gnewuch, H. Renner. *Mode-independent attenuation in evanescent-field sensors.* Applied Optics **34** (1995), 1473–1483.

[236] *HITRAN database.* https://hitran.org/ [accessed 16-Dec-2023].

[237] K. Sung, L. Brown, X. Huang, D. Schwenke, T. Lee et al. *Extended line positions, intensities, empirical lower state energies and quantum assignments of NH_3 from 6300 to 7000 cm^{-1}.* Journal of Quantitative Spectroscopy & Radiative Transfer **113** (2012), 1066–1083.

[238] M. E. Webber. *Diode Laser Measurements of Ammonia and Carbon Dioxide for Combustion and Bioreactor Applications.* Ph.D. thesis, Stanford University (2001).

[239] M. E. Webber, D. S. Baer, R. K. Hanson. *Ammonia monitoring near 1.5 μm with diode-laser absorption sensors.* Applied Optics **40** (2001), 2031–2042.

[240] J. Kim, J. Bürger, B. Jang, M. Zeisberger, J. Gargiulo et al. *3D-nanoprinted on-chip antiresonant waveguide with hollow core and microgaps for integrated optofluidic spectroscopy.* Optics Express **31** (2023), 2833–2845.

[241] N. M. Litchinitser, S. C. Dunn, B. Usner, B. J. Eggleton, T. P. White et al. *Resonances in microstructured optical waveguides.* Optics Express **11** (2003), 1243–1251.

[242] Z. Yu, S. Fan. *Extraordinarily high spectral sensitivity in refractive index sensors using multiple optical modes.* Optics Express **19** (2011), 10029–10040.

[243] J. Homola, S. S. Yee, G. Gauglitz. *Surface plasmon resonance sensors: Review.* Sensors and Actuators B: Chemical **54** (1999), 3–15.

[244] J. Kim, R. Förster, T. Wieduwilt, B. Jang, J. Bürger et al. *Locally Structured On-Chip Optofluidic Hollow-Core Light Cages for Single Nanoparticle Tracking.* ACS Sensors **7** (2022), 2951–2959.

[245] H. Du, R.-C. A. Fuh, J. Li, L. A. Corkan, J. S. Lindsey. *PhotochemCAD: A computer-aided design and research tool in photochemistry.* Photochemistry and Photobiology **68** (1998), 141–142.

[246] E. L. Cussler. *Diffusion: Mass Transfer in Fluid Systems.* Cambridge University Press, New York, 2nd ed. (1997).

[247] U. Dragosits, M. Theobald, C. Place, E. Lord, J. Webb et al. *Ammonia emission, deposition and impact assessment at the field scale: A case study of sub-grid spatial variability.* Environmental Pollution **117** (2002), 147–158.

[248] J. Wang, W. Zhang, L. Li, Q. Yu. *Breath ammonia detection based on tunable fiber laser photoacoustic spectroscopy.* Applied Physics B: Photophysics and Laser Chemistry **103** (2011), 263–269.

[249] B. Timmer, W. Olthuis, A. van den Berg. *Ammonia sensors and their applications—a review.* Sens. Actuators, B **107** (2005), 666–677.

[250] N. Matsuda, A. Takatsu, K. Kato. *Absorption spectra of rhodamine 6G by slab optical waveguide spectroscopy.* Chemistry Letters **25** (1996), 105–106.

[251] D. J. Sirbuly, A. Tao, M. Law, R. Fan, P. Yang. *Multifunctional nanowire evanescent wave optical sensors.* Advanced Materials **19** (2007), 61–66.

[252] L. Jiang, S. Pau. *Integrated waveguide with a microfluidic channel in spiral geometry for spectroscopic applications.* Applied Physics Letters **90** (2007), 111108.

[253] L. Kröckel, T. Frosch, M. A. Schmidt. *Multiscale spectroscopy using a monolithic liquid core waveguide with laterally attached fiber ports.* Analytica Chimica Acta **875** (2015), 1–6.

[254] M. Nikodem, G. Gomółka, M. Klimczak, D. Pysz, R. Buczyński. *Demonstration of mid-infrared gas sensing using an anti-resonant hollow core fiber and a quantum cascade laser.* Optics Express **27** (2019), 36350–36357.

[255] J. Bürger, J. Kim, B. Jang, J. Gargiulo, M. A. Schmidt et al. *Ultrahigh-aspect-ratio light cages: Fabrication limits and tolerances of free-standing 3D nanoprinted waveguides.* Optical Materials Express **11** (2021), 1046.

[256] I. Bufetov, A. Kosolapov, A. Pryamikov, A. Gladyshev, A. Kolyadin et al. *Revolver hollow core optical fibers.* Fibers **6** (2018), 39.

[257] T. A. Birks, G. J. Pearce, D. M. Bird. *Approximate band structure calculation for photonic bandgap fibres.* Optics Express **14** (2006), 9483–9490.

[258] T. P. White, R. C. McPhedran, C. M. de Sterke, N. M. Litchinitser, B. J. Eggleton. *Resonance and scattering in microstructured optical fibers.* Optics Letters **27** (2002), 1977–1979.

[259] D. Pudis, M. Goraus, P. Urbancova. *Optical properties of woodpile structures for application on the surface of photonic devices.* Applied Surface Science **461** (2018), 227–232.

[260] J. Lölsberg, A. Cinar, D. Felder, G. Linz, S. Djeljadini et al. *Two-photon vertical-flow lithography for microtube synthesis.* Small **15** (2019), 1901356.

[261] W. H. Teh, U. Dürig, U. Drechsler, C. G. Smith, H.-J. Güntherodt. *Effect of low numerical-aperture femtosecond two-photon absorption on (SU-8) resist for ultrahigh-aspect-ratio microstereolithography.* Journal of Applied Physics **97** (2005), 054907.

[262] K. Vanmol, S. Tuccio, V. Panapakkam, H. Thienpont, J. Watté et al. *Two-photon direct laser writing of beam expansion tapers on single-mode optical fibers.* Optics & Laser Technology **112** (2019), 292–298.

[263] M. Kavaldzhiev, J. E. Perez, Y. Ivanov, A. Bertoncini, C. Liberale et al. *Biocompatible 3D printed magnetic micro needles.* Biomedical Physics & Engineering Express **3** (2017), 025005.

[264] P.-I. Dietrich, R. J. Harris, M. Blaicher, M. K. Corrigan, T. J. Morris et al. *Printed freeform lens arrays on multi-core fibers for highly efficient coupling in astrophotonic systems.* Optics Express **25** (2017), 18288–18295.

[265] J. C. Ramirez, J. N. Schianti, M. G. Almeida, A. Pavani, R. R. Panepucci et al. *Low-loss modified SU-8 waveguides by direct laser writing at 405 nm.* Optical Materials Express **7** (2017), 2651–2659.

[266] H. Wei, S. Krishnaswamy. *Direct laser writing of a phase-shifted Bragg grating waveguide for ultrasound detection.* Optics Letters **44** (2019), 3817–3820.

[267] G. Testa, G. Persichetti, R. Bernini. *Liquid core ARROW waveguides: A promising photonic structure for integrated optofluidic microsensors.* Micromachines **7** (2016), 47.

[268] M. A. Schmidt, N. Granzow, N. Da, M. Peng, L. Wondraczek et al. *All-solid bandgap guiding in tellurite-filled silica photonic crystal fibers.* Optics Letters **34** (2009), 1946–1948.

[269] M. Sumetsky, Y. Dulashko. *Radius variation of optical fibers with angstrom accuracy.* Optics Letters **35** (2010), 4006–4008.

[270] J. Purtov, A. Verch, P. Rogin, R. Hensel. *Improved development procedure to enhance the stability of microstructures created by two-photon polymerization.* Microelectronic Engineering **194** (2018), 45–50.

[271] E. D. Lemma, F. Rizzi, T. Dattoma, B. Spagnolo, L. Sileo et al. *Mechanical Properties Tunability of Three-Dimensional Polymeric Structures in Two-Photon Lithography.* IEEE Transactions on Nanotechnology **16** (2017), 23–31.

[272] J. Kim, B. Jang, T. Wieduwilt, S. C. Warren-Smith, J. Bürger et al. *On-chip fluorescence detection using photonic bandgap guiding optofluidic hollow-core light cage.* APL Photonics **7** (2022), 106103.

[273] A. Shahzad, M. Knapp, M. Edetsberger, M. Puchinger, E. Gaubitzer et al. *Diagnostic Application of Fluorescence Spectroscopy in Oncology Field: Hopes and Challenges.* Applied Spectroscopy Reviews **45** (2010), 92–99.

[274] J. Cheong, H. Yu, C. Y. Lee, J.-u. Lee, H.-J. Choi et al. *Fast detection of SARS-CoV-2 RNA via the integration of plasmonic thermocycling and fluorescence detection in a portable device.* Nature Biomedical Engineering **4** (2020), 1159–1167.

[275] J. R. Lakowicz, ed. *Principles of Fluorescence Spectroscopy.* Springer US, Boston, MA (2006).

[276] M. A. Rizzo, G. H. Springer, B. Granada, D. W. Piston. *An improved cyan fluorescent protein variant useful for FRET.* Nature Biotechnology **22** (2004), 445–449.

[277] F. del Monte, D. Levy. *Formation of Fluorescent Rhodamine B J-Dimers in Sol-Gel Glasses Induced by the Adsorption Geometry on the Silica Surface.* The Journal of Physical Chemistry B **102** (1998), 8036–8041.

[278] K. Kemnitz, N. Tamai, I. Yamazaki, N. Nakashima, K. Yoshihara. *Fluorescence decays and spectral properties of rhodamine B in submono-, mono-, and multilayer systems.* The Journal of Physical Chemistry **90** (1986), 5094–5101.

[279] A. Karabchevsky, A. Katiyi, A. S. Ang, A. Hazan. *On-chip nanophotonics and future challenges.* Nanophotonics **9** (2020), 3733–3753.

[280] J. Kim. *Investigation of 3D Nano Printed On-Chip Hollow Core Waveguides.* Ph.D. thesis, Friedrich Schiller University Jena (2023).

[281] J. Bürger, A. C. Valero, T. Weiss, S. A. Maier, M. A. Schmidt. *Impact of coordinate frames on mode formation in twisted waveguides.* arXiv (2023), 2311.15770.

[282] J. Qian, C. Hussey. *Circular birefringence in helical-core fibre.* Electronics Letters **22** (1986), 515–517.

[283] M. V. Berry. *Interpreting the anholonomy of coiled light.* Nature **326** (1987), 277–278.

[284] B. O'Neill, ed. *Elementary Differential Geometry.* Academic Press, Boston, 2nd ed. (2006).

[285] J. F. Bauters, M. J. R. Heck, D. D. John, J. S. Barton, C. M. Bruinink et al. *Planar waveguides with less than 0.1 dB/m propagation loss fabricated with wafer bonding.* Optics Express **19** (2011), 24090–24101.

[286] D. Dai, J. Bauters, J. E. Bowers. *Passive technologies for future large-scale photonic integrated circuits on silicon: Polarization handling, light non-reciprocity and loss reduction.* Light: Science & Applications **1** (2012), e1.

[287] H. Lee, T. Chen, J. Li, O. Painter, K. J. Vahala. *Ultra-low-loss optical delay line on a silicon chip.* Nature Communications **3** (2012), 867.

[288] M. V. Berry. *Quantal Phase Factors Accompanying Adiabatic Changes.* Proceedings of the Royal Society of London. Series A, Mathematical and Physical Sciences **392** (1984), 45–57.

[289] A. Tomita, R. Y. Chiao. *Observation of Berry's Topological Phase by Use of an Optical Fiber.* Physical Review Letters **57** (1986), 937–940.

[290] R. Y. Chiao, Y.-S. Wu. *Manifestations of Berry's Topological Phase for the Photon.* Physical Review Letters **57** (1986), 933–936.

[291] D. Soh, J. Nilsson, J. Sahu, L. Cooper. *Geometrical factor modification of helical-core fiber radiation loss formula.* Optics Communications **222** (2003), 235–242.

[292] G. Shvets, S. Trendafilov, V. I. Kopp, D. Neugroschl, A. Z. Genack. *Polarization properties of chiral fiber gratings.* Journal of Optics A: Pure and Applied Optics **11** (2009), 074007.

[293] D. Marcuse. *Field deformation and loss caused by curvature of optical fibers.* Journal of the Optical Society of America **66** (1976), 311.

[294] M. Heiblum, J. Harris. *Analysis of curved optical waveguides by conformal transformation.* IEEE Journal of Quantum Electronics **11** (1975), 75–83.

[295] R. T. Schermer, J. H. Cole. *Improved Bend Loss Formula Verified for Optical Fiber by Simulation and Experiment.* IEEE Journal of Quantum Electronics **43** (2007), 899–909.

[296] A. Lorenz. *Modenstabilität Optischer Fasern Mit Geringem Brechzahlkontrast.* Diploma thesis, Friedrich Schiller University Jena (2011).

[297] X. Jiao, H. Zhang, X. Zhang, H. Li, J. Wei et al. *Performance of circular photonic crystal fiber transmitting orbital angular momentum modes under macro-bending.* Journal of Optics **21** (2019), 065703.

[298] H. Yan, S. Li, Z. Xie, X. Zheng, C. Du et al. *Deformation of orbital angular momentum modes in bending ring-core fiber.* Chinese Optics Letters **15** (2017), 030501–30505.

[299] D. Marcuse. *Curvature loss formula for optical fibers.* JOSA **66** (1976), 216–220.

[300] E. A. J. Marcatili. *Bends in Optical Dielectric Guides.* Bell System Technical Journal **48** (1969), 2103–2132.

[301] R. W. Smink, B. P. De Hon, A. G. Tijhuis. *Bending loss in optical fibers—a full-wave approach.* Journal of the Optical Society of America B **24** (2007), 2610.

[302] A. Aiello, P. Banzer, M. Neugebauer, G. Leuchs. *From transverse angular momentum to photonic wheels.* Nature Photonics **9** (2015), 789–795.

[303] P. Lodahl, S. Mahmoodian, S. Stobbe, A. Rauschenbeutel, P. Schneeweiss et al. *Chiral quantum optics.* Nature **541** (2017), 473–480.

[304] A. M. Smith. *Polarization and magnetooptic properties of single-mode optical fiber.* Applied Optics **17** (1978), 52.

[305] M. C. Rechtsman, J. M. Zeuner, Y. Plotnik, Y. Lumer, D. Podolsky et al. *Photonic Floquet topological insulators.* Nature **496** (2013), 196–200.

[306] A. Szameit, S. Nolte. *Discrete optics in femtosecond-laser-written photonic structures.* Journal of Physics B: Atomic, Molecular and Optical Physics **43** (2010), 163001.

[307] S. Gross, M. J. Withford. *Ultrafast-laser-inscribed 3D integrated photonics: Challenges and emerging applications.* Nanophotonics **4** (2015), 332–352.

[308] P. S. Salter, A. Jesacher, J. B. Spring, B. J. Metcalf, N. Thomas-Peter et al. *Adaptive slit beam shaping for direct laser written waveguides.* Optics Letters **37** (2012), 470–472.

[309] P. S. Salter, M. J. Booth. *Adaptive optics in laser processing.* Light: Science & Applications **8** (2019), 110.

[310] N. Choksi, Y. Liu, R. Ghasemi, L. Qian. *Sub-megahertz spectral dip in a resonator-free twisted gain medium.* Nature Photonics **16** (2022), 498–504.

[311] S. C. Rashleigh, R. Ulrich. *Magneto-optic current sensing with birefringent fibers.* Applied Physics Letters **34** (1979), 768–770.

[312] R. Ulrich, A. Simon. *Polarization optics of twisted single-mode fibers.* Applied Optics **18** (1979), 2241.

[313] P. S. J. Russell, P. Hölzer, W. Chang, A. Abdolvand, J. C. Travers. *Hollow-core photonic crystal fibres for gas-based nonlinear optics.* Nature Photonics **8** (2014), 278–286.

[314] T. A. Birks, J. C. Knight, P. S. J. Russell. *Endlessly single-mode photonic crystal fiber.* Optics Letters **22** (1997), 961–963.

[315] T. Erdogan. *Fiber grating spectra.* Journal of Lightwave Technology **15** (1997), 1277–1294.

[316] V. A. Pivovarov, A. S. Sheremet, L. V. Gerasimov, J. Laurat, D. V. Kupriyanov. *Quantum interface between light and a one-dimensional atomic system.* Physical Review A **101** (2020), 053858.

[317] X. Ma. *Understanding and Controlling Angular Momentum Coupled Optical Waves in Chirally-Coupled-Core (CCC) Fibers.* Ph.D. thesis, University of Michigan (2011).

[318] M. Napiorkowski, W. Urbanczyk. *Role of symmetry in mode coupling in twisted microstructured optical fibers.* Optics Letters **43** (2018), 395.

[319] P. Measor, S. Kühn, E. J. Lunt, B. S. Phillips, A. R. Hawkins et al. *Multi-mode mitigation in an optofluidic chip for particle manipulation and sensing.* Optics Express **17** (2009), 24342.

[320] R. Kirchner, N. Chidambaram, M. Altana, H. Schift. *Surface smoothening of the inherent roughness of micro-lenses fabricated with 2-photon lithography.* In: *SPIE Nanophotonics Australasia 2017*, 64 (2018).

[321] B. Bai, Y. Svirko, J. Turunen, T. Vallius. *Optical activity in planar chiral metamaterials: Theoretical study.* Physical Review A **76** (2007), 023811.

[322] E. Plum, V. A. Fedotov, N. I. Zheludev. *Extrinsic electromagnetic chirality in metamaterials.* Journal of Optics A: Pure and Applied Optics **11** (2009), 074009.

[323] J. Jiménez, L. Cerdán, F. Moreno, B. L. Maroto, I. García-Moreno et al. *Chiral Organic Dyes Endowed with Circularly Polarized Laser Emission.* The Journal of Physical Chemistry C **121** (2017), 5287–5292.

[324] V. I. Kopp, Z.-Q. Zhang, A. Z. Genack. *Lasing in chiral photonic structures.* Progress in Quantum Electronics **27** (2003), 369–416.

[325] E. Plum, N. I. Zheludev. *Chiral mirrors.* Applied Physics Letters **106** (2015), 221901.

[326] K. Voronin, A. S. Taradin, M. V. Gorkunov, D. G. Baranov. *Single-Handedness Chiral Optical Cavities.* ACS Photonics **9** (2022), 2652–2659.

[327] L. Bougas, J. Byron, D. Budker, J. Williams. *Absolute optical chiral analysis using cavity-enhanced polarimetry.* Science Advances **8** (2022), eabm3749.

[328] P. Scott, X. Garcia-Santiago, D. Beutel, C. Rockstuhl, M. Wegener. *On enhanced sensing of chiral molecules in optical cavities.* Applied Physics Reviews (2020).

[329] D. Sofikitis, L. Bougas, G. E. Katsoprinakis, A. K. Spiliotis, B. Loppinet et al. *Evanescent-wave and ambient chiral sensing by signal-reversing cavity ringdown polarimetry.* Nature **514** (2014), 76–79.

[330] A. Maksimov, E. Filatov, I. I. Tartakovskii, V. Kulakovskii, S. Tikhodeev et al. *Circularly Polarized Laser Emission from an Electrically Pumped Chiral Microcavity.* Physical Review Applied **17** (2022), L021001.

[331] H. Hübener, U. De Giovannini, C. Schäfer, J. Andberger, M. Ruggenthaler et al. *Engineering quantum materials with chiral optical cavities.* Nature Materials **20** (2021), 438–442.

[332] W. H. Louisell. *Analysis of the Single Tapered Mode Coupler.* Bell System Technical Journal **34** (1955), 853–870.

[333] A. K. Taras, A. Tuniz, M. A. Bajwa, V. Ng, J. M. Dawes et al. *Shortcuts to adiabaticity in waveguide couplers–theory and implementation.* Advances in Physics: X **6** (2021), 1894978.

[334] L. Zhang, Y. Liu, Y. Zhao, T. Wang. *High Sensitivity Twist Sensor Based on Helical Long-Period Grating Written in Two-Mode Fiber.* IEEE Photonics Technology Letters **28** (2016), 1629–1632.

[335] C. G. Askins, G. A. Miller, E. J. Friebele. *Bend and twist sensing in a multi-core optical fiber.* In: *LEOS 2008 - 21st Annual Meeting of the IEEE Lasers and Electro-Optics Society*, 109–110 (2008).

[336] Y.-P. Wang, J.-P. Chen, Y.-J. Rao. *Torsion characteristics of long-period fiber gratings induced by high-frequency CO_2 laser pulses.* Journal of the Optical Society of America B **22** (2005), 1167.

[337] V. I. Kopp, V. M. Churikov, A. Z. Genack. *Synchronization of optical polarization conversion and scattering in chiral fibers.* Optics Letters **31** (2006), 571–573.

[338] B. Schwarz, P. Reininger, D. Ristanić, H. Detz, A. M. Andrews et al. *Monolithically integrated mid-infrared lab-on-a-chip using plasmonics and quantum cascade structures.* Nature Communications **5** (2014), 4085.

[339] O. Frazão, J. Santos, F. Araújo, L. Ferreira. *Optical sensing with photonic crystal fibers.* Laser & Photonics Reviews **2** (2008), 449–459.

[340] D. J. Laser, J. G. Santiago. *A review of micropumps.* Journal of Micromechanics and Microengineering **14** (2004), R35.

[341] S. Haeberle, R. Zengerle. *Microfluidic platforms for lab-on-a-chip applications.* Lab on a Chip **7** (2007), 1094–1110.

[342] D. Erickson, D. Li. *Integrated microfluidic devices.* Analytica Chimica Acta **507** (2004), 11–26.

[343] E. Verpoorte. *Microfluidic chips for clinical and forensic analysis.* Electrophoresis **23** (2002), 677–712.

[344] S. N. Bhatia, D. E. Ingber. *Microfluidic organs-on-chips.* Nature Biotechnology **32** (2014), 760–772.

[345] P. Vaiano, B. Carotenuto, M. Pisco, A. Ricciardi, G. Quero et al. *Lab on Fiber Technology for biological sensing applications: Lab on Fiber Technology for biological sensing applications.* Laser & Photonics Reviews **10** (2016), 922–961.

[346] W. Ouyang, X. Xu, W. Lu, N. Zhao, F. Han et al. *Ultrafast 3D nanofabrication via digital holography.* Nature Communications **14** (2023), 1716.

[347] V. Hahn, T. Messer, N. M. Bojanowski, E. R. Curticean, I. Wacker et al. *Two-step absorption instead of two-photon absorption in 3D nanoprinting.* Nature Photonics **15** (2021), 932–938.

[348] J. Moughames, X. Porte, M. Thiel, G. Ulliac, L. Larger et al. *Three-dimensional waveguide interconnects for scalable integration of photonic neural networks.* Optica **7** (2020), 640.

[349] Z. Chen, A. Sludds, R. Davis, I. Christen, L. Bernstein et al. *Deep learning with coherent VCSEL neural networks.* Nature Photonics **17** (2023), 723–730.

[350] X. Lin, Y. Rivenson, N. T. Yardimci, M. Veli, Y. Luo et al. *All-optical machine learning using diffractive deep neural networks.* Science **361** (2018), 1004–1008.

[351] H.-S. Zhong, H. Wang, Y.-H. Deng, M.-C. Chen, L.-C. Peng et al. *Quantum computational advantage using photons.* Science **370** (2020), 1460–1463.

[352] *Statement by the Executive Committee of the Deutsche Forschungsgemeinschaft (DFG, German Research Foundation) on the Influence of Generative Models of Text and Image Creation on Science and the Humanities and on the DFG's Funding Activities.* https://www.dfg.de/download/pdf/dfg_im_profil/geschaeftsstelle/publikationen/stellungnahmen_papiere/2023/230921_statement_executive_committee_ki_ai.pdf [accessed 16-Dec-2023].

Acknowledgements

The work presented in this thesis would not have been possible without contributions from many different people - be it in the form of bright ideas, transfer of knowledge, or companionship in solving challenging experimental problems.

First, I want to thank my supervisor **Prof. Stefan Maier** for the numerous possibilities he offered me during my whole time at the chair, learning different techniques and working on a variety of projects. The collaborative and culturally diverse atmosphere he created within just a few years after starting the chair in Munich was outstanding. Furthermore, I am sincerely grateful for his continued support during a personally difficult time, always being encouraging and leaving enough freedom to develop own ideas.

Equally, I want to thank **Prof. Markus Schmidt** for countless discussions, taking the time to look at all the results in detail, and always being able to direct me in the right direction if something did not work as planned. Markus' vast knowledge of fibers and waveguides was what made all the projects of this thesis possible. Along this line, many thanks go to all members of Markus' group I met online or during our mutual visits between Munich and Jena: **Dr. Jisoo Kim, Dr. Bumjoon Jang, Dr. Matthias Zeisberger, and Vera Schalles**. I always felt very welcome when coming to Jena and want to thank all of you for the time there.

Of course, special thanks belong to **Prof. Leonardo Menezes** for shouldering the large workload that a new optics lab brings with it. Unknowingly how Leo manages it among his other responsibilities, he was almost always present in the lab to discuss the experiments and make sure that all the equipment runs smoothly.

For his valuable advice on the theory of twisted waveguides, I want to express my gratitude to **Prof. Thomas Weiss** and all members of his group. The time in Graz was very nice and a great help in moving the project forward.

Many thanks also go to **Dr. Haoran Ren** and **Dr. Julián Gargiulo** for their guidance during the beginning of my time at the chair. For going through the pains of aligning and fine-tuning the home-built single particle circular dichroism setup with me, I want to express huge thanks to **Dr. Fedja Wendisch**, **Chenghao Fan**, and to **Prof. Seunghoon Lee** for his patience during this time.

I find it hard to list everyone who made life at the chair such a vibrant and stimulating atmosphere. A huge thanks goes to **all of my colleagues**. I wish I would have been more capable to join you during all the fun activities around Munich and elsewhere.

When everything runs smoothly, you tend to forget the huge amount of technical and administrative work that goes on in the background. Here, I want to greatly thank **Martina Edenhofer**, **Denise Wedemeyer**, **Reinhold Rath**, and **Namvar Jahanmehr** for immediately helping with all matters that you bring to them.

Many aspects of my life changed during the last few years and I cannot express enough how grateful I am to all my **friends** - both in Munich and elsewhere - for their unwavering support and encouragement. You are the best and played an essential part in the fact that this thesis exists.

Finally, **Christiane and Rainer**. What seemed normal when growing up, having someone supportive and knowledgable around you who can explain everything you ask in such detail and spark your curiosity to learn more, is now - reflecting back on this journey - something that I value very much. I am deeply grateful for the incredible parents you are and have made me who I am today.

In terms of employed tools, I acknowledge the use of the language model **ChatGPT**. It has been used in some paragraphs for: (1) generating suggestions to improve writing and readability (using prompts like "Please improve the writing style of this paragraph." or "Please shorten this paragraph to 75% of its length."), and (2) generating simple Python code (using prompts like "Can you write a multithreaded version of this section of my Python code?"). All suggestions were checked for accuracy. ChatGPT has not been used to generate specific content for the thesis. This usage is in line with the recently published guideline of the DFG (German Research Foundation) on "generative models of text and image creation in science and the humanities" [352]. The guideline clearly states that "[in] view of its considerable opportunities and development potential, the use of generative models in the context of research work should by no means be ruled out" [352].

Furthermore, the online tool **Grammarly** was used to check spelling and grammar.